



Radiation of nonequilibrium recombining plasma flows

Augustin Tibere-Inglesse

► To cite this version:

Augustin Tibere-Inglesse. Radiation of nonequilibrium recombining plasma flows. Chemical and Process Engineering. Université Paris-Saclay, 2019. English. NNT : 2019SACL077 . tel-02454286

HAL Id: tel-02454286

<https://theses.hal.science/tel-02454286>

Submitted on 24 Jan 2020

HAL is a multi-disciplinary open access archive for the deposit and dissemination of scientific research documents, whether they are published or not. The documents may come from teaching and research institutions in France or abroad, or from public or private research centers.

L'archive ouverte pluridisciplinaire **HAL**, est destinée au dépôt et à la diffusion de documents scientifiques de niveau recherche, publiés ou non, émanant des établissements d'enseignement et de recherche français ou étrangers, des laboratoires publics ou privés.

Radiation of nonequilibrium recombining plasma flows

Thèse de doctorat de l'Université Paris-Saclay
préparée à CentraleSupélec

École doctorale n°579 Sciences mécaniques et énergétiques,
Matériaux et géosciences (SMEMAG)
Spécialité de doctorat : énergétique

Thèse présentée et soutenue à Gif-sur-Yvette, le 27/09/2019 par

Augustin Tibère-Inglesse

Composition du Jury :

M. Brett Cruden	
Research Scientist, NASA Ames Research Center	Rapporteur
M. Richard Miles	
Professor, Texas A&M University	Rapporteur
Mme. Brigitte Attal-Trétout	
Directrice de Recherche, ONERA (Palaiseau)	Examinateuse
Mme. Annarita Laricchiuta	
Senior Researcher, ISTP (CNR Bari)	Examinateuse
M. Stefan Löhle	
Research Scientist, IRS (University of Stuttgart)	Examinateur
M. Richard Morgan	
Professor, University of Queensland (Center for Hypersonics)	Examinateur
Mme. Marie-Yvonne Perrin	
Directrice de Recherche, CNRS (EM2C – UPR-288)	Présidente
Christophe Laux	
Professeur, CentraleSupélec (EM2C – UPR-288)	Directeur de thèse
Sean McGuire	
Professeur, CentraleSupélec (EM2C – UPR-288)	Encadrant
Philippe Tran	
Ingénieur Expert, ArianeGroup	Invité

Random quote :

« L'utopie ne signifie pas l'irréalisable, mais l'irréalisé.
L'utopie d'hier peut devenir la réalité. »

Théodore Monod

Remerciements

Je tiens tout d'abord à remercier les professeurs et chercheurs qui ont accepté de faire partie de mon jury de thèse. Merci à Brett Cruden et à Richard Miles d'avoir accepté être mes rapporteurs et d'être venu de si loin pour participer à ma soutenance de thèse. Vos commentaires et corrections ont grandement amélioré la clarté et la qualité de mon manuscrit final. Leur nombre montre à quel point vous avez minutieusement lu mon manuscrit tout en y apportant des remarques et des améliorations très pertinentes. J'imagine que le manuscrit devait être intéressant pour y passer autant de temps, du moins c'est que j'aime à penser, et cela m'a beaucoup encouragé pour ma soutenance. Merci également à mes examinateurs, Brigitte Attal-Trétout, Stefan Löhle, Richard Morgan, Annarita Laricchiuta, Philippe Tran et Marie-Yvonne Perrin pour tous leurs commentaires positifs et toutes les discussions enrichissantes que nous avons eu pendant la soutenance. J'ai également beaucoup apprécié discuter avec vous après la soutenance, même si cela a été trop bref, je suis sûr que nous aurons l'occasion de nous recroiser. J'ai été très honoré d'avoir un jury si nombreux composé d'autant d'experts dans leurs domaines et je souhaite sincèrement vous remercier pour l'intérêt que vous avez montré pour nos recherches.

Ensuite, j'aimerais remercier ArianeGroup pour m'avoir permis de faire cette thèse. Merci notamment à mes encadrants Laurent Visconti et Philippe Tran. Laurent, merci d'avoir toujours été disponible pour moi, pour ta gentillesse et pour l'intérêt que tu as porté à nos travaux. Philippe, j'ai énormément apprécié discuter avec toi durant ma thèse. Malgré ton emploi du temps chargé, tu as toujours pris le temps de suivre ma thèse et je t'en remercie. Ta vision plus industrielle m'a vraiment forcé à questionner les intérêts et objectifs plus globaux de mes travaux. Ces questions étaient souvent parmi les plus difficiles pour moi et étaient toujours pertinentes. Je pense que ta vision de la recherche en entreprise est la bonne vision à avoir et que l'on gagnerait beaucoup à avoir plus d'ingénieurs comme toi. Enfin merci à Coumar Odéa pour toute l'aide que tu as apportée afin que cette thèse se déroule au mieux.

Ensuite j'aimerais remercier le laboratoire EM2C de m'avoir accueilli. Je remercie particulièrement Sébastien Ducruix qui en plus d'être directeur du laboratoire était également avec moi lors des Conseils Du Laboratoire (CDL). Cela a été l'occasion de beaucoup discuter et j'ai pu voir à quel point tu te souciais du bien-être des doctorants du laboratoire. Tu as toujours su nous écouter malgré ton emploi du temps chargé et je t'en remercie grandement.

Merci également aux personnels du laboratoire, les ITAs. Derrière cet acronyme barbare se cache des personnes extraordinaires qui participent grandement à la réussite de toutes les thèses. Je tiens donc à remercier Brigitte, Nathalie et Noï

pour leur réactivité et leur efficacité. Malgré ma tête en l'air, vous avez toujours été là pour m'aider, et ce dans des délais parfois courts (où j'en étais la cause évidemment). Votre soutien est d'une valeur souvent sous-estimée, autant d'un point de vue technique que moral, car je savais qu'en cas de problèmes, vous seriez là pour les résoudre. De plus, votre bonne humeur permanente est contagieuse ce qui rend les journées plus agréables. Je remercie également Yannick et Erika pour des raisons similaires. Votre aide constante nous fait gagner un temps fou, et la qualité de nos thèses est grandement augmentée par votre réactivité et votre efficacité. De même, votre gentillesse ne fait que rendre nos échanges plus faciles. Votre gestion des problèmes que j'ai pu rencontrer lors de ma thèse (torche cassée...) m'a montré votre maîtrise de la gestion des priorités et des urgences, ainsi qu'un soutien technique et moral indéniable. Je remercie également tous les autres ITAs du laboratoire, avec qui j'ai peut-être moins interagi, mais qui m'ont toujours aidé quand cela était nécessaire.

J'en viens maintenant à une des grandes forces du laboratoire, ceux qui sont toujours en première ligne : les doctorants. L'ambiance au laboratoire est une chose très importante. Une thèse connaît certainement des hauts et des bas, sans doute plus de bas que de hauts. Avoir des gens avec qui partager tout ça le rend beaucoup plus supportable. Rien de tel que de critiquer la politique de Macron pendant 10 minutes pour être de nouveau capable de travailler quelques heures de plus. Pour commencer, j'aimerais remercier Erwan avec qui j'ai débuté ma carrière dans la recherche pendant la troisième année de Centrale. J'ai pris un peu de retard par rapport à toi au début, en ne commençant pas tout de suite ma thèse, mais je suis ravi d'avoir pu combler ce retard, surtout car cela a permis que l'on reste ensemble jusqu'à la fin de ma thèse. Nos discussions et ton soutien ont toujours été indispensables. Je suis certain que nous finirons par trouver le sens de nos vies. Ensuite, merci à Pierre, qui doit faire le sale boulot et donner un sens aux résultats que j'ai pu observer. Tu dois maintenant te douter que j'ai évidemment truqué ces résultats pour te faire une blague, avoue qu'elle est quand même pas mal. Les blagues les plus courtes sont les meilleures dis-t-on, mais après m'avoir côtoyé tu dois savoir que je ne suis pas d'accord avec ça. Blague à part, merci d'avoir été là pendant tout ce temps, tu as contribué de tant de manières à ma thèse que j'aime à penser que c'est également en partie la tienne. Ta maîtrise de tant de sujets m'a impressionné et je suis sûr que cela sera apprécié et remarqué lors de ta propre soutenance. Merci ensuite à Minou pour sa bonne humeur permanente (surtout quand il est en couple), pour nos vacances (ou conférences ?) et pour son soutien. Merci aussi à Sergey pour son fatalisme assumé et sa gentillesse. Je tiens aussi à remercier le petit nouveau, Corentin, à qui je laisse la torche sans hésiter. Ta venue au laboratoire a vraiment été aussi imprévue qu'appréciée. Tu es arrivé à un moment de ma thèse pas facile et tu as toujours été d'un grand soutien. J'ai été impressionné par ta grande humanité et ta force mentale, et je suis certain que tu

réussiras tout ce que tu entreprendras. Enfin merci à toute l'équipe plasma (aussi appelée Dream Team) dans son ensemble : Fab (bien que tu sois Mélanchoniste), Arnaud (pour nos discussions sincères), Ciprian (notre futur français), Victorien (même si tu fais un peu de la combustion...), Arthur (même s'il fallait attacher tous ses équipements), Jean (a.k.a. Spiderman), Ulysse (9h → café) et Valentin (notre bouc émissaire). Ensuite, merci également à mes cobureaux : Milan, Preethi, Robin, Pédro, David et les plasmiciens déjà cité. Nos diverses formations transverses ont beaucoup aidé pour Adum. Votre soutien, surtout en fin de thèse, était inestimable. Les pauses café et le RU représentent autant de bons souvenirs et permettent de garder le moral (du moins d'essayer). Comme je commence déjà à être trop long, je vais également remercier tous les autres doctorants du labo avec qui j'ai pu discuter au RU ou lors des nombreuses pauses café. Même si je ne vous cite pas directement ici (et même si vous êtes combustionnistes), sachez que je vous aime ! Merci également aux permanents du laboratoire avec qui j'ai pu discuter et qui ont toujours été très gentils et disponibles. Un merci particulier au responsable café Aymeric Vié, et à l'espionne (et ex-polarde, maintenant prenant ses demi-journées pour remplir son rôle de maman) au rire assourdissant Bénédetta.

Ensuite je tiens à remercier mes amis pour m'avoir soutenu pendant toutes ces années. Merci tout d'abord au 3G, même si vous êtes partis de Centrale, je suis resté pour garantir la transmission de notre esprit. Merci en particulier à Maxime, Arthur et Nicolas d'avoir été là le jour J, à Armand pour m'avoir suivi en streaming (j'ai lu tes commentaires après coup, c'était bien drôle) et à tous les autres qui, je sais, aurait voulu être là. Merci à Clara de s'être levée si tôt pour pouvoir m'écouter et de m'avoir soutenu surtout à la fin de ma thèse où je n'étais pas toujours de bonne humeur. La limite entre famille et ami peut être délicate à tracer et je vais donc remercier ici Pauline, Pierre, Mathieu et Julie. Il y a de nombreuses raisons de le faire. Cette thèse n'a pas toujours été facile autant professionnellement que personnellement et vous avez toujours été là quelle que soit l'épreuve. Merci infiniment et sachez que je vous aime beaucoup.

Je tiens également à remercier ma famille, papa, pour toujours avoir été là pour moi et d'avoir été présent ce jour, maman pour toujours avoir pris soin de moi et m'avoir permis de devenir qui je suis maintenant. Merci ensuite à mes frères et sœur, en commençant par les deux noobs Arnaud et Adrien pour m'avoir soutenu pendant toutes ces années. Je sais que je pourrai toujours compter sur vous. Merci ensuite à Sophie d'être venue me voir, malgré les circonstances, je t'aime socurette. Merci également à Sylvie et Hervé, je sais que vous auriez voulu être là et que vous m'avez accompagné par la pensée. Merci également à mes neveux et nièces et à tout le reste de ma nombreuse famille. J'ai conscience de la chance de tous vous avoir.

Enfin pour finir, je tiens à grandement remercier mes encadrants : Sean et Christophe. Sean, ta rencontre au laboratoire a été probablement le meilleur moyen

de commencer ma thèse. Je ne pense pas que j'aurais pu faire la moitié de celle-ci sans ton aide. Ta connaissance scientifique m'a permis de prendre rapidement en main mon sujet et ton aide permanente a été un atout majeur tout au long de ma thèse. De plus, ta gentillesse paraît sans limite et je suis plus que ravi d'avoir eu la chance de te rencontrer et d'avoir trouvé non un collègue de travail mais un ami. Christophe, j'ai réussi mon objectif de te faire pleurer lors de ma soutenance de thèse, je n'essaierai donc pas de le réitérer ici. Tout était profondément sincère. J'ai souvent pensé à ce que j'aurais fait si je n'avais pas eu la chance de te rencontrer, quelle voie aurait pu être la mienne et je suis convaincu que celle-ci aurait été bien moins intéressante. J'ai énormément apprécié travailler avec toi et j'espère pouvoir continuer à le faire. Comme je te l'ai dit, tes qualités scientifiques sont indéniables, mais je pense qu'elles sont surpassées par tes qualité humaines et sociales. Ton soutien permanent a été indispensable à de nombreux moments et jusqu'au bout. Merci beaucoup à vous deux, du fond du cœur.

PS : je tiens évidemment à remercier Pikachu et tous ses amis Pokémons pour leur soutien durant ma soutenance de thèse.

Résumé

La phase d'entrée atmosphérique est l'un des plus grands défis d'une mission spatiale. Les capsules spatiales arrivent dans l'atmosphère à des vitesses hypersoniques ce qui comprime le gaz à l'avant de l'appareil et résulte en une augmentation de température jusqu'à la dissociation et l'ionisation du gaz. Ces phénomènes engendrent un rayonnement intense du gaz. Pour les missions de retour de Mars, le flux radiatif arrivant sur la capsule est la principale source de chauffage mais de grandes incertitudes demeurent dans sa prédition. En conséquence, le bouclier thermique est surdimensionné, augmentant la masse totale de l'appareil et diminuant sa charge utile. Ces incertitudes sont maximales sur l'arrière-corps de l'appareil où le plasma l'entourant est forcé de se recombiner hors équilibre. Cette thèse présente des études expérimentales et numériques de plasma d'air et d'azote en recombinaison dans des écoulements laminaires et turbulents. L'objectif est de comprendre les phénomènes gouvernant le rayonnement de ces plasmas de recombinaison afin de réduire les incertitudes susmentionnées pour les entrées terrestres.

Une torche à plasma inductive a été utilisée pour produire un plasma à l'équilibre d'air ou d'azote dans des conditions proches de celles rencontrées lors d'une entrée atmosphérique. Le plasma est forcé de se recombiner en s'écoulant à travers un tube refroidi par eau. Des mesures de température ont été effectuées par spectroscopie Raman et spectroscopie d'émission. La spectroscopie Raman donne des mesures de température de l'état fondamental des molécules d'azote qui sont représentatives de la température du gaz. En revanche, la spectroscopie d'émission mesure la température d'états excités du gaz. Deux principaux résultats sont à retenir. Tout d'abord, les codes de mécanique des fluides numériques sont incapables de prédire la baisse de température mesurée. Ensuite, dans certaines conditions, le plasma n'est plus à l'équilibre chimique. Dans ce cas, les mesures de la température rotationnelle de $N_2(B^3\Pi_g)$ et $N_2(C^3\Pi_u)$ par spectroscopie d'émission sont en accord avec la température du gaz mesurée par spectroscopie Raman. Cependant, la température rotationnelle de $N_2^+(B^2\Sigma_u^+)$ est plus élevée dans certains cas. Une étude bibliographique a permis d'identifier différents critères à

vérifier afin que les mesures de température par spectroscopie d'émission puissent être utilisées comme mesure de température du gaz.

Des mesures de spectre d'émission ont été effectuées de l'ultraviolet au proche infrarouge. En plus des mesures de température rotationnelle, ces données ont été analysées pour déterminer la densité des niveaux vibrationnels de $N_2(B^3\Pi_g)$, $N_2(C^3\Pi_u)$ et $N_2^+(B^2\Sigma_u^+)$, niveaux fortement surpeuplés par rapport à leur densité d'équilibre à la température mesurée par spectroscopie Raman. Le rayonnement mesuré résultant est environ 100.000 fois plus fort qu'à l'équilibre. Les densités mesurées ont également été comparées avec les prédictions d'un modèle à deux températures qui sous-estime les densités mesurées. Le rayonnement résultant prédit reste 10 fois plus faible que la mesure. Malgré cette différence, on peut noter que ce modèle à deux températures est bien plus proche des mesures que le modèle d'équilibre utilisant une température.

Enfin, une mesure indirecte utilisant la densité mesurée de $N_2(B^3\Pi_g)$ a permis d'obtenir une mesure de la densité de l'état fondamental de l'azote atomique. Des mesures de spectroscopie d'émission dans l'ultraviolet lointain ($\lambda < 200$ nm) ont été effectuées pour obtenir la densité des premiers niveaux excités d'azote atomique, les mesures précédemment présentées dans le visible et le proche infrarouge permettant de mesurer la densité des états plus hauts en énergie. La distribution des états excités d'azote atomique n'est plus Boltzmannienne et les états les plus hauts en énergie se rapprochent de la distribution de Saha-Boltzmann, comme cela a été prédit par des codes collisionnels-radiatifs.

Tous ces résultats permettent d'obtenir des précieuses informations sur les états fondamentaux et excités de l'azote atomique et moléculaire. Ces mesures ont pour but d'être utilisées pour la validation des codes de cinétique chimique des plasmas de recombinaison, tels ceux des arrière-corps lors des entrées atmosphériques.

Abstract

Planetary entry is one of the main challenges for spaceflight. The hypersonic velocity of the entering capsule results in strong gas compression leading to extreme gas heating, dissociation and ionization. These phenomena lead to intense gas radiation. For Mars return missions, the radiative flux encountered by the capsule during reentry into Earth's atmosphere is an important source of heating, but the prediction of this flux suffers from large uncertainties. This may lead to an overdesign of the thermal protection system (TPS), increasing the total mass or decreasing the payload of the capsule. These uncertainties are highest in the afterbody region where the plasma recombines and departs from equilibrium. This thesis presents experimental and numerical studies of recombining nitrogen and air plasma flows in a simple configuration, for conditions ranging from chemical equilibrium to nonequilibrium and from laminar to turbulent flows. The goal is to quantify the parameters controlling the radiation of recombining plasmas in order to reduce the aforementioned uncertainties for Earth reentry.

An Inductively Coupled Plasma (ICP) torch is used to provide an equilibrium nitrogen or air plasma at conditions close to those encountered in the shock layer during atmospheric reentry. The plasma is then forced to recombine by flowing through water-cooled tubes of various lengths. Temperature measurements are performed using both Spontaneous Raman Spectroscopy and Optical Emission Spectroscopy (OES). The former yields measurements of the temperature of ground state nitrogen molecules. OES yields rotational and vibrational temperatures of various excited electronic states. Two key results follow from this. First, we find that advanced CFD codes are not able to predict the measured temperature drop for any of the test-cases considered in this thesis, even when the plasma remains in Local Thermodynamic Equilibrium (LTE) throughout the tubes. Second, for the test-cases showing a departure from LTE, rotational temperature measurements obtained by OES with $N_2(B^3\Pi_g)$ and $N_2(C^3\Pi_u)$ emission are found to yield good agreement with the Raman temperature measurements. This is not true however for the rotational temperature of $N_2^+(B^2\Sigma_u^+)$ which is found to overestimate the gas temperature. We perform a literature review and discuss criteria for when OES

measurements of the rotational temperature of excited states are representative of the gas temperature.

The OES measurements performed in this thesis span the ultraviolet to the near infrared (NIR) spectral regions. In addition to obtaining measurements of rotational temperatures, we extracted vibrationally specific excited state densities for the $N_2(B^3\Pi_g)$, $N_2(C^3\Pi_u)$ and $N_2^+(B^2\Sigma_u^+)$ states. These vibrational levels are found to be highly overpopulated relative to equilibrium at the measured Raman temperature. The total measured radiation is up to 100,000 times stronger than the corresponding equilibrium radiation at the measured Raman temperature. This is consistent with previous results obtained in recombining nitrogen plasmas. We compare these measured densities with 2-temperature model predictions and find that the 2-temperature model underpredicts them. It also underpredicts the measured gas radiation by a factor of 10.

Finally, the population distributions of the electronic states of atomic nitrogen were measured using a combination of OES measurements. The atomic nitrogen ground state density was determined from the emission of predissociated vibrational levels of $N_2(B^3\Pi_g)$. Other electronic states were obtained thanks to OES measurements in the vacuum ultraviolet (VUV), the visible and the near infrared spectral ranges. A departure from a Boltzmann distribution at the gas temperature is observed for the levels above 10 eV whose densities tend to follow the Saha-Boltzmann distribution, in accordance with previous predictions for nonequilibrium flows.

Taken together, this comprehensive dataset yields quantitative information on ground and excited state densities for both atomic and molecular species. These measurements provide a new database to test kinetic and CFD codes for recombining nitrogen flows, which is of particular interest to simulate afterbody radiation in atmospheric reentry conditions.

Table of Contents

Chapter 1 Introduction	1
1.1 Overview of science progress and space exploration	1
1.1.1 History of progress	1
1.1.2 Definition of progress in the mid-19 th century.....	3
1.1.3 Critique of progress.....	3
1.1.4 Does human space exploration represent progress?.....	4
1.1.5 Conclusion.....	6
1.2 Atmospheric entry phase	7
1.3 Forebody heat flux uncertainties	12
1.4 Afterbody heat fluxes uncertainties	14
1.5 Scope and overview of the thesis.....	16
Chapter 2 Ground testing facilities for radiation studies	19
2.1 Shock Tubes	19
2.1.1 Principle.....	19
2.1.2 Studies and diagnostics	21
2.2 Plasma wind tunnels and arcjets	22
2.2.1 Principle.....	22
2.2.2 Studies and diagnostics	24
2.3 Plasma torches	24
2.3.1 Principle.....	24
2.3.2 The TAFA Model 66 plasma torch at CentraleSupélec	25
2.4 Optical diagnostics	30
2.5 Scope of the thesis	36
Chapter 3 Raman spectroscopy	39
3.1 Theory.....	39
3.2 Experimental setup.....	47
3.3 Validation of the technique with equilibrium plasmas	50
3.3.1 Air plasma at the exit of the 5-cm diameter nozzle	50
3.3.2 Air plasma at the exit of the 30-cm tube:.....	55
3.3.3 Air/argon plasma at the exit of the 1-cm diameter nozzle.....	58
3.3.4 Beam steering:.....	62
3.4 Temperature measurements by Raman spectroscopy in recombining plasma test-cases	64
3.4.1 Air/Ar case	64
3.4.2 N ₂ /Ar high flowrate case:	66

3.4.3	Temperature profiles	69
3.5	Conclusion	69
Chapter 4 Temperature measurements by Optical Emission Spectroscopy		70
4.1	Introduction	70
4.1.1	$N_2(B)$ rotational temperature	70
4.1.2	$N_2(C)$ rotational temperature	72
4.1.3	$N_2^+(B)$ rotational temperature.....	73
4.2	Results.....	74
4.2.1	Air/Ar mixture	74
4.2.2	N_2/Ar mixture, low flowrate.....	75
4.2.3	N_2/Ar mixture, high flowrate	76
4.2.4	Analysis of the nitrogen/argon results.....	77
4.2.5	Comparison with Raman spectroscopy	77
4.2.6	Interpretation of the differences between the rotational temperatures ...	78
4.2.7	Conclusions	84
Chapter 5 CFD modeling of recombining equilibrium air plasmas		86
5.1	Pure air plasma	86
5.1.1	CFD modeling.....	86
5.1.2	Results	89
5.2	Air/Ar plasma.....	96
5.3	Conclusions.....	98
Chapter 6 Molecular radiation		99
6.1	Method for the determination of excited state densities.....	99
6.1.2	Spectrum between 500 and 900 nm	101
6.1.3	Spectrum between 250 and 450 nm	107
6.1.4	Influence of the rotational temperature	109
6.2	Air/Ar case.....	111
6.3	N_2/Ar low flowrate case.....	113
6.3.1	Emission spectra at 10 and 15 cm	114
6.3.2	Measured densities of $N_2(B)$, $N_2(C)$, and $N_2^+(B)$ at 10 and 15 cm	116
6.3.3	Total molecular radiation	123
6.4	N_2/Ar high flowrate case	124
6.4.1	Emission spectra at 10 and 15 cm	124
6.4.2	Measured densities of $N_2(B)$, $N_2(C)$, and $N_2^+(B)$ at 10 and 15 cm.	127
6.4.3	Total molecular radiation	133
6.5	Conclusions.....	134

Chapter 7 Atomic Radiation	136
7.1 Introduction	136
7.2 N(⁴ S ⁰) density measurements	137
7.2.1 Method.....	137
7.2.2 Results	138
7.3 N(² D ⁰) density measurements	140
7.4 Excited N-atoms density measurements.....	143
7.4.1 Considered levels and measurement technique	143
7.4.2 VUV optical emission spectroscopy setup.....	146
7.4.3 Analysis of the nitrogen lines at 149 and 174 nm	148
7.5 Electron number density measurements.....	151
7.5.1 Method.....	151
7.5.2 Results	154
7.5.3 Conclusion.....	157
7.6 Results on atomic line measurements	157
7.6.1 N ₂ /Ar LF case.....	157
7.6.2 N ₂ /Ar high flowrate case	171
7.7 Conclusions.....	180
Chapter 8 Power Balance	182
8.1 Power balance assuming equilibrium	182
8.1.1 Model.....	182
8.1.2 Results	185
8.2 Power balance including chemical nonequilibrium	187
8.2.1 Chemical energy storage.....	187
8.2.2 Results	189
8.3 Conclusion.....	191
Chapter 9 Conclusions	192
9.1 Contributions of this thesis.....	192
9.2 Recommendations for future work	194

Chapter 1 Introduction

1.1 Overview of science progress and space exploration

The exploration of our solar system represents the next frontier in human exploration. Within this context, Mars represents a realistic destination of interest for a manned mission. Its relative proximity and similarity to Earth in terms of climate and gravity make this a logical next step for a manned mission beyond Earth orbit. This thesis aims to look at a small subset of scientific and technological challenges that must be overcome to make such a journey possible. This subset of challenges pertains to the design of the thermal heat shield used to protect the space capsule during its entry into the Martian atmosphere and its subsequent reentry into the Earth's atmosphere.

Here, in the first section of this thesis, I wish to diverge slightly and look at the motivation for this work from a more philosophical perspective. This is more from a personal desire rather than anything else. This section reflects interrogations that, I think, should be asked to decide to pursue human space exploration or not. Indeed, this is certainly an issue that is debated in public policy circles. This section is not necessary for the technical content that follows.

1.1.1 History of progress

The notion of progress, as we understand it¹, is a relatively recent addition to mainstream human understanding. For example, the philosophers Plato (428-348 BC) and Aristotle (384-322 BC) saw the world as cyclic. In a given cycle, Aristotle postulated that improvements in human society are made - for example in politics (Aristotle, n.d.) - until an ideal “golden age” is reached. However, he argued that all political systems are ultimately unstable leading eventually to decline. Plato gives an example from the natural order, noting that “the human race has been repeatedly annihilated by floods and plagues and many other causes, so that only a fraction of it survived” (Plato, n.d.). This idea of a cyclic world was adopted for years after their work. However, Saint Augustine (354-430 C.E.) presented a rather

¹ When I use the word “progress”, it should be understood to mean “progress as we understand it”

new vision of humanity, rejecting the cyclical vision of the world in favor of a linear one (Saint Augustine, n.d.), more along the lines of what we would recognize today.

The notion of progress was formally defined much later during the age of Enlightenment. Major scientific advances, particularly within the field of astronomy, were made beginning in the 15th century. Copernicus (1473-1543) rejected the geocentric theory for the heliocentric one. This heliocentric theory was later confirmed by Galileo (1564-1642) through observations and resulted in Kepler's (1571-1630) laws of planetary motion. Finally, Newton (1642-1727) synthesized the work of his predecessors to propose the universal law of gravitation. These advances had a strong impact on philosophy and the scientists themselves played a role in the development of our understanding of progress. They presented two different ways of measuring scientific and human progress – namely, they used what are known as *empiricism* and *rationalism*. Francis Bacon (1561-1626) was the first to define empiricism. This method is based on experimental observations to develop scientific theories, one of the most famous examples being the apple story of Newton. While this story may be a myth, Newton's approach to science was certainly that of an empiricist. By contrast, rationalism relies upon human reasoning alone to arrive at the truth. Rationalism is represented within the famous quote of Descartes (1596-1650) - “I think therefore I am”, which is based not on experimental observations but only on logic. These two doctrines – empiricism and rationalism - were opposed to one another during the 17th century. Rationalism was more dominant in scientific thought in France, whereas empiricism was more dominant in England. Although they differed in their methods for making progress, both Bacon and Descartes had similar views in that progress represented somehow man's control over nature (Descartes, 1637), thus making it closely linked to science.

Another more philosophical view of progress as pertaining to the human mind was given by Turgot (1727-1781) (Turgot, 1750). Nicolas de Condorcet followed up Turgot's work (De Condorcet, 1795) and their collective work resulted in a formal theory on progress. They posited that a stable political system with fair laws, more freedom and equality will favor scientific progress. A more authoritarian society will slow down this progress. This drew a link between progress in science and progress in the socio-political realm – the two, in essence, feeding on one another. Scientific and technical progress is therefore not independent of progress in the social and political areas. When taken together, these two aspects represent human progress.

1.1.2 Definition of progress in the mid-19th century

In the dictionary, progress is defined as “forward motion towards a destination”. For human progress, such an absolute definition does not apply as the “destination” is often unclear and, for the most part, depends on the individual. In the middle of the 19th century, progress could be roughly divided into three different categories:

- Scientific progress: this is the most commonly agreed upon category of progress. Progress is defined as achieving an accurate and more detailed understanding of natural phenomena.
- Cultural/moral progress: this represents the evolution of the human mind in such manner that the arts and culture also evolve. This can include sharing the common general knowledge and, by extension, education. Education and cultural exchange are ways to develop metaphysical thinking and progress of the human mind. The development of morality results from it.
- Political/social progress: as noted above, other forms of progress (e.g. scientific and technical forms) require a stable society. This includes democracy with fair laws and free and equal population. Thus political/social progress means moving towards such a stable system.

Human progress as a whole requires all three of these categories. These aspects are interconnected and coupled. Of the three categories, scientific progress is the easiest to quantify. The other aspects are more subjective and controversial. The definitions that I gave above, I believe, represent the philosophical literature on the subject.

1.1.3 Critique of progress

During the 19th century, the view that scientific progress was good in and by itself was carried by philosophers such as Auguste Comte (1798-1857). Another, Herbert Spencer (1820-1903), wanted to extend Darwin’s theory of evolution to social issues including the removal of social protection systems, social aids for the poorest and charitable behavior. He believed that the “survival of the fittest” was needed for human progress (Spencer, 1864). This represents a confusion between scientific progress, including the theory of evolution, and social progress where science was not intended to be used and started to raise criticism when scientific developments began to have a much larger impact on society. Critiques argue that science and technology must be somehow controlled so as not to inhibit the other forms of progress necessary for human advancement – specifically, the cultural/moral and

social/political forms of progress. Rather, these must evolve in parallel. The two world wars gave weight to these arguments. The development of nuclear weapons showed that scientific progress was leading to advances that could not be controlled via existing social structures. George Orwell (1903-1950), in his book *1984*, offers a critique of uncontrolled technical progress leading to alienation of the individual (Orwell, 1949). Climate change is another example, where the energy consumption of mankind, made possible by scientific progress, is having an unintentional impact on the Earth's climate. There are many other examples of critiques focusing on uncontrolled scientific progress. Laws are supposed to respond to these critiques but, in responding to the particular scientific source that necessitates them, come at a later point in time. Beyond offering a critique of uncontrolled scientific progress, detractors often highlight the paradox that infinite progress in a finite world is not possible.

Such critiques of uncontrolled scientific progress are gaining traction and many scientists are pushing for a more ethical and comprehensive view of scientific progress. The argument is essentially that science needs to advance in parallel with the other forms of progress outlined above. Science is advancing fast. However, whether we are making adequate social progress to accompany this effort is debatable. As an example, between 1950 and 2000 the median income per person declined in 100 out of 174 countries considered (Programme, 2000). Life-expectancy also declined. These social inequalities continue to increase and serve to destabilize society. As of 2017, the 8 wealthiest men own as much as the 3.6 trillion poorest. These examples represent social regression and, when contrasted with the huge scientific advances, may suggest rather an absence of total progress.

It is within this context that, I believe, space exploration should be considered and evaluated as to whether it represents an important source of progress or not.

1.1.4 Does human space exploration represent progress?

In 2014, the Committee on Human Spaceflight from the US National Research Council published a report with data concerning past and future space missions (Committee on Human Spaceflight, 2014). For past missions, they investigated the impact and outcomes of space exploration and human spaceflight. We will summarize here their conclusions, splitting them into the three aspects of progress outlined in section 1.1.2: a scientific, a cultural and a political aspect.

Space exploration resulted in many scientific achievements and discoveries that impacted humanity beyond the accomplishments of the human space program

alone (Committee on Human Spaceflight, 2014). The past missions resulted in the launch of multiple satellites in orbit around the Earth, which, among other things, have enabled advances in guidance, communication systems and internet access. The satellites are also used for weather forecasting, which has had a large impact on scientific fields spanning from meteorology to renewable energy production and agriculture. The International Space Station (ISS) has permitted scientific experiments to be carried out in zero-g and in space environments. This has permitted advances in biology, medicine and materials science. This list is not exhaustive, but it is clear that space exploration has resulted in scientific progress.

Has space exploration resulted in cultural/moral progress for humanity? Space exploration programs have produced collaboration between countries, some hostile to one another, thus providing a means for developing connections and reducing the probability of armed conflict. The space race to go on the Moon served as a surrogate for armed conflict between the USA and USSR. The ISS, for example, involves USA, Canada, Russia and Europe. Space missions, such as the Apollo missions, inspire people to devote themselves to a goal larger than themselves. This includes getting an advanced education and developing critical reasoning skills. Thus, while certainly hard to quantify, space exploration can result in cultural/moral progress.

From a social/political perspective, space exploration has driven advances in Defense technology with, for example, the improvement of missile systems. Whether this is a good or bad way of promoting a stable society is up for debate. Beyond this, the US space exploration programs (Committee on Human Spaceflight, 2014) have stimulated the economy and lead to improvements in social conditions. This latter point can also be a controversial statement and the individual effect of federal funding into space exploration could not be accurately assessed in the report (Committee on Human Spaceflight, 2014). Considering these different points, it could be argued that the space exploration programs have enhanced the political and social conditions to a degree. A more definitive statement would, however, require further study.

Regarding manned missions in particular, the conclusion of the NRC report was clear: “No single rationale seems to justify the value of pursuing human spaceflight” (Committee on Human Spaceflight, 2014). While robotic missions still have an interest, the committee was not convinced by the pursuit of human spaceflight missions. The study asked US citizens if space exploration was still a field of interest for the USA. The exhaustive results can be found in (Committee on Human

Spaceflight, 2014) but some key results will be summarized here. Regarding the cost of space exploration missions, only 12% of the respondents considered that the US was spending too little on this field in 2007 but this number increased by 10% in 2012. Interestingly, the number of people thinking that the US spent too much decreased by 5% within the same time frame (41% in 2012). While still relatively low, these numbers show a growing interest for space exploration. A majority of citizens sampled considered that the Apollo missions were worth it (70% in 2012, constant since 2000) and remain favorable to a manned mission to Mars (51% in 2012, relatively constant since 1995). On the benefits for future space missions, the public points out scientific advances (74% favorable) and the fostering of education (74%). There is, therefore, interest in space exploration.

Questions were also asked regarding the beneficial outcomes of the space program. These questions were asked to people both within and outside of the space industry. The respondents highlighted the increase in knowledge and scientific understanding (78%) and technological advances (35%). These, of course, represent only scientific progress. The other reasons cited for space exploration were the “basic human drive to explore new frontiers” (32%) which can be attributed to a cultural/morality argument and “human economic activity beyond Earth” (11%), which can be seen as a way to improve economic conditions (e.g. mining the surface of the Moon, etc...). The scientific aspect alone is therefore largely used for justifying space exploration. It is interesting to note the answers to questions regarding manned versus robotic missions. A decrease of about 20% was observed in all questions regarding manned missions. While reasons to support space exploration are numerous, the advantage of human over robotic missions is not well quantified, which is one conclusion of this report. Finally, for future missions, the main interest remains in low Earth orbit missions such as the ISS (79%), whereas landing humans on Mars finds less interest but still is significant (48%).

Finally, the report highlights the advances in science due to space exploration. Cultural and social advances were harder to quantify but appear to be most appropriately addressed via low Earth orbit or robotic missions.

1.1.5 Conclusion

Mars exploration certainly presents scientific problems that need to be solved and that will serve to increase global scientific knowledge. In these terms, it represents one aspect of progress as defined in section 1.1.2 – namely scientific progress. A journey to and back from Mars would present numerous scientific challenges for various phases of the mission. This thesis will focus on the atmospheric reentry

phase of the mission. However, as I have tried to argue here, improvements in cultural and social conditions due to Mars exploration should be kept in mind, even if they remain difficult to quantify and are outside the scope of this thesis.

1.2 Atmospheric entry phase

Atmospheric entry refers to the entry of an object into a planet's atmosphere (we will use the term “reentry” when talking about missions entering the Earth’s atmosphere). This entry phase represents a very small portion of the total flight time for most missions, typically lasting for only a few minutes, whereas a total mission can take several years - 16 years for the case of the Stardust mission. Atmospheric entry occurs at very high speeds, leading to high heat load, heat fluxes, and aerodynamic forces. These must be accurately accounted for the design of the capsule in order to avoid destruction of the vehicle, and this is done by using models to predict these effects. Examples of velocity trajectories for past and future missions are plotted in Figure 1. Orion is a capsule designed by NASA for missions ranging from low Earth orbit to lunar return (Bihari, et al., 2011). The FIRE II project was an experiment conducted by NASA in 1966 to obtain flight data during reentry (Wright, et al., 2003). Stardust was a NASA sample return mission that reentered the Earth’s atmosphere in 2006 (Jenniskens, 2010). Hayabusa was also a successful sample return mission by JAXA (Grinstead, et al., 2011). The line labeled “Shuttle” represents a typical Space Shuttle reentry trajectory from the International Space Station. These missions often provided radiation measurements and are therefore useful for the reentry community.

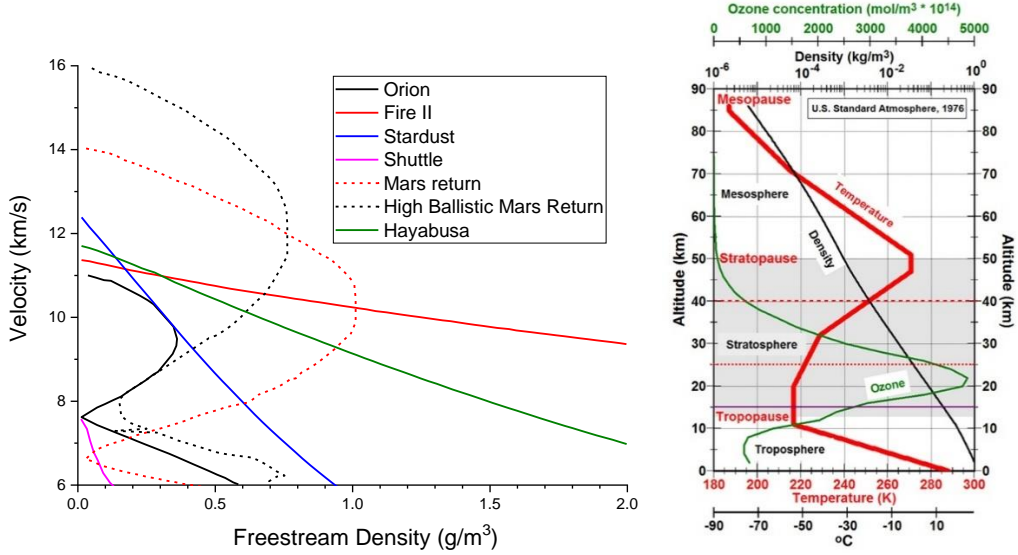


Figure 1: Velocities during Earth atmospheric reentry for past and future missions. The velocities are presented as a function of the free stream density (left, data taken from (Brandis & Cruden, 2017)). Dashed lines represent potential future missions. The density can be linked to the altitude using the US Standard Atmosphere model (Krueger & Minzner, 1976)(right).

During atmospheric entry, the capsule travels at hypersonic velocities. This results in the formation of a strong shockwave in front of the capsule (Anderson Jr, 2006). For the Stardust reentry, the capsule entered the Earth's atmosphere at a velocity exceeding 12 km/s. The shockwave that forms in front of the capsule heats the gas to temperatures up to 12000 K (Johnston & Brandis, 2015). The high gas temperatures lead to molecular dissociation, ionization, excitation, and intense gas radiation. Furthermore, at these temperatures, the electron density is sufficiently high to form a weakly ionized plasma. This plasma then interacts with the vehicle surface and heats it. Different portions of the capsule must be protected to varying degrees. The forebody region, just behind the shock, must resist the largest forces and heat fluxes. The high temperature/pressure plasma in the forebody expands into the afterbody region via a hydrodynamic expansion around the shoulder of the capsule. This expansion causes rapid gas cooling and can force the fluid out of equilibrium, leading to a large uncertainty on the predicted heat fluxes in this region. Figure 2 summarizes the various effects that occur and must be taken into account to safely design the capsule heat shield. Due to the complexity and intercoupling of the phenomena involved, the entry phase represents a very challenging problem – the goal being to correctly account for, understand and model all relevant phenomena.

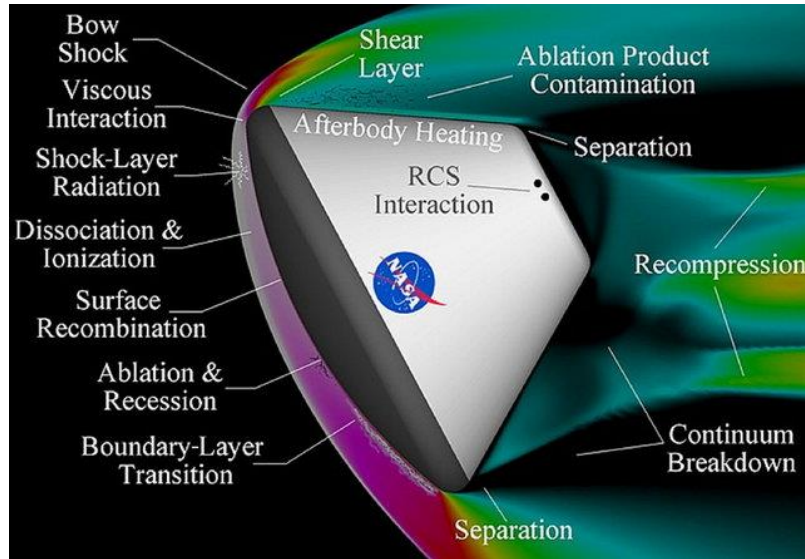


Figure 2: Physical phenomena occurring during entry (credit NASA)

The high heat flux on the capsule surface is comprised of two sources – convection and radiation. Depending upon the reentry speed, one may dominate, or both may be important. The convective flux is expected to be linear with the plasma temperature whereas the radiative flux is exponential. At low Earth reentry speeds, the convective flux dominates. However, as the reentry velocity increases, radiation becomes more important and eventually becomes dominant. The convective and radiative fluxes at the stagnation point encountered during Earth reentry are plotted in Figure 3. The radiative flux is significant above 9 km/s (as shown by (Gnoffo, 1999)) and becomes dominant above 11 km/s.

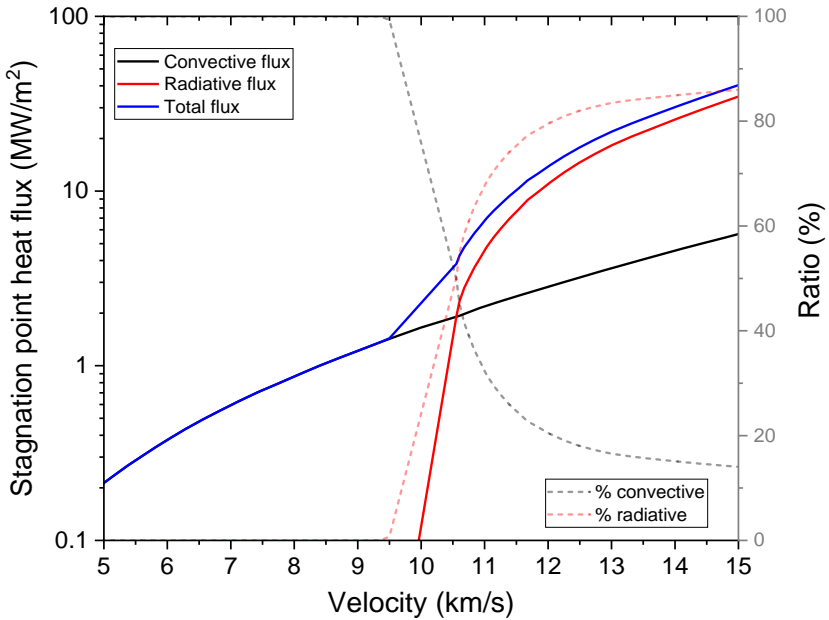


Figure 3: Typical convective and radiative fluxes encountered during Earth reentry and their respective contributions (data taken from (Anderson, 1969))

To sustain the extreme heat fluxes during atmospheric entry, a heat shield, or Thermal Protection System (TPS) is required. Initially, TPS designs were based on a heat sink composed of thick copper that absorbed the heat accumulated during reentry. Another concept, known as the hot structure, was composed of high emissivity heat-resistant materials that radiated away the thermal energy from the surface. Transpiration cooling using evaporating water was also proposed (Heppenheimer, 2007). The use of material ablative for the heat shield was proposed by the U.S. and was adopted for the Apollo missions. Sutton pursued the study of ablative materials for more severe reentry conditions (Sutton, 1982) and these materials were found to be very effective at protecting the capsule. The mechanism of ablation is complex, and details can be found in (Laub & Venkatapathy, 2003). In essence, the thermal energy is carried away via endothermic chemical reactions including pyrolysis and carbon sublimation. The material also has a relatively low thermal conductivity for thermal protection. Figure 4 summarizes the various ablation mechanisms that occur during entry. While ablative materials are the best TPS choices for the high heat fluxes associated with high entry speeds, reusable TPS materials are also used for lower velocity entry (Johnson, 2013). These materials are composed of a low conductivity TPS with a high emissivity coating that radiates the thermal energy away. These materials are mainly used for low Earth orbit reentry as shown in Figure 5.

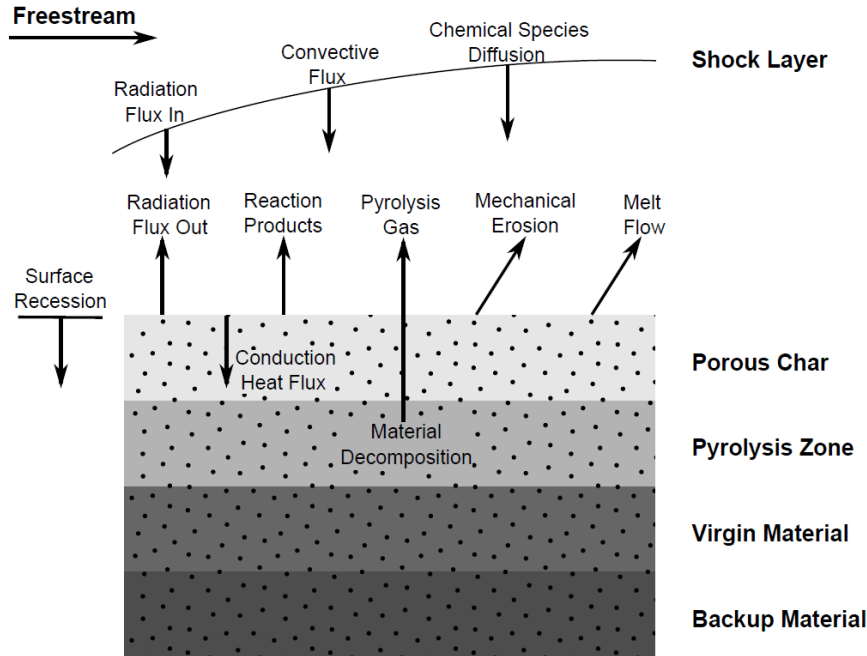


Figure 4: Physical mechanisms of ablative TPS materials (figure taken from (Wei, 2017) reproduced from (Laub & Venkatapathy, 2003))

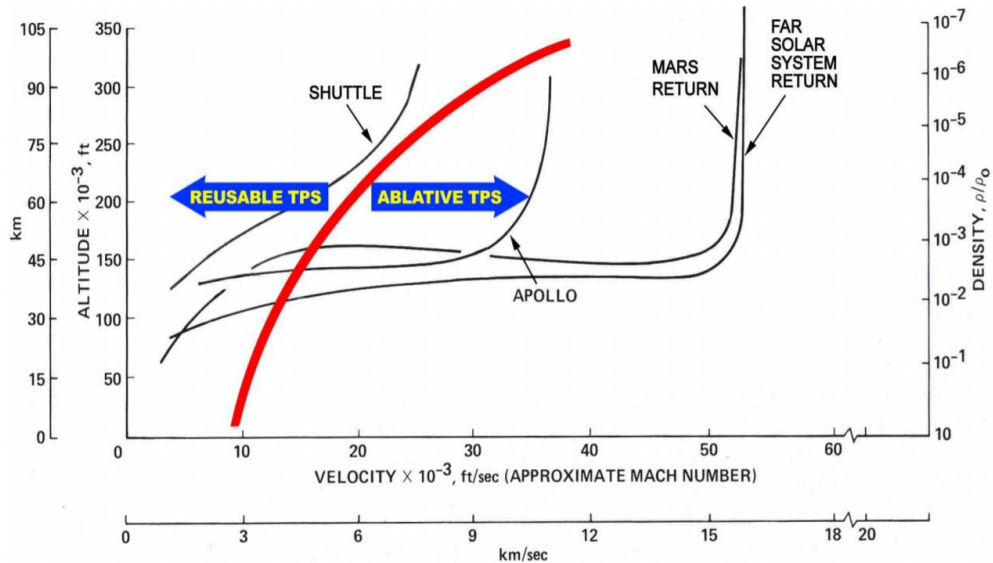


Figure 5: TPS used for various missions (figure taken from (Johnson, 2013))

The amount of TPS needed to survive the entry phase needs to be accurately determined via predictive models of the heat fluxes encountered. We will focus on two regions of the capsule: the forebody and the afterbody.

1.3 Forebody heat flux uncertainties

During the entry phase, a shock layer forms at the forebody of the capsule. For earth reentry, air is compressed from low pressure (10^{-4} , 10^{-5} atm) to a relatively high pressure (0.5 atm) in the shock layer. This compression leads to rapid translational and rotational excitation (Potter, 2011) (Johnston, 2006). The vibrational modes of molecules are then excited by the translational-rotational excited modes via collisions. This latter step requires a certain induction time determined by the collisional energy transfer rates. This leads to the formation of a so-called thermal nonequilibrium region, where translational and rotational modes remain at a temperature elevated with respect to the vibrational and electronic modes within the shock layer. These modes then relax towards each other to finally reach thermal and chemical equilibrium. Near the surface of the capsule, interactions between the plasma and the ablator impose cooling, surface recombination and ablation. A summary of these effects is presented in Figure 6.

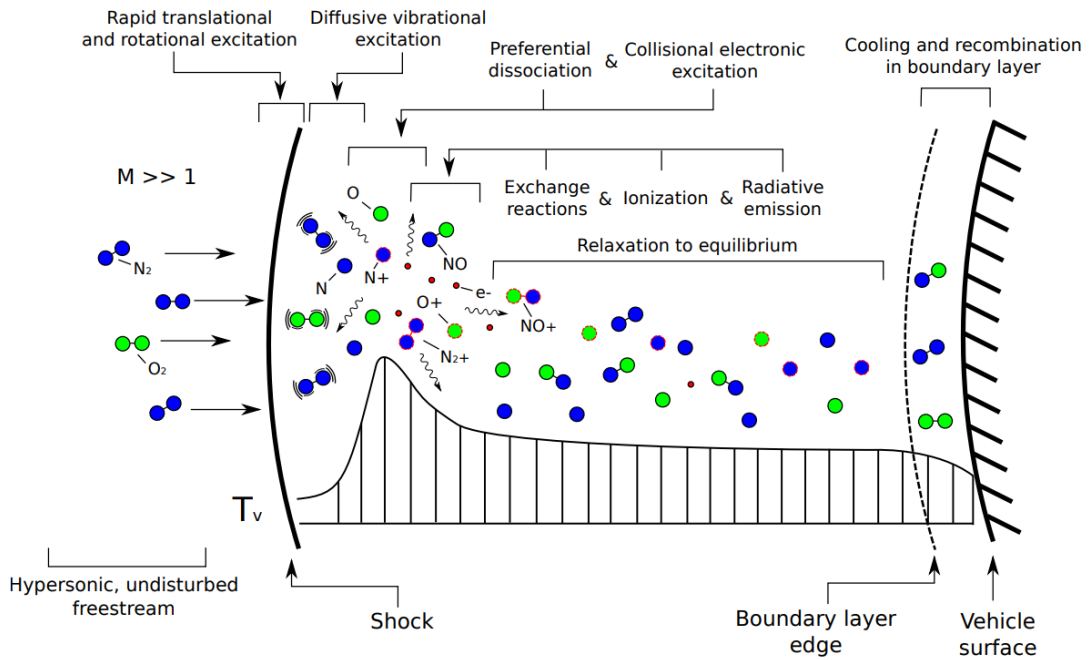


Figure 6: Schematic of kinetics occurring along the stagnation streamline for Earth reentry. The nonequilibrium region is observed near the shock and the gas relaxes to equilibrium in the shock layer (figure taken from (Potter, 2011))

The composition and properties of the nonequilibrium region in the shock are difficult to correctly model because the chemical kinetics must be accurately known. Earlier work by Park (Park, 1993) and Gupta (Gupta, et al., 1990) provided estimates of these rates, and their results are still used today.

The existence of both the nonequilibrium and equilibrium regions within the shock layer led experimentalists to define a metric to clearly identify these regions as a function of entry velocity, vehicle dimensions, and vehicle shape. Several metrics were proposed in (Brandis, et al., 2013). These metrics have separate advantages according to the desired experiment. One metric distinguishing between these two regions was simply defined as the region 2 cm from the shock front. Broadly speaking, the effect on the surface radiative heat flux coming from the nonequilibrium region is not negligible depending on vehicle and entry condition. For example, previous work (Laux, et al., 2009) showed that, for an Apollo type capsule vehicle at reentry velocity of 10.5 km/s, the nonequilibrium region of the shock was responsible for 26% of the total radiative flux. The thickness of this nonequilibrium region and its emission as a portion of the total become smaller at higher entry velocities. This has been shown in shock tubes experiments (Brandis & Cruden, 2017). Therefore, for a Mars return reentry trajectory, where the velocity will be above 12 km/s, the nonequilibrium region is expected to be very small. Therefore, despite increasing significantly the total heat flux encountered, high entry velocities for future Mars missions may actually reduce the importance of this nonequilibrium region of the shock for the total heat flux.

Predicting the heat flux on the forebody of the vehicle for the case of a Mars return reentry has been the focus of past research. Early work by Tauber *et al* (Tauber & Sutton, 1991) showed only a 23% discrepancy between the predictions of different simulations for entry velocities between 9 to 15 km/s. However, the authors assumed equilibrium in the shock layer, which may only be valid for the higher velocities considered. For a lunar return mission, three examples representative of such missions are presented in (Johnston & Kleb, 2012). In this case, both the nonequilibrium and equilibrium regions were considered, and the total uncertainties on the radiative heat fluxes were below 30%. These uncertainties resulted from the collective uncertainties of many parameters that never individually exceeded 7%. Improving the accuracy of the prediction on this heat flux then requires targeted research in many areas (Wright, et al., 2011): heat transfer, trajectory prediction, spectroscopic constant, material thermal response and kinetics.

Experimental data were also obtained during a real flight sample return mission named Hayabusa. Computations were performed for the Hayabusa missions and compared with experimental data (Winter, et al., 2019). Hayabusa entered the atmosphere at a velocity above 12 km/s (Figure 1), which makes it representative of a Mars return reentry scenario. In this reference, the influence of ablation products on the heat flux was also considered. The uncertainties on the computed

radiative heat flux were found to be between 30 and 40%. The influence of these ablation products was also studied in the case of the Stardust reentry (Taylor & Jenniskens, 2010). The authors measured atomic lines of carbon during the Stardust entry with a 20% accuracy. These data can be used to test the influence of ablation products.

The TPS design margins depend on uncertainties on many parameters beyond the total heat flux: aerodynamics for the angle of reentry and the trajectory, thermal response of the material, etc. Statistical Monte Carlo methods have been developed to compute the total uncertainties and the resulting margins needed for the success of the mission. In (Wright, et al., 2011), the authors developed a new methodology that could have reduced the margins on the TPS used for the Stardust mission by 40%.

In summary, uncertainties on the forebody heat fluxes are on the order of 30%. As mentioned, improving these predictions will require a lot of effort across several areas.

1.4 Afterbody heat fluxes uncertainties

The heat flux in the afterbody region is lower than on the forebody. For the Stardust reentry, the total heat flux on the afterbody is approximately 20 W/cm² as compared to 100 W/cm² (Johnston & Brandis, 2015) on the forebody. Over the last years, studies of the afterbody heat fluxes have seen an increase in interest, especially with regards to the radiative flux. Comparisons between simulations and measurements performed using radiometers on the back shell of the FIRE II mission showed a disagreement of up to 100% on some regions in the afterbody (Johnston & Brandis, 2015). Similar errors are expected for the Stardust mission because the mission profile was similar.

In (Johnston, et al., 2013), simulations for a sphere entering Earth's atmosphere at 14 km/s were performed. This represents a typical Mars return reentry. Uncertainties of approximately 100% were found in the afterbody region. Note that these simulations took into account the influence of ablative products. This simplified geometry (sphere) could also underestimate the errors for a real reentry scenario. As an example, for the same test case, uncertainties of 10% were estimated on the forebody whereas the actual error was found to be on the order of about 20-30% when compared with the real case (section 1.3).

These high uncertainties/errors come from two primary physical phenomena that take place in the afterbody region. The first is the presence of significant quantities of carbon in the plasma, introduced via the ablative heat shield in front of the capsule. The carbon sublimates from the forebody heat shield and recombines in the flow, forming molecules such as CN and CO that emit and absorb radiation in the afterbody region. Simulations performed for a sphere entering the atmosphere at 14 km/s using an ablative wall in the forebody showed the presence of CO in mass concentrations of about 50% in the afterbody (Johnston, et al., 2013). Measurements performed on the boundary layer of an ablative sample in a plasma torch facility (McGuire, et al., 2016) indicated also the presence of CO with concentrations up to 20%. The influence of carbon-containing molecules on the total radiation is not easy to determine as these species may both emit and absorb radiation contributing to the heat flux (Johnston & Brandis, 2015). Measurements performed in wind tunnel facilities showed that using different ablative materials resulted in different stagnation-point radiative heat fluxes (Hermann, et al., 2017). These authors measured atomic lines of N in the VUV region and observed an increase in radiation using a carbon preform (Calcarb) material compared to copper, but a decrease by a factor of 20 with a carbon phenolic ablator (ASTERM). The second phenomenon of relevance for the afterbody region is the hydrodynamic expansion of the plasma as it passes over the capsule shoulder from the forebody to the afterbody region. This expansion rapidly cools the plasma, forces plasma recombination, and can lead to a departure from chemical equilibrium. This chemical nonequilibrium and the resulting radiation, especially the atomic radiation, are not accurately modeled at the moment (Johnston & Brandis, 2015). For lack of experiments looking at the afterbody region, high uncertainties remain on modeling these two phenomena and, consequently, the total radiative heat flux. Note that the radiative heat flux is expected to be the main source of heat flux for a Mars reentry scenario in the afterbody region (Johnston & Brandis, 2015). Work is in progress, in particular numerical simulations, to reduce these uncertainties (Johnston, et al., 2016). There is, however, a lack of experimental data for model validation.

Finally, note that despite the lower heat fluxes in the afterbody region, knowledge of these heat fluxes is still important because the surface of the afterbody often represents a dominant fraction of the total surface of the capsule, approximately 2/3 for the MSL capsule for instance (Figure 7). In the case of the Stardust reentry, the heat flux on the afterbody was about 5 times lower than on the forebody (about 20 W/cm² as compared to 100 W/cm² (Johnston & Brandis, 2015)). Uncertainties

on the afterbody heat flux can be up to 200%. Due to the margins on the TPS, it will lead to a significative mass increase of the capsule, making it a very relevant topic of research. Focusing on the afterbody, rather than the forebody, appears to be necessary to optimize the TPS mass.

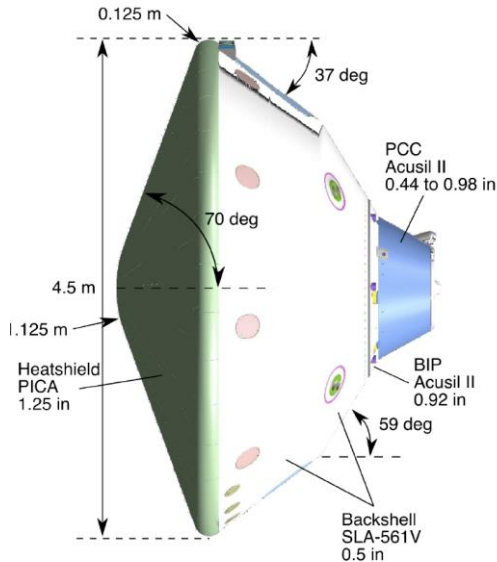


Figure 7: Geometry and Thermal Protection System of the MSL Aeroshell
 (figure taken from (Edquist, et al., 2009))

1.5 Scope and overview of the thesis

The goal of the work outlined in this thesis is to increase the accuracy of the predictions for the afterbody radiative heat fluxes encountered during Earth reentry. The thesis will focus on an experimental setup using the plasma torch facility of CentraleSupélec. Briefly, the experimental setup consists of a water-cooled tube mounted on top of an inductively coupled plasma torch. The plasma produced by the torch is rapidly cooled in the water-cooled tube, forcing plasma recombination. This allows us to study, using a relatively simple configuration, the thermal and chemical evolution of a recombining flow such as those occurring in the afterbody during reentry. Our work will focus mainly on recombining nitrogen plasmas.

First, an overview of the different ground testing facilities will be presented. Advantages and disadvantages of each facility will be noted to understand how our facility can be complementary to other ones currently in use. The thesis also represents the continuity of another thesis performed in the 90's at Stanford

University. The experimental setup of this prior thesis was reused and will be presented. The main results of this prior thesis will also be summarized.

The next chapters will focus on temperature measurements within the plasma as it traverses the water-cooled tube and recombines. The gas temperature is an important physical property with a large influence on radiation. For these measurements, both Optical Emission Spectroscopy (OES) and Raman scattering are used. We distinguish between test cases where the plasma remains in equilibrium and those where the plasma departs from equilibrium. The equilibrium test cases provide useful data for comparison with CFD codes, which are currently not capable of predicting the measured temperature variation in the water-cooled tube. The nonequilibrium test cases provide useful data for validation of nitrogen chemical kinetic models.

In Chapter 5, the measured temperature profiles for the equilibrium test cases are compared with results from a CFD code Eilmer3 to check the ability of an established CFD code to predict the measured temperature drop in water-cooled tubes of various lengths.

Chapters 6 and 7 will focus on the radiation emitted by the recombining plasma. The radiative flux is an important physical parameter that needs to be correctly predicted for reentry applications. In Chapter 6, molecular radiation is measured. For certain test cases, the measured radiation will be found to be out of equilibrium. The absolutely calibrated molecular spectra will then be used to measure the vibronic population distributions of N_2 and N_2^+ . The total radiative flux coming from the plasma will also be measured and compared with classic multi-temperature models used in the hypersonic community.

Chapter 7 presents measurements of atomic radiation from the Vacuum Ultra-violet (VUV) to the Near InfraRed (NIR) region. Atoms are the main source of radiation in a real reentry case scenario at high velocities. The intensity of various atomic transitions will be used to measure the density of the excited states of atomic nitrogen. The distribution of N atoms will be given and will be found to be non-Boltzmann in the nitrogen/argon plasmas. These preliminary experimental results will be compared with previous numerical predictions.

Chapter 8 will present power balance measurements performed for our test cases. This chapter ensures the consistency of the measurements previously discussed to provide confidence and a measure of coherence and consistency.

Finally, the main results of the thesis will be summarized, and the main advances will be given.

Chapter 2 Ground testing facilities for radiation studies

2.1 Shock Tubes

Shock tubes are widely used to study shock wave phenomena related to reentry conditions and we will present here a summary of some important experimental facilities.

2.1.1 Principle

A detailed description of the working principles of shock tubes can be found in (Igra & Houas, 2016). Briefly, a shock tube is a ground test facility that produces shock waves. A shock tube is composed of two chambers containing a driver gas at high pressure and a driven gas at low pressure, as presented in Figure 8. The two chambers are separated by a diaphragm. When the pressure in the driver section reaches a certain threshold, the diaphragm breaks and a shock wave propagates through the driven section. Details on supersonic and hypersonic shock wave propagation can be found in (Anderson Jr, 2006). The changes of temperature and pressure during the shock propagation are qualitatively plotted in Figure 8. The pressure ratio and the speed of sound in the driver ultimately determine the shock Mach number.

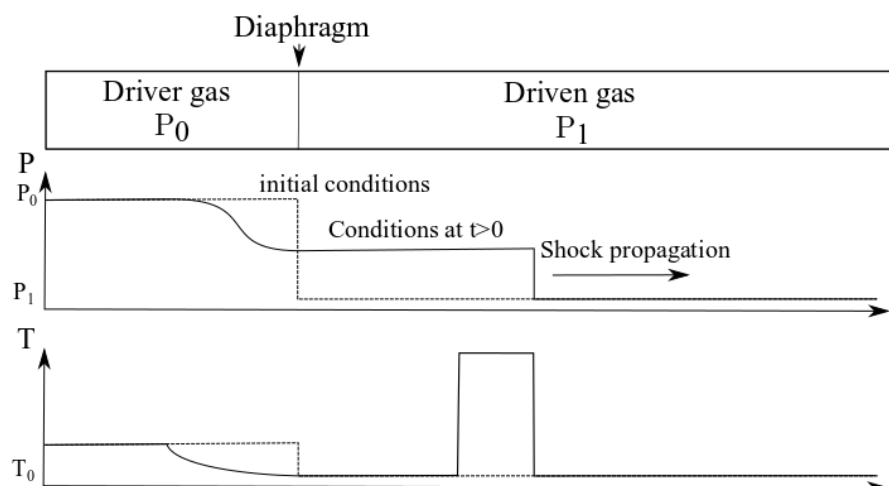


Figure 8: Description of a shock tube facility

The high pressure of the driver gas can be reached using different methods. For example, the free piston driver invented in Australia by Stalker (Stalker, 1967) uses the velocity of a heavy moving piston to compress the gas and increase the pressure in the driver section until the diaphragm breaks. Other facilities rapidly heat the driver gas to increase the pressure – e.g. the NASA EAST facility uses an electric arc to heat the gas (Bogdanoff, 2009). The expansion tube is a variant of the shock tube. For this configuration, a second shock tube is mounted in series with the first one. The incident shock from the first tube impinges on a secondary diaphragm which subsequently breaks, leading to the further acceleration of the shock in the subsequent section. This is done, for example, at the University of Queensland (Gildfind, et al., 2016). A schematic of their X2 expansion tube facility is presented in Figure 9.

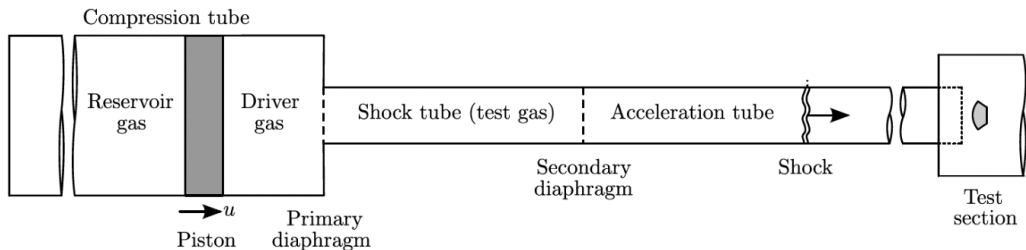


Figure 9: The X2 expansion tube at the University of Queensland. Figure taken from (Gildfind, 2012)

The driven gas can be chosen to match the composition of various planetary atmospheres. Velocities in shock tubes can vary from one facility to another but typical values are between 4 and 15 km/s. The shock tube can reproduce very accurately the shock experienced during atmospheric entry. It is for this reason that these facilities are widely used to study the shock waves and associated hydrodynamic phenomena encountered during atmospheric entry. The main disadvantages of shock tubes are the relatively low-test durations (between 1 μ s and 100 ms) and, for some shock tubes, a relatively low shot-to-shot reproducibility. Another disadvantage is that the exact post-shock properties of the gas (pressure, temperature, chemical conditions, equilibrium/nonequilibrium...) in the test section are not perfectly known and must be estimated by means of numerical simulations or semi-empirical calculations (for example, pitot probe measurements or measured shock speed) (Sharma, et al., 2018) (Wei, 2017).

An exhaustive list of all shock tube facilities around the world can be found in (Igra & Seiler, 2016) and will not be reproduced here. Upcoming facilities include one at Oxford University (T6 free piston shock tube (McGilvray, et al., 2015)) and the European Shock-Tube for High Enthalpy Research (ESTHER) (Da Silva & Carvalho, 2016), a combustion-driven shock-tube in Lisbon inaugurated in July 2019.

2.1.2 Studies and diagnostics

To measure the properties of shock tubes flows, many diagnostic techniques are used and only a few will be discussed here. Aerodynamic sensors such as pitot or static pressure probes are used to measure the pressure at different positions in the shock tube. In the test-section, due to the small test duration and the extreme conditions, non-intrusive time-resolved diagnostics are applied. Schlieren is widely used to measure gas density. Emission and absorption spectroscopy are also a main diagnostic for shock tubes, providing information on the thermodynamic state of the gas and radiation, one of the main interests for reentry applications.

Many studies have been conducted for Earth reentry. Measurements of particular relevance to the work of this thesis were conducted in the EAST facility at relatively low shock speeds (7-9 km/s) to study nonequilibrium radiation (Cruden & Brandis, 2017). These measurements showed relatively poor agreement between current models and experiments at temperatures close to those (around 6000-7000 K) presented in this thesis. Also, in the EAST facility, experiments were recently conducted to investigate fundamental issues in pure nitrogen (Brandis & Cruden, 2018). Nitrogen is not only important for Earth entry but also for Titan. Our current study also aims to provide more data for nitrogen. Finally, a recent study using the X2 expansion tube at the University of Queensland investigated the radiation of plasma flows expanding over a wedge (Wei, 2017) (Wei, et al., 2017). A schematic of the wedge configuration is shown in Figure 10. VUV emission spectroscopy measurements were performed to measure atomic radiation in recombining air flows. This experiment is complementary of those proposed in the current thesis.

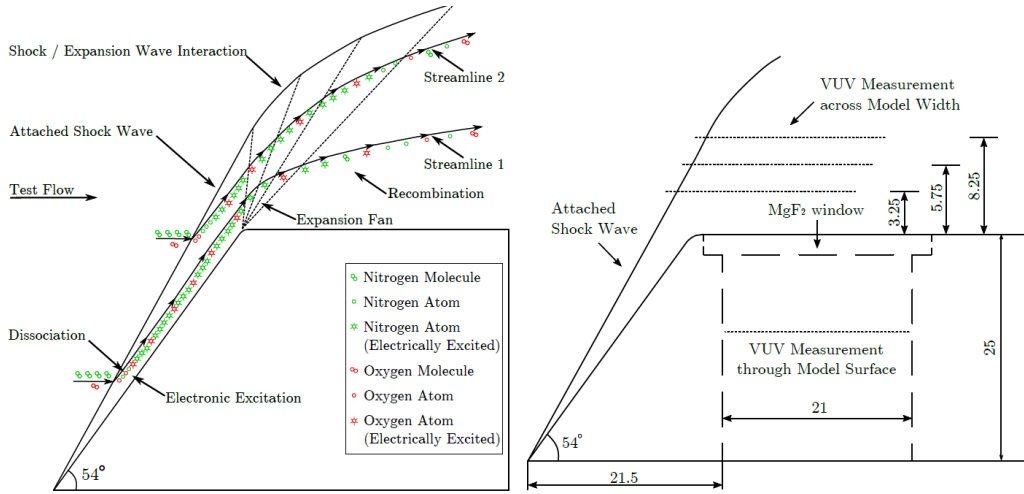


Figure 10: Wedge configuration and measurements performed in the X2 facility. Figures taken from (Wei, 2017).

2.2 Plasma wind tunnels and arcjets

2.2.1 Principle

Plasma wind tunnels (or arcjets) are facilities providing high enthalpy flows at supersonic to hypersonic velocities. These facilities are composed of a gas supply system and a heating system to heat the gas to the desired enthalpy. Then the flow is expanded to supersonic or hypersonic velocities. A comparison of the performance of different arcjets facilities was presented by (Smith, et al., 1998). The various technologies are summarized in Figure 11.

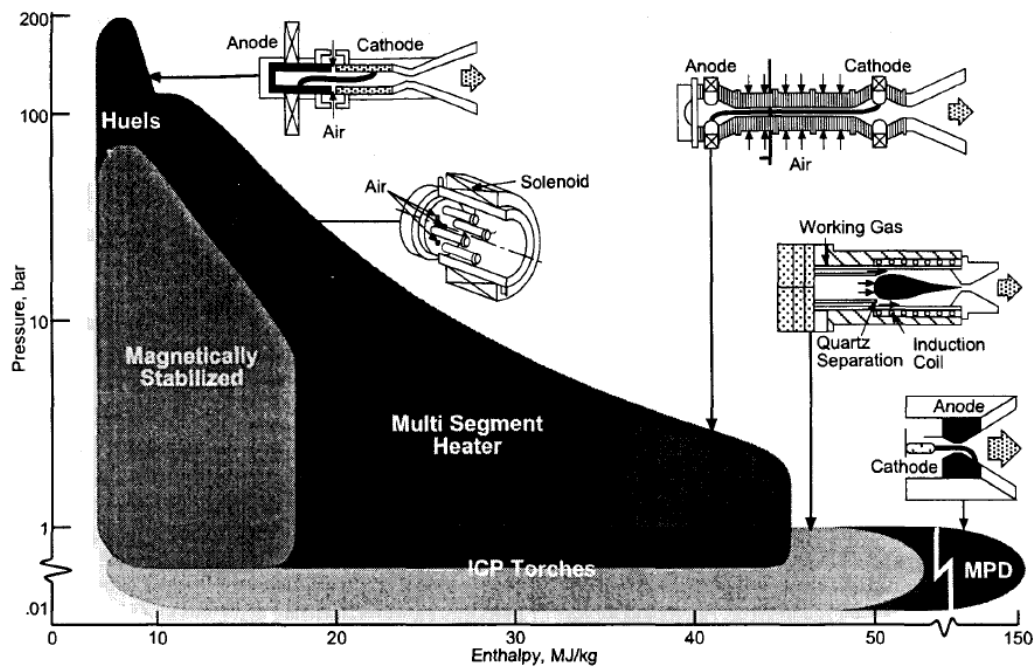


Figure 11: Pressure and enthalpy envelopes for plasma wind tunnels, arcjets and other plasma devices used for high enthalpy flows (Smith, et al., 1998).

The main advantage of these facilities is that they can operate under steady-state conditions. Unlike shock-tubes, however, they do not replicate the shock front in a real entry scenario because the incoming flow is partly excited, dissociated and ionized. Nevertheless, they can match the enthalpy of the shock layer and the heat flux encountered during a real entry scenario, which makes them useful to test thermal protection systems (TPS) (Laub, 2006) and specifically their thermal response over long test times. They can also be used to measure radiation from high enthalpy flows. However, the presence of electrodes in the heating system introduces impurities into the flow due to electrode evaporation and sputtering. This adds a degree of uncertainty to their measurements. In addition, due to the expansion through the nozzle, the flow may also be under nonequilibrium conditions and not completely characterized. Numerical simulations are then required to predict the pre-shock conditions, which again adds a degree of uncertainty. A list of existing facilities is presented in (Smith, et al., 1998) and will not be reproduced here.

2.2.2 Studies and diagnostics

The previously mentioned diagnostics used in shock tube facilities are well suited for arcjets. Thermocouples and pressure gauges can be installed at different points of the facility to get information on flow conditions. Due to the longer test durations, additional diagnostics that are less robust to SNR considerations may be used – these include Laser Induced Fluorescence (LIF or TALIF) and laser scattering diagnostics (Rayleigh, CARS, CRDS...). Also, for TPS testing, pyrometer or thermocouples can be used to measure surface temperature.

These facilities are widely used to test the TPS material used for atmospheric entry (Agrawal, et al., 2010) (Löhle, et al., 2018) and the thermal response. These results are used as validation data for thermal numerical codes (Dec, et al., 2011). It is worth noting also that the boundary layers forming around the ablators are also studied using non-intrusive diagnostics such as emission spectroscopy. (Hermann, et al., 2019) is one such example, where emission spectra in the boundary layer are measured from the VUV to NIR.

2.3 Plasma torches

2.3.1 Principle

Two main categories of plasma torches are identified according to the electron excitation process, either induction heating (Inductively coupled plasma (ICP) torch), or microwave heating (Microwave Plasma Torch (MPT)). An example of an ICP facility is the VKI plasmatron, a high-power facility (1.2 MW, 400 kHz) operating at sub-atmospheric pressure between 5 and 500 mbar, producing plasmas of argon, N₂, CO₂, air at temperatures up to about 10000 K. The plasma torch used in this thesis is an ICP plasma torch and therefore we will focus on this technology.

The main advantages of these facilities are the following:

- Steady-state operation, allowing high Signal-to-Noise Ratio (SNR) measurements
- The absence of electrodes in contact with the flow, ensuring a gas without impurities

However, the conditions reached in our ICP facility (8000K, 1 atm in this study for example) differ largely from real entry scenarios. Entry heat fluxes can still be reached (MacDonald, et al., 2015) but other properties such as the dynamic pressure cannot. These facilities can then be used to test the thermal response of ablators, but not necessarily their mechanical response. Finally, the relatively high temperature provided by these facilities can be used to study radiation under well characterized equilibrium conditions. These can, in turn, be compared with state-of-the-art radiative codes for validation. This latter point will be the interest of the current study.

2.3.2 The TAFA Model 66 plasma torch at CentraleSupélec

The plasma torch facility used here is a TAFA Model 66 inductively coupled plasma (ICP) torch powered by a 120-kVA radio frequency LEPEL Model T-50-3 power supply. The power supply operates at 4 MHz and can provide a maximum of 12 kV DC and 7.5 A to the oscillator plates. Details of the plasma torch facility are provided in many publications (see for example (Laux, 1993) (Gessman, 2000) (MacDonald, et al., 2015) (Laux, et al., 2012)). The plasma nozzle exit diameter varies from 1 to 7 cm. The plasma velocity at the exit of the torch then varies from about 10 to 1000 m/s at the center. Note that we do not currently have diagnostics to measure the plasma velocity, only the total mass flow rate. The radial velocity profile $v(r)$ is therefore estimated by assuming a profile self-similar to the measured temperature profile:

$$v(r) = \bar{T}(r) \cdot \frac{\dot{m}_{tot}}{\int_r^R \rho(\bar{T}(r)) dS} = \bar{T}(r) \cdot v_{ave} \quad (2.1)$$

where $\bar{T}(r)$ is the radial normalized (by area) temperature profile (with $\bar{T}(r=R)=0$), ρ the gas density and \dot{m}_{tot} the total mass flowrate injected in the torch, both parameters being measured. This is justified by the Prandtl number being close to unity (Taine, et al., 2008). The experimental setup of the plasma torch facility is shown in Figure 12.

One main advantage of this plasma torch is that it operates at atmospheric pressure. The high collisionality at this pressure ensures that the plasma is in Local Thermal Equilibrium (LTE). This means that numerical codes are not required to simulate the exit conditions. Rather, the exit conditions can be easily measured and characterized by a single parameter – temperature.

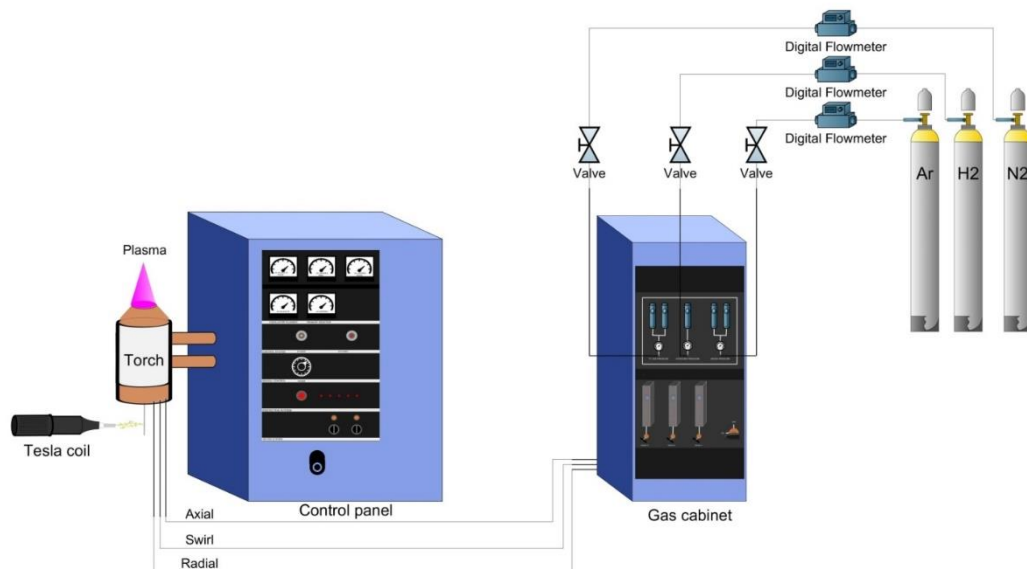


Figure 12 : Plasma torch facility. Gas mixtures can be changed to match the desired experimental conditions.

The plasma torch provides a stable equilibrium atmospheric plasma at maximum temperatures from 6000 to 8000 K at the exit of the nozzle. These conditions are not too far from the post-shock conditions in front of a capsule during reentry (0.5 atm, 10.000K in the shock layer). It is possible to operate the torch with several gas mixtures to study different planetary entry scenarios. The experimental facility is currently equipped to operate with a variety of gases: N₂, air, oxygen, argon, helium, hydrogen, methane, and CO₂. A summary of the different planetary atmospheres that may be studied in the facility is given in Table 1.

Table 1 : Composition of different planetary atmospheres (on the surface) - only gases that may be injected into the plasma torch facility are shown.

Datas taken from (Basilevsky & Head, 2003), (Mahaffy, et al., 2013), (Atreya, et al., 1999), (Niemann, et al., 2005)

Object	Nitrogen	Oxygen	Argon	CH ₄	H ₂	Helium	Carbon dioxide
Venus	3,5%						96,5%
Earth	78%	21%	0,9%				0,04%
Mars	1, 9%	0,15%	1,9%				96%
Jupiter				0,1%	86%	13%	
Saturn					96%	4%	
Titan	97%				3%		

Uranus	2%	83%	15%
--------	----	-----	-----

A schematic of the torch is shown in Figure 13. Gas is injected at the bottom of the torch using a combination of various injection modes: swirl, radial and axial. The total gas flow rates are usually between 1.5 g/s and 4 g/s.

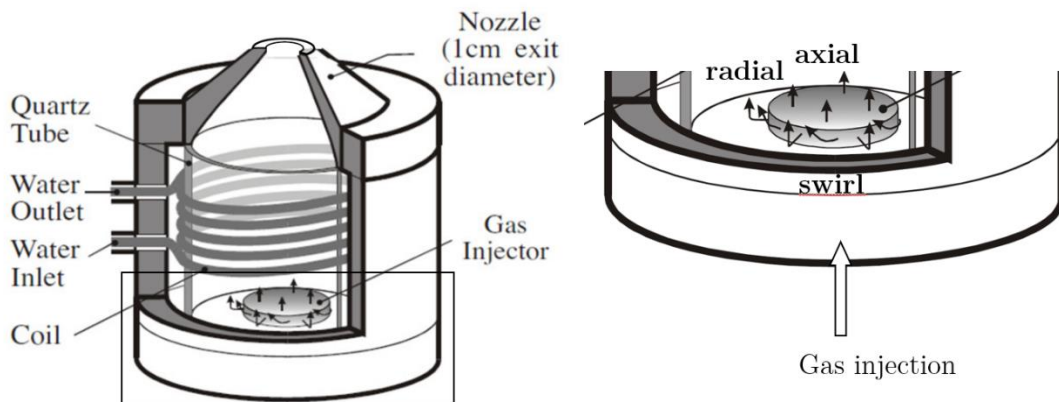


Figure 13 : Schematic of the plasma torch facility and the different injections modes

The radial/swirl ratio has an influence on the plume of the plasma jet. An example of three different ratios are presented in Figure 14. The units are given in Standard Liter Per Minute (slpm). The higher the ratio of radial to swirl injection, the longer the plume. The radial/swirl injection ratio also affects the centerline gas temperature at the exit. Increasing the swirl will primarily result in a flatter temperature profile with a decrease of the centerline temperature by a few hundred degrees, for the same power per unit of volume injected. The axial injection makes the torch unstable with most of the gas and therefore is usually not used.

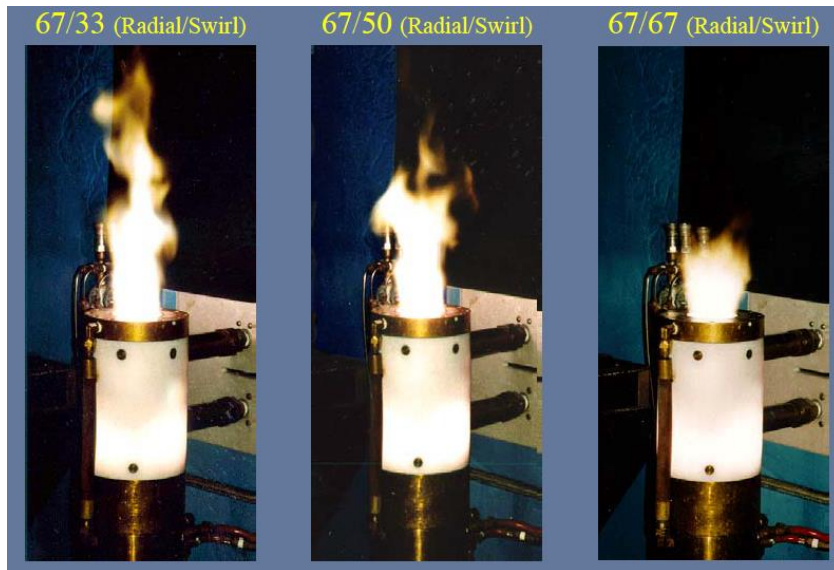


Figure 14: Air plasma plume for three conditions of the radial/swirl flowrates.

Several studies have shown that the plasma at the exit of the torch is in equilibrium (Laux, 1993) (MacDonald, et al., 2015). This assumption was also verified in this study by comparing measured and computed LTE emission spectra at the exit of the plasma torch, which were found to be in excellent agreement.

The range of wavelengths studied here spans the VUV to NIR region. Other studies were previously performed in the IR region (Laux, et al., 1995). Good agreement was always obtained between measured and computed LTE spectra. Note that the plasma in the coil region is expected to be under nonequilibrium conditions, however, a previous study (Laux, 1993) showed using a kinetic model that the plasma has sufficient time to relax to equilibrium conditions by the time it reaches the nozzle exit. In summary, the plasma torch provides a steady, LTE plasma flow.

A water-cooled tube can be mounted at the exit of the torch nozzle in order to rapidly cool the plasma. This is the same tube used for previous experiments performed by Gessman *et al* (Gessman, 2000) to create a recombining plasma at the exit of the torch (Gessman, 2000). The tube is made of brass and is modular in length up to 60 cm. Emission and Raman diagnostics are performed at the entrance and exit of the modular tube.

During reentry, the plasma loses enthalphy while flowing to the afterbody due to the loss of pressure. The differential enthalpy per unit mass dh of the plasma flowing from the forebody to the afterbody can be written as:

$$dh = T ds + \frac{1}{\rho} dP = \frac{1}{\rho} dP$$

where T and P are the temperature and pressure of the gas, respectively, s the entropy per unit mass, ρ the density of the gas. The transformation is assumed to be isentropic in this region, assuming a reversible (ideal) and adiabatic (negligible heat transfer to the wall) transformation. The change of enthalpy leading to plasma recombination is therefore imposed by the drop of pressure.

In our case, assuming that the plasma produced by the plasma torch is ideal, we have:

$$dh = T ds + \frac{1}{\rho} dP = Tds$$

because the plasma stays at atmospheric pressure. Note that the pressure drop is assumed to be negligible as confirmed by CFD simulations. Therefore, a drop of enthalpy can be imposed by imposing a drop in entropy. Instead of creating a strong expansion as with an entering capsule, the plasma is instead forced to recombine by imposing rapid cooling via the cold wall (maintained at approximately 300 K) decreasing gas entropy. This setup is therefore intended as a simplified experimental model of a real atmospheric entry scenario. Details of the experimental setup are presented in Figure 15. Note that the temperature of the cooling water at the inlets and outlets of the tube are measured to perform a power balance.

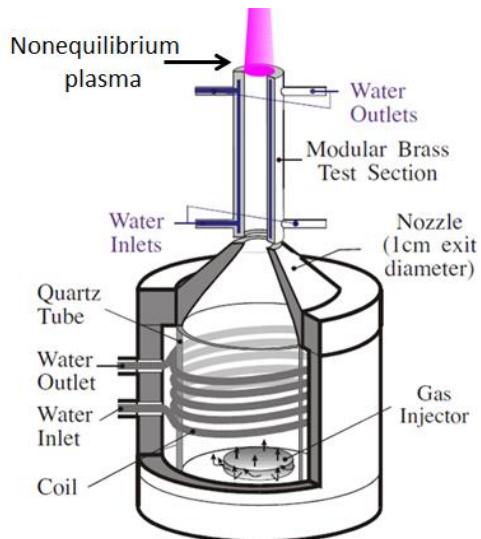


Figure 15 : Water-cooled test-section mounted on top of the plasma torch

2.4 Optical diagnostics

Optical Emission Spectroscopy (OES) is a non-intrusive diagnostic technique for radiating gases and is well suited for plasma applications. However, OES only gives the temperatures of excited states of atoms or molecules and may not be representative of the gas temperature. When the gas is in Local Thermodynamic Equilibrium (LTE), any temperature measurement provides the gas temperature and therefore OES is a useful technique as it offers high signal-to-noise ratio measurements. Under nonequilibrium conditions, however, different species and different states within each species may be associated with a different temperature. A common approach is to measure a rotational temperature and assume that it is equilibrated with the translational temperature owing to the short Rotational-Translational (RT) relaxation time (Parker, 1959). (Bruggeman, et al., 2014) performed a review of rotational temperature measurements in nonequilibrium plasmas and defined conditions for which the rotational lines of $N_2(C)$ and $N_2^+(B)$ can be used to determine gas temperature. The authors mainly focused on low temperature plasmas in thermal nonequilibrium (temperature of electrons different than the translational gas temperature) due to the presence of electric fields. This was the focus of many studies for low temperature plasmas, see for example Refs. (Linss, et al., 2004) (Chan, et al., 2011) (Sonnenfroh & Leone, 1989) (Brussaard, et al., 1998) for temperature measurements under thermal nonequilibrium

conditions. We will focus here on thermal equilibrium cases with potential chemical nonequilibrium.

OES is also used in the hypersonics community as previously mentioned in sections 2.1 and 2.2. It is used for example to measure temperatures in the shock layer (Sharma & Gillespie, 1991) (Sharma, 1992). Similar work was performed by Fujita *et al* (Fujita, et al., 2002) (Yamada, et al., 2008). OES is also used in shock tubes to determine the radiation and the temperatures from the shock layer, see for example (Cruden & Brandis, 2017) (Brandis & Cruden, 2018) (Wei, et al., 2017), as well as in wind tunnels or arcjets facilities (Hermann, et al., 2019) (Cipullo, et al., 2012).

In this thesis, we resort to Optical emission spectroscopy (OES) to determine the state of the gas at the exit of the plasma torch. We will detail here the procedure used to measure absolute emission spectra. Two parabolic mirrors collimate the light emitted by the plasma and refocus it onto the entrance of the spectrometer. The focal lengths of the mirrors can be adjusted to obtain the desired magnification. Parabolic mirrors were preferred over lenses as we will perform measurements on a wide range of wavelength and their focal lengths do not depend on the wavelength (no chromatic aberration). A periscope is also used to rotate the image by 90 degrees to align the spectrometer entrance slit parallel to the tube or nozzle exit. For most experiments presented on this thesis, the plasma torch exit nozzle diameter was 1 cm. The magnification is of the optical train is around unity and allows to acquire spectra across the diameter of the tube. The emission spectroscopy setup is shown in Figure 16.

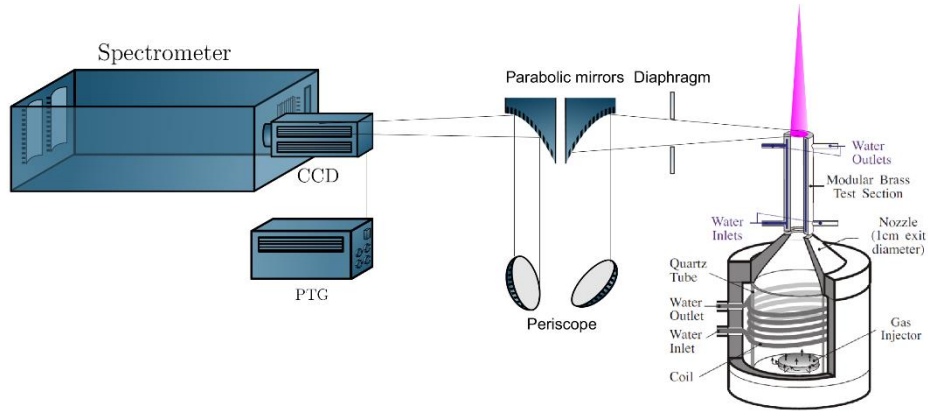


Figure 16 : Experimental setup for emission spectroscopy in the plasma torch facility

The spectrometer is an Acton Instrument 2500i with three different gratings, 600, 1200 and 2400 gr/mm with a UV enhanced Princeton Instruments PI-MAX II intensified camera mounted at the exit port, allowing to measure spectra from 250 to 900 nm. The measured spectra have units of pixel counts as a function of wavelength. In order to arrive at the true value of the intensity for quantitative analysis, a calibration is needed. Note that the response of the camera used was found to be linear with the integration time if the integration time does not vary by more than 2 orders of magnitude (Rusterholtz, 2012). For the absolute calibration, a stable light source, with a known radiance over the relevant range of wavelengths is needed. A spectrum of this calibrated source is taken with the spectrometer using the same optical configuration as in the experiment. This yields a spectrum in counts. The calibration source used in this study was an Optronics Laboratories tungsten lamp (model OL550) which has a calibration traceable to NIST standard. An alternative calibration source also used was a GE tungsten lamp that behaves as a grey body but with an emissivity varying with temperature and wavelength. This emissivity was previously measured by (Larrabee, 1957). Measuring the temperature with a pyrometer allows one to calculate the emitted spectra. The tungsten temperature measurement was performed for every calibration set. Note the ability to adjust the tungsten lamp temperature is useful to get good signal over a large range of wavelengths. Because the radiance is known, we can calculate the theoretical spectrum in units of spectral radiance ($\text{W}/\text{cm}^2/\text{sr}/\text{nm}$). The ratio with the two spectra gives a calibration factor (with wavelength dependence) in $(\text{W}/\text{cm}^2/\text{sr}/\text{nm})/\text{counts}$. We multiply all experimental

spectra measured with the same optical train by this factor to obtain a calibrated spectrum in true intensity units. The final calibrated intensity $I(\lambda)$ in $\text{W}/\text{cm}^2/\text{sr}/\text{nm}$ is then:

$$I(\lambda) = S_{\text{plasma}}(\lambda) \cdot \frac{I_{\text{Tungsten}}(\lambda, T)}{S_{\text{tungsten}}(\lambda)} \quad (2.2)$$

where S_{plasma} is the spectrum of the plasma collected by the CCD camera, I_{tungsten} is the theoretical intensity of the tungsten filament at the measured temperature T (if the GE lamp is used) and S_{tungsten} is the measured spectrum of the tungsten lamp using the same optical setup as for the plasma measurements.

To analyze the data from the axisymmetric plasma produced by the torch, an Abel-inversion is used to convert the measured spectra from lateral line-of-sight measurements to radial quantities. To this end, spectra are taken along the line of sight at n lateral locations. We consider that the plasma properties are homogeneous in each of the n corresponding radial rings. The n line-of-sight measurements form a discrete representation of $F_r(\lambda)$, the function describing the spatial dependence of this line-of-sight emission. The volumetric emission is described by the function $f_r(\lambda)$. We have for example: $F_0(\lambda) = \int_{-R}^R f(r, \lambda) dr$. An Abel-inversion algorithm can be used to calculate f from F . All the measured spectra can thus be Abel-inverted to obtain the volumetric emission of the plasma. In this thesis, the spectra were Abel-inverted using POLAB4 (Laux, 1993), an Abel-inversion program capable to calculate also the propagated uncertainties. Note that the Abel-inversion algorithm assumes that the plasma is optically thin. Therefore, this procedure will only be used after checking this assumption. Finally, note that the axisymmetric assumption needed for the Abel inversion is confirmed by measuring the full radial profile of the torch. The two half profiles are then measured and are found to be very close. The Abel-inversion procedure is summarized in Figure 17.

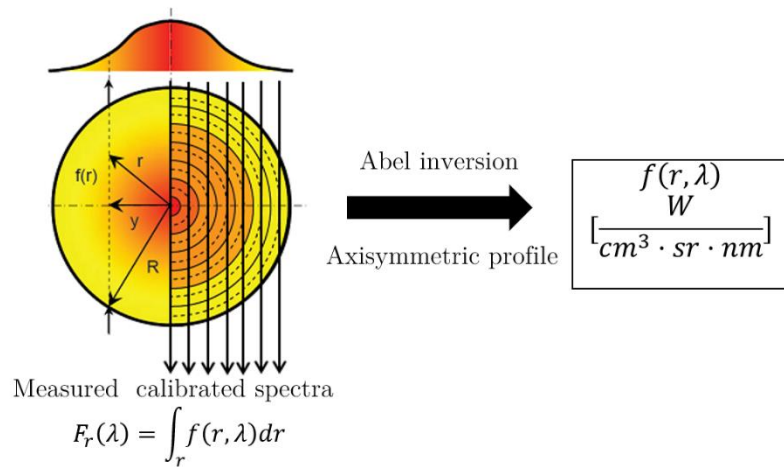


Figure 17 : Abel inversion procedure

An example of Abel-inverted spectrum is given in Figure 18. This corresponds to a N₂/Ar plasma at the exit of the torch. The spectrum shown in the figure includes 3 lines of N, 4 lines of argon, and a molecular band of N₂.

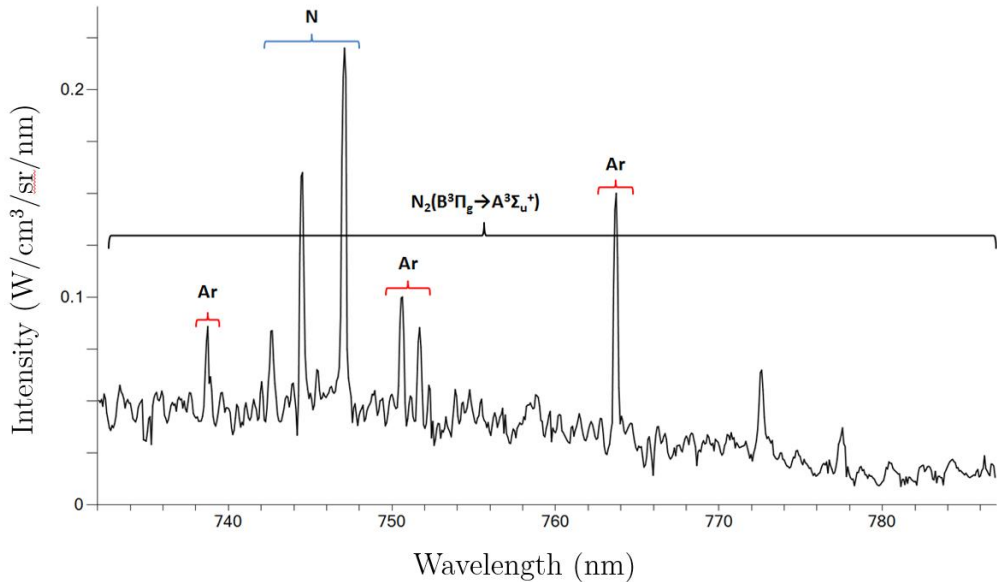


Figure 18: Abel-inverted emission spectrum of a N₂/Ar plasma at the exit of the torch. The atomic and molecular transitions are identified.

The procedure to determine the temperature of the plasma is detailed by (Laux, 1993) but is summarized again here. For a plasma in LTE, the LTE temperature

is defined by the relationship between the density of the emitting electronic level u and the total number density of the species, as given by the Boltzmann relation:

$$\frac{n_u}{g_u} = \frac{n_s(T_{LTE})}{Q_{el}^s(T_{LTE})} e^{-\frac{\epsilon_u}{kT_{LTE}}} \quad (2.3)$$

where g_k is the degeneracy of the k^{th} level, ϵ_u is the electronic energy of level u , and n_s is the number density of the considered species. Under LTE conditions, n_s is given by:

$$n_s = x_s(T_{LTE}) \frac{P}{k T_{LTE}} \quad (2.4)$$

where x_s is the mole fraction of species s and P the pressure. The mole fraction can be found using the NASA CEA chemical equilibrium code (McBride & Gordon, June 1996). Reorganizing these equations yields an implicit equation for T_{LTE} :

$$\frac{n_u}{g_u} = \frac{x_s(T_{LTE})P}{Q_{el}^s(T_{LTE})k T_{LTE}} e^{-\frac{\epsilon_u}{kT_{LTE}}} \quad (2.5)$$

The number density of an excited state n_u can be measured by using emission spectroscopy to target a specific atomic transition. The emissivity ε from an optically thin spectral line is related to the number density of the transition's upper state (emitting level) via the following expression:

$$\varepsilon = n_u \frac{A_{ul}}{4\pi} (\epsilon_u - \epsilon_l) \quad (2.6)$$

where A_{ul} (sec^{-1}) is the Einstein A coefficient for the radiative transition from level u to level l , ϵ_u and ϵ_l are the energies of the upper and lower states of the transition, respectively. Combining equations (2.5) and (2.6), it is then possible to determine an LTE temperature for each measured atomic line. To check the equilibrium assumption, we usually performed this analysis on multiple atomic lines with different emitting levels and from different species (namely N and Ar). Agreement between all measured LTE temperatures gives confidence in the LTE assumption. Otherwise, the plasma is in nonequilibrium.

Rotational temperature measurements from excited electronic states of N_2 or N_2^+ can also be performed using emission spectroscopy. The method will be explained in Chapter 4. It should be noted that these measurements do not always give temperatures representative of the gas in nonequilibrium conditions (Bruggeman,

et al., 2014). Analyses will be performed when rotational temperatures are determined to ensure that they are indeed representative of the gas temperature.

Finally, Spontaneous Raman scattering spectroscopy was also used as an optical diagnostic. The technique will be presented in more detail in Chapter 3.

2.5 Scope of the thesis

The experimental configuration presented in Figure 15 was previously studied at Stanford University by Gessman *et al* (Gessman, 2000). Some key results will be summarized here. Gessman *et al* focused on a nitrogen/argon mixture with 1.9 g/s of nitrogen and 1.5 g/s of argon injected in the torch. Argon was required to ensure plasma stability. Gessman *et al* showed that the plasma was in equilibrium at the inlet of the tube, and in nonequilibrium at 15 cm. The degree of nonequilibrium was quantified by measuring the overpopulation of nitrogen excited states such as N₂(B), N₂(C), and N₂⁺(B). Moreover, the temperature was measured using emission spectroscopy. At the inlet of the tube (0 cm), they used the absolute intensity of different atomic lines with the procedure detailed in section 2.4 to determine the temperature. At 15 cm, the temperature was measured using rotational lines of N₂⁺(B) with the procedure detailed in (Laux, et al., 2001). Candler *et al* (Candler, et al., 1998) (Nagulapally, et al., 1998) performed CFD simulations of this configuration to predict the temperature drop in the tube. A comparison between the experiments and the simulations is presented in Figure 19. The CFD simulations were not able to predict the measured drop of temperature. Along the tube, the CFD only predicts at best a drop of 400 K whereas the measurements showed a 2350 K decrease.

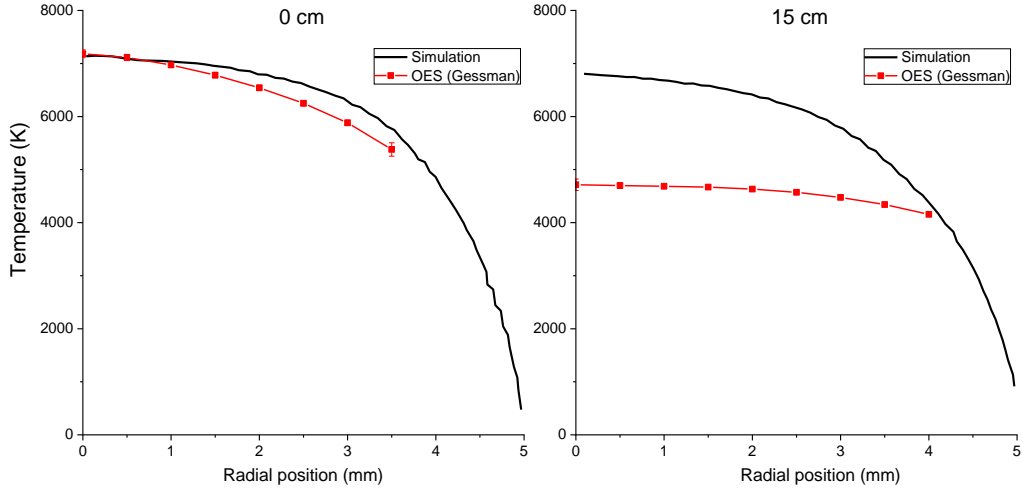


Figure 19: Comparison between the temperatures profiles measured by (Gessman, 2000) (red) and the simulations of (Nagulapally, et al., 1998) (black) in the case of an N_2/Ar plasma mixture at 0 cm (left) and 15 cm (right).

The large difference between CFD and experiments remains unexplained. Simulations taking into account a swirling component of the flow were performed, without significant improvement (Nagulapally, et al., 1998). A possible reason for this discrepancy could come from the diagnostics used to measure the temperature. The measured temperature was obtained as the rotational temperature of an excited state of N_2^+ , namely $\text{N}_2^+(\text{B}^2\Sigma_g^+)$. This temperature is not representative of the bulk temperature in many cases (Bruggeman, et al., 2014).

This thesis is in the continuity of Gessman's thesis. To remove doubts about the temperature measurements, a spontaneous Raman spectroscopy setup was developed to measure the temperature of the ground state of nitrogen, which is more representative of the gas temperature than the rotational temperature of $\text{N}_2^+(\text{B})$. Other temperature measurements using emission spectroscopy will also be presented in the following chapters.

Ultimately, the fluid dynamics and plasma kinetics within the water-cooled tube are coupled. To decouple these effects, experiments were performed for a variety of conditions presented in Table 2. The conditions range from laminar to turbulent regimes and from chemical equilibrium to nonequilibrium. The chemical conditions (equilibrium or nonequilibrium) are estimated based on the results of Gessman *et al* (Gessman, 2000) and will be verified in the following chapters. Note that the

measurements for the “pure air” case are taken from Gessman *et al* (Gessman, 2000). We repeated these experiments and obtained the same results, which are therefore not presented here. For all other cases, the reported results are from the measurements performed during this thesis. The plasma torch cannot be operated with pure N₂ and thus the N₂/Ar mixture is necessary for studying nitrogen kinetics. The case labeled “N₂/Ar HF” corresponds to the case previously studied by Gessman (Gessman, 2000). The Air/Ar mixture was chosen for comparison with the N₂/Ar HF case, keeping the same mass flow rate, hence aerodynamic regime, in order to isolate the effects related to chemical kinetics. Note that the turbulent energy of the flow was not measured. The labels “laminar” and “turbulent” are based on the Reynolds number estimates.

Table 2: Measured mass flow rates and expected conditions for the different plasma cases studied

	Mass flow rate	Radial/Swirl injection ratio	Estimated Reynolds number based on the tube diameter	Chemical conditions
Pure air	$\dot{m}_{Air} = 1.9 \text{ g/s}$	65/35	~1900 (laminar)	Equilibrium
Air/Ar	$\dot{m}_{Air} = 1.9 \text{ g/s}$ $\dot{m}_{Ar} = 1.5 \text{ g/s}$	75/25	~3600 (turbulent)	Equilibrium
N ₂ /Ar LF	$\dot{m}_{N_2} = 1.2 \text{ g/s}$ $\dot{m}_{Ar} = 1.5 \text{ g/s}$	70/30	~2700 (turbulent)	Nonequilibrium
N ₂ /Ar HF	$\dot{m}_{N_2} = 1.9 \text{ g/s}$ $\dot{m}_{Ar} = 1.5 \text{ g/s}$	75/25	~3600 (turbulent)	Nonequilibrium

Chapter 3 Raman spectroscopy

In this Chapter, we will present the measurements made using spontaneous Raman scattering spectroscopy in the recombining plasma test cases presented in Chapter 2. Previous temperature measurements were performed using emission spectroscopy. However, emission spectroscopy only yields the temperature of excited states and therefore such temperature measurements may not be representative of the gas temperature for certain nonequilibrium cases, in particular the nonequilibrium plasmas produced at the exit of the water-cooled tube (Bruggeman, et al., 2014). Raman spectroscopy was therefore applied to measure both the rotational and vibrational temperature of the ground state of molecular nitrogen, which is close to the bulk gas temperature.

3.1 Theory

When monochromatic radiation of frequency ω_0 is incident on a particular medium, such as a molecular gas, photons can either be absorbed, scattered, or transmitted. Scattering can either be elastic or inelastic (Long, 2002). The frequency of the scattered radiation depends on the type of event. The frequency of elastically scattered photons is left mostly unchanged, with small alterations coming from Doppler or pressure broadening effects. This is generally categorized as Rayleigh or Brillouin scattering, depending on the regime of elastic scattering. If the photon is scattered inelastically, pairs of photons at new frequencies $\omega_0 \pm \omega_1$ will appear. This inelastic scattering is termed Raman scattering. ω_1 is a Raman shift characteristic of the particle responsible for scattering the photon. The scattered photon of frequency $\omega_0 - \omega_1$ is called Stokes and the $\omega_0 + \omega_1$ Anti-Stokes. The magnitude of this frequency shift depends on the energy of the internal levels of the molecule. The energy exchanged between the photon and the molecule corresponds to the energy of the transition between the rotational, vibrational, and electronic levels of the molecule. The Raman scattering signal is therefore species specific and proportional to the species number density. Interferences between different gas species are rare for vibrational Raman scattering (Eckbreth, 1996).

Figure 20 summarizes Rayleigh and Raman effects.

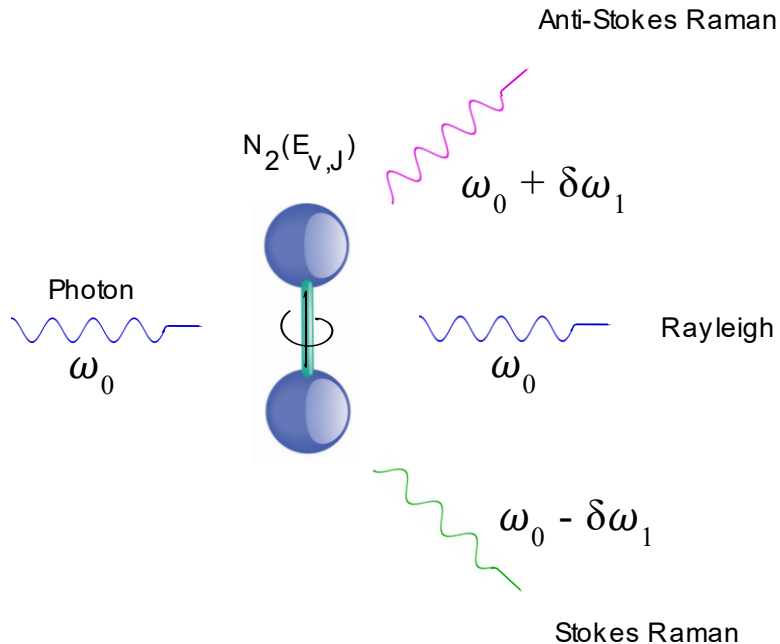


Figure 20: Rayleigh and Raman scattering.

To interpret the measurements, a Raman model was developed. First some terms need to be defined. An incident electromagnetic wave (the incident photon in the measurements) induces a polarization of matter. Raman effect is related to the molecular polarizability a defined by:

$$\vec{p} = a\epsilon_0 \vec{E} \quad (3.1)$$

where \vec{p} is the dipole moment induced by the incident electric field \vec{E} , and where ϵ_0 is the permittivity of vacuum. The polarizability depends on the positions of the atomic nuclei and therefore on the vibrational modes of the considered molecule. Let's consider a molecule which is free to vibrate but does not rotate relatively to the considered referential. We will consider a diatomic molecule as it will be the case of interest the current study. A diatomic molecule has only one normal mode vibration associated to a normal coordinate Q representing the positions of nuclei away from the equilibrium position. The variation of the polarizability with the vibrational mode of the molecule can be decomposed using a first order Taylor series with a mean and static term a_0 , representing the value at the equilibrium position, and a polarizability derivative to the normal position Q , representing the variation of a due to the vibrational mode of the molecule:

$$a = a_0 + \left(\frac{\delta a}{\delta Q} \right) Q \quad (3.2)$$

Where $(\delta a / \delta Q) = a'$ is called the derived polarizability tensor. Since \vec{p} and \vec{E} are vectors, then a and a' are tensors - symmetric ones in most cases of interest (Eckbreth, 1996). In Raman experiments, we measure intensities of scattering light relative to space-fixed axes (laboratory axes) from molecules free to rotate. To get the measured intensity, we need to average the scattering for all orientations of the molecule relating to the laboratory axes. The averaging is largely explained by (Long, 2002) for different bases. The main result is that it highlights the existence of three rotational invariants of the axis system of the polarizability tensor which will be important in the Raman effect modelling. The polarizability tensor can be written in a cartesian basis as:

$$a = \begin{matrix} a_{xx} & a_{xy} & a_{xz} \\ a_{yx} & a_{yy} & a_{yz} \\ a_{zx} & a_{zy} & a_{zz} \end{matrix} \quad (3.3)$$

This notation allows to define the three rotational invariants, the mean or isotropic polarizability α , the antisymmetric anisotropy δ and the anisotropic polarizability γ as explained by (Long, 2002):

$$\begin{aligned} \alpha &= \frac{1}{3} (a_{xx} + a_{yy} + a_{zz}) \\ \delta^2 &= \frac{3}{4} (|a_{xy} - a_{yx}| + |a_{yz} - a_{zy}|^2 + |a_{zx} - a_{xz}|^2) \\ \gamma^2 &= \frac{1}{3} (|a_{xx} - a_{yy}|^2 + |a_{yy} - a_{zz}|^2 + |a_{zz} - a_{xx}|^2) \\ &\quad + \frac{3}{4} (|a_{xy} + a_{yx}|^2 + |a_{xz} + a_{zx}|^2 + |a_{yz} + a_{zy}|^2) \end{aligned} \quad (3.4)$$

In this thesis, a model was implemented for the Stokes ($\Delta v = 1$) vibrational Raman spectrum of N₂(X), following the model proposed by (Lo, et al., 2012). First, the energies of the rovibronic levels of N₂ were calculated using the Dunham series expansion (Lofthus & Krupenie, 1977):

$$\begin{aligned} E_{v,J} &= T_e + \omega_e \left(v + \frac{1}{2} \right) - \omega_e x_e \left(v + \frac{1}{2} \right)^2 + \omega_e y_e \left(v + \frac{1}{2} \right)^3 \\ &\quad + \omega_e z_e \left(v + \frac{1}{2} \right)^4 + B_v J (J+1) - D_v J^2 (J+1)^2 \end{aligned} \quad (3.5)$$

$$\begin{aligned} B_v &= B_e - \alpha_e \left(v + \frac{1}{2} \right) + \gamma_e \left(v + \frac{1}{2} \right)^2 \\ D_v &= D_e + \beta_e \left(v + \frac{1}{2} \right) \end{aligned} \quad (3.6)$$

where $E_{v,j}$ is the energy of vibrational level v and rotational level J , and where T_e , ω_e , $\omega_e x_e$, $\omega_e y_e$, $\omega_e z_e$, B_e , α_e , γ_e , D_e , and β_e are the Dunham coefficients taken from (Huber & Herzberg, 1939).

Selection rules for vibrational Raman scattering impose a change in the rotational levels of $\Delta J = -2$, $\Delta J = 0$ and $\Delta J = 2$ for the O, Q, and S branches, respectively.

The intensities of the O- and S-branches only depend on the anisotropic contribution γ and the Q-branch depends on both the isotropic and anisotropic terms. For linear molecules, the isotropic term is much larger than the anisotropic one (Eckbreth, 1996). Thus, the Q-branch is the most intense component of the Raman spectrum. If the anisotropic contribution of the Q-branch is neglected, the relative intensity of Raman lines is given simply by (McGuire, et al., 2017):

$$I_{v,J}^Q = N_{v,J} (v + 1) \quad (3.7)$$

where $N_{v,J}$ is the number density of molecules in vibrational state v and rotational state J .

A more complete model is needed to compute the Stokes vibrational-rotational spectra $\Delta v = 1$ including the Q, O and S branches. We implemented such a model and we validated it against previous Raman models presented in Refs. (Lo, et al., 2012) (Lempert & Adamovich, 2014).

The intensity of the scattered light depends on the propagation axis of the incident light, its polarization, and on the angle at which the scattered light is collected relative to the direction of propagation of the incident field (Eckbreth, 1996). To simplify, in all experiments using a cartesian basis, the incident light will propagate along the y axis, polarized along the z axis, and the scattered light will be collected along the x axis. The integrated intensities of the Raman Stokes lines for the O, Q

and S branches are given in this case by (Long, 2002) (Lo, et al., 2012) (Lempert & Adamovich, 2014) (Eckbreth, 1996):

$$I_{v,J}^O = \frac{h}{8\epsilon_0^2 \Delta\sigma_O} (\sigma_0 - \Delta\sigma_O)^4 \left(\frac{4}{45} b_{J,J-2}(\gamma')^2 \right) N_{v,J} P_L \quad (3.8)$$

$$I_{v,J}^Q = \frac{h}{8\epsilon_0^2 \Delta\sigma_Q} (\sigma_0 - \Delta\sigma_Q)^4 \left((\alpha')^2 + \frac{4}{45} b_{J,J}(\gamma')^2 \right) N_{v,J} P_L \quad (3.9)$$

$$I_{v,J}^S = \frac{h}{8\epsilon_0^2 \Delta\sigma_S} (\sigma_0 - \Delta\sigma_S)^4 \left(\frac{4}{45} b_{J,J+2}(\gamma')^2 \right) N_{v,J} P_L \quad (3.10)$$

where h is the Planck constant, ϵ_0 the permittivity of vacuum, σ_0 the laser wavenumber, $\Delta\sigma_O, \Delta\sigma_Q$, and $\Delta\sigma_S$ the Raman shifts for the O-, Q- and S-branches, respectively, equal to $E_{v,J} - E_{v-1,J+(2,0,-2)}$ computed using Eq (3.5), $b_{J,J'}$ the Placzek-Teller coefficients (Eckbreth, 1996) representing the dependence of the rotational Raman line with the rotational levels, α' and γ' the mean and anisotropic part of the derived polarizability tensor, respectively, and P_L the laser irradiance (in W/m²) of the incident laser beam. Note that this model can take into account a possible nonequilibrium of the rovibrational state distribution. The resulting measured spectra also includes a line shape for each of these lines due to broadening effects such as Doppler or natural broadening (Long, 2002). However, in our case the broadening of the Raman lines is dominated by the instrumental broadening and therefore will be the only one modeled. The slit function was experimentally measured as it will be presented in section 3.3.

The Raman line intensities are calculated taking into account the contribution of both anharmonicity and vibration-rotation interactions, following the work by (Lo, et al., 2012). The vibration-rotation interactions are described using the Herman-Wallis factors (Herman & Wallis, 1955) , $F_{v,v'}^\mu$, for both the isotropic ($\mu = \alpha$) and anisotropic ($\mu = \gamma$) components of the polarizability tensor (Long, 2002):

$$(\mu')^2 = \langle v, J | \mu | v', J \rangle^2 = F_{v,v'}^\mu(J) \langle v | \mu | v' \rangle^2 , \quad \mu = \alpha, \gamma \quad (3.11)$$

where $\langle v | \mu | v' \rangle$ are the vibrational matrix transition elements. We used the v-dependent Herman-Wallis factors proposed for N₂ by (Buldakov, et al., 2002):

$$F_{v,v+1}^\mu(J) = 1 + A_{v,v+1}^\mu + B_{v,v+1}^\mu m + C_{v,v+1}^\mu m^2 , \quad \mu = \alpha, \gamma \quad (3.12)$$

where $m = 2J + 1$ for the O-branch, $m = J(J + 1)$ for the Q-branch and $m = 2J + 3$ for the S branch. The parameters A, B and C are given in Table 3 and were taken from (Lo, et al., 2012) following the work by (Buldakov, et al., 2002).

Table 3: Herman-Wallis factors used for the Raman model of N₂. For the Q-branch, A_{v,v+1}^α, A_{v,v+1}^γ, C_{v,v+1}^α and C_{v,v+1}^γ are equal to zero. Data taken from (Lo, et al., 2012).

O- and S-branches		Q-branch	
$A_{v,v+1}^{\gamma}$	$1.04 \times 10^{-5} - 0.09 \times 10^{-6} v$	$B_{v,v+1}^{\alpha}$	$1.1 \times 10^{-5} - 0.61 \times 10^{-7} v$
$B_{v,v+1}^{\gamma}$	$-2.2 \times 10^{-3} - 0.37 \times 10^{-4} v$	$B_{v,v+1}^{\gamma}$	$0.14 \times 10^{-4} - 0.12 \times 10^{-6} v$
$C_{v,v+1}^{\gamma}$	$0.45 \times 10^{-5} + 0.11 \times 10^{-7} v$		

We also used the anharmonicity corrections for the potential curve of N₂ proposed by (Buldakov, et al., 2002):

$$\langle v \mid \mu \mid v + 1 \rangle = \sqrt{(v + 1) \left(\frac{B_e}{\omega_e} \right)} (c_0^\mu + c_1^\mu v), \quad \mu = \alpha, \gamma \quad (3.13)$$

where $c_0^\alpha = 1.871 \text{ \AA}^3$, $c_1^\alpha = 0.0105 \text{ \AA}^3$, $c_0^\gamma = 2.25 \text{ \AA}^3$ and $c_1^\gamma = 0.019 \text{ \AA}^3$.

Examples of spectra obtained with this model are given in Figure 21 with and without convolution using a slit function, and for a laser excitation wavelength of 281 nm. Spectra are computed from 300 to 7000 K as this is the expected range of temperatures in our experiments. We only show here spectra calculated under equilibrium conditions with T_{rot}=T_{vib}. However, the model can also be used to analyze spectra with different temperatures for rotation and vibration.

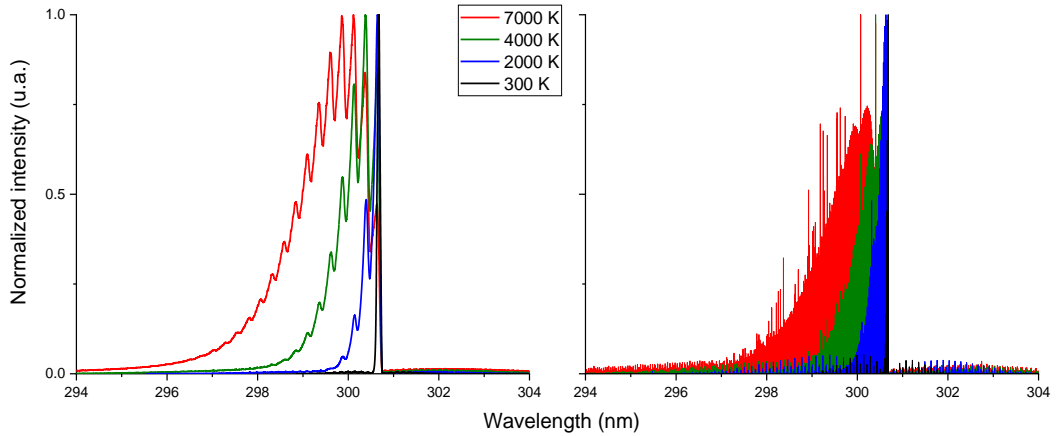


Figure 21: Modeled Raman spectra of N_2 (normalized in intensity) for $T_{\text{vib}} = T_{\text{rot}} = 300, 2000, 4000$, and 7000 K . Left: Modeled spectra convolved with a triangular instrumental function of $\text{FWHM} = 0.065 \text{ nm}$. Right: No slit function. Laser excitation wavelength: 281 nm .

As a verification step, Figure 22 compares the results of our model with those obtained by (Lo, et al., 2012). Because we made the same assumptions as (Lo, et al., 2012), results should be the same. As an example, the theoretical spectrum computed by (Lo, et al., 2012) with $T_{\text{rot}} = 618 \text{ K}$ and $T_{\text{vib}} = 2942 \text{ K}$ is compared with the implemented model. We also used the same instrumental function than (Lo, et al., 2012). The two sets of calculations are in good agreement. The small differences are attributed to errors in the digitization of the spectrum and of the instrumental function of (Lo, et al., 2012).

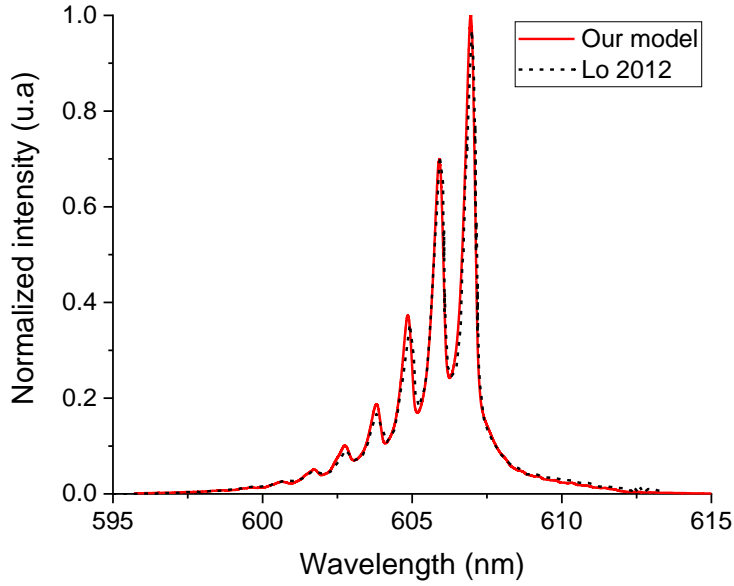


Figure 22: Comparison between the Raman model developed in this work and the one developed by Lo et al. (Lo, et al., 2012). $T_{rot} = 618$ K, $T_{vib} = 2942$ K.

To understand the importance of the various branches and of the anharmonicity and rotation-vibration interactions, we compare three models: the simple Q-branch model of Eq (3.7), the refined Q-branch model including anharmonicity and rotation-vibration interactions, and the full model including all three branches. Three temperature cases are tested: 300, 3000 and 7000 K with $T_{rot} = T_{vib}$. In each case, the spectra are convolved with a triangular slit of 0.05 nm FWHM. The laser wavelength is 281 nm. Results are shown in Figure 23. At 300K, there are essentially no differences between the models, as expected, because the corrections considered in the full model only affect the high vibrational levels. At 3000 and 7000K, a small difference is observed between the full and the simple models. This is because the full model increases the population of the higher v states relative to the lower ones. The effect of the O- and S-branches is negligible below 3000 K and starts to be seen at 7000 K, especially in the tail of the Raman spectrum. At 3000 K, the difference between the full model and the simple Q-branch model is about 6%, and the difference between the full model and the refined Q-branch model is about 4%. At 7000K, these differences increase to 9.5% and 5%, respectively. At 300K, the only difference (about 1%) is due to the O- and S-branches. As expected, the difference between the models increases with the temperature because at high temperature the high (v,J) energy states are more

populated, leading to a non-negligible effect of the rotation-vibration interactions and anharmonicity.

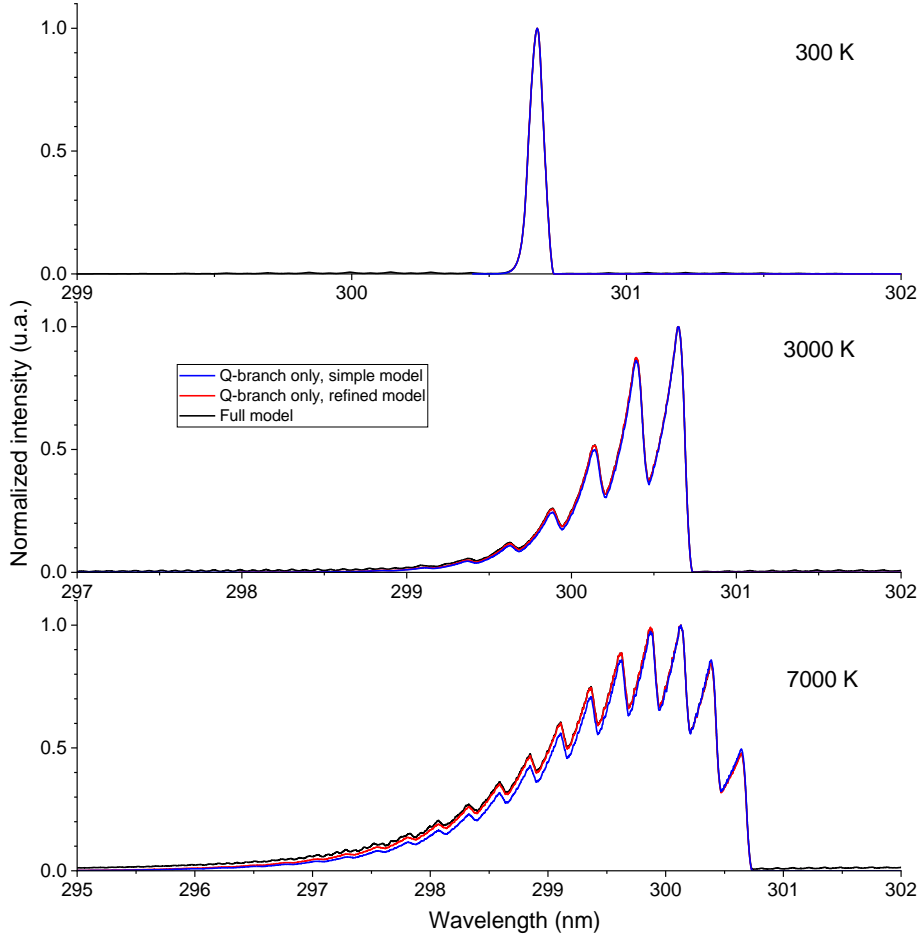


Figure 23: Comparison between the three N_2 Raman models at $T_{\text{rot}} = T_{\text{vib}} = 300 \text{ K}$ (top), 3000 K (middle) and 7000 K (bottom). Laser excitation wavelength 281 nm .

3.2 Experimental setup

A frequency-doubled Continuum dye laser ND6000, pumped by a Continuum Nd:YAG laser (model PR 8010 DLS, pulse energy at $1064 \text{ nm} \sim 1 \text{ J}$) was used to generate a 10-ns, 30-mJ ultraviolet pulse at 281 nm and at a frequency of 10 Hz. Rhodamine 590 dye was used to supply a laser beam at 562 nm , which was then frequency-doubled to produce the final output at 281 nm . We chose to operate in the ultraviolet spectral range because the Raman cross-sections are higher at lower wavelengths. This was necessary to maximize the Raman signal, especially at the

exit of the plasma torch where the high temperature (about 7000 K) implies a low gas density and a high degree of nitrogen dissociation. The quadrupled output of Nd:YAG laser at 266 nm could also have been used, but the ability to tune the dye laser offered the possibility to choose a wavelength region with minimal laser-induced interferences. The chosen wavelength of 281 nm represents a compromise between avoiding these interferences, in particular laser-induced fluorescence of OH⁽²⁾, and maximizing the laser power and the resulting Raman signal. The laser output beam was focused onto the exit of the torch via a 50-cm plano-convex CaF₂ lens (see Figure 24). For imaging, two plano-convex quartz lenses were used in conjunction with a 90° image rotator. The optical magnification from the measurement point to the CCD camera was approximately 0.8. The Raman signal was detected with an Acton SP2500 spectrometer fitted with a UV-enhanced intensified CCD camera (Princeton Instruments PI-MAX 1). The spectrometer was equipped with a 2400-groove/mm grating blazed at 240 nm. The width of the spectrometer entrance slit was varied between 100 and 300 μm, corresponding to an instrumental FWHM from about 0.05 to 0.15 nm. The slit width was chosen to maximize the spectral resolution while keeping a sufficiently high signal-to-noise ratio. The instrumental function was measured using the Rayleigh signal as explained in detail in the following section.

² OH may be present in the plasma due to small impurities of water in the injected gas

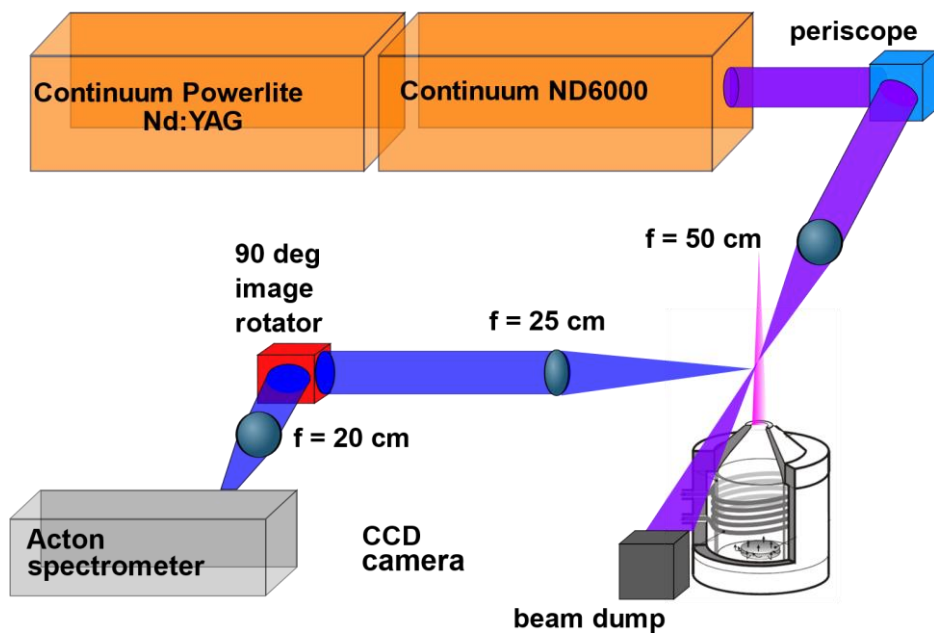


Figure 24: Experimental setup for UV Raman scattering measurements. A periscope consisting of two quartz prisms allows to adjust the height and direction of the laser beam. The 90° image rotator serves to horizontally align the laser beam with the spectrometer entrance slit.

The scattered signal was imaged with the PI-MAX camera operated in gate mode (gate width of 20 ns) and maximum gain (255) for all measurements. The spectral range detected was typically from 298 to 301 nm. The spatial window captured by the camera, about 4 mm wide, was centered around the centerline of the plasma. Depending on the case, the pixels were binned to produce a spectrum at several lateral positions. Typically, we binned 30 pixels to obtain Raman spectra every millimeter. This was again a compromise between high spatial resolution and high signal-to-noise ratio. To increase the signal-to-noise ratio, we performed 50 on-CCD accumulations and 100 software accumulations. The total time to obtain a single Raman spectrum was about 8 minutes. Note that the torch is stable over that time period as confirmed by emission spectroscopy and good reproducibility between experiments.

3.3 Validation of the technique with equilibrium plasmas

To validate our Raman-measurement technique, we first performed measurements in atmospheric pressure plasmas known to be in Local Thermodynamic Equilibrium (LTE) at a known temperature measured by emission spectroscopy. We then compared this temperature with the one measured using Raman spectroscopy. The Raman measurements and analysis are explained in this section. Three cases will be presented. The first case corresponds to an air plasma at the exit of the torch fitted with a 5-cm diameter nozzle. The second is also an air plasma, at the exit of a 30-cm long tube placed right at the exit of the torch fitted with a 1-cm diameter nozzle. The third case is the Air/Ar mixture presented in Chapter 2, directly at the exit of the 1-cm diameter torch exit nozzle. Both the Stokes and anti-Stokes spectra were measured for these cases but we will only present the Stokes spectra as both gave similar results, with a better signal-to-noise ratio for the Stokes spectra.

3.3.1 Air plasma at the exit of the 5-cm diameter nozzle

In this case, 1.5 g/s of air was injected in the plasma torch and the 5-cm diameter nozzle was used. This configuration has been studied extensively and has been shown to produce an air plasma in LTE (Laux, 1993). Emission spectroscopy was performed to measure the absolute intensity of the atomic oxygen triplet at 777 nm to get the radial temperature profile 1 cm downstream of the nozzle exit. The Stokes signal was measured at the same location. The signal was binned over 4 mm to increase the signal-to-noise ratio. A background spectrum was measured at 120 nm and subtracted from the measured Raman spectrum to eliminate the dark current and a possible stray light contribution. At this wavelength, the room air is absorbing and therefore any signal on the camera can be attributed to noise or stray light. The instrumental function was measured using the Rayleigh scattering signal centered at 281 nm. For each Raman measurement, a corresponding Rayleigh signal was measured to determine the instrumental broadening. The measured instrumental broadening function was then convolved with the theoretical spectrum computed with the Raman model. The measured Rayleigh signal measured for this case is presented in Figure 25.

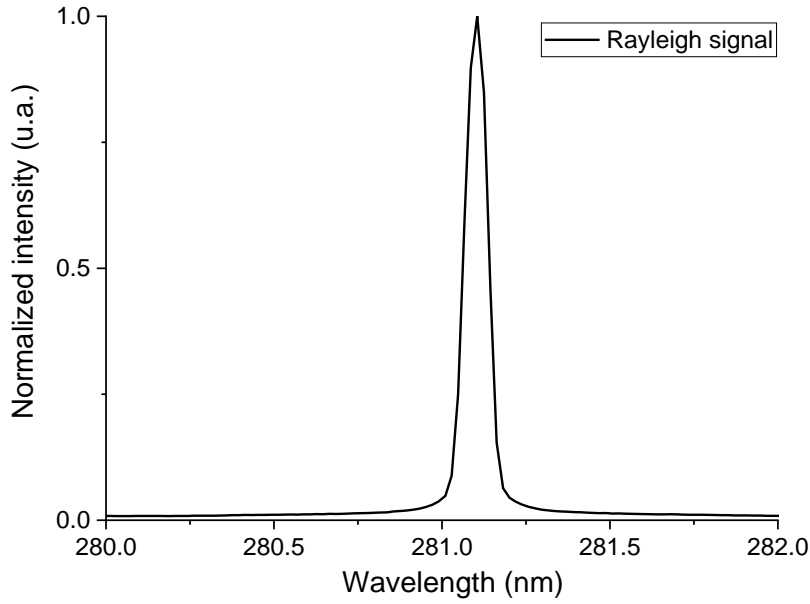


Figure 25 : Normalized Rayleigh spectrum obtained for the air case. The slit width was 300 μm . This spectrum was taken in ambient air (300 K, 1 atm).

The equivalent FWHM is about 0.15 nm.

The Raman spectrum depends on both the rotational and vibrational temperatures. To determine these temperatures, we computed theoretical Raman spectra for various pairs of $(T_{\text{rot}}, T_{\text{vib}})$. For each computed spectrum, $\text{Stokes}_{T_{\text{rot}}, T_{\text{vib}}}(\lambda)$, we calculated the relative error with the experimental spectrum, $\text{Exp}(\lambda)$, using an L^2 norm:

$$L_{T_{\text{rot}}, T_{\text{vib}}}(\text{Exp}, \text{Stokes}_{T_{\text{rot}}, T_{\text{vib}}}) = \frac{\sqrt{\sum_{\lambda} |\text{Exp}(\lambda) - \text{Stokes}_{T_{\text{rot}}, T_{\text{vib}}}(\lambda)|^2}}{\sqrt{\sum_{\lambda} \text{Exp}(\lambda)^2}} \quad (3.14)$$

Note that for this case both the theoretical and experimental spectra were normalized to compute the error, because relative intensities are sufficient to determine the temperatures. We obtained a 2D map of the error as a function of the rotational and vibrational temperatures used in the model. Results for this case are shown in Figure 26.

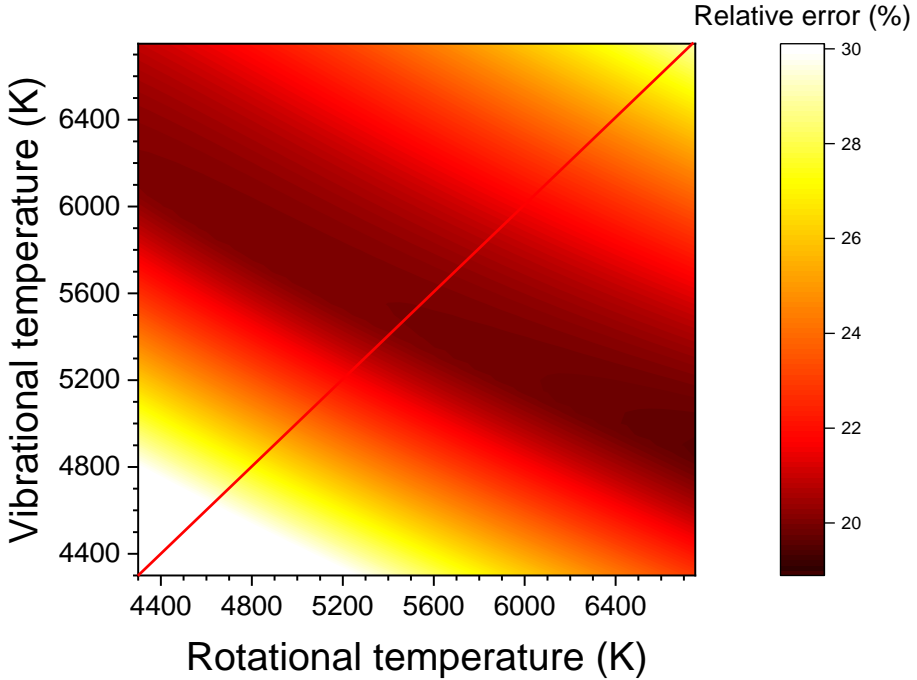


Figure 26: Relative error between computed Stokes spectra at $(T_{\text{rot}}, T_{\text{vib}})$ and the measured Stokes spectrum. The red line corresponds to $T_{\text{rot}}=T_{\text{vib}}$ (equilibrium). Measurements taken in the air plasma, 1 cm downstream of the 5-cm nozzle.

The error is relatively high in this case, as expected due to the high dissociation of N₂ and low gas density, coupled with the fact that a wide slit was used to maximize the signal strength. To determine what constitutes an acceptable measurement, in terms of the residual between experiment and model, an uncertainty analysis was performed. The experimental noise amplitude in the measured Stokes signal was determined by looking at the pixel count fluctuations in regions where there is no signal. This noise was then artificially added as gaussian noise to a theoretical spectrum. An additional source of error related to wavelength uncertainty was also taken into account. We experimentally observed a small spectral dispersion between the experimental and computed spectra, even though the spectrometer was calibrated in wavelength. This dispersion was found to be relatively small (about 0.002 nm) but the resulting error could be significant in some cases. Given these two sources of error, we started with the computed Stokes spectrum corresponding to $T_{\text{rot}} = T_{\text{vib}} = 5700 \text{ K}$ as a reference spectrum. The uncertainties were added as gaussian noise as shown in Eq (3.15):

Error Limit =

$$\frac{\sum_{i=0}^{i=1000} L_{T_{\text{rot}}, T_{\text{vib}}} \left(\text{Stokes}_{T_{\text{rot}}, T_{\text{vib}}}, \text{Stokes}_{T_{\text{rot}}, T_{\text{vib}}} + \sigma_i(\lambda) + \frac{d\text{Stokes}_{T_{\text{rot}}, T_{\text{vib}}}}{d\lambda} \delta\lambda \right)}{1000} \quad (3.15)$$

where $\sigma_i(\lambda)$ correspond to different values of the random noise of maximum amplitude equal to the experimental noise. The averaged experimental error on the wavelength was found to be $\delta\lambda = 0.002 \text{ nm}$ which corresponds to a dispersion of 1 pixel every 20 pixels.

The relative error between the new computed spectrum including these errors and the reference spectrum was then calculated. We performed this for 1000 different values of the random noise. This average error is then taken as the limit below which the experimental fit is deemed acceptable. Here, the error limit was found to be about 21%. The range of acceptable T_{rot} and T_{vib} is delimited by the black lines in Figure 27.

We see that the spectrum is much more sensitive to T_{vib} than to T_{rot} . However, because previous studies of this plasma have proven it to be in LTE (a result also confirmed by recent complementary Rayleigh measurements presented by (McGuire, et al., 2017)), we further impose $T_{\text{vib}} = T_{\text{rot}}$. With this assumption and the 21% error limit, we obtained a best estimate range of temperatures, as shown with the hatched area in Figure 27.

The best estimate of the temperature is then $5700 \pm 450 \text{ K}$. Note that this temperature corresponds to an average over the central 4 mm of the plasma because the Stokes signal was binned. A comparison between the measured spectrum, the best fit, and the spectra calculated with the upper and lower temperature limits, is shown in Figure 28. This restriction diminished the range of possible temperature solutions. With this assumption and the 21% error limit we determined a best estimate range of temperatures, as summarized in Figure 27.

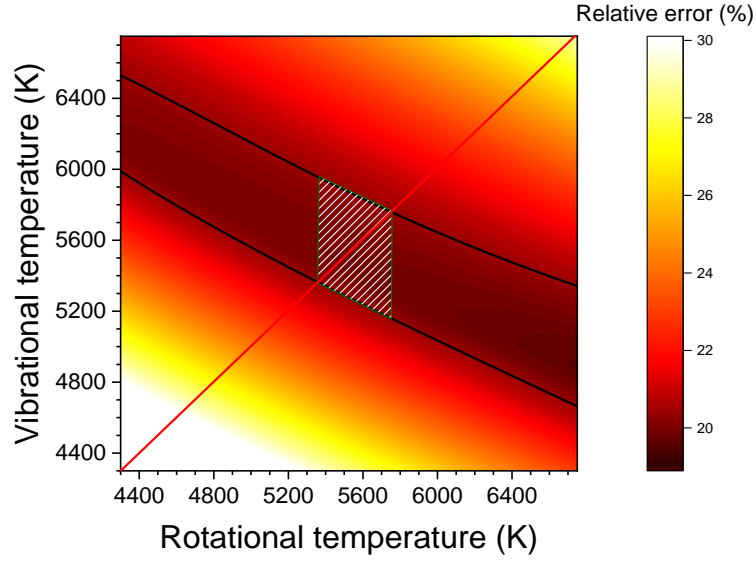


Figure 27: Relative error between the computed Raman spectra at $(T_{\text{rot}}, T_{\text{vib}})$ and the measured Stokes spectrum. The black lines define the area where the error is below 21%. The white-hatched region corresponds to the range of acceptable values for $(T_{\text{rot}}, T_{\text{vib}})$. Measurements taken in the air plasma, 1 cm downstream of the 5-cm nozzle.

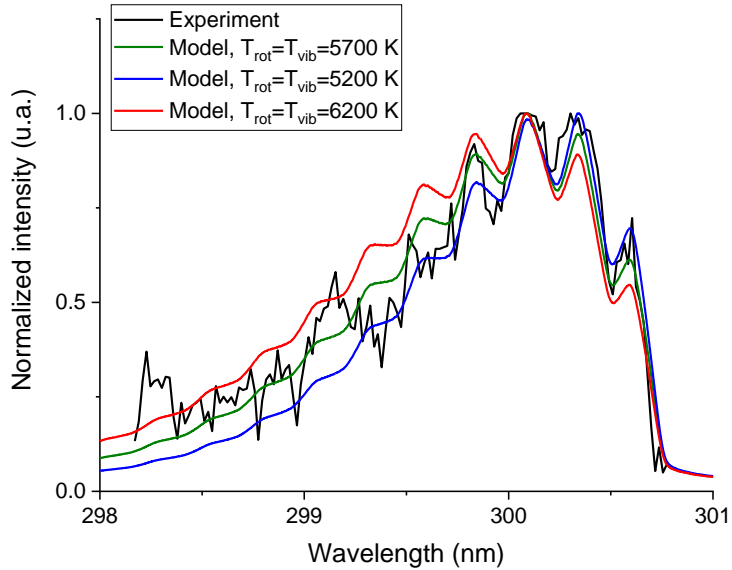


Figure 28: Comparison between the measured Stokes spectrum (black), the best fit corresponding to $T_{\text{rot}} = T_{\text{vib}} = 5700 \text{ K}$ (green), and the lower and upper uncertainty limits: $T_{\text{rot}} = T_{\text{vib}} = 5700 - 500 = 5200 \text{ K}$ (blue) and $T_{\text{rot}} = T_{\text{vib}} = 5700 + 500 = 6200 \text{ K}$ (red).

Finally, we compared the temperature measured using Raman spectroscopy with the temperature profile measured using emission spectroscopy (atomic oxygen line at 777 nm). Results are shown in Figure 29. Despite the large uncertainties of the Raman measurements, we observe a good agreement between the two diagnostics. This equilibrium case serves as a first validation case for the Raman measurement.

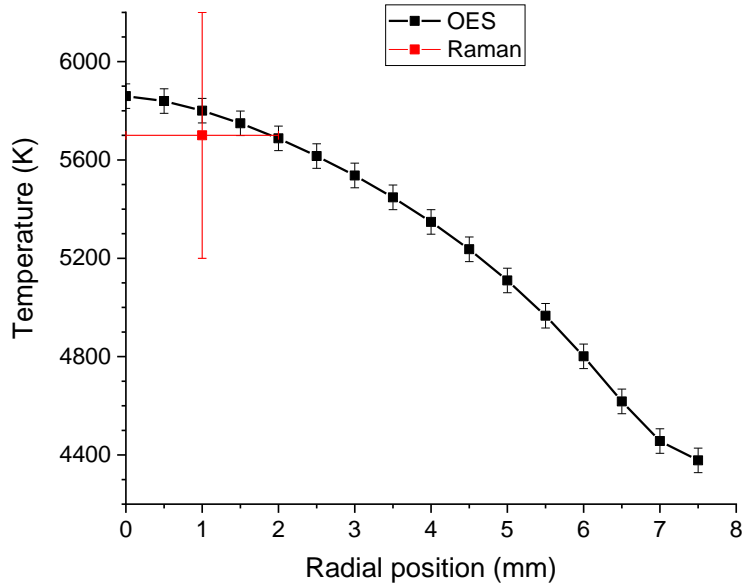


Figure 29 : Temperature profiles measured with Raman (red) and emission (black) spectroscopy. Measurements taken in the air plasma, 1 cm downstream of the 5-cm nozzle.

3.3.2 Air plasma at the exit of the 30-cm tube:

In this section, we consider the case of the 30-cm long tube mounted on top of the 1-cm diameter nozzle. The inner diameter of the tube is 1 cm. The tube is used to cool the plasma produced inside the torch in order to operate at higher gas densities and thus increase the strength of the Raman signal. As in the previous case, 1.5 g/s of air is injected into the torch. This case was previously studied and analyzed at Stanford University using the same plasma torch (Gessman, 2000), and the plasma was also found to be in LTE. Here, we measured again the radial temperature profile at the exit of the tube from the absolute emission intensity of the oxygen triplet at 777 nm. For the Raman spectroscopy measurements, the laser was focused at the same location as for the emission measurements, i.e. 1 cm above the tube exit. The Raman spectrum was binned over 4 mm. Because laser-induced

interferences were observed below 299.5 nm, we limited our analysis to the Stokes spectrum signal above 299.5 nm. The method for data analysis is the same as in Section 3.3.1. The error limit taking into account experimental noise and wavelength dispersion is 20 %. The relative error map between experimental and computed spectra is shown in Figure 30. The measured temperature is $T_{\text{rot}} = T_{\text{vib}} = 4200 \pm 300$ K. Note that this temperature corresponds to an average over 4 mm wide region centered around $r = 0$ mm. A comparison between the measured Raman spectrum and the spectra computed at 3900, 4200 and 4500 K is shown in Figure 31.

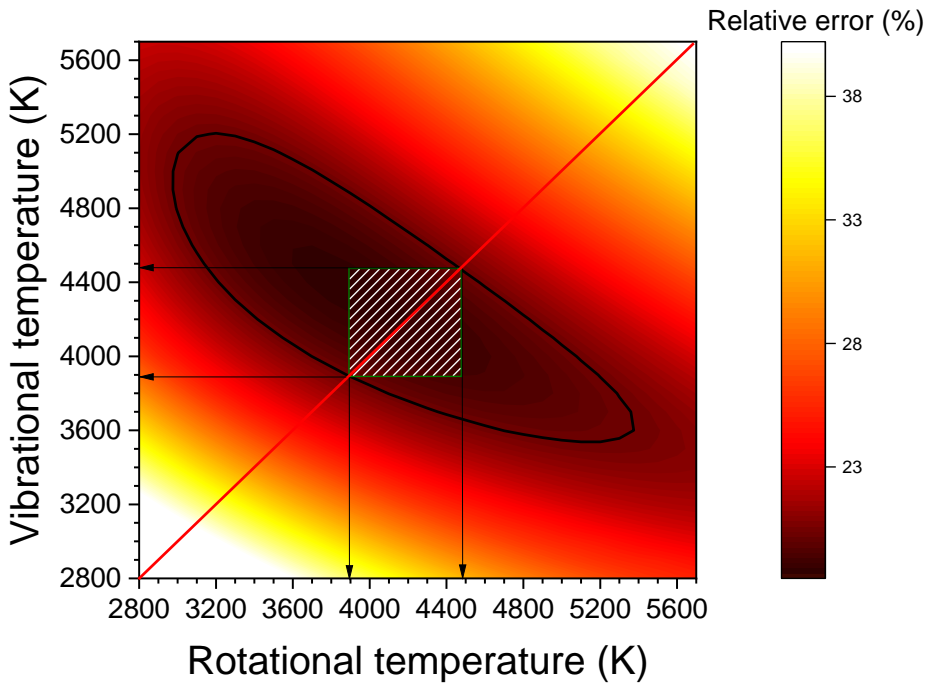


Figure 30: Relative error between the Raman spectra computed at $(T_{\text{rot}}, T_{\text{vib}})$ and the measured Stokes spectrum. The black lines indicate the range of temperatures where the error is below 20% (limit of acceptable fits). The white hatched region corresponds to the acceptable values for $(T_{\text{rot}}, T_{\text{vib}})$ assuming that the plasma is close to equilibrium. Measurements taken in the air plasma, 1 cm downstream of the exit of the 30-cm tube

The temperature profiles measured with Raman and emission spectroscopy (O⁷⁷⁷ line) are compared in Figure 32. Despite larger uncertainty bars, we observe a good agreement between the two diagnostics. Note that due to the lower temperature than before, the uncertainties were reduced. This gives confidence in the ability to

measure lower temperature than 4200 K. A final validation case will be presented to prove the ability to measure temperatures above 6000 K with the Raman spectroscopy setup..

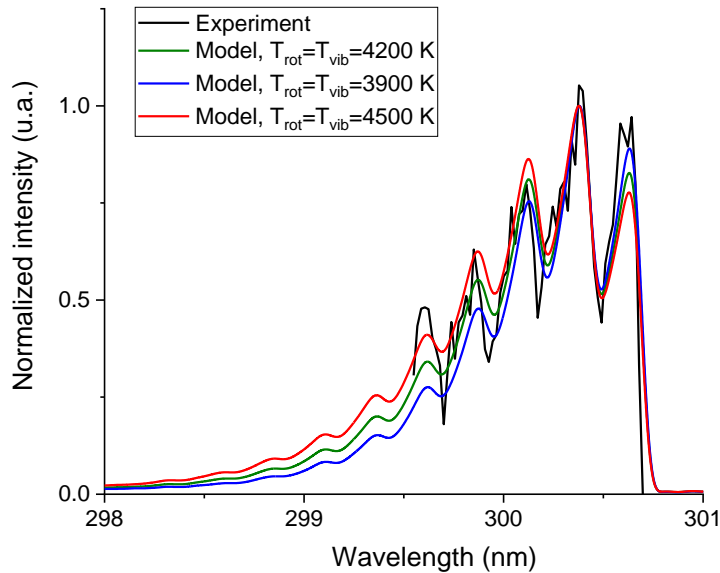


Figure 31: Comparison between the measured Stokes spectrum (black) and the computed equilibrium spectra at 3900 K (blue), 4200 K (green) and 4500 K (red). Measurements taken in the air plasma, 1 cm downstream of the exit of the 30-cm tube.

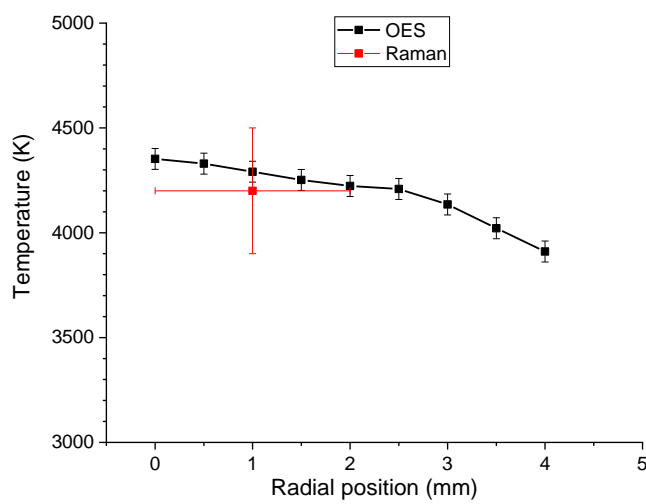


Figure 32: Temperature profiles measured with Raman (red) and O 777 emission (black) spectroscopy. Measurements taken in the air plasma, 1 cm downstream of the exit of the 30-cm tube.

3.3.3 Air/argon plasma at the exit of the 1-cm diameter nozzle

This case corresponds to the Air/argon mixture studied in next chapters. The flowrate was 1.9 g/s for air and 1.5 g/s for argon. Temperature measurements obtained by emission spectroscopy will be presented in Chapter 4 and the results will be used here for comparison with Raman spectroscopy. The Stokes signal was binned over 4 mm to increase signal-to-noise ratio.

Calibration of the measured Stokes Raman intensity:

A Raman Stokes signal was also measured in cold air. This measurement will be used to calibrate the integrated Stokes Raman spectrum of the plasma. Only the Q-branch was measured for this case. Using Eq (3.9), the integrated Stokes Raman spectrum is assumed to be decomposed into:

$$A = \sum_{v,J} I_{v,J}^Q = \sum_{v,J} \left(\frac{h}{8\epsilon_0^2 \Delta\sigma_Q} (\sigma_0 - \Delta\sigma_Q)^4 \times \left((\alpha')^2 + \frac{4}{45} b_{J,J}(\gamma')^2 \right) N_{v,J} P_L \right) = B F(T_{vib}) N_{N_2} \quad (3.16)$$

where B is a constant in a given experimental condition (angle, laser power, integration time, etc.), F is a function that only depends on the distribution of the vibrational energy levels of N₂ (due to the dependency of α and γ on v), and N_{N_2} is the density of N₂ in the gas. Note, however, that this decomposition can only be made if the contribution of the anisotropy, introducing the J dependent $b_{J,J}$ factors, is negligible as it was supposed in our first simple model. This assumption is not expected to introduce important errors, especially for lower temperature, as the contribution of the anisotropic part is relatively weak in our conditions as presented in Figure 23. The constant B can be determined using the Raman signal in cold air, using the same optical setup, camera settings and laser power for each experiment. If A_{air} is the area beneath the Raman spectrum measured in cold air, we have:

$$B = \frac{A_{air}}{F(300 K) N_{N_2}(air)} \quad (3.17)$$

Therefore, the theoretical area I_{N_2} beneath any Raman spectrum of N₂ in the same experimental conditions becomes:

$$I_{N_2} = \frac{A_{air}}{F(300 \text{ K}) N_{N_2}(\text{air})} F(T_{vib}) N_{N_2} \quad (3.18)$$

The density of N_2 assuming chemical equilibrium can be found using the NASA CEA code. This density depends on the gas temperature. The temperature of the gas is close to the rotational temperature of $N_2(X)$ owing to the fast R-T relaxation. We then have $I_{N_2} = B F(T_{vib}) N_{N_2}^{eq}(T_{rot})$. We can then compute the error between the measured and theoretical areas, I_{N_2} , depending on both T_{rot} and T_{vib} , as done previously.

The 2D error map between the normalized experimental spectrum and computed one is shown in Figure 33. The error limit was found to be 9%. This lower value in this case is due to an increased number of averaged images. The 2D error map between experimental and computed area is plotted in Figure 34. Taking into account the experimental noise, we found that the acceptable errors were about 14 %.

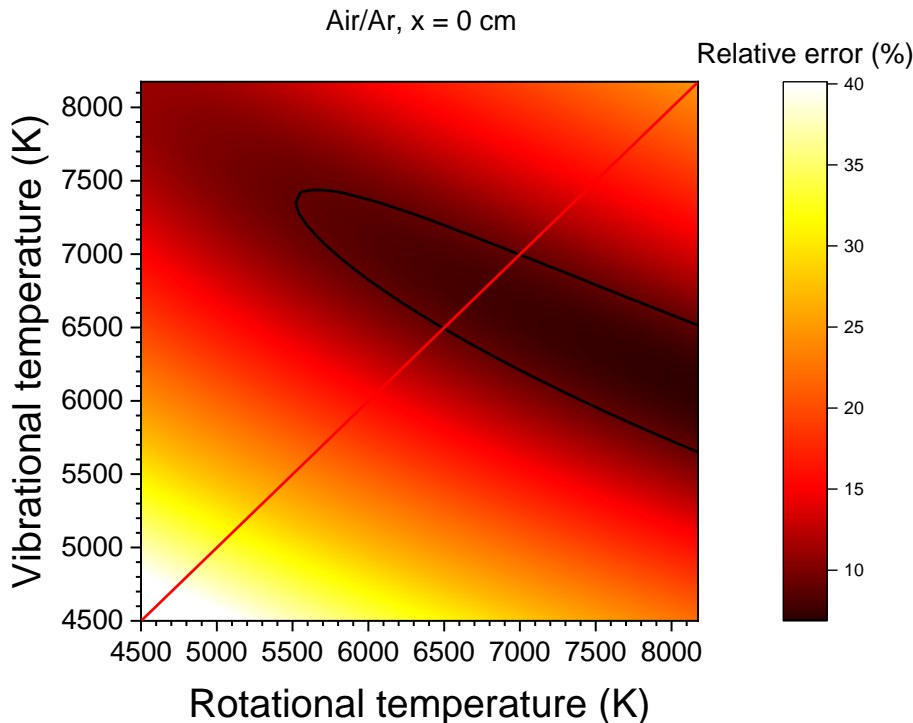


Figure 33: Relative error between the computed Stokes spectra at (T_{rot}, T_{vib}) and the measured Stokes spectrum. The black lines circle the values below

9%. Measurements taken in the air/argon plasma, 1 cm downstream of the exit of the 1-cm diameter nozzle.

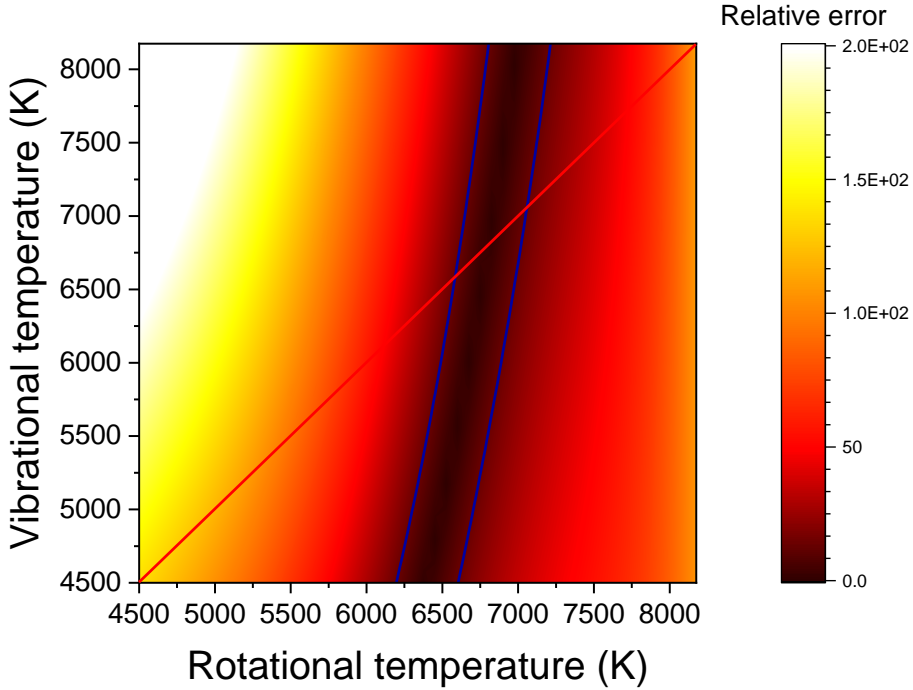


Figure 34: Relative error between computed area at $(T_{\text{rot}}, T_{\text{vib}})$ and the measured area of the Stokes spectrum. The blue lines circle the values below 14%. Measurements taken in the air/argon plasma, 1 cm downstream of the exit of the 1-cm diameter nozzle.

The error maps of Figure 33 and Figure 34 are combined in Figure 35. The intersection of both contours of acceptable values represents the best fits and gives an estimation of the temperature. The final temperature found in this case is 6750 ± 250 K. Despite the relatively high temperature, the uncertainties are actually lower than for the case presented in Section 3.3.1, thanks to both the increased average time and the density analysis. This also allows us to relax the assumption of equal vibrational and rotational temperatures.

The temperature measured using emission spectroscopy is also plotted in Figure 35 (yellow square). A comparison between the best fits and the measured spectra is shown in Figure 36. The good agreement between the best fit gives us confidence in this analysis. Note that this analysis confirms the equilibrium between rotational and vibrational temperatures (or at least within a 300 K difference).

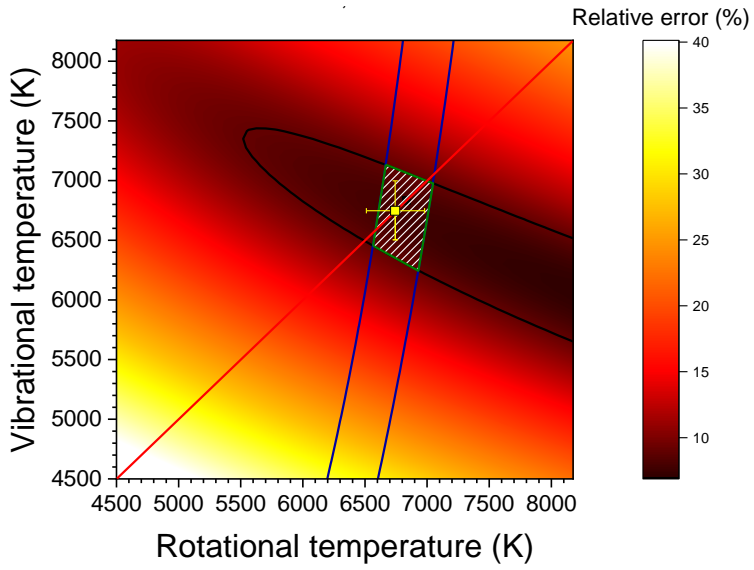


Figure 35: Relative error between computed Stokes spectra at $(T_{\text{rot}}, T_{\text{vib}})$ and the measured Stokes spectrum. The black lines circle the values below 9%. The blue lines circle the values below 14% for the density analysis. The white hatched region corresponds to the acceptable values for $(T_{\text{rot}}, T_{\text{vib}})$. The yellow square corresponds to the temperature measured using emission spectroscopy. Measurements taken in the air/argon plasma, 1 cm downstream of the exit of the 1-cm diameter nozzle.

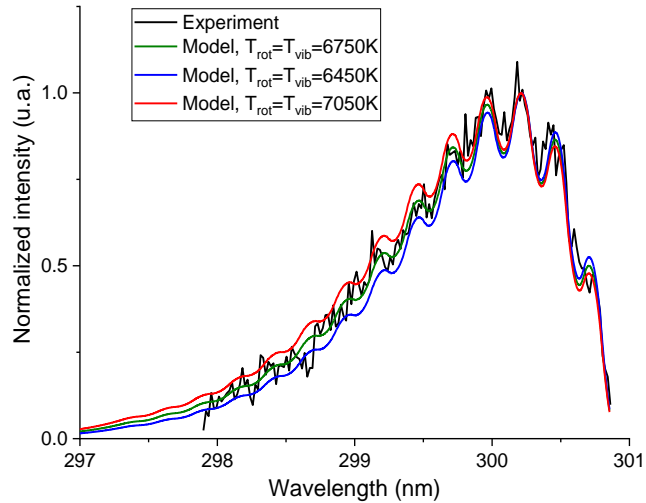


Figure 36: Comparison between the measured Stokes spectrum (black) and the Stokes spectrum computed assuming equilibrium at 6450 K (blue), 6750 K (green) and 7050 K (red). Measurements taken in the air/argon plasma, 1 cm downstream of the exit of the 1-cm diameter nozzle.

Finally, a comparison of the temperature profiles measured with emission and Raman spectroscopy is shown in Figure 37. Good agreement is obtained between the two diagnostic techniques.

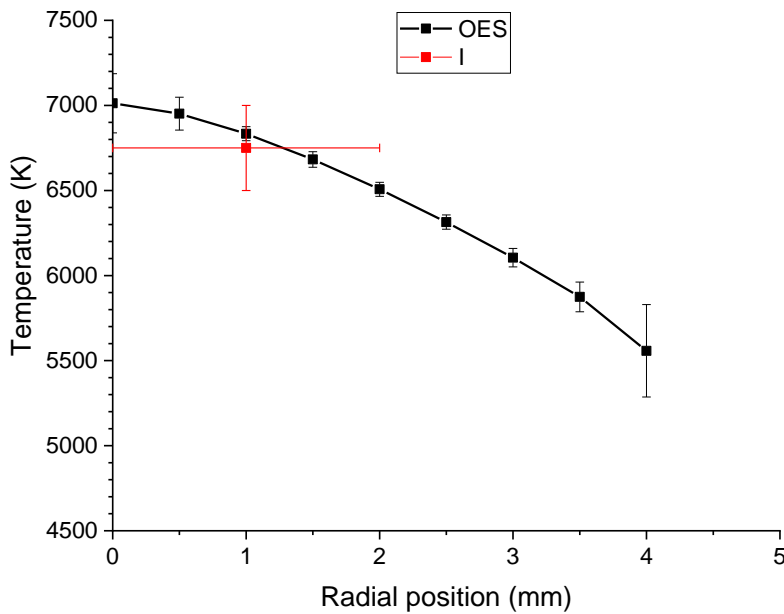


Figure 37: Temperature profiles measured with Raman (red) and emission (black) spectroscopy. Measurements taken in the air/argon plasma, 1 cm downstream of the exit of the 1-cm diameter nozzle.

In the three different equilibrium cases investigated in Sections 3.3.1-3.3.3, both Raman and emission spectroscopy yield similar results. Note however that the uncertainties of the Raman measurement are higher and the spatial resolution lower. For this reason, emission spectroscopy measurements will be preferred to Raman measurements when dealing with equilibrium plasmas.

3.3.4 Beam steering:

Because of the high density gradient between the edges and the center of the high temperature (up to 7000 K) plasma, beam steering could potentially deflect the laser beam. In that case, the the laser beam would not probe the expected centerline region of the plasma. To check for potential beam steering, we directly imaged the laser beam with and without plasma. The setup is shown in Figure 38.

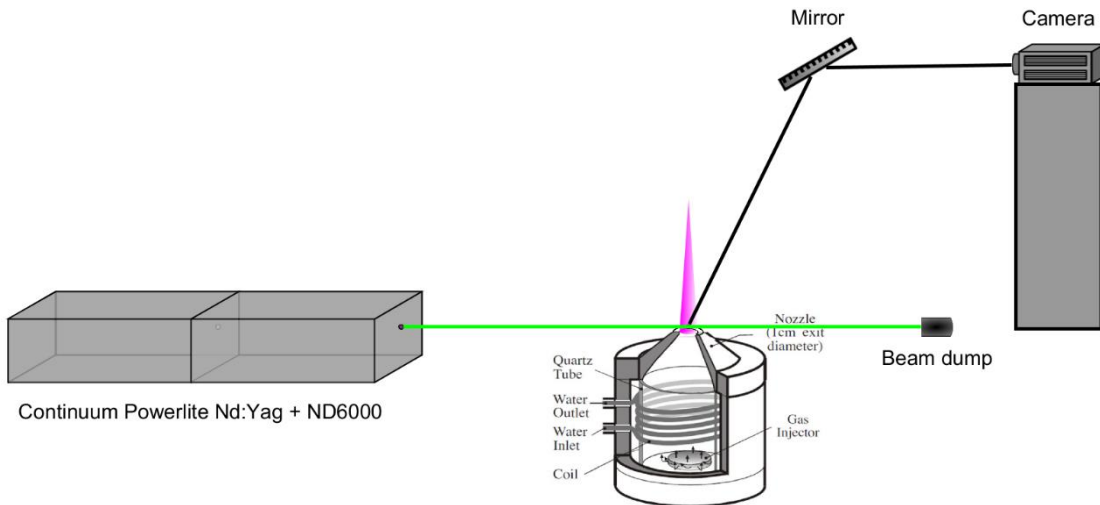


Figure 38: Experimental setup for beam steering detection

The two images of the laser beam shown in Figure 39 were taken with the torch off and then on. The inner and outer diameters of the nozzle are highlighted for clarity. As can be seen from the images, the laser beam is not deflected by the plasma. Therefore, we are confident in the fact that the laser beam actually probes the center region of the plasma.

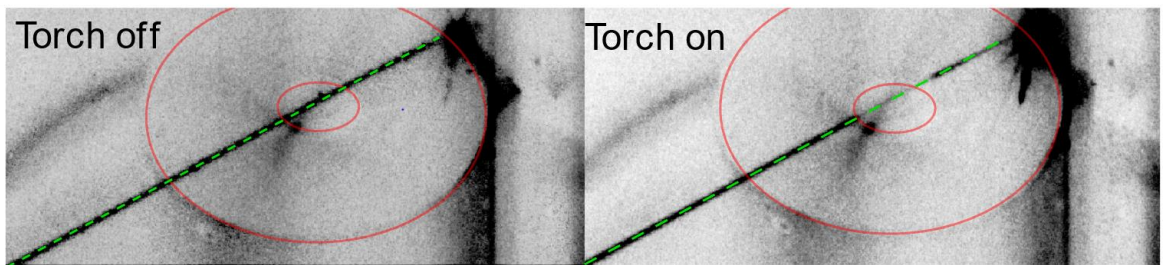


Figure 39: Images taken to check potential beam steering effects. The inner and outer contours of the nozzle are drawn in red. The laser beam corresponding to Rayleigh scattering is highlighted in green. Left: torch off. Right: torch on (the light scattered by the laser beam is lower when it crosses the hot plasma). No significant deviation (< 1 mm) of the beam is observed.

Conditions: Those of Section 3.3.3

3.4 Temperature measurements by Raman spectroscopy in recombining plasma test-cases

The results presented in Section 3.3 served as a validation of the Raman measurement technique in atmospheric pressure, LTE air plasmas at temperatures up to 7000 K. We will now use this technique to study several nonequilibrium plasma cases. This section focuses on the three test cases considered in this thesis, already introduced in Chapter 2: the air/argon mixture at low flowrate, and the N₂/argon mixture at low and high flowrates.

3.4.1 Air/Ar case

The results at 0 cm were already reported in Figure 37. We present below the temperature measurements obtained at the exit of the tubes of 10 and 15 cm. In both cases, the Stokes spectrum was binned spatially over 4 mm around the center part of the plasma in order to maximize the signal-to-noise ratio.

3.4.1.1 10 cm

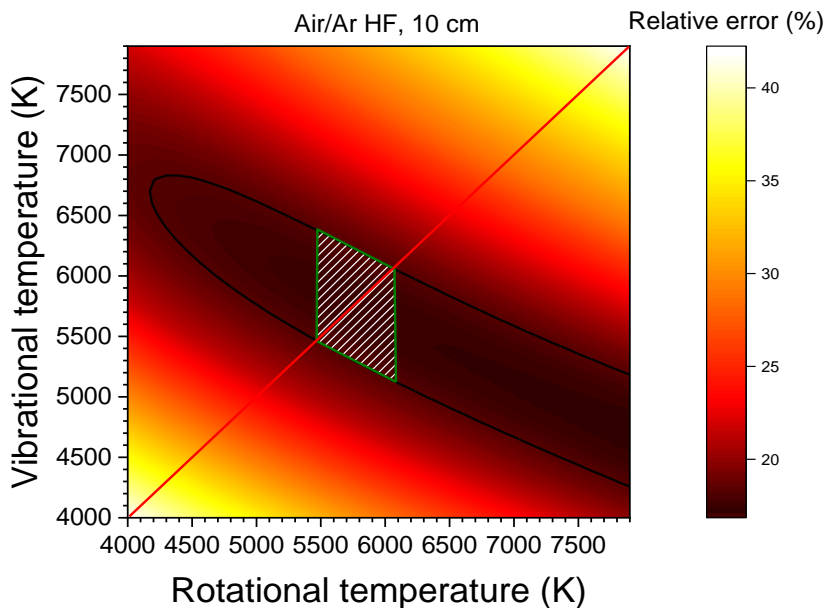


Figure 40: Relative error between computed Stokes spectra at $(T_{\text{rot}}, T_{\text{vib}})$ and the measured Stokes spectrum. The black lines circle the values below 18%. The white hatched region corresponds to the acceptable values for $(T_{\text{rot}}, T_{\text{vib}})$. Measurements taken in the air/argon plasma, 1 cm downstream of the exit of the 10-cm tube.

The 2D error map is shown in Figure 40. The error limit was found to be 18%. The measured temperature is 5750 ± 250 K.

3.4.1.2 15 cm

Both temperature and density analysis were performed here. For the density analysis, chemical equilibrium was assumed *a-priori*. This assumption is validated in Chapter 4 and was previously observed by (Gessman, 2000). The error limit for the temperature analysis is 13% and 5% for the density analysis. The 2D error map from temperature analysis is shown in Figure 41. Note that the contour from the density analysis is also plotted in the figure. The final temperature measured is 4600 ± 150 K. The best fit and the measured spectrum are shown in Figure 42.

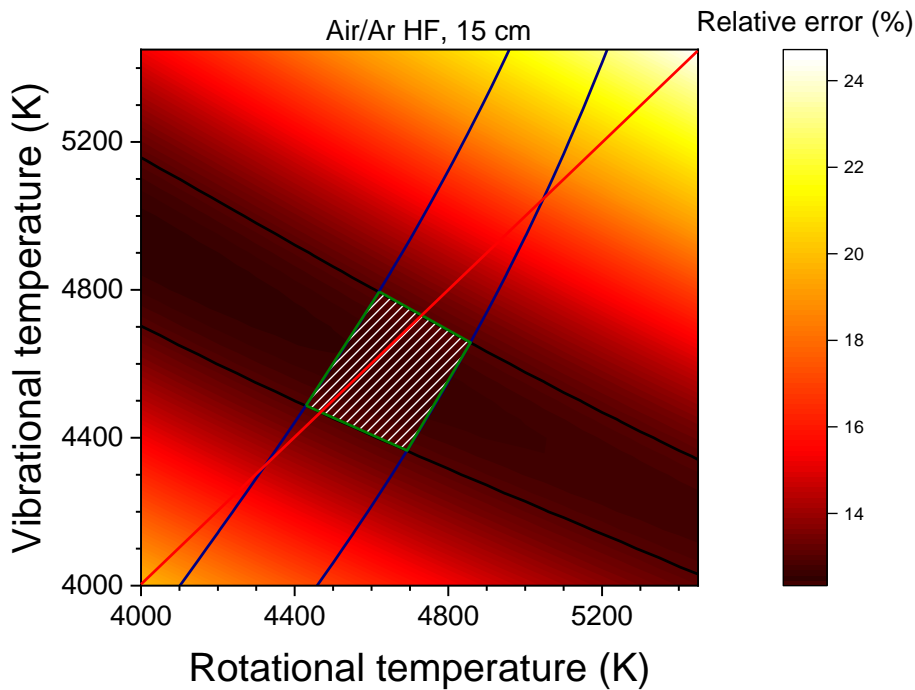


Figure 41: Relative error between computed Stokes spectra at $(T_{\text{rot}}, T_{\text{vib}})$ and the measured Stokes spectrum. The black lines circle the values below 13%. The blue lines circle the values below 5% for the density analysis. The white hatched region corresponds to the acceptable values for $(T_{\text{rot}}, T_{\text{vib}})$. Measurements taken in the air/argon plasma, 1 cm downstream of the exit of the 15-cm tube.

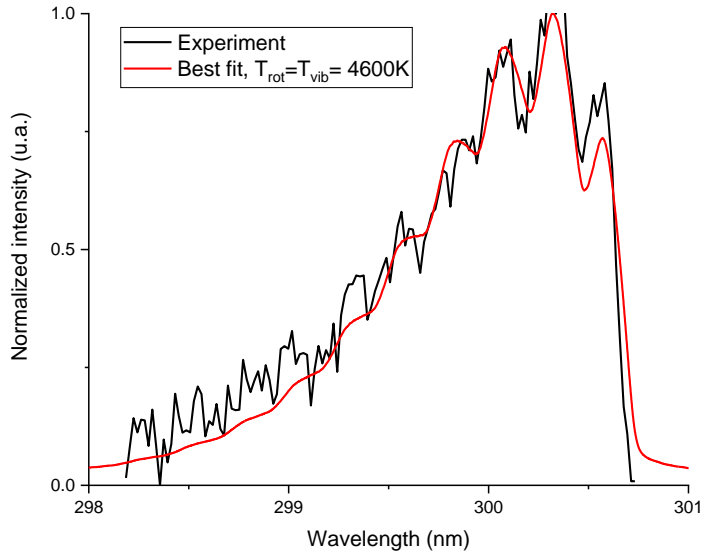


Figure 42: Comparison between the measured Stokes spectrum (black) and the computed Stokes spectrum assuming equilibrium at 4600 K (red). Measurements taken in the air/argon plasma, 1 cm downstream of the exit of the 15-cm tube.

3.4.2 N₂/Ar high flowrate case:

In this section, we present the analysis and results for the high flowrate N₂/Ar mixture at the exit of the 15-cm tube. We performed a similar analysis at the exit of the nozzle and of the 10-cm tube, and we will only give the resulting temperature profiles.

3.4.2.1 15 cm

In this case, due to the relatively high signal to noise ratio, the Stokes spectrum was binned over 0.5 mm. We performed measurements from 0 to 4 mm to get a resolved temperature profile. Note that in this case, we are not supposed to be under equilibrium conditions and the chemical equilibrium needed for the density analysis does not hold anymore. However, a modified version of this analysis may still be used. The overpopulation of atomic nitrogen may be directly measured via emission spectroscopy as outlined in Chapter 7. We used these results to get the associated underpopulation of N₂ and apply it to the results from the NASA CEA code to perform the density analysis. The uncertainties on these underpopulation were taken into consideration in the uncertainty analysis for the density measurements. The 2D map error for the density analysis is shown in Figure 43

and the acceptable values are highlighted. The 2D map error on the temperature measurements is shown in Figure 44. The error limit for the temperature (9%) and density (8%) analysis are also plotted. The final measured temperature is $3100 \pm 100K$.

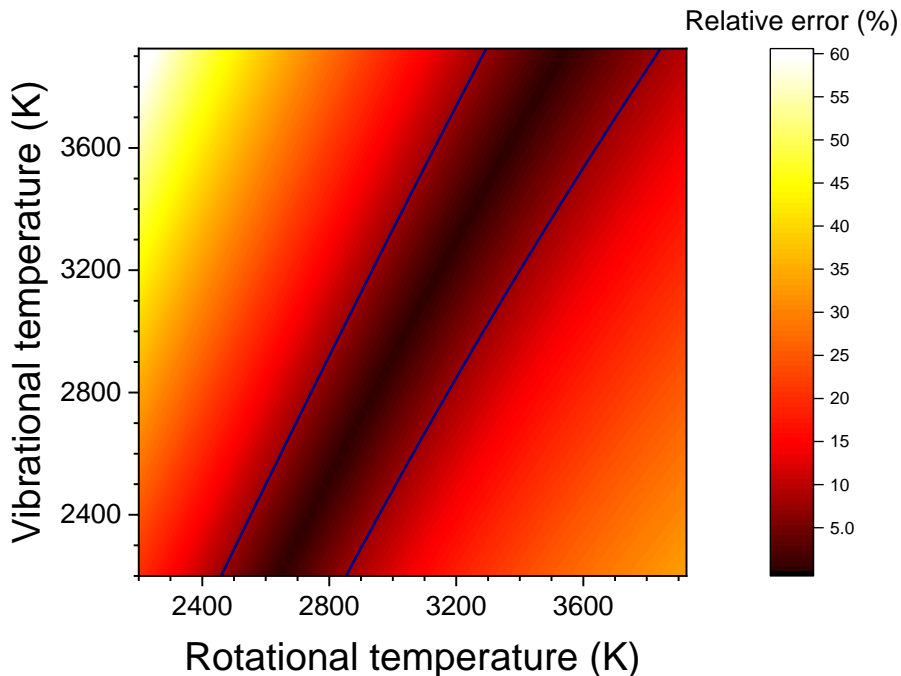


Figure 43: Relative error, in the density analysis, between computed area using ($T_{\text{rot}}, T_{\text{vib}}$) and the measured area of the Stokes signal at the exit of a 15-cm nozzle for the N₂/Ar mixture at high flowrate. The blue lines circle the values below 8%.

The measured temperature was lower than the emission temperature measurements value of around 4600K (Gessman, 2000). The comparison between the measured Stokes signal and the model is shown in Figure 45. Note also that a clear difference is observed in Figure 45 between the best fit and the higher and lower temperatures. Note also that a potential beam steering could deviate the laser into colder region of the plasma, but this assumption has been discarded in section 3.3.

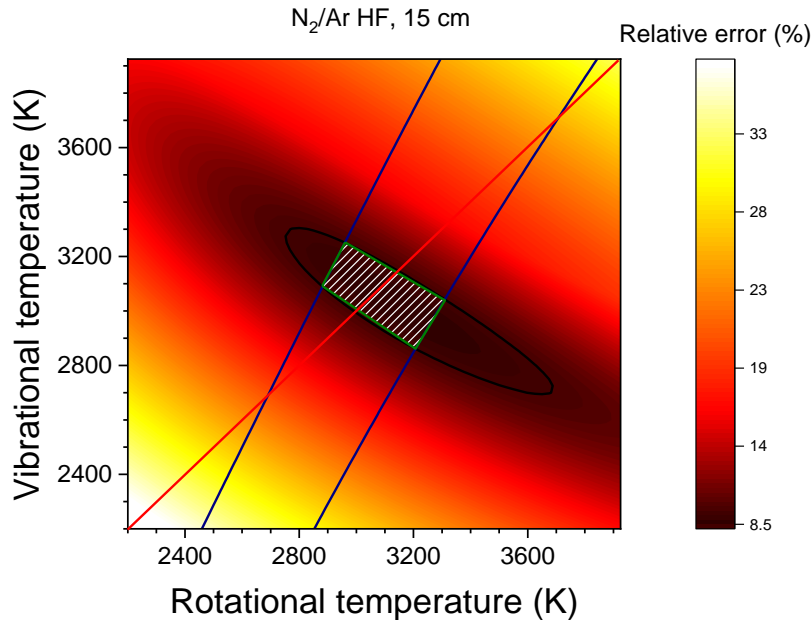


Figure 44: Relative error between computed spectra using $(T_{\text{rot}}, T_{\text{vib}})$ and the measured Stokes signal at the exit of a 15-cm tube for the N_2/Ar mixture at high flowrate. The black lines circle the values below 9% The blue lines circle the values below 8% for the density analysis. The white dash region corresponds to the acceptable values for $(T_{\text{rot}}, T_{\text{vib}})$.

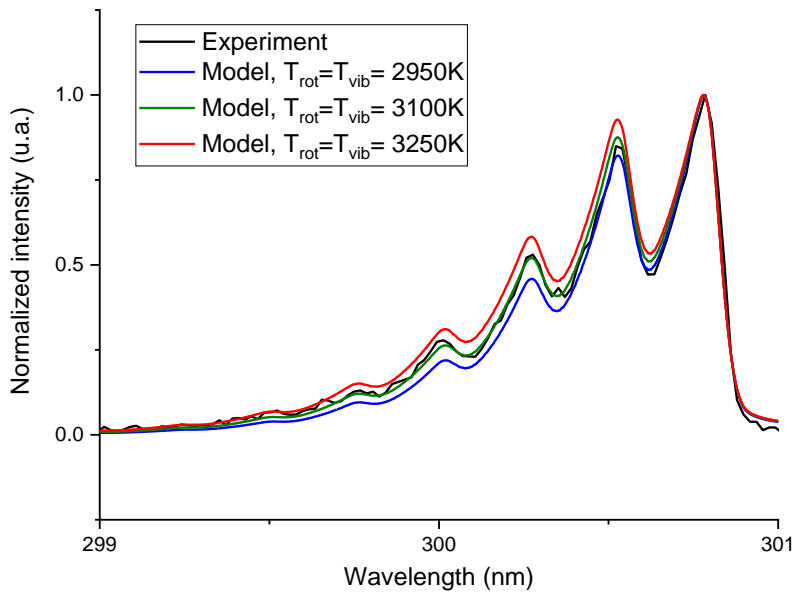


Figure 45: Comparison between measured spectrum (black) and computed spectrum assuming equilibrium at 2950K (blue), 3100K (green) and 3250K (red).

3.4.3 Temperature profiles

A summary of all measured temperature using Raman spectroscopy for the three different cases is presented in Figure 46. Only the profile at 15 cm N₂/Ar HF case has a spatially resolved profile. The other ones represent an average over the given radial distance. The temperature profiles of the N₂/Ar LF case are also presented. Comparison between these Raman profiles and the ones obtained using emission spectroscopy will be discussed in Chapter 4.

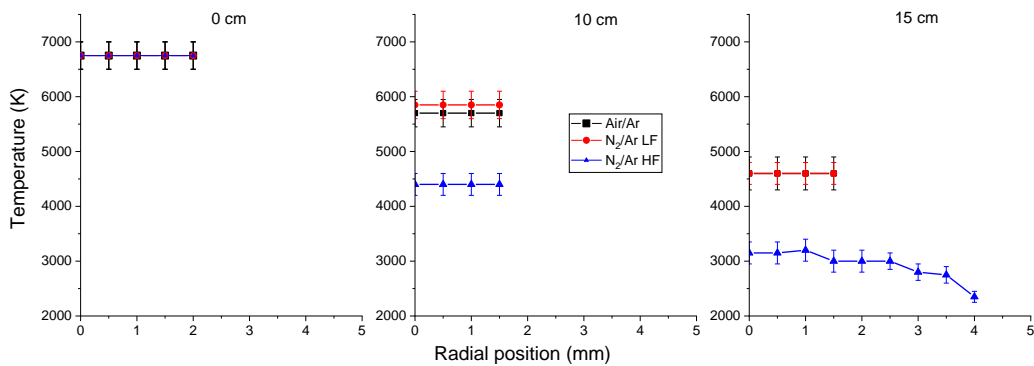


Figure 46: Measured temperature profiles using Raman spectroscopy for the three different cases at 0cm (left), 10cm (middle) and 15cm (right).

3.5 Conclusion

A vibrational Raman Stokes model has been presented and was implemented. As a verification step, this model has been compared with previous ones published in the literature. Moreover, it has been validated up to a temperature of 7000K for conditions close to equilibrium. The ability to measure rotational and vibrational temperatures in highly out of equilibrium conditions has not been proved as it was not the case in our conditions.

We performed Raman spectroscopy in the three cases of interest and obtained results at three different locations: 0, 10 and 15 cm. The radial spatial resolution was relatively low due to the high temperature encountered and corresponding low signal levels. Nevertheless, the results at 15 cm for the high flowrate N₂/Ar case suggests that the temperature of the gas is lower than the one measured using emission spectroscopy previously measured by Gessman and presented in Figure 19. This was not expected, and this discrepancy will be the focus of Chapter 4.

Chapter 4 Temperature measurements by Optical Emission Spectroscopy

4.1 Introduction

In the previous chapter, we presented temperature measurements obtained with Raman spectroscopy. In this section, the temperature is measured using Optical Emission Spectroscopy (OES). While Raman spectroscopy yields both the vibrational and rotational temperatures of the ground state, emission spectroscopy gives access to the temperature of various excited states. In Chapter 2, a procedure using the absolute intensity of atomic lines was presented. This technique gives access to the electronic state density which, with the assumption of chemical equilibrium, can be linked to the temperature. Here, we extend these emission spectroscopy measurements to molecular species. In particular, we study the first and second positive systems of N₂ and the first negative system of N₂⁺ to obtain the rotational temperatures of N₂(B), N₂(C) and N₂⁺(B). The measurements are performed with the same experimental setup as in Chapter 2. The results are compared with the Raman spectroscopy measurements to determine if the rotational temperatures determined by emission spectroscopy are close to the gas temperature.

4.1.1 N₂(B) rotational temperature

The rotational temperature of N₂(B) is obtained from emission spectra measured between 740 and 775 nm using the 1200 gr/mm grating. This range of wavelengths corresponds to the $\Delta v = 2$ bands of the N₂ first positive system. The Full Width at Half Maximum of the instrumental apparatus was 0.09 nm. For the nitrogen and argon mixtures, it should be noted that the plasma is not in chemical equilibrium at the exit of the 10 and 15 cm tubes. This was discussed in Chapter 2 and will be proven in Chapter 6. In particular, the N₂(B) vibrational levels do not follow a Boltzmann distribution. The rotational temperature measurements must therefore account for this non-Boltzmann vibrational distribution. We used

the following procedure. First, a rotational temperature was selected. Vibrational overpopulation factors were determined based on the measured absolute density of vibrational levels of N₂(B) (see Chapter 6 for a detailed explanation of this procedure). Second, the experimental spectrum was normalized at the bandhead and the residual between the experimental and SPECAIR spectra was calculated. This procedure was repeated for various rotational temperatures. The rotational temperature resulting in the minimum residual was taken as the rotational temperature estimate. Typical results are shown in Figure 47. Note that the chosen wavelength range, corresponding to the (2,0), (3,1) and (4,2) vibrational bands, is a trade-off between having a good signal-to-noise ratio and a relatively constant overpopulation factor of the emitting levels, the first levels of N₂(B) being close to following a Boltzmann distribution (see Chapter 6). Note also that the contribution coming from the $\Delta v = 1$ band is also considered in SPECAIR but its contribution is found to be negligible.

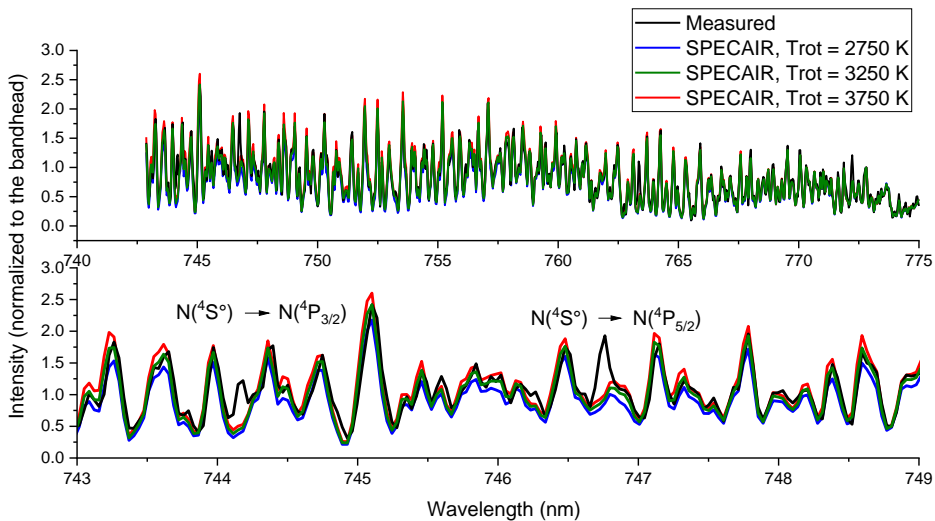


Figure 47: Determination of the N₂(B) rotational temperature. Measured and computed spectra for the N₂/Ar HF case at the exit of the 15-cm tube for the (2,0), (3,1) and (4,2) vibrational bands. Top: spectra between 740 and 775 nm. Bottom: zoom over the range 743 - 749 nm. The green spectrum (3250 K) is the best match. Note the presence of two atomic nitrogen lines that were not included in the SPECAIR calculations.

The best fit was found by taking the minimum of the relative error between the experimental and computed spectra, calculated with a L_2 norm. The uncertainties of the measurements were found by adding a random noise, equal in amplitude to the observed experimental noise, to the theoretical spectra and repeating the fitting procedure, in the same manner as described in Chapter 3.

4.1.2 $N_2(C)$ rotational temperature

To obtain the $N_2(C)$ rotational temperature, we measured emission spectra between 370 and 381 nm, corresponding to the (0,0) and (1,1) vibrational bands. This wavelength range was chosen to maximize the emission of $N_2(C)$ compared to $N_2^+(B)$. We used the 2400 gr/mm grating with a resulting FWHM = 0.07 nm. In this wavelength range, the spectrum is dominated by either $N_2(C)$ or $N_2^+(B)$ emission, depending on the conditions. We only considered the cases where $N_2(C)$ was the dominant emitter. When this was not the case, we did not determine the rotational temperature of $N_2(C)$ because the strong interference from $N_2^+(B)$ could not be easily separated. We followed the same procedure as outlined for the $N_2(B)$ rotational temperature determination using SPECAIR. The uncertainties were also obtained with the same technique. Note that the vibrational levels of $N_2(C)$, like those of $N_2(B)$, may not follow a Boltzmann distribution. This problem is addressed by normalizing all computed spectra to their respective bandheads at 375.5 and 380.5 nm: the spectrum is cut in two, the first between 375.5 to 381 nm and normalized to the bandhead at 380.5 nm and the second between 371 to 375.5 nm and normalized to the bandhead at 375.5 nm. Typical results are presented in Figure 48.

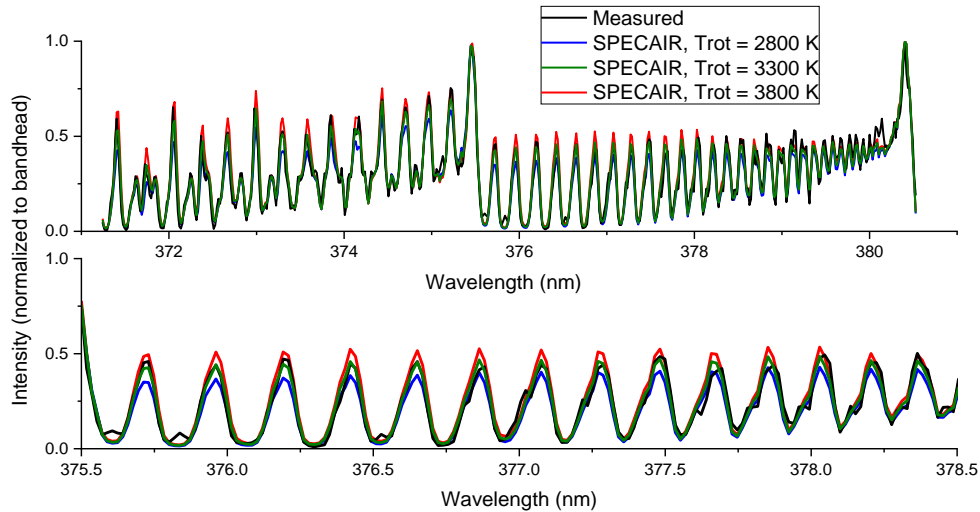


Figure 48: Measured and computed spectra for the rotational temperature measurement of $\text{N}_2(\text{C})$. Top: spectrum between 371 and 381 nm used for the measurement. Bottom: zoom over the range 375.5 to 378.5 nm. The green spectrum (3300 K) is the best fit.

4.1.3 $\text{N}_2^+(\text{B})$ rotational temperature

Two different methods were applied to determine this temperature. The first one is detailed by (Laux, et al., 2001). Briefly, the rotational temperature is determined from the ratio between the bandhead of the (0,0) band and the spectral feature corresponding to the sum of the R(70) and Q(97) rotational lines of the (0,0) vibrational band. This procedure assumes a Boltzmann rotational distribution of the rotational levels which may be erroneous here as the rotational temperature of $\text{N}_2^+(\text{B})$ can be different from the gas temperature in some cases and potentially non Boltzmann (Bruggeman, et al., 2014). To check this assumption, the second method was based on a global fit of the (0,0) band between 388 and 428 nm. If the measured temperature resulting from this global fit yield similar results, it will support the Boltzmann assumption for rotational levels of $\text{N}_2^+(\text{B})$. The spectra were measured with the 2400 gr/mm spectrometer grating ($\text{FWHM} = 0.07 \text{ nm}$). In this wavelength range, $\text{N}_2^+(\text{B})$ is the main emitter. A non-negligible contribution from $\text{N}_2(\text{C})$ was accounted for by using the temperature of $\text{N}_2(\text{C})$ measured previously. The fitting procedure and resulting uncertainties were the same as those presented before. Typical results are presented in Figure 49. Note that the best fit is not clearly distinguishable on this figure, but the uncertainty analysis yields good results.

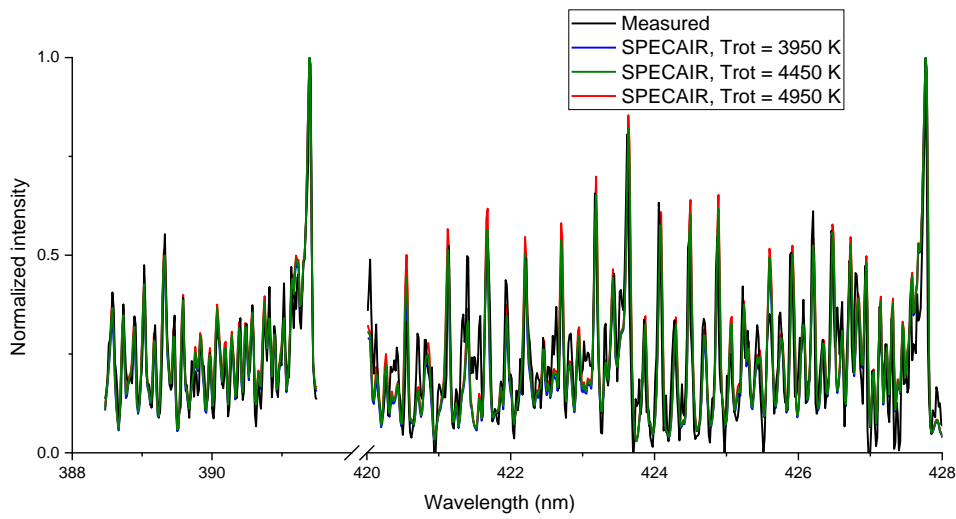


Figure 49: Measured and computed spectra for the determination of the rotational temperature of $\text{N}_2^+(\text{B})$. The green curve ($T=4450\text{K}$) is the best fit.

4.2 Results

The three different cases, namely the Air/Ar case and the two nitrogen argon mixtures at low and high flowrates, were investigated. The rotational temperatures were determined with the methods presented in section 4.1. The temperature measurements are not shown for the cases in which the uncertainty was deemed too large.

4.2.1 Air/Ar mixture

This case is expected to stay under LTE, according to the investigations previously performed by Gessman (Gessman, 2000), and as will be confirmed in Chapter 6. Therefore, the temperature can be measured using the absolute intensities of atomic lines. For this particular case, we only present OES measurements of atomic lines. The measurements were performed at 0, 10 and 15 cm. Several atomic lines (argon at 738, 750, 751 and 763 nm, nitrogen at 742, 744, 746 nm and oxygen at 777 nm) were used and all yielded the same temperature within experimental uncertainty. Only the 777-nm triplet will be presented as it gives the most precise estimate of temperature. The temperatures measured using OES and Raman spectroscopy are compared in Figure 50. Good agreement between the diagnostics is observed at all locations. This observation supports the equilibrium assumption for this case. The

temperature measured using OES is therefore representative of the gas temperature.

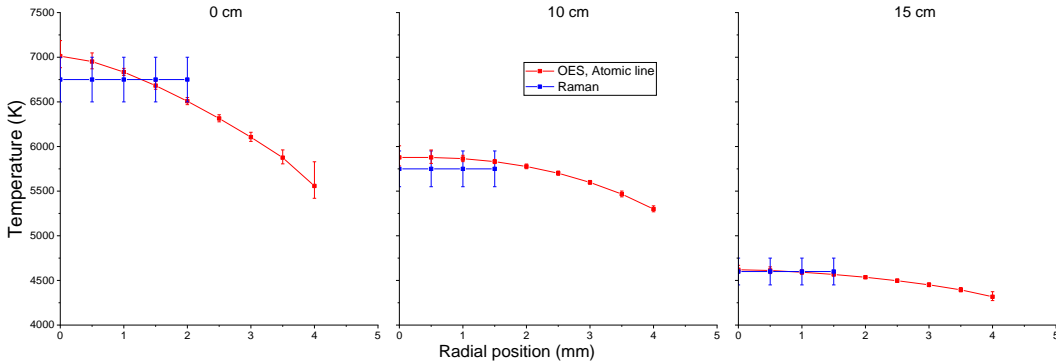


Figure 50: Temperature profiles measured using OES and Raman spectroscopy for the Air/Ar plasma case.

4.2.2 N₂/Ar mixture, low flowrate

The temperature profiles measured using emission spectroscopy for the low flowrate case are presented in Figure 51. All atomic lines (argon at 738, 750, 751 and 763 nm, nitrogen at 742, 744, 746 nm) yield the same temperature profile within experimental uncertainty. Therefore, we only present the temperature profile from the nitrogen line at 746 nm, which had the best signal-to-noise ratio. At 10 cm, a small difference is observed between the temperature measured using atomic lines and the N₂(B) rotational temperature. Note that if the plasma is not under chemical equilibrium at 10 cm, this temperature is not expected to be representative of the gas temperature. Note also that the temperature could not be measured using N₂⁺(B) and N₂(C) at 10 cm due to interferences of other emission leading to very uncertain measurements. At 15 cm, the temperatures measured using atomic could not be obtained and the temperatures of N₂⁺(B) obtained with the two methods are similar. However, the temperature of N₂(B) differs from that of N₂⁺(B). This difference will be discussed in section 4.2.4. Note that the data labeled “T_{rot} N₂⁺(B), ratio” correspond to the measurements obtained with the method by (Laux, et al., 2001), whereas the other rotational temperature of N₂⁺(B) was obtained with the global fitting method presented in section 4.1.3. Note that the rotational temperature of molecular species was not measured at 0 cm.

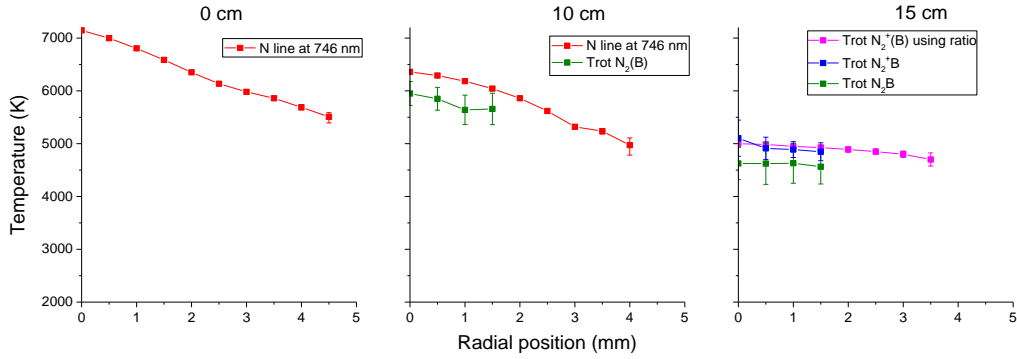


Figure 51: Temperature profiles for the N_2/Ar LF case using emission spectroscopy.

4.2.3 N_2/Ar mixture, high flowrate

The temperature profiles measured using emission spectroscopy for the N_2/Ar mixture at high flowrate are presented in Figure 52. The atomic lines used for the temperature measurements are the same as for the low flowrate case and gave similar results. We only show the profile obtained with the nitrogen line at 746 nm. At 10 cm, all measured temperatures are different. Note the large difference between the rotational temperatures of $\text{N}_2^+(\text{B})$ and $\text{N}_2(\text{B})$. At 15 cm, both methods using $\text{N}_2^+(\text{B})$ rotational lines yield similar results. The rotational temperatures of $\text{N}_2(\text{B})$ and $\text{N}_2(\text{C})$ are in agreement but largely differ from the rotational temperature of $\text{N}_2^+(\text{B})$.

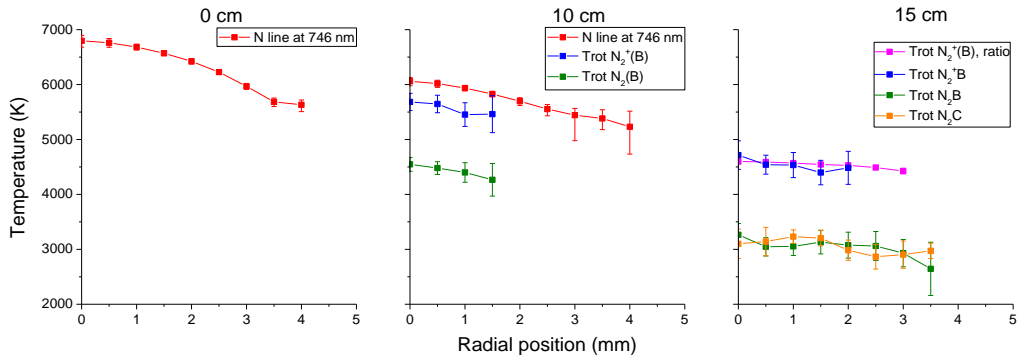


Figure 52: Temperature profiles for the N_2/Ar HF case using emission spectroscopy.

4.2.4 Analysis of the nitrogen/argon results

At 10 cm, the temperature measured using atomic lines differs from the rotational temperatures of the excited electronic states of N_2 and N_2^+ . At this location, the plasma is not in LTE, as previously observed by Gessmann (Gessman, 2000) and as will be confirmed in Chapter 6. Under the conditions encountered in nonequilibrium recombining flows, the electronic levels of atomic species tend to depart from a Boltzmann distribution (Johnston & Brandis, 2015). Therefore, the atomic lines cannot be used to determine the temperature. They are only reported here for comparison with Gessman's results (Gessman, 2000).

At 15 cm, the rotational temperature of $N_2^+(B)$ measured with the two methods is similar. This may indicate that the rotational levels of $N_2^+(B)$ follow a Boltzmann distribution at least for low J levels. It also highlights the accuracy of the method detailed by (Laux, et al., 2001), given that the uncertainties obtained with this method are actually smaller than those obtained with the global fitting method. Therefore, for the rest of this thesis, only the method by (Laux, et al., 2001) will be used.

4.2.5 Comparison with Raman spectroscopy

The various temperature profiles determined with emission and Raman spectroscopy for both N_2/Ar cases at the exit of the 10- and 15-cm tube are compared in Figure 53. Because the temperature determined with Raman spectroscopy is the most representative of the gas temperature, we use it as a baseline to assess the various rotational temperatures obtained with emission spectroscopy in nonequilibrium plasmas. As can be seen from Figure 53, the rotational temperature of $N_2^+(B)$ always differ from the Raman temperature. In contrast, the rotational temperatures of $N_2(B)$ and $N_2(C)$ are found to be close to the Raman temperature. These temperatures are therefore representative of the gas temperature.

The differences observed between the various rotational temperatures are the focus of the next section.

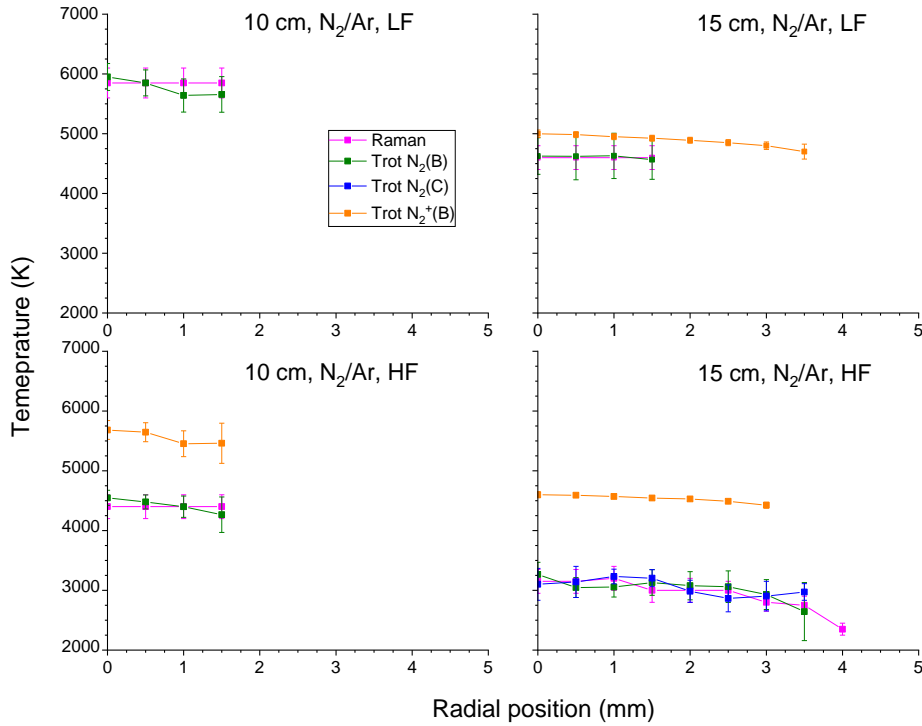


Figure 53: Temperature profiles measured with Raman and emission spectroscopy. Top: N_2/Ar , LF case. Bottom: N_2/Ar , HF case. Left: exit of 10-cm tube. Right: exit of 15-cm tube.

4.2.6 Interpretation of the differences between the rotational temperatures

For both N_2/Ar cases, the rotational temperatures of $N_2(B)$ and $N_2(C)$ (when measured) are in good agreement but differ from $N_2^+(B)$. This is surprising because the rotational modes equilibrates quickly with the translational modes at atmospheric pressure. Indeed, the rotation-translation (R-T) relaxation time in our conditions (1 atm, 3000-7000K) is between 6 and 10 ns (Parker, 1959). To understand the observed differences, we present below a kinetic analysis of the excited states of N_2 and N_2^+ .

Given that the plasma is in steady-state, the characteristic production time of each species must be equal to its characteristic depletion time. Depletion occurs by collisional quenching and radiative transitions. The R-T relaxation times of the excited electronic states of N_2 and N_2^+ were taken equal to those of the corresponding ground state molecules, estimated using results from (Parker, 1959).

The various characteristic times were estimated at 3200 K, which is the lowest measured temperature (corresponding to the measured Raman temperature at the exit of the 15-cm tube in the N₂/Ar HF case), and at 7000K (the highest measured temperature). The results are presented in Table 4. Note that only the quenching rates by N₂ molecules are given but we will assume that other partner of collisions (N and Ar for example) have the same rates. This should yield a correct order of magnitude of quenching as N₂ is the main partner in our experiments for temperature below 6500K. The quenching rate of N₂(B) by argon atoms, given by (Shneider, et al., 2011), is $0.8 \cdot 10^{-11} \text{ cm}^3/\text{s}$ as compared to $2.5 \cdot 10^{-11} \text{ cm}^3/\text{s}$ which is about the same order of magnitude.

Table 4: Characteristic times for quenching and R-T relaxation estimated at the lowest (3200K) and highest (7000K) measured temperatures of the three plasma cases investigated. P = 1 atm.

	Quenching Rate by N ₂ ($10^{-10} \text{ cm}^3/\text{s}$)	Characteristic quenching time (ns) [3200 K; 7000 K]	Radiative lifetime for v = 0 (ns)
N ₂ (B)	0.25 (Rusterholtz, 2012)	[32; 68]	13000 (Laux, 1993)
N ₂ (C)	0.11 (Rusterholtz, 2012) (Valk, et al., 2010)	[24; 69]	37 (Werner & Reinsch, 1984)
N ₂ ⁺ (B)	4.6 (Valk, et al., 2010)	[2; 4]	60 (Dotchin, et al., 1973)
R-T relaxation		[6; 10] (Parker, 1959)	

The rotational relaxation varies according to different references. It is estimated to be about 6 ns at the exit of a 15-cm tube conditions using correlations by Parker (Parker, 1959). However, the RT relaxation time proposed by Park is supposed to be well adapted for high temperatures (Park, 2004) and yield a result of 20 ns. Finally, Panesi *et al* (Panesi, et al., 2013) using new rates proposed another RT time which yield a value of 4.3 ns at 5000K. N₂⁺(B) is therefore quenched before it

has time to thermalize to the background gas temperature, no matter which RT is considered. It is possible to compare the RT time from various sources as a function of temperature. This is performed in Figure 54. Note that the RT time computed by Panesi is only available above 5000K and the one computed by Parker was only validated for low temperatures (<1500K). The RT computed by Parker and Panesi agrees within a factor 2 while the one computed by Park is one order of magnitude higher. In Figure 54, we also plotted the characteristic time of destruction of $N_2(B)$, $N_2(C)$ and $N_2^+(B)$ in our condition. Note that this destruction time is a combination of quenching and radiative lifetime. The quenching rate is assumed independent of the temperature for this calculation. All calculations are made assuming equilibrium at atmospheric pressure. The conditions corresponding to a 0-, 10- and 15-cm tube are also shown in Figure 54 for comparison.

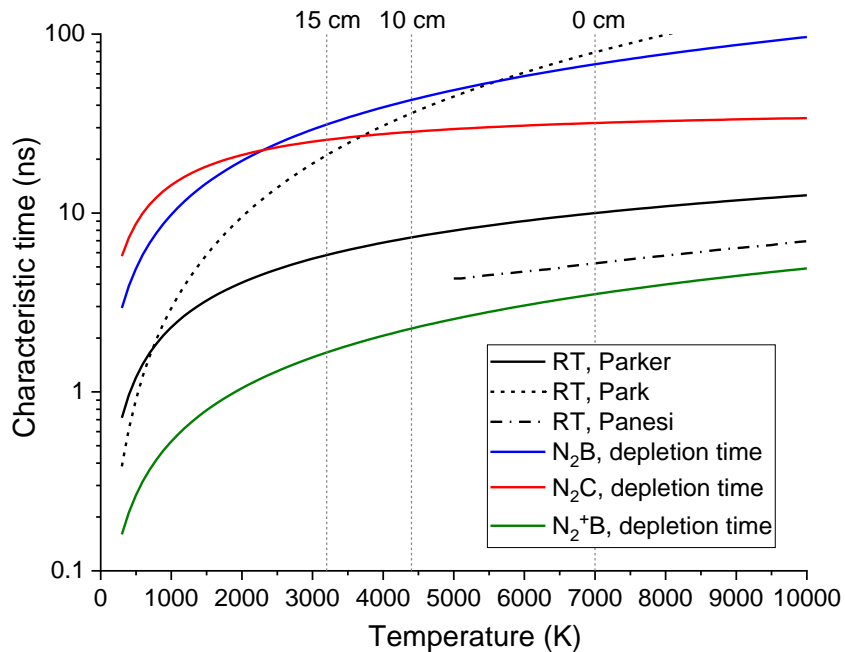


Figure 54: Comparison between RT relaxation times of $N_2(X)$ computed by (Parker, 1959), (Park, 2004) and (Panesi, et al., 2013) as a function of temperature. The characteristic depletion time (quenching + radiative) of $N_2(B)$, $N_2(C)$ and $N_2^+(B)$ are also plotted for comparison. Calculations are made assuming equilibrium at atmospheric pressure. Finally, the temperature corresponding to the conditions of the 0-cm, 10-cm and 15-cm tube of the N2/HF case are also shown.

The depletion of $N_2(B)$ and $N_2^+(B)$ is dominated by collisional quenching as the radiative lifetimes are higher than the characteristic quenching times. The depletion of $N_2(C)$ occurs from both quenching and radiative decay. The quenching time of $N_2^+(B)$ is found to be smaller than its R-T relaxation time independently of the reference. Therefore, the rotational temperature of this state may not be representative of the bulk temperature. In contrast, the depletion time of $N_2(B)$ and $N_2(C)$ is longer than the R-T relaxation time at 15 cm for each reference. Their rotational temperatures are therefore equilibrated with the translational temperature and yield temperature estimates representative of the bulk gas. Note that the R-T time computed by Park seems to be overestimated compared to other references.

All temperature measurements are therefore consistent: the thermalized species $N_2(B)$ and $N_2(C)$ yield rotational temperature measurements close to the translation temperature, whereas $N_2^+(B)$ does not.

Nonequilibrium rotational distribution of $N_2^+(B)$:

For both N_2 plasma cases, the temperature of $N_2^+(B)$ is observed to be higher than the gas temperature. A review of the literature on recombining plasmas suggests that the rotational temperature of $N_2^+(B)$ may not be in equilibrium with the translational temperature (Studer & Vervisch, 2007). Additional studies in shock tubes (Fujita, et al., 2002) (Sharma, 1992) also showed that the rotational temperatures of the N_2^+ first negative system could be significantly different from the gas temperature. These studies noted a similar trend for $N_2(C)$. In addition, using the N_2^+ first negative system, Venable *et al* (Venable, 1969) measured rotational temperatures of $N_2^+(B)$ higher than the gas temperature. Devoto *et al* (Devoto, et al., 1978) noted a difference between the temperature using only the bandhead of the N_2^+ first negative system and that measured using all lines of this system. Both Venable and Devoto suggested that the population distribution of the rotational levels of $N_2^+(B)$ can feature an overpopulation of the high rotational levels with respect to a Boltzmann distribution. Their conclusions were based on the work of (Griem, 2005), according to which such conditions can occur when the collisional-radiative relaxation time of a given state of an ion becomes lower than the thermalization time of electrons. This can occur for example when a steep gradient of temperature exists. There is therefore a significant body of evidence showing that the $N_2^+(B)$ state can give erroneous estimates of the bulk gas

temperature under a wide variety of conditions. However, the rotational temperature measurements of $N_2^+(B)$ do not suggest that the high-lying rotational levels are non-Boltzmann which may discard this mechanism.

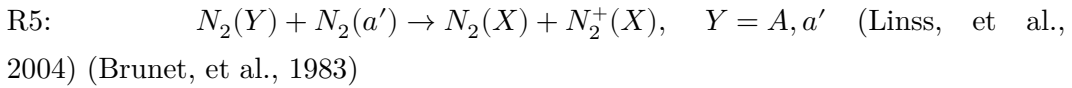
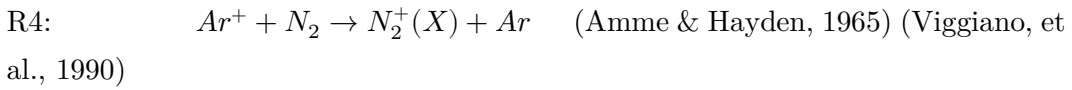
We have studied the reaction kinetics of $N_2^+(B)$ in order to compare its production timescale with the R-T relaxation timescale. Kistemaker et al (Kistemaker & De Vries, 1975) investigated both experimentally and theoretically the effect of noble gases on the rotational relaxation of nitrogen. For N_2/Ar mixtures, they found rotational relaxation times close to those in pure nitrogen, or at most 30% lower. If this is the case, the R-T relaxation time would be about 4 ns at 3200 K and 7 ns at 7000 K. The main reaction for depletion of $N_2^+(B)$ is collisional quenching with N_2 (Valk *et al* (Valk, et al., 2010)):



In our case, this gives a quenching time around 2 ns, which is smaller than the R-T relaxation time even when taking into account the effect of argon.

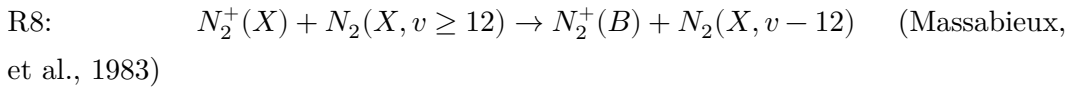
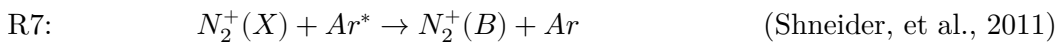
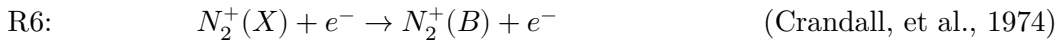
Given that the plasma is in steady state at the exit of the water-cooled tube, the timescale for the production of $N_2^+(B)$ must be equal to the timescale for the recombination $N_2^+(B)$, i.e. about 2 ns. The mechanism responsible for such a fast production of $N_2^+(B)$ is not fully understood at present. We review below several possible mechanisms, including direct production of $N_2^+(B)$ or excitation of $N_2^+(X)$ (Linss, et al., 2004).

We first investigate the production of $N_2^+(X)$. Three main reactions are considered, with reaction rates taken from the given references:



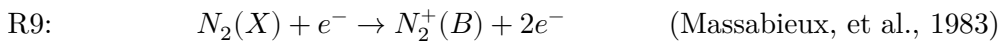
Only reaction R4 is fast enough (~ 2 ns) when comparing with the R-T relaxation time. (Sonnenfroh & Leone, 1989) directly measured rotational temperature of

$N_2^+(X)$ and experimentally observed that reaction R4 produces $N_2^+(X)$ at rotational temperatures higher than those of the reactants. This could explain the high measured rotational temperature of $N_2^+(B)$ if a fast reaction between $N_2^+(B)$ and $N_2^+(X)$ exists. Note however that the rotational temperature of $N_2^+(B)$ is found to be in equilibrium with the gas temperature for the air/Ar case which may discard the argon as in the mechanism of formation of rotationally excited $N_2^+(B)$. $N_2^+(B)$ can be produced by excitation of $N_2^+(X)$ via the following reactions:



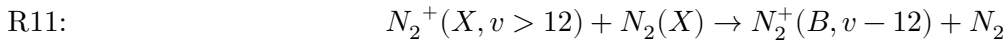
The R7 rate constant was assumed here to be similar to that excitation of $N_2(X)$ by collisions with metastable argon atoms given by (Shneider, et al., 2011). R7 and R8 are the fastest reactions ($\sim 10 \mu s$) but are still much slower than R-T relaxation. Note that high vibrational levels of $N_2(X)$ can be populated via reactions with argon metastable atoms (Touzeau & Pagnon, 1978). This could decrease the characteristic time of R8 by an order of magnitude.

$N_2^+(B)$ can also be produced directly via:



R10 is faster than R9 for the creation of $N_2^+(B)$ ($\sim 1 \mu s$) but is still slow compared to its recombination time and the R-T relaxation time.

Other reactions probably also contribute to the production of $N_2^+(B)$ at time scales of less than 2 ns. These reactions are likely two-body reactions, but at present their rate constants are not known. Among various possibilities, we may have:



Note that the rates of the reaction and the composition used in these calculations are summarized in Appendix A) and the characteristic times were computed assuming equilibrium. In the N₂/Ar mixtures, the plasma is not in equilibrium and some of the reactants and products of the reactions above may be overpopulated which could change significantly these times. In conclusion, we know that the rate of production of N₂⁺(B) should be equal to its depletion rate given that the torch is in steady-state. The time scale of depletion by collisional quenching is about 2 ns, which is smaller than the R-T relaxation time (~8 ns). It is therefore likely that N₂⁺(B) is produced at high rotational temperature and does not have time to thermalize before it reacts. This would explain the higher measured rotational temperature of N₂⁺(B) at the exit of a 15-cm tube for the N₂/Ar mixture cases.

4.2.7 Conclusions

Various temperatures were measured in recombining plasmas using emission spectroscopy: the electronic temperature of atoms and the rotational temperatures of N₂(B), N₂(C) and N₂⁺(B). The temperature representative of the bulk was previously measured using Raman spectroscopy. When the plasma is not in equilibrium, the electronic temperature of atoms is not representative of the gas temperature, as expected. The rotational temperature of N₂⁺(B) also disagrees with the Raman temperature in nonequilibrium cases. Despite being at atmospheric pressure, the R-T relaxation time is slow compared to the quenching time of N₂⁺(B). The rotational temperature of N₂⁺(B) is therefore not well suited to estimate the gas temperature. We discussed several works in the literature that arrived at similar conclusions. On the other hand, the N₂(B) and N₂(C) states have a slower quenching time and are therefore thermalized. We confirmed that their rotational temperatures are equilibrated with the gas temperature under our experimental conditions.

This study shows that the temperatures measured using emission spectroscopy in nonequilibrium plasmas are not always representative of the gas temperature, even at atmospheric pressure. Certain assumptions must be checked before – essentially, a lower rotational-translational relaxation timescale compared to the quenching timescale is a sufficient assumption. Raman spectroscopy yields temperature measurements of the ground state of the N₂ molecule and therefore gives a good estimate of the gas temperature. In the following chapters, we will always take the

temperature measured using Raman spectroscopy for all nonequilibrium recombining plasma cases.

Chapter 5 CFD modeling of recombining equilibrium air plasmas

As discussed in the previous chapters, the recombining air plasma was found to remain at or close to LTE whereas the N₂/Ar plasmas depart from chemical equilibrium. The goal of these experiments was to provide data for CFD model validation. Previous modeling attempts showed that CFD models are unable to predict the measured temperature profiles at various locations along the axis of the tube (Candler, et al., 1998) (Nagulapally, et al., 1998). To model the nonequilibrium N₂/Ar case, CFD codes must capture both the hydrodynamics and the chemical kinetics. To decouple the validation of the hydrodynamics and the kinetics, we first focus on the equilibrium air mixture. This relatively simple test case enables us to test the ability of CFD codes to capture the relevant flow physics before proceeding to the more complex nonequilibrium test cases.

5.1 Pure air plasma

5.1.1 CFD modeling

The equilibrium air plasma test case was already studied by Gessman et al (Gessman, 2000). Our studies of this case confirmed their results. Therefore, the data for this case are taken from the reference case of Gessman et al (Gessman, 2000). 1.9 g/s of air is injected into the torch. For this case, the measured spectra match the calculated spectra assuming LTE conditions. The Reynolds number is approximately 1900 based on the radially averaged velocity and tube diameter. For pipe flows, the flow is laminar for $Re < 2300$ (Taine, et al., 2008), which is the case here. The velocity profile was estimated by assuming self-similarity with the temperature profile as explained in Eq (2.1). The velocity amplitude is then adjusted to match the measured gas flowrate. Temperature profiles measured at 0, 15, 20 and 25 cm will be compared with the CFD calculations.

The CFD simulations presented here were performed using the Eilmer3 code, a finite-volume Navier-Stokes flow solver (Gollan & Jacobs, 2013) implemented on block-structured grids and developed at the Centre for Hypersonics at the University of Queensland. The calculations were performed using the explicit AUSMDV scheme (Wada & Liou, 1994). The flow is assumed axisymmetric and a 2D simulation is performed. The computational domain corresponds to a 0.5-cm radius tube that is 25 cm in length. The mesh is decoupled into $20 \times 50 = 1000$ cells. There are 20 cells radially, with a refinement close to the wall, and 50 cells of equal length axially. The chosen mesh is presented in Figure 55. More refined meshes were studied but yielded similar results.

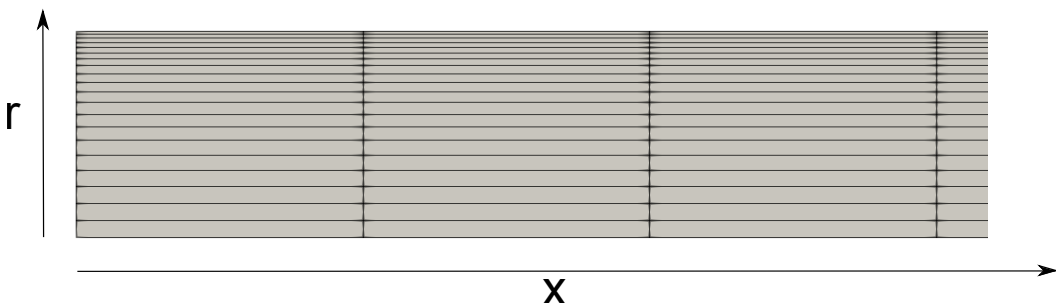


Figure 55: Mesh used for the CFD calculations. Only the first 4 axial cells are shown.

For the outlet boundary condition, the pressure is fixed at atmospheric pressure. As an alternate boundary condition at the tube exit, we also considered a reservoir placed at the exit of each test-section (10, 20 and 25 cm). This was performed by adding an extra domain of dimension $1 \times 1 \text{ m}^2$ at the exit of the test-section. The reservoir pressure was fixed at 1 atm. This increased the computational time without changing the results. Therefore, most of the simulations presented here were performed without the reservoir. For the inlet boundary condition, the temperature profile is specified by extrapolating the measured temperature profile out to the wall whose temperature is fixed at 300 K. The velocity profile is assumed to be self-similar with the temperature profile, as mentioned earlier and is assumed to be fully developed. Then, we let the plasma flow through cells placed upstream and outside the computational domain (ghost cells) to insure a fully developed velocity profile before entering the domain. The inlet temperature and velocity profiles used for the calculations are presented in Figure 56.

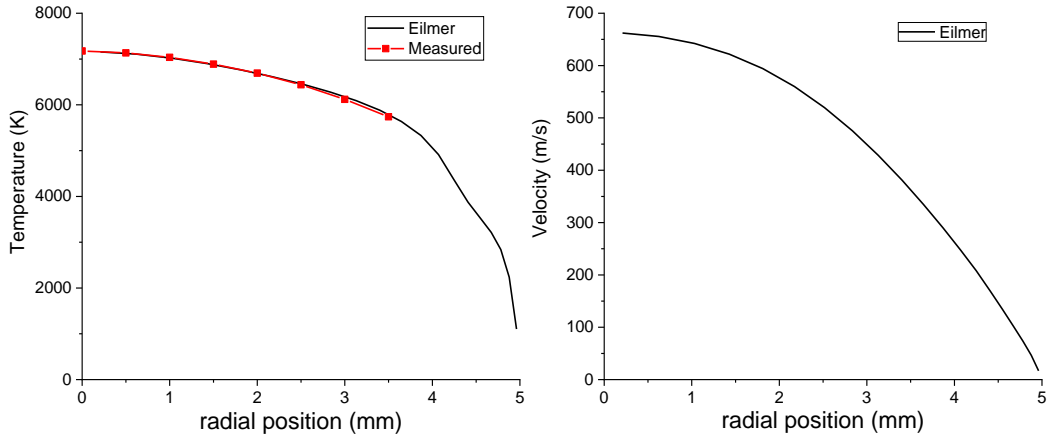


Figure 56: Left - Inlet temperature profiles used for the CFD calculations (black line) and corresponding measurements (red). Right – predicted velocity profile at the inlet of the tube

At the wall, we impose a boundary condition using ghost cells with a fixed temperature of 300 K along the tube wall. The heat flux exchanged with the wall is calculated using Fourier's law between the ghost cell and the last cell in the plasma. The flow is assumed laminar, and therefore no turbulence models are used. The gas is assumed to be in LTE everywhere inside the tube, consistent with the conclusions of the measurements by (Gessman, 2000). The thermophysical properties (viscosity, thermal conductivity, density...) of the plasma are calculated using the NASA CEA code (McBride & Gordon, June 1996) to generate a database of transport properties as a function of temperature for use by the Eilmer3 code. Note that the transport properties are based on equilibrium chemistry – as opposed to frozen chemistry which gives significantly different values. Taking into account the equilibrium chemistry allows us to take into account the reactive conductivity, for example, as part of the thermal conductivity. The reactive conductivity represents the diffusion of species, which introduces an additional energy transfer mechanism. At equilibrium, the gradient of species concentrations is directly related to the gradient of temperature and the diffusion of species can be expressed as a part of the thermal conductivity. Comparisons between thermal conductivities computed with CEA assuming frozen (i.e. the gas is treated as undissociated air) or equilibrium chemistry, presented in Figure 57, shows the increase of the conductivity due to species diffusion. Note that the two local maxima around 3500 K and 7000 K correspond to the dissociation of oxygen and nitrogen, respectively.

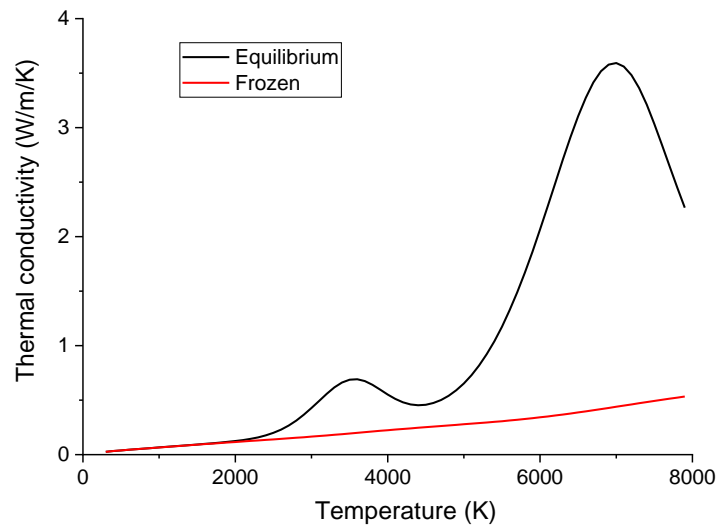


Figure 57: Thermal conductivities computed using the CEA code assuming equilibrium (black) or frozen (red) chemistry.

5.1.2 Results

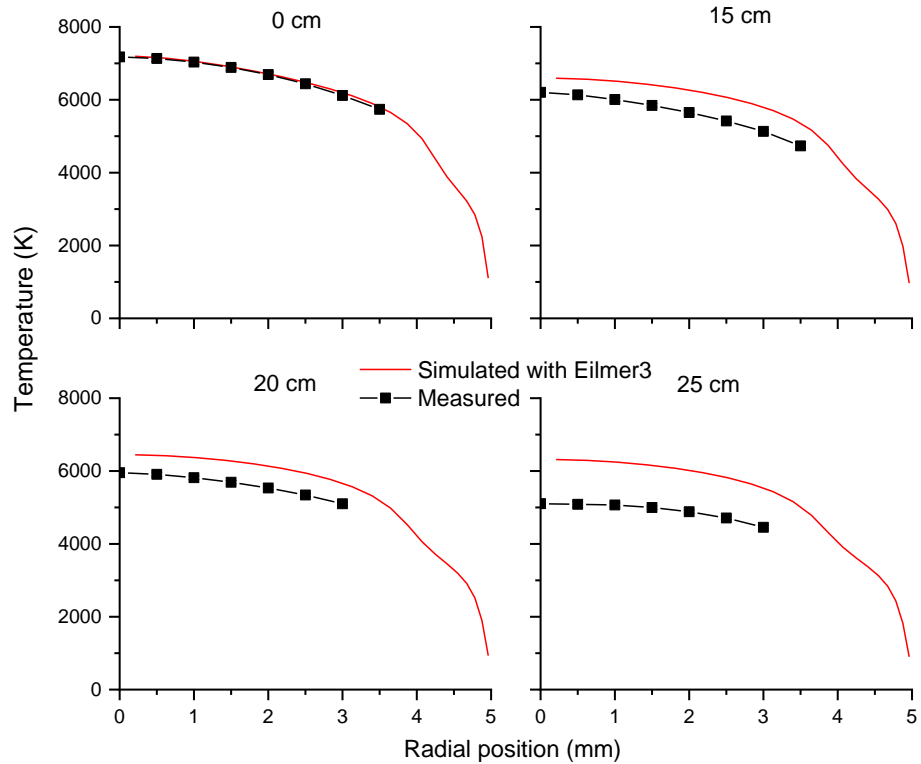


Figure 58: Comparison of measured and simulated (Eilmer3) temperature profiles at 0, 15, 20 and 25 cm for the pure air plasma.

Comparisons of the simulated temperature profiles with the experimental temperature profiles of Gessman *et al* are presented in Figure 19. Note that the experimental uncertainties are plotted but are too small to be seen.

For this laminar equilibrium case, Figure 58 shows that the numerical predictions differ from the measurements at 15, 20, and 25 cm. The slight change of the slope in the temperature profile near the wall is due to the presence of a local minimum in the equilibrium heat capacity around 4000 K, as calculated with CEA. This corresponds to the temperature interval between oxygen and nitrogen dissociation (also observed in Figure 57 for the thermal conductivity). In Figure 59, a comparison between the measured power removed by water cooling and the power loss to the wall in the simulation is presented. The computed power removed is smaller than measured one, explaining the difference in the temperature profiles.

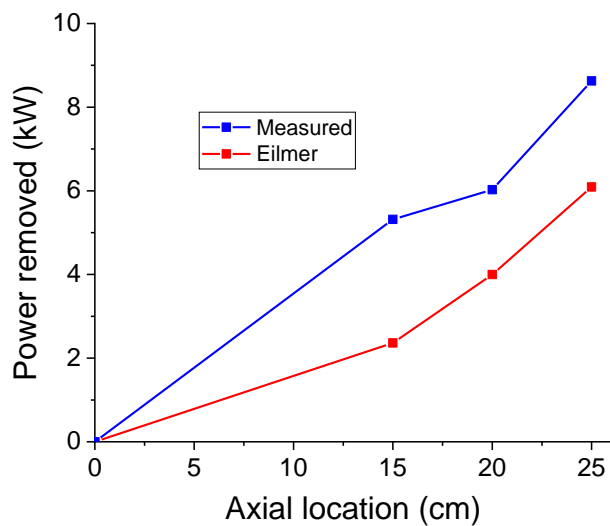


Figure 59: Comparison between measured (blue) and computed (red) power removed to the wall for the pure air case

It appears that the cause for the discrepancy is not due to an error in modeling the wall heat transfer but, rather, to an underprediction of radial heat transfer within the gas. To confirm that the radial heat transfer within the gas is important, we performed a parametric study on the thermal conductivity of the plasma. First, we multiplied the thermal conductivity of CEA by a factor of 2.5, which was found to yield good agreement between the calculations and the experiments as presented below.

As a second test, we added a conductivity varying exponentially with the temperature to model a possible radiative conductivity. The radiative conductivity of an air plasma may be estimated using the Rosseland approximation built in SPECAIR. The Rosseland approximation leads to the following radiative conductivity for a semitransparent medium:

$$\lambda_R(T) = \frac{4\pi}{3} n^2 \int_0^\infty \frac{1}{k_\lambda} \frac{d}{dT} I^\circ_\lambda(T) d\lambda \quad (5.1)$$

where n is the index of refraction, I°_λ the radiance of the black-body (Planck's law), and k_λ the spectral absorption coefficient (Taine, et al., 2008). The Rosseland approximation assumes that the plasma is optically thick. However, for our conditions, the plasma is not optically thick across a large portion of the spectrum. It is, for example, optically thick in part of the VUV region and optically thin in the visible. In the regions where the plasma is optically thin, k_λ is very small, which causes the conductivity integral to diverge. Therefore, the range of wavelengths used in the integral must be carefully chosen. However, there are no well-defined and physically meaningful criteria for selecting this range and, furthermore, a small modification in this choice can have a large impact on the resulting conductivity. Thus, the Rosseland conductivity is ill-defined here.

With these limitations in mind, we took as a starting reference point the radiative conductivity of an argon plasma reported in (Owano, et al., 1993). To obtain reasonable agreement between the Eilmer3 model and the measurements, the radiative conductivity must be 300 times higher than this reference value. The conductivities taken for this calculation are shown in Figure 60 and the results in Figure 61. Note that the equilibrium conductivity calculated using CEA corresponds to the sum of both the thermal and the reactive conductivities.

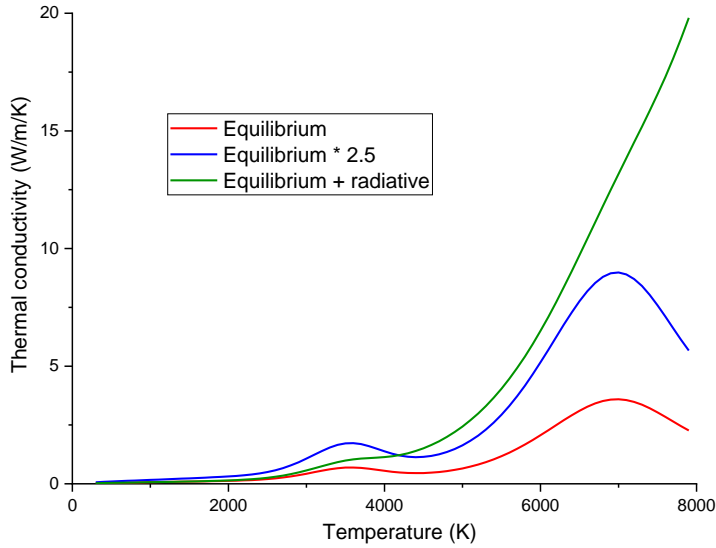


Figure 60: Thermal conductivities taken for our simulations as a function of the temperature. Red: equilibrium conductivity computed by the CEA code.

Blue: same conductivity multiplied by 2.5. Green: the equilibrium conductivity plus the argon radiative conductivity multiplied by 300

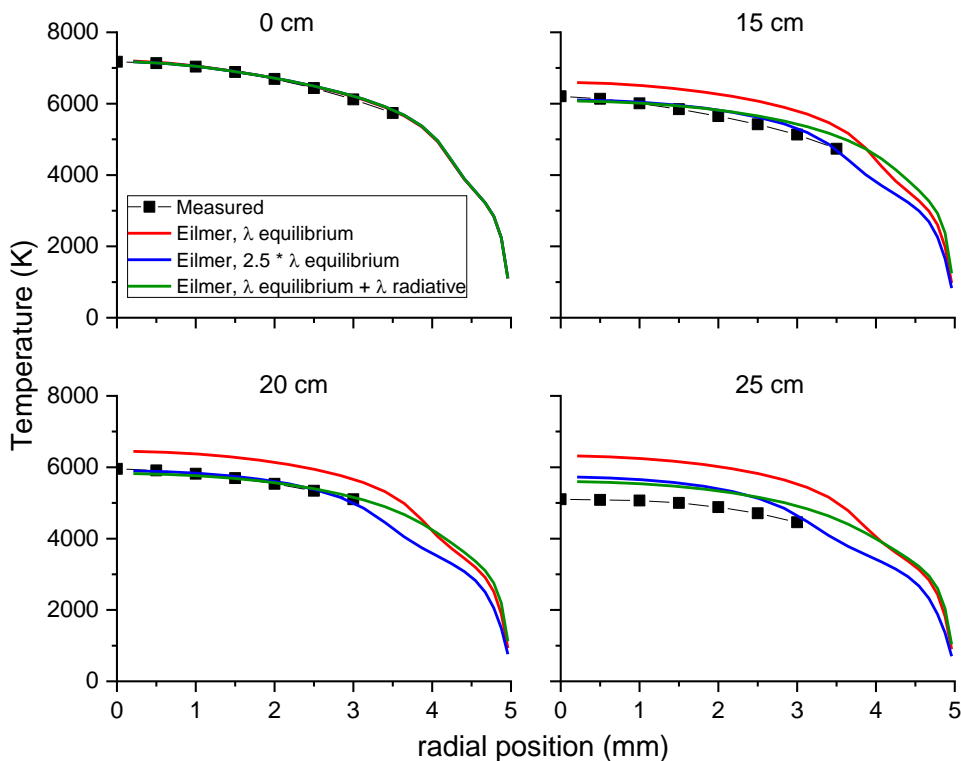


Figure 61: Comparison of the measured temperature profiles with those simulated with Eilmer3 for different thermal conductivities (λ).

For both cases, the results between experiments and numerical simulations are in good agreement at 15 and 20 cm with the assumed thermal conductivity, but there is still a discrepancy at 25 cm. This could come from effects due to turbulence. Turbulence would not only increase the heat transfer to the wall, but also the radial diffusion via the turbulent conductivity. The Reynolds number of 1900 is estimated based on the conditions at 0 cm. However, its value changes along the tube. The mass flowrate is constant, but the dynamic viscosity decreases along the tube as the plasma cools down. Thus, the Reynolds number increases along the tube. At 25 cm, the Reynolds number is about 2600, which may indicate the presence of turbulence, and could help explain the observation that the drop in temperature between 20 and 25 cm is much higher than between 15 and 20 cm. Additional measurements such as schlieren or shadowgraph should be made to validate this prediction. If turbulence is experimentally observed, it must be taken into account in the Eilmer3 simulations.

To support both the presence of turbulence and the inadequate modeling of the radial heat diffusion, we developed a simple 1-D model using the heat transfer correlations of (Taine, et al., 2008). For a fully developed laminar flow (which is expected to be the case at the nozzle exit), the Nusselt number is constant ($Nu = 3.66$) and the heat transfer coefficient to the wall can be obtained from the following relation:

$$h (W \cdot m^{-2} \cdot K^{-1}) = Nu_D \lambda(T_m)/D \quad (5.2)$$

where λ is the thermal conductivity of the gas taken at the mixture temperature T_m defined as $T_m = (T_{gas} + T_{wall})/2$, and D the diameter of the tube. A power balance yields:

$$\dot{m} c_p(T(x)) dT(x) = h (T(x) - T_{wall}) dS_{cyl} \quad (5.3)$$

where x is the axial position, dS_{cyl} is a surface element in the axial direction, \dot{m} is the mass flow rate and c_p the specific heat capacity. It is then possible to compute the temperature evolution using the heat transfer correlations. Note that the Reynolds number changes along the tube. When $Re > 2300$, we use the correlation for turbulent pipe flows (Taine, et al., 2008):

$$Nu_D = 0.023 Re_D^{0.8} Pr^{0.3} \quad (5.4)$$

Figure 62 compares the centerline temperatures computed with Eilmer3, the measured centerline temperatures, and the computed temperatures obtained with this 1-D model using the laminar and/or turbulent correlations. The laminar model agrees relatively well with the measured temperatures up to 20 cm. This is surprising because the transition to turbulence is expected to appear around 10 cm, which seems to be too early in comparison with the measurements.

Nevertheless, the simple model can be used to highlight two points: (1) the change of slope of the measured temperature profiles may be attributed to the transition to a turbulent flow; (2) the heat transfer to the wall is better predicted using the correlations than with the Eilmer3 code, and therefore the radial heat diffusion computed with Eilmer3 may be incorrect, probably because we may be lacking some physics in the calculation of the thermal conductivity.

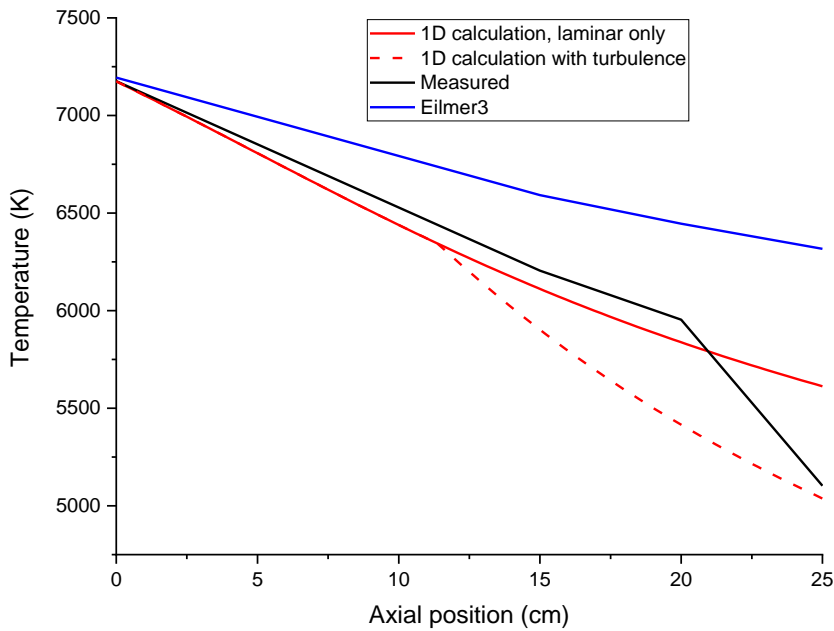


Figure 62: Comparison between axial temperature profiles. Red line: profile computed using the 1D model using the laminar correlation only. Rad dashed line: profile computed using the 1D model using laminar and turbulent correlations for Re below and above 2300, respectively. Black: measurements. Blue: profile computed using Eilmer3.

The velocity profile was not experimentally measured and therefore the velocity used in the CFD calculations could be different from the experiments. To test the sensitivity of the CFD results to the imposed inlet velocity profile, we performed a parametric study on the velocity. The mass flow rate was adjusted by $\pm 20\%$ relative to the measured one. The resulting velocity profiles were then used as new inlet conditions. The various velocity profiles used for the calculations are presented in Figure 63 and the results of the corresponding simulations in Figure 64.

In both cases, the results of the CFD calculations still largely differ from the experimental data. In the best case (-20% flowrate), the temperature drop is 1000 K at 25 cm, versus a temperature drop of 900 K for the baseline case, and 800 K for a flowrate 20% higher than the baseline case. These parametric studies indicate that the resulting temperature profile is not very sensitive to the input velocity profile and that our uncertainty in the velocity profile cannot explain the inability of the CFD code to predict the temperature drop.

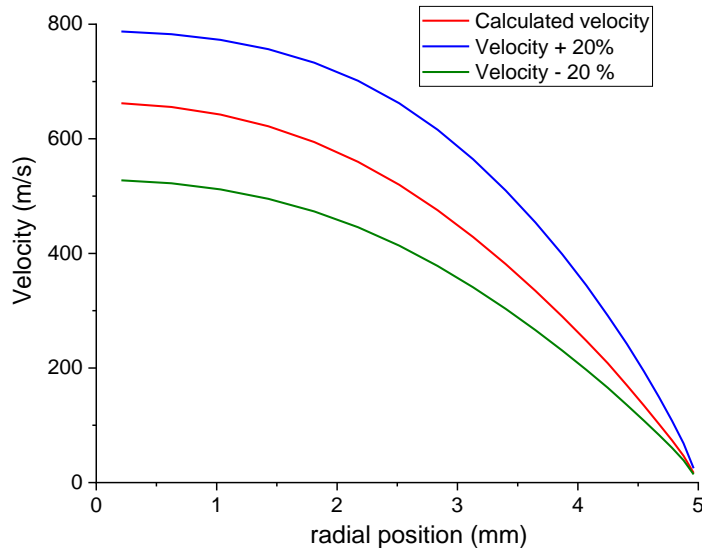


Figure 63: Velocity profiles used for the CFD calculations. Red: Velocity profile corresponding to the measured mass flowrate. Blue: Velocity profile corresponding to the measured mass flowrate + 20%. Green: Velocity profile corresponding to the measured mass flowrate - 20%.

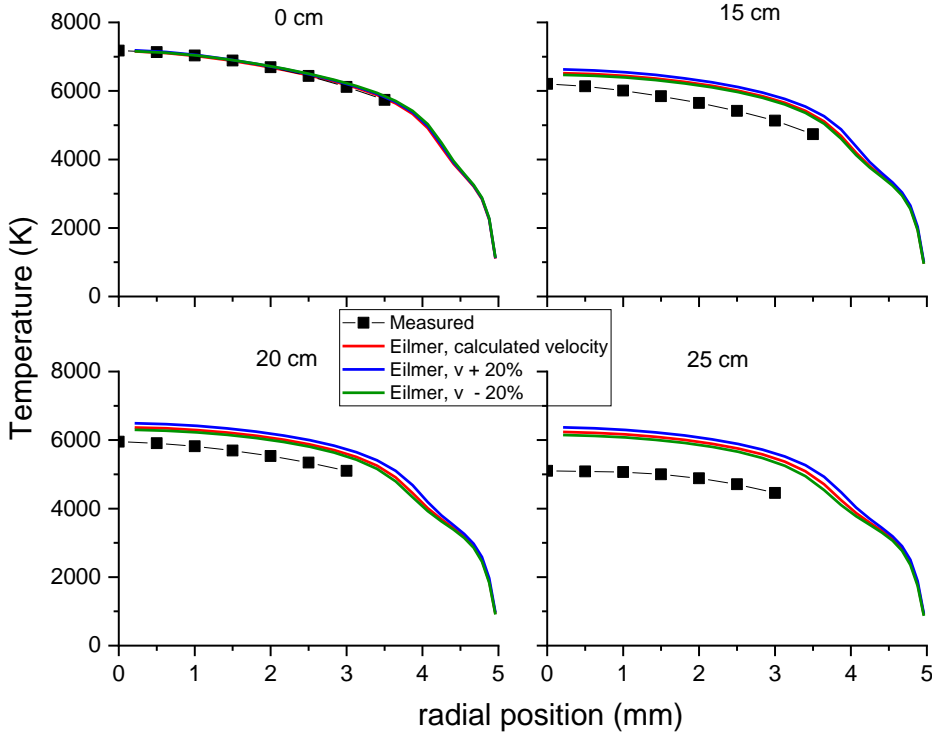


Figure 64: Comparison between experiments and CFD simulations with the velocity profiles plotted in Figure 63.

Finally, we should note that swirl was not taken into account in our simulations, whereas the experimental flow has a swirling component. Note that 35% of the total mass flow rate comes from the swirled injector for this case (see Table 2). However, the swirling effects were previously studied by (Nagulapally, et al., 1998), and it was shown that they did induce any significant change on the drop of temperature. Therefore, this study was not reproduced here.

5.2 Air/Ar plasma

This case corresponds to the Air/Ar plasma presented in Chapter 2. For numerical simulations of this test case, we once again assumed that the gas was in LTE and all thermodynamic properties were calculated using the NASA CEA code. The estimated Reynolds number is about 3600. As of now, we have no measurements of the turbulent energy at the inlet of the tube and therefore we cannot provide an input condition for the turbulence model in Eilmer3. Therefore, our model assumes that the flow is laminar. Comparisons between the experimental and computed radial temperature profiles are presented in Figure 65. The assumption of a laminar

flow is potentially erroneous and could lead to an underprediction of the heat transfer if indeed turbulence is present. However, given the relatively small Reynolds number and the fact that the tube surface is smooth, the flow is not expected to be strongly turbulent and the simulation should give reasonable results. Simulations of this test case were also performed by Candler *et al* in (Candler, et al., 1998) (Nagulapally, et al., 1998) without a turbulence model. Therefore, this test case allows us to compare the Eilmer3 simulations with those of Candler et al.

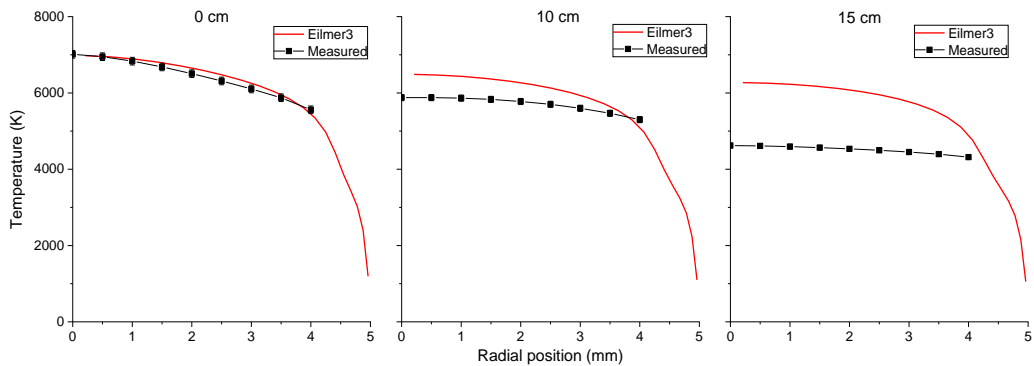


Figure 65: Comparison of the measured radial temperature profiles with those simulated using Eilmer3. The black curve represents the measurements and the red one the simulations. The axial positions are shown at the top of each graph.

As can be seen from Figure 65, the CFD simulations largely underpredict the drop in temperature at 10 and 15 cm. At 15 cm, the measured centerline temperature drop is 2400 K whereas the predicted one using Eilmer3 is 700 K. This is comparable with the difference between the measurements and CFD predictions obtained by Candler *et al* in (MacDonald, et al., 2015) (Nagulapally, et al., 1998): the measured temperature drop at 15 cm was 2350 K and the CFD predicted only a 400 K decrease. The measurements show that the plasma is in, or at least close to, equilibrium. Therefore, this discrepancy should be due to a fluid effect, and not to a chemical kinetics effect.

Finally, simulations of a turbulent flow were done using a k-omega turbulence model. Even by arbitrarily imposing the inlet turbulent intensity (which was not measured), we were unable to match the measured temperature profiles at each axial position.

5.3 Conclusions

Simulations performed with the Eilmer3 code were not able to reproduce the measured temperature drop for the two equilibrium cases (pure air and air/argon) considered in this thesis. Given the discrepancy between the predictions and the measurements for these equilibrium cases, a comparison with the more complex nonequilibrium N₂/Ar test cases was not performed. Nevertheless, the results obtained for the pure air case suggest that radiation transport may play an important role. Our model for the radiation transport was quite crude and, in the future, we intend to model this more accurately by coupling the flow code with radiation transport. The observed discrepancy is believed to come from an inadequate model of the radial energy transport in the plasma. Note also that for the N₂/Ar cases and the Air/Ar case, the flow is expected to be at least mildly turbulent. This turbulence should be taken into account in the CFD model. Temporally resolved velocity measurements are required to supply an estimate of the turbulent kinetic energy and some possible instabilities.

Chapter 6 Molecular radiation

In this chapter, the measured emission spectra obtained between 250 and 900 nm for the three cases referenced in previous chapters (Air/Ar, N₂/Ar LF, and N₂/Ar HF) are analyzed. The experimental setup for these measurements was presented in Chapter 2. In some cases, the plasma is expected to be in nonequilibrium, resulting in a higher radiation than at equilibrium (Gessman, et al., 1997). A method to infer excited state densities of N₂ from the measured spectra was developed and will be detailed here. The resulting density measurements form a complete data set for comparison with kinetic model predictions.

6.1 Method for the determination of excited state densities

To assess the degree of departure from equilibrium in the various cases considered, the radiation code SPECAIR (Laux, et al., 2003) and the NASA CEA code (McBride & Gordon, June 1996) are used. The CEA code is used to compute the equilibrium mole fractions of the gas mixture (N₂/Ar or Air/Ar here). These mole fractions are then passed to SPECAIR as inputs. SPECAIR also requires the gas temperature, which is taken from the measured temperature profiles using Raman spectroscopy (presented in Chapter 3). In all cases, the pressure is 1 atm. The spectra computed with SPECAIR are then compared with the measured spectra, which are calibrated in absolute intensity as explained in Chapter 2 and Abel-inverted to get volumetric emission. Note that the Abel-inversion was possible in the 250-900 nm range because the plasmas are optically thin.

As a first step, we compare the measured spectra with those computed with SPECAIR, assuming LTE at the measured gas temperature. Any disagreement indicates that the plasma is nonequilibrium. As an example, Figure 66 shows a comparison between the experimental and computed LTE spectra at the measured temperature of 3200 K (obtained from Raman spectroscopy) at the exit of the 15-cm tube for the N₂/Ar HF case. The large difference between the two indicate that the plasma is out of equilibrium. We will now explain how the procedure employed in this thesis to quantify the degree of departure from equilibrium in the measured spectrum.

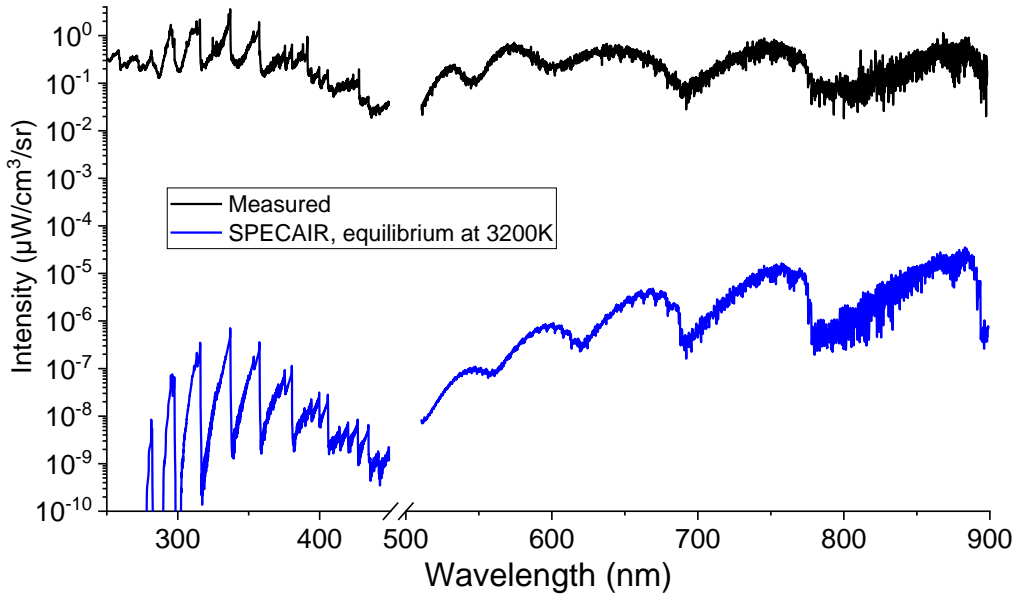


Figure 66: Comparison between experimental (black) and computed (blue) spectra at the exit of the 15-cm tube for the N_2/Ar HF case. The computed spectrum assumes equilibrium at the measured temperature (3200 K).

Emission spectra yield information on the upper state of a given transition. Let's consider a molecular transition $M(e', v', J') \rightarrow M(e, v'', J'')$ from the upper rovibronic state (e', v', J') to the lower rovibronic state (e'', v'', J'') of a given molecule M. If the plasma is optically thin, the intensity of the corresponding rovibronic line is given by:

$$I_{e',v',J' \rightarrow e'',v'',J''} = n_{e',v',J'} \frac{A_{e'v'-e''v''}}{4\pi} (\epsilon_{e',v',J'} - \epsilon_{e'',v'',J''}) \quad (6.1)$$

where $n_{e',v',J'}$ is the number density of vibrational level v' and rotational level J' of the e' state and $\epsilon_{e',v',J'}$ its corresponding energy, $A_{e'v'-e''v''}$ the Einstein coefficient of the transition, and $\epsilon_{e'',v'',J''}$ is the energy of vibrational level v'' and rotational level J'' of the e'' state. The set of rotational lines from v' to v'' is called a vibrational band. The energies of the rovibronic states and the Einstein coefficients are calculated for each rovibrational line in the SPECAIR code, as explained by (Laux, 1993).

The measured line intensities can be used to determine the number density of the rovibronic levels of the upper state of the transition. In Chapter 4, we presented spectra where each rotational line was resolved. In this Chapter, we have

broadband spectra at lower resolution, permitting us only to distinguish the envelope of the vibrational bands. Thus, only the densities of the vibrational levels of the upper state of the transition were measured. Under equilibrium conditions, the vibrational levels follow a Boltzmann distribution at the gas temperature. When the plasma is not in equilibrium, the vibrational levels may follow a Boltzmann distribution at a temperature different from the gas temperature or may not follow a Boltzmann distribution. The radiation code SPECAIR allows us to alter the population of each vibrational level individually for each transition in order to consider non-Boltzmann distributions. SPECAIR was then used measure the vibrational population distributions of the observed transitions.

To simplify the analysis, the spectra measured between 250 and 900 nm were split into two sections corresponding to different transitions: below 450 nm and above 500 nm. The 450-500 nm range was not studied as almost no emission was observed in that range. Table 5 shows the transitions considered and their spectral range of emission. For the main transitions (corresponding to N₂ systems), we did not assume a Boltzmann distribution for the vibrational levels of the upper state. For the other, less intense transitions, we assumed a Boltzmann distribution. Table 5 indicates the assumptions made for each transition. Note that transitions such as CN violet and NH A-X were experimentally observed in the N₂/Ar mixture case. They are attributed to H₂O and CO₂ impurities in the gas injected in the plasma torch.

6.1.2 Spectrum between 500 and 900 nm

In this region, the main emitter is the N₂ first positive system. Atomic transitions are also observed. As shown in Figure 66, at the exit of a 15-cm tube for the N₂/Ar HF case, the plasma is not in equilibrium. The measured spectrum is used to obtain the vibrational population distribution in the N₂(B) state to characterize the degree of nonequilibrium. For this case, the gas temperature measured using Raman spectroscopy is about 3200 K. The measured radiation is many orders of magnitude higher than its equilibrium value. The population distribution does not correspond to a Boltzmann distribution at a temperature higher than the gas temperature. To show this, several spectra were computed using SPECAIR assuming Boltzmann vibrational distributions at different temperatures. A comparison between these computed spectra and the experimental spectra, all normalized in intensity, is

presented in Figure 67. The comparison shows that the measured distribution does not follow a Boltzmann distribution.

Table 5: transitions considered in SPECAIR for the spectral analysis.

Name	Transition	Region of emission	Vibrational distribution
N ₂ first positive	N ₂ : B ³ Π _g → A ³ Σ _u ⁺	500-900 nm	Non-Boltzmann
N ₂ ⁺ Meinel	N ₂ ⁺ : A ² Π _u → X ² Σ _g ⁺	500-900 nm	Boltzmann
N ₂ second positive	N ₂ : C ³ Π _u → B ³ Π _g	250-450 nm	Non-Boltzmann
N ₂ first negative	N ₂ ⁺ : B ² Σ _u ⁺ → X ² Σ _g ⁺	300-450 nm	Non-Boltzmann
CN violet	CN: B ³ Σ _u ⁻ → X ³ Σ _g ⁻	350-430 nm	Boltzmann
NH A-X	NH: A ³ Π _i → X ³ Σ ⁻	300-350 nm	Boltzmann
OH A-X	OH: A ² Σ ⁺ → X ² Π _i	300-330 nm	Boltzmann
NO systems	NO β: B ² Π _r → X ² Π _r NO β': B' ² Δ → X ² Π _r NO δ: D ² Σ ⁺ → X ² Π _r NO ε: E ² Σ ⁺ → X ² Π _r	< 400 nm	Boltzmann
N, O, Ar	Atomic transitions of N, O, and Ar atoms	All wavelengths	Boltzmann

The $\Delta v = 1$ band series of the measured spectrum are better predicted by the computed spectrum at 3200 K. The $\Delta v = 2$ band series are better predicted by the spectrum at 4000 K and the $\Delta v = 3$ band series with the computed spectrum at 6000 K. This result indicates that the vibrational levels of N₂(B) do not follow a Boltzmann distribution.

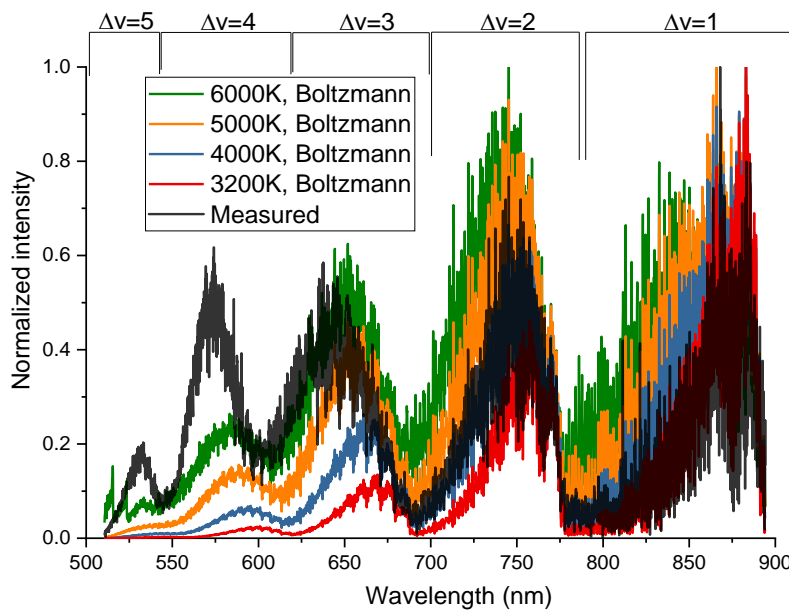


Figure 67: Comparison between experimental and computed spectra at different temperatures. The intensities are normalized. Each computed spectrum assumes a Boltzmann distribution of the vibrational levels at the indicated temperature. The rotational temperature is taken equal to the gas temperature. The vibrational bands of the N_2 first positive systems are also indicated.

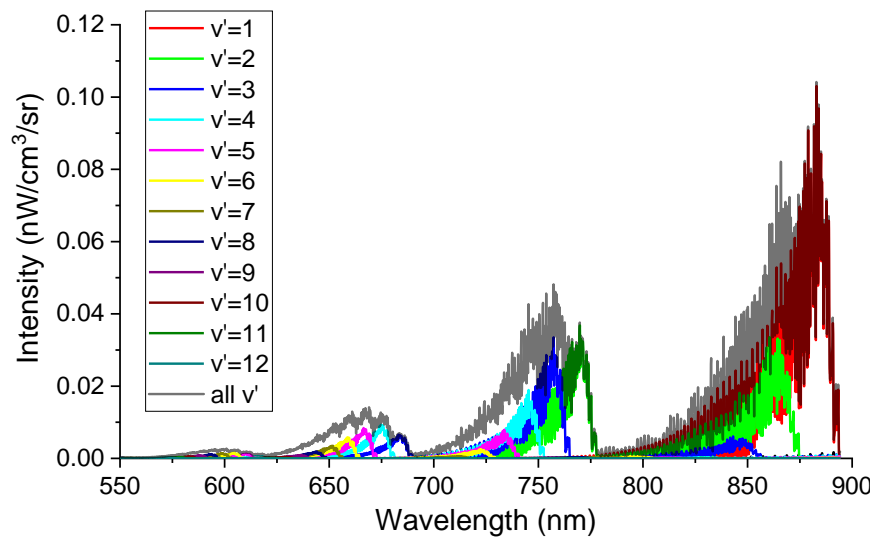


Figure 68: Emission spectra from individual upper vibrational levels, assuming $T_{\text{rot}} = T_{\text{gas}} = 3200 \text{ K}$. The cumulative spectrum representing LTE is also plotted in grey. The emission pathlength is 1 cm.

To determine the densities of the various excited levels, we separated the N₂ first positive system into 21 spectra ($S_i(\lambda)$, $i = 1 \dots 21$), each representing only the transition from one vibrational level at equilibrium at the gas temperature. Figure 68 shows the computed spectrum at 3200 K and the first 12 individual spectra from one vibrational level only. Note that the number of spectra considered was fixed at 21 as the higher levels were not experimentally observed. We then build the spectrum S_{fit} as a linear combination of each individual spectra:

$$S_{fit}(x_0, \dots, x_N, \lambda) = \sum_{i=0}^{i=N} x_i S_i(\lambda) \quad (6.2)$$

where S_i represents the spectrum from the vibrational level i and x_i is a scaling factor. S_{fit} is therefore a linear combination of all S_i spectra. Note that it is also possible to add other atomic and molecular transitions to S_{fit} . In this example, we added a spectrum representing the N₂⁺ Meinel transition (assuming a Boltzmann distribution) and a spectrum comprising the atomic transitions. The best fit was found by minimizing the error between S_{fit} and the measured spectrum S_{meas} . This was done using an optimization algorithm to minimize the error using a L₂ norm between the two spectra:

$$L_2(x_0, \dots, x_N) = \sqrt{\sum_i (S_{meas}(i) - S_{fit}(x_0, \dots, x_N, i))^2} \quad (6.3)$$

The results give the best estimate of the vector $X = (x_0, \dots, x_N)$ and the resulting spectrum S_{best} . The initial condition X_0 was chosen to satisfy $\int_{\lambda} S_{meas} d\lambda = \int_{\lambda} S_{fit}(X_0, \lambda) d\lambda$. The spectrum resulting from this minimization algorithm is compared with the experimental spectrum in Figure 69. Individual spectra (S_i) are also shown to show the contribution of each vibrational level to the final spectrum. Note that a given vibrational level contributes to the spectrum through several vibrational bands in the spectrum, and therefore there is a unique solution to the minimization problem. This was also proved numerically by changing the initial condition X_0 to a random value. The results always yield the same value of the X vector.

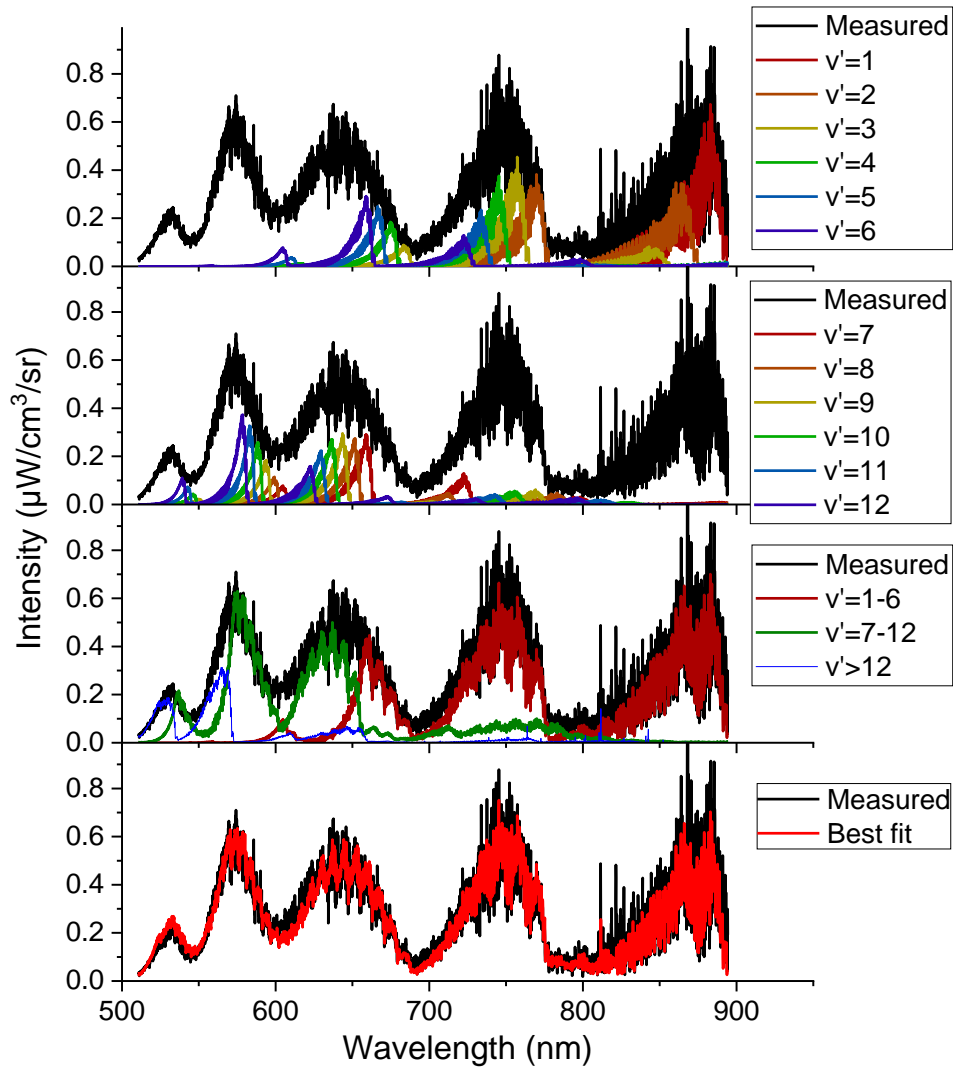


Figure 69: Comparison between the spectrum computed with the minimization algorithm and the experimental one. The contribution of single vibrational levels is shown in the top plots and the final spectrum at the bottom.

From Eq (6.1)(2.4), it is possible to relate the vector X to the density of the excited vibrational levels of the N_2 first positive system, each S_i spectrum being proportional to the density of vibrational level i . For a given vibrational level i , the following relation holds:

$$n_{N_2(B)v_{meas}} = x_i \cdot n_{N_2(B)v_{eq}} \quad (6.4)$$

In this case, x_i represents the overpopulation factor of the vibrational level i of $N_2(B)$, noted $\rho(N_2B(i))$, defined as $\rho = n_{meas}/n_{equilibrium}$. The density at equilibrium depends on the mole fraction of N_2 , which can be calculated using the CEA code, and from the Boltzmann fraction of the given vibrational level. The overpopulation factors and corresponding densities determined with this method are presented in Figure 70.

To quantify the uncertainties, we used a bootstrapping method, as explained next. First a random noise is added to the computed spectra. The amplitude of the noise is adjusted to match the experimental uncertainty, found as the sum of the measured random noise and the uncertainties propagated through the Abel inversion algorithm. The uncertainties vary from experiment to experiment, but the typical value is 5% at the centerline of the tube and below 30% elsewhere. Then the optimization algorithm is run on these new spectra and the error for the best fit is computed. This procedure is repeated 100 times for each spectrum. Above 100 times, both the standard deviation and the mean of the error do not change significantly and therefore 100 times is found to be sufficient. The standard deviation of the results is taken as the uncertainty on the measurement. This procedure tests the sensitivity of our algorithm to the experimental noise and yields a good estimate of the uncertainty of the fits. The uncertainties on both the overpopulation factors and the corresponding densities are also reported in Figure 70. Note that for the densities, the uncertainties appear very small because of the log scale.

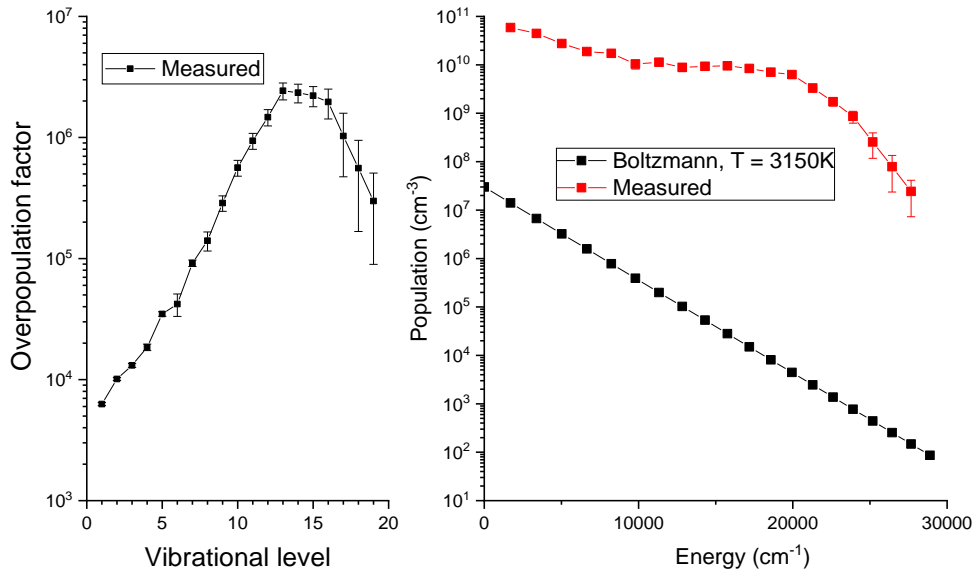


Figure 70: Left: Measured overpopulation resulting from the minimization algorithm. Right: equilibrium and measured densities of the vibrational levels of $\text{N}_2(\text{B})$.

The vibrational level $v = 0$ is not reported in Figure 70 because the bands emitted from $v=0$ are at wavelengths above 1 μm , which outside the accessible spectral range of our spectrometer. Level $v = 20$ is not reported either because its emission is negligible.

6.1.3 Spectrum between 250 and 450 nm

The measured spectrum between 250 and 450 nm obtained at the exit of a 15-cm tube for the N_2/Ar experiment was already presented in Figure 66. Again, a large departure from equilibrium is observed, both for the N_2 second positive and N_2^+ first negative systems. Some emission from the CN violet, OH A-X, NH A-X, and NO systems are also observed. Note that these systems were observed in the N_2/Ar mixture because of the presence of H_2O and CO_2 impurities in the gas. These systems are considered in the fitting procedure but are treated by assuming a Boltzmann distribution for the emitting levels. The same minimization algorithm presented in section 6.1.2 is used, here with 13 different spectra: 5 vibrational levels of $\text{N}_2(\text{C})$, 4 vibrational levels of $\text{N}_2^+(\text{B})$, and global spectra for CN violet, OH A-X, NH A-X and the NO systems. The contributions of each transition to the final spectrum are presented in Figure 71. They were obtained as the best fit of the algorithm.

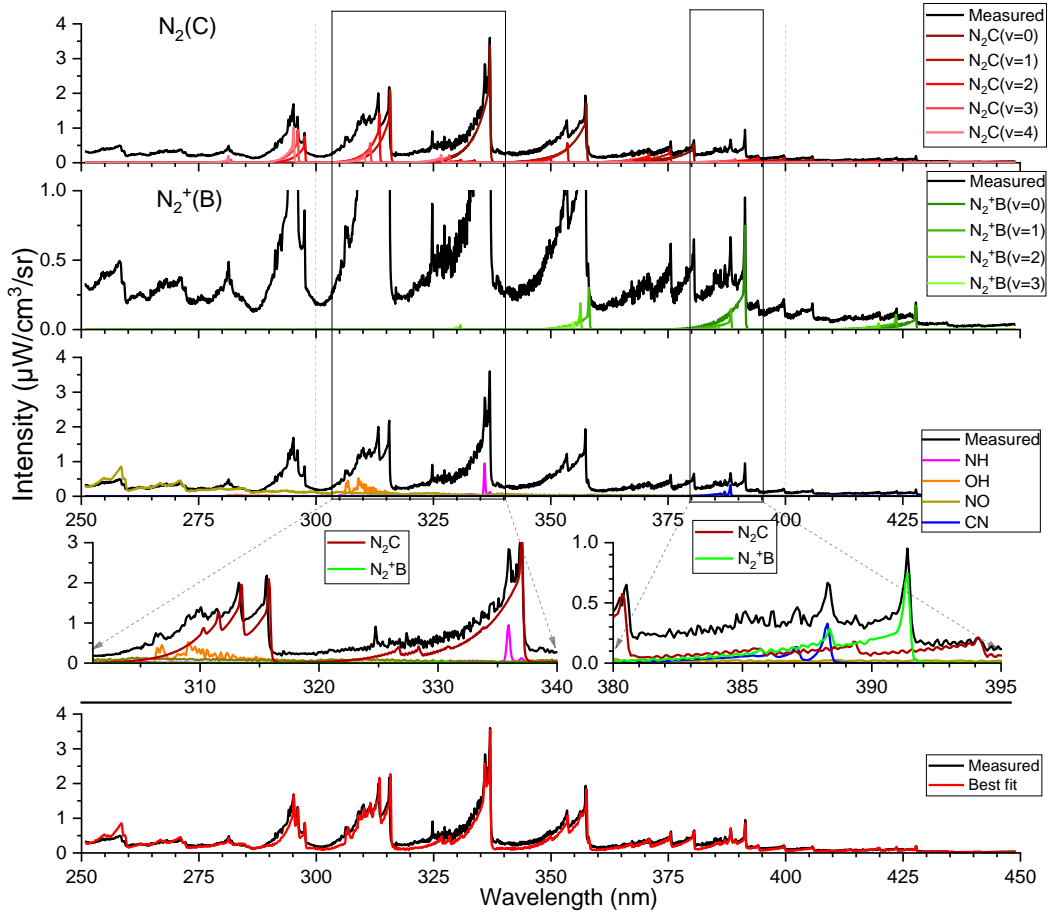


Figure 71: Comparison between the spectrum resulting from the minimization algorithm and the measured spectrum (bottom). The contributions of each transition are shown on the top graphs.

To ensure optimal agreement between the computed and experimental spectra, the spectral contribution of OH, NH, and NO (resulting from impurities) had to be taken into account. An uncertainty analysis similar to that presented in section 6.1.2 was performed. The resulting uncertainties on the overpopulation factors and densities of $N_2(C)$ and $N_2^+(B)$ are presented in Figure 72.

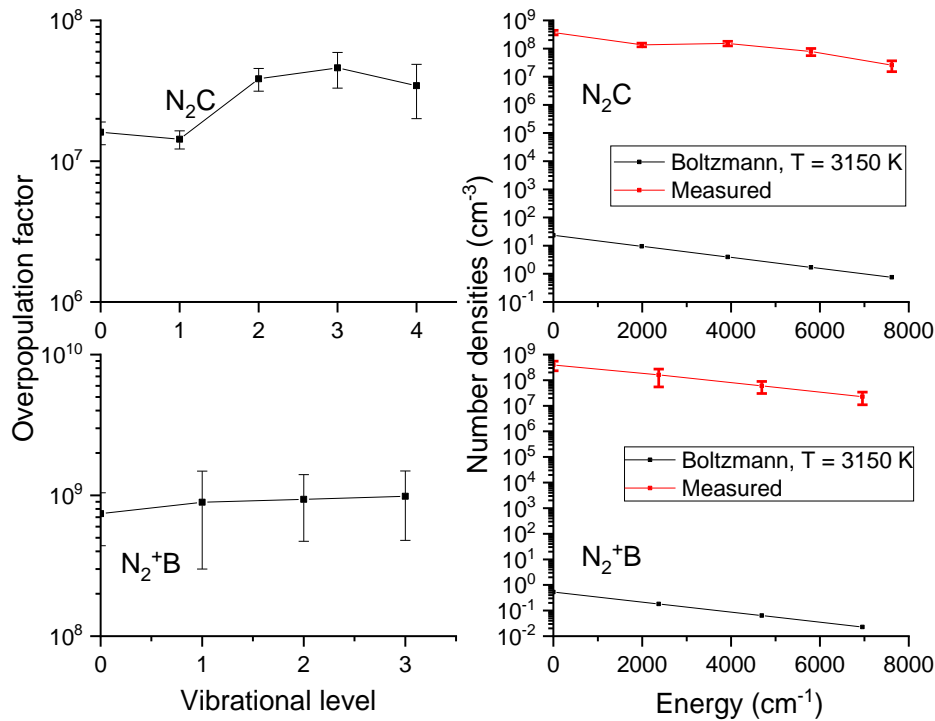


Figure 72: Overpopulation factors (left) for $\text{N}_2(\text{C})$ (top) and $\text{N}_2^+(\text{B})$ resulting from the minimization algorithm and comparison between the measured and equilibrium densities (left).

6.1.4 Influence of the rotational temperature

The procedure detailed above allowed us to measure the absolute densities of the vibrational levels of various excited molecules. These measurements are independent of the translational temperature (which only changes the total density), the electronic temperature (which only changes the relative density of the electronic states) and the vibrational temperature (which is not even considered as we allow non-Boltzmann distributions). However, the rotational temperature is still an input parameter for the algorithm and may influence the results. As presented in Chapter 4, the rotational temperature of the excited states may be different from the gas temperature. It is the case for $\text{N}_2^+(\text{B})$ for example. The influence of the rotational temperature on the results of the algorithm will be tested here. The measured spectra presented in sections 6.1.2 and 6.1.3 were considered for this analysis. Different rotational temperatures, namely 2150, 3150, 4150, and 5150 K, were taken as inputs of the minimization algorithm. The spectra computed at these different rotational temperatures are compared with the experimental spectrum in

Figure 73. Each computed spectrum is in good agreement with the experiments, (the relative errors between the best fits and the measurement are within 1%) is thus indicating that the analysis is not sensitive to the rotational temperature.

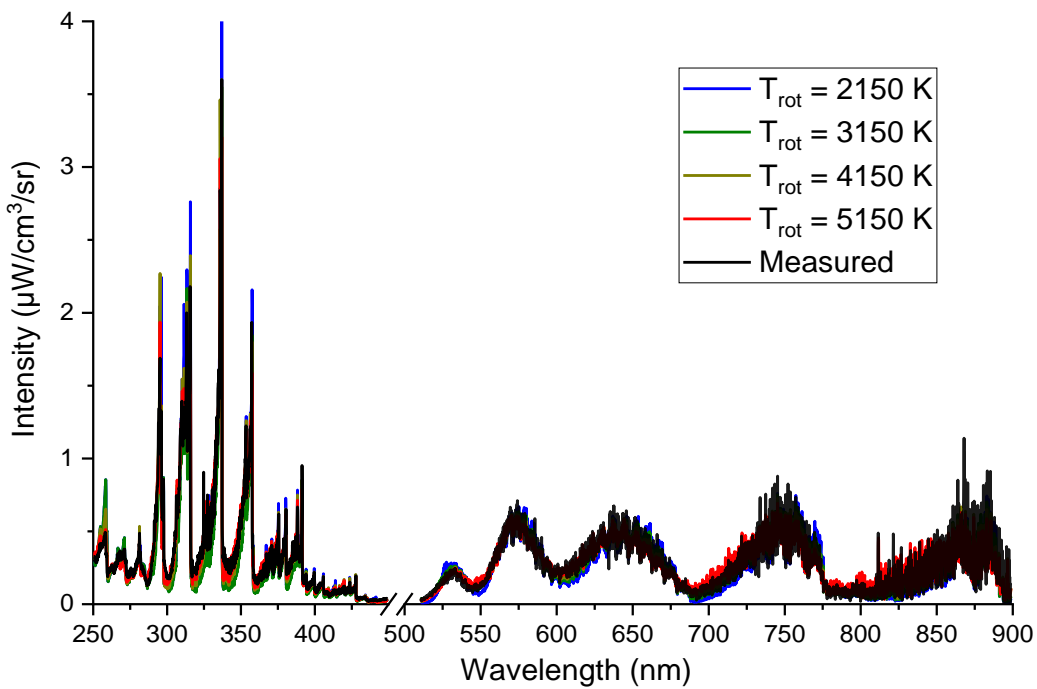


Figure 73: Comparison between the experimental spectrum and the computed spectra resulting from the minimization algorithm for different input rotational temperatures.

We also compared the sensitivity to the rotational temperature of the absolute vibrational population distributions. Results for the vibrational levels of $\text{N}_2(\text{B})$, $\text{N}_2(\text{C})$ and $\text{N}_2^+(\text{B})$ are presented in Figure 74. The differences between the densities obtained with the various rotational temperatures are typically within the error bars, for almost all levels. For high vibrational levels of $\text{N}_2(\text{B})$ ($v > 14$) and the first few levels of $\text{N}_2^+(\text{B})$, the influence of the rotational temperature is higher, however the error bars are also larger, and the results remain reasonably close, within an order magnitude. Therefore, we conclude that the analysis is not very sensitive to the rotational temperature and that an accurately measured rotational temperature is not required to obtain the densities of the vibrational levels.

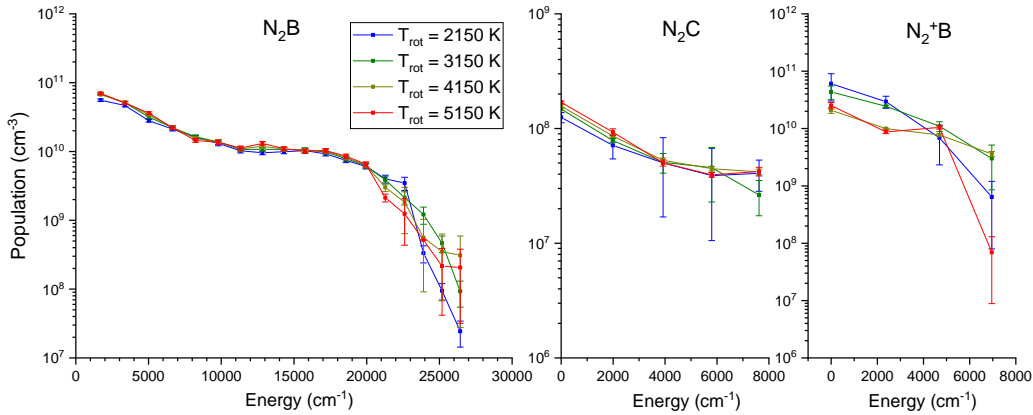


Figure 74: Vibrational population distribution for $\text{N}_2(\text{B})$ (left), $\text{N}_2(\text{C})$ (middle) and $\text{N}_2^+(\text{B})$ (right) for different input rotational temperatures.

The procedure detailed in this section will be used for the three different test cases: Air/Ar, N_2/Ar LF and HF at the three different axial positions 0, 10, and 15 cm. This will allow us to get measurements of the vibrational distributions of $\text{N}_2(\text{B})$, $\text{N}_2(\text{C})$ and $\text{N}_2^+(\text{B})$ and to study their spatial evolution in the tube.

6.2 Air/Ar case

The air/argon experiments were conducted with a mixture of 1.9 g/s of air and 1.5 g/s of argon injected into the torch. The plasma in this case is expected to stay in LTE throughout the recombination tube, as shown by Gessman (Gessman, 2000). This assumption will be tested here by comparing the measured emission spectrum between 200 and 800 nm with an equilibrium spectrum computed with SPECAIR. The experimental spectrum was obtained with a 600 grooves/mm grating. The slit function was measured using a He-Ne laser and the measured instrumental line shape is shown in Figure 75. The FWHM is 0.3 nm (spectrometer slit width = 50 μm).

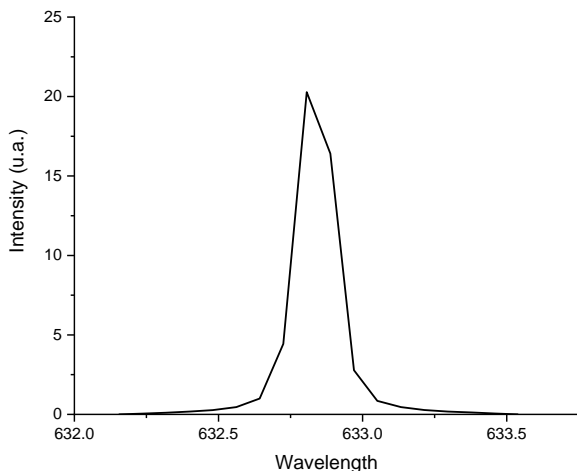


Figure 75: Slit function measured using a He-Ne laser

Optical filters were used to remove potential second order emission. Below 300 nm, no filter was used. Between 300 and 550 nm, we used a 300-nm high-pass filter, and a 550-nm-high pass filter above 550 nm. The results at the exit of a 15-tube will be presented now. The ICCD camera acquired 50 images with an integration time of 500 ms below 550 nm and 10 images with an integration time of 10 s above 550 nm. The gain was set at the maximum value (255). The camera response was found to be linear with integration time in the range 1 ms to 10 s, as also previously shown by (Rusterholtz, 2012). The measured spectra were calibrated and Abel-inverted as explained in Chapter 2. Note that for this case, the stray light entering the spectrometer was relatively high and special care had to be taken in order to reduce it by enclosing the optical path to prevent direct access to the spectrometer. In addition, a non-reflective black screen was placed on the side of the plasma opposite to the detector in order to eliminate the contribution of reflections to the stray light level.

The measured temperature at the center of the tube using both OES and Raman spectroscopy was 4660 K. This temperature was used to compute the equilibrium spectrum using SPECAIR. The mole fractions were calculated using the NASA CEA code. The computed and experimental spectra are compared in Figure 76. The good agreement between the two spectra supports the equilibrium assumption for this case. Note that the slight discrepancy around 600 nm may come from second order emission from the second positive system despite the presence of a high pass filter, the grating being blazed at 300 nm and the camera being very responsive in the UV.

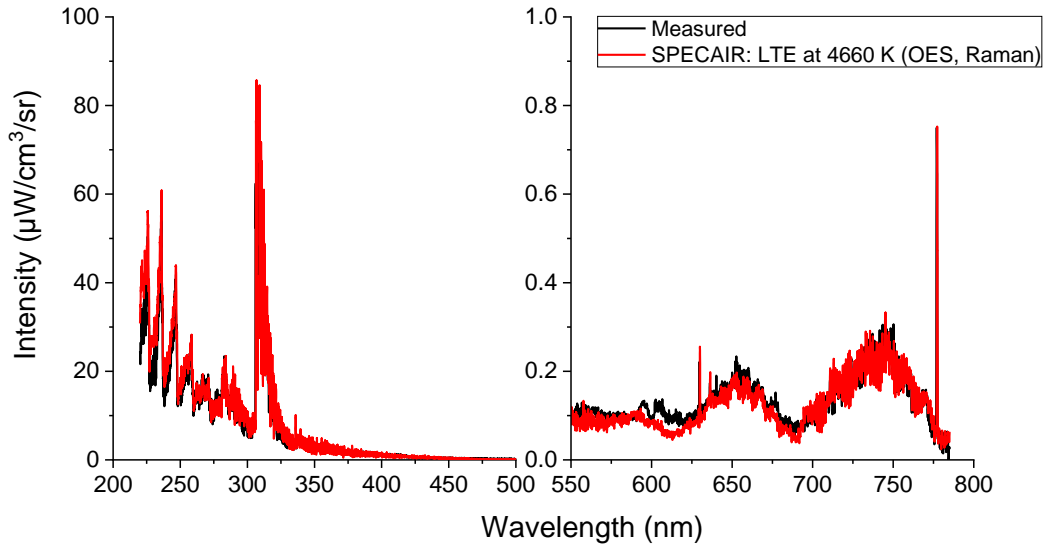


Figure 76: Comparison between experimental (black) and computed (red) spectrum using SPECAIR assuming equilibrium at the measured temperature (4660 K) at the center of the tube ($r = 0$ mm) for the Air/Ar gas mixture.

Similar good agreement was found at the exit of the 10-cm tube. These results support the equilibrium assumption for this Air/Ar case along the tube. This case is useful to test both experimental and numerical techniques under simple conditions. The reason why the air plasma remains in equilibrium was explained by Gessman *et al* (Gessman, 2000) and is due to the fast recombination reaction $N + O + M \rightarrow NO + M$. In plasmas without oxygen, the recombination of N atoms proceeds through the much slower reaction $N + N + M \rightarrow N_2 + M$ (Gessman *et al* (Gessman, 2000)). Therefore, more nonequilibrium is expected in nitrogen or nitrogen/argon plasmas, as will be confirmed in the following sections.

6.3 N_2/Ar low flowrate case

The plasma is comprised of 1.2 g/s of N_2 and 1.5 g/s of argon. The plasma is under equilibrium at the exit of the torch, with the measured temperature profile given in Chapter 3. This was confirmed by the good agreement between the measured spectrum and the equilibrium spectrum computed with SPECAIR. At 10 and 15 cm, the plasma was found to be out of equilibrium and the procedure detailed in section 6.1 was applied to determine the nonequilibrium population distributions of the excited electronic states.

6.3.1 Emission spectra at 10 and 15 cm

At 10 and 15 cm, spectra were measured between 250 and 900 nm. The OES setup was the same as in Chapter 2. The camera settings were changed to improve the signal-to-noise ratio and are summarized in Table 6.

Table 6: Camera settings used for OES for the N₂/Ar LF case

Axial position	Below 450 nm		Above 450 nm	
	Integration time	Software accumulations	Integration time	Software accumulations
10 cm	100 ms	50	2 s	10
15 cm	500 ms	100	10 s	10

A comparison between computed spectra assuming equilibrium or nonequilibrium and the measured spectrum at 10 cm is presented in Figure 77. The measured spectrum was Abel-inverted and only the volumetric emission of the center of the plasma is plotted. The measured and equilibrium densities of N₂(B), N₂(C) and N₂⁺(B) used for the SPECAIR calculations are also plotted. The measured spectrum appears close to equilibrium with a slight overpopulation of the excited states of nitrogen. Similar agreement between the computed spectrum resulting from the fitting algorithm and the experimental one for each radial position were observed. Note that mole fractions of 0.5% of H₂O and 0.1% of CO₂ were added to the chemical composition to match the observed NH and CN transitions.

A similar comparison at the exit of a 15-cm tube is presented in Figure 78. The plasma is further away from equilibrium in this case as the excited states of nitrogen are more overpopulated resulting in a higher radiation than at equilibrium. All Abel inverted spectra were analyzed to get radial distributions of the vibrational levels for the three excited electronic states considered. Similar fits were performed at each radial position, but they are not presented here for the sake of clarity.

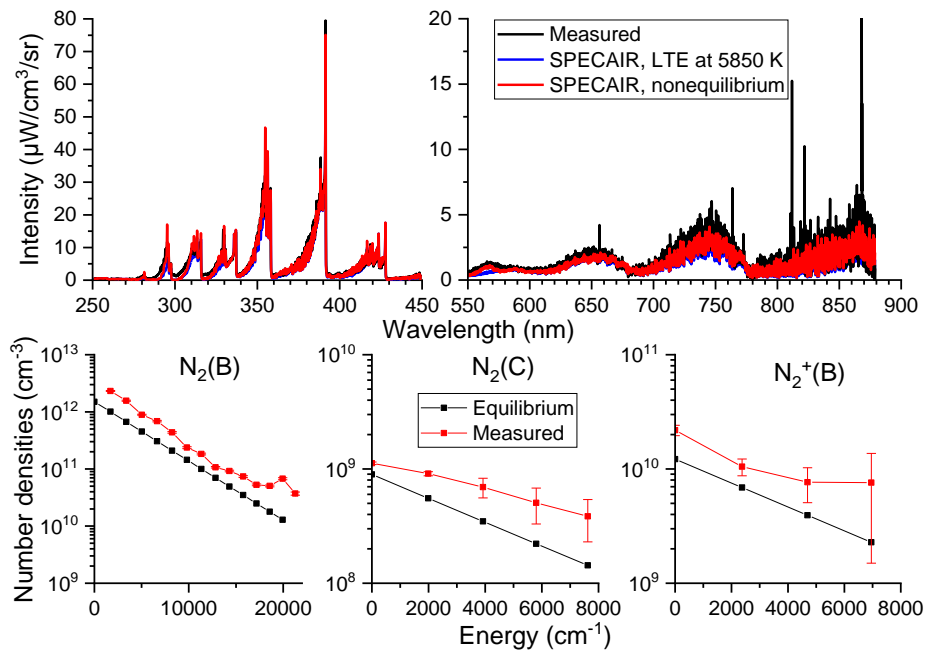


Figure 77. Top: comparison between measured and computed spectra at the exit of the 10-cm tube for the N_2/Ar LF case at the center of the tube ($r = 0$ cm). Equilibrium spectrum (blue) and fitted spectrum (red). Bottom: equilibrium and measured populations of emitting levels used for SPECAIR calculations.

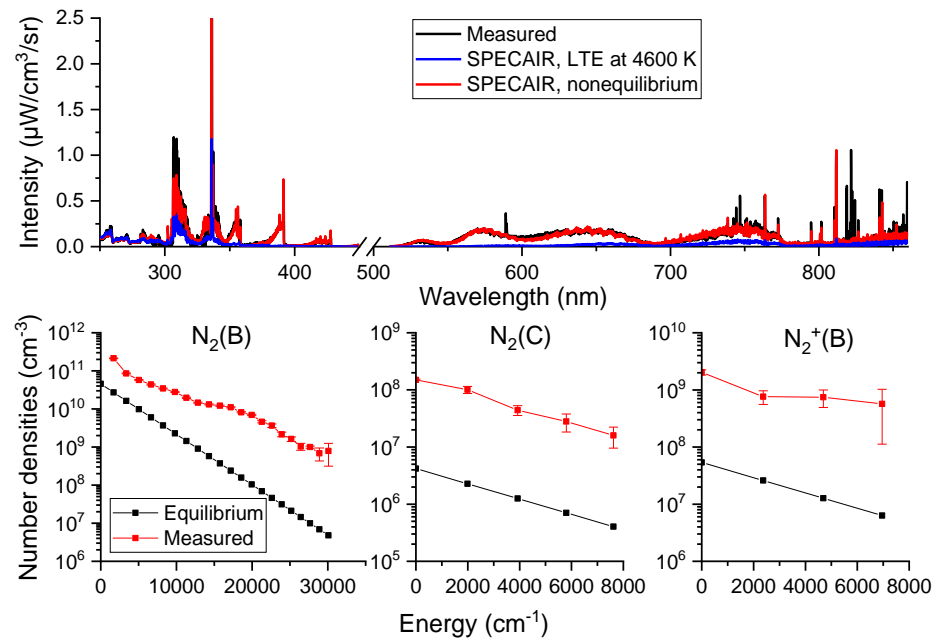


Figure 78: Top: comparison between measured and computed spectra at the exit of the 15-cm tube for the N_2/Ar LF case at the center of the tube ($r = 0$

cm). Equilibrium spectrum (blue) and fitted spectrum (red). Bottom: equilibrium and measured populations of emitting levels used for SPECAIR calculations.

6.3.2 Measured densities of $\text{N}_2(\text{B})$, $\text{N}_2(\text{C})$, and $\text{N}_2^+(\text{B})$ at 10 and 15 cm

6.3.2.1 Radial distributions

The radial distributions of the vibrational level densities of $\text{N}_2(\text{B})$, $\text{N}_2(\text{C})$ and $\text{N}_2^+(\text{B})$ are presented in Figure 79. Between 0 and 1 mm, the vibrational levels of the three electronic states are slightly overpopulated compared to their equilibrium population. At 1.5 mm, a small underpopulation is observed for $\text{N}_2(\text{C})$ and $\text{N}_2^+(\text{B})$. Note however that the measured densities at radii greater than 1 mm remain close to the equilibrium densities, within the uncertainties associated with the measured temperature. In summary, the measured densities remain close to equilibrium at all radial positions and do not change significantly with the radius.

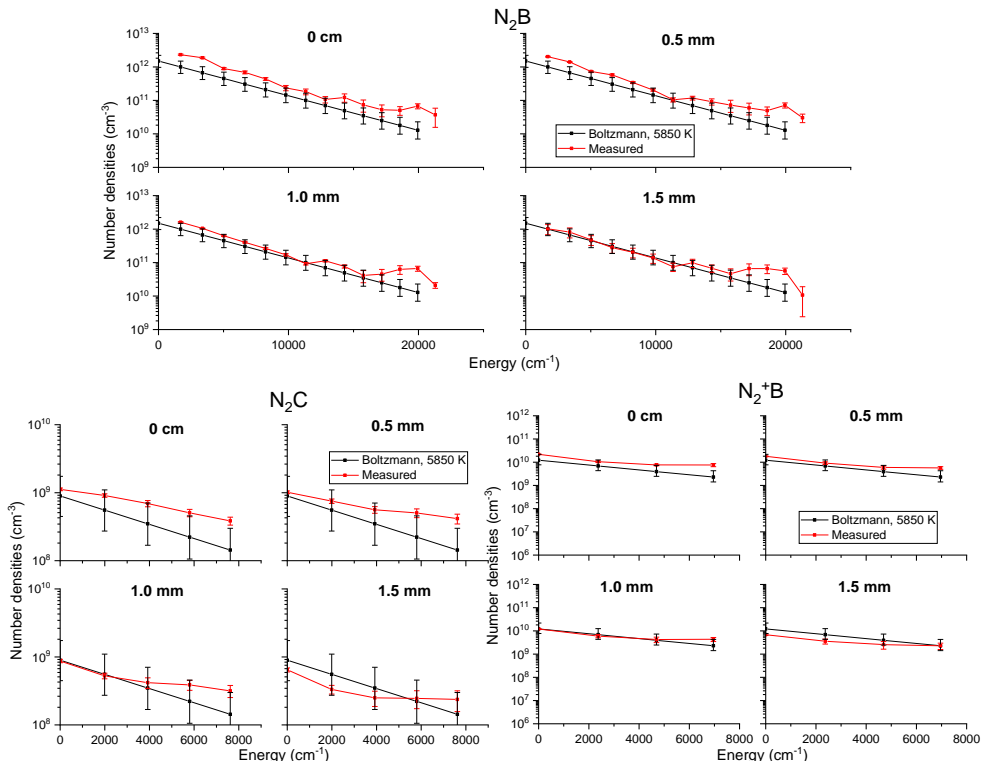


Figure 79: Radial distribution of measured and equilibrium densities of $\text{N}_2(\text{B})$ (top), $\text{N}_2(\text{C})$ (bottom left) and $\text{N}_2^+(\text{B})$ (bottom right) for the N_2/Ar LF case at the exit of the 10-cm tube.

The measurements performed at the exit of the 15-cm tube are presented in Figure 80. All excited states are overpopulated with respect to equilibrium at each radial position. The degree of nonequilibrium increases with the tube length as these levels are more overpopulated than at 10 cm. Note that the measured $\text{N}_2(\text{B})$ vibrational distribution is no longer Boltzmann. A change of slope in this distribution is observed around level $v = 13$. As will be explained in Chapter 7, the overpopulation of level $v = 13$ is caused by the direct recombination of nitrogen atoms into this vibrational level via inverse predissociation. The $\text{N}_2(\text{C})$ and $\text{N}_2^+(\text{B})$ vibrational levels are overpopulated and small deviation from Boltzmann distribution may be observed at some radial locations. Overall, their distributions remain relatively close to Boltzmann.

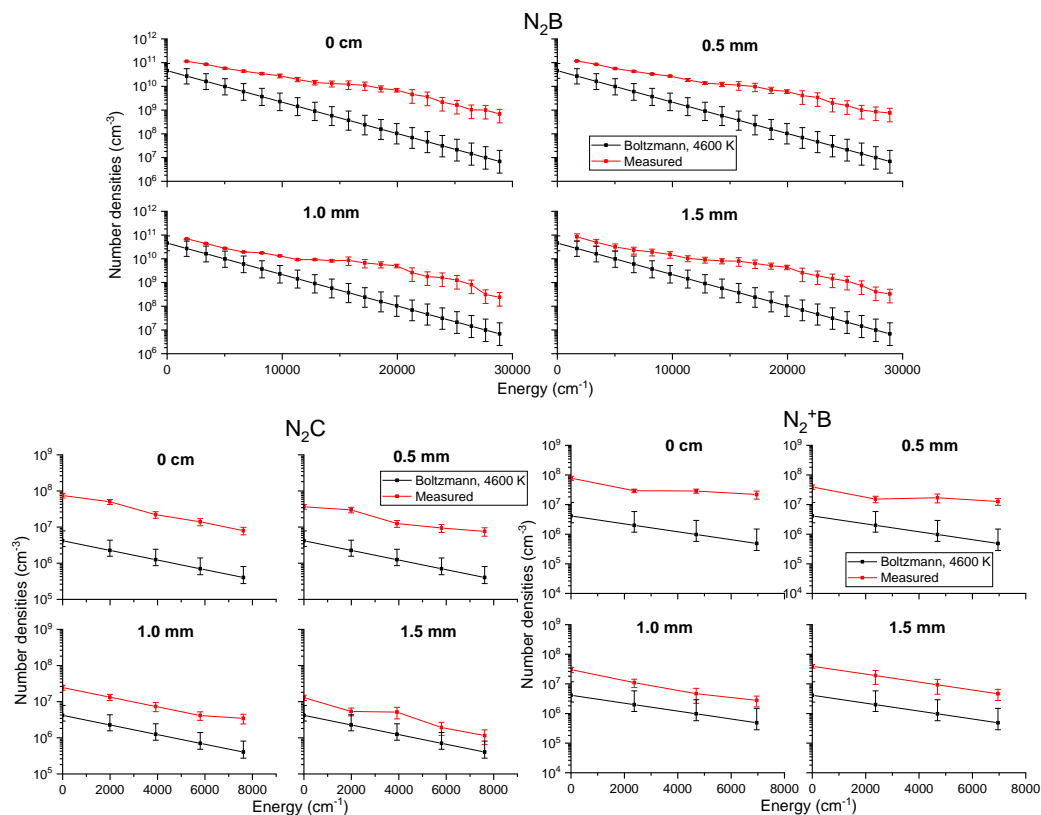


Figure 80: Radial distribution of measured and equilibrium densities of $\text{N}_2(\text{B})$ (top), $\text{N}_2(\text{C})$ (bottom left), and $\text{N}_2^+(\text{B})$ (bottom right) for the N_2/Ar LF case at the exit of the 15-cm tube.

6.3.2.2 Boltzmann diagram

It is interesting to combine on a Boltzmann diagram the densities of the vibrational levels of the various electronic states of N_2 . These include the first three vibrational levels of $\text{N}_2(\text{X})$, measured using Raman spectroscopy, and the vibrational levels of $\text{N}_2(\text{B})$ and $\text{N}_2(\text{C})$ obtained with emission spectroscopy. These measured densities are divided by the degeneracy of the state and their rotational partition function Q_{rot} . Note that $Q_{\text{rot}} = T/\Theta_{\text{rot}} = k_b T/\sigma h c B_e$, where B_e is the rotational constant of the electronic state under consideration, h the Boltzmann constant, and σ is a symmetry factor, equal to two for homonuclear diatomic molecules (Herzberg, 1950). The Boltzmann diagrams are presented in Figure 81.

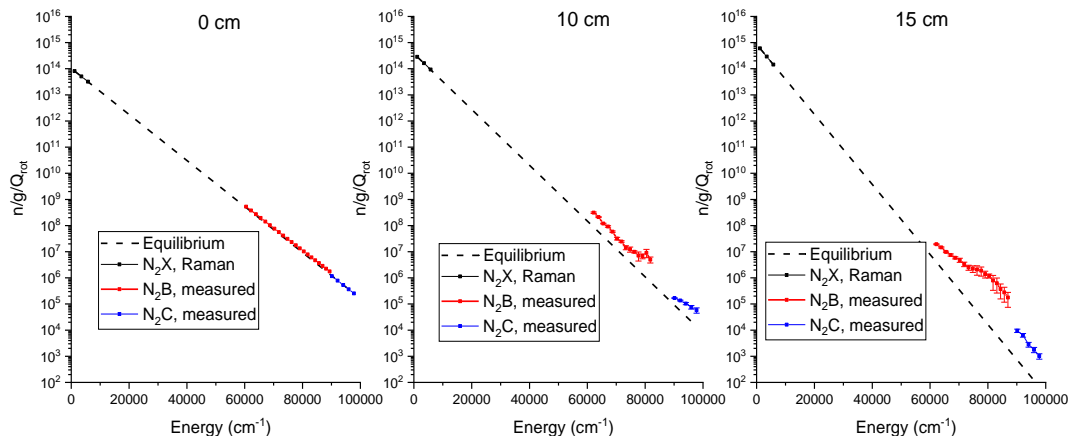


Figure 81: Boltzmann diagrams of the measured vibronic population distributions for the N_2/Ar LF case at 0, 10 and 15 cm

Note that the first vibrational levels of $\text{N}_2(\text{B})$ and $\text{N}_2(\text{C})$ tend to fall on a line with lower slope than the equilibrium distribution. From a modeling point of view, their populations can be approximated by a Boltzmann distribution using an electronic temperature higher than the translational temperature.

The CFD codes used for hypersonic flows often resort to a two-temperature model (Candler, 1988) (Gollan, 2008) (Casseau, et al., 2016), with a translational-rotational temperature T_{tr} and a vibrational-electronic temperature T_{ve} . In these models, the R-T relaxation times are assumed to be fast enough to consider a single temperature for translation and rotation, and the vibrational and electronic temperatures are considered to be equal. An energy source term is added to the

transport equations to compute the vibration-translation relaxation (V-T transfer) using the Landau-Teller equation:

$$\frac{dE_{ve,s}}{dt} = \sum_c \left(x_c \frac{E_{ve,s}(T_{tr}) - E_{ve,s}(T_{ve})}{\tau_{V-T}^{s-c}} \right) \quad (6.5)$$

where $E_{ve,s}$ is the vibronic energy of species s, x_c the mole fraction of the colliding particle c, and τ_{V-T}^{s-c} the relaxation time of the species s colliding with species c. The vibronic energy of species s is the sum of the vibrational and electronic energies:

$$\begin{aligned} E_{ve,s} &= E_{vib,s} + E_{elec,s} \\ E_{vib,s} &= R_s \frac{\theta_{v,s}}{\exp\left(\frac{\theta_{v,s}}{T_{ve,s}}\right) - 1} \\ E_{el,s} &= \frac{R_s \sum_{i=1}^{\infty} g_{i,s} \theta_{el,i,s} \exp\left(-\frac{\theta_{el,i,s}}{T_{ve,s}}\right)}{\sum_{i=1}^{\infty} g_{i,s} \exp\left(-\frac{\theta_{el,i,s}}{T_{ve,s}}\right)} \end{aligned} \quad (6.6)$$

where R_s is the specific gas constant, $\theta_{v,s}$ the characteristic vibrational temperature of species s, $\theta_{el,i,s}$ the characteristic electronic temperature of electronic state i of species s, and $g_{i,s}$ the degeneracy of electronic state i of species s. The vibrational relaxation time can be calculated using the semi-empirical correlation of Millikan and White (Millikan & White, 1963) (Millikan & White, 1964) with the correction of Park (Park, 1993) to account for the inaccuracy the collision cross-sections at high temperatures. The vibrational relaxation time of particles p colliding with particles q is then:

$$\begin{aligned} \tau_{V-T}^{p-q} &= (\tau_{V-T}^{p-q})_{MW} + (\tau_{V-T}^{p-q})_{Park} \\ \ln(P(\tau_{V-T}^{p-q})_{MW}) &= (1.16 \times 10^{-3}) \mu^{\frac{1}{2}} \theta_{v,p}^{\frac{4}{3}} \left(T^{-\frac{1}{3}} - 0.015 \mu^{\frac{1}{4}} \right) - 18.42 \\ (\tau_{V-T}^{p-q})_{Park} &= \frac{1}{\bar{c}_p \sigma_{v,p} n_{p,q}} \end{aligned} \quad (6.7)$$

where P is the partial pressure of the colliding species, μ is the reduced molecular weight, \bar{c}_p is the average molecular speed ($\bar{c}_p = \sqrt{8R_p T_{tr}/\pi}$), $n_{p,q}$ is the number density of the colliding pair (v,p), and $\sigma_{v,p}$ is a characteristic collision cross-section defined as follows by Park (Park, 1993):

$$\sigma_{v,p} = 3 \cdot 10^{-21} \left(\frac{50000}{T_{tr}} \right)^2 \quad (6.8)$$

The total vibrational relaxation time τ_{V-T} calculated with this model for the N₂/argon mixture is plotted in Figure 82. VT relaxation is fast at high temperature but slows down considerably at low temperature. For the N₂/Ar HF case, the residence time in the tube is about 150 μ s. Therefore, we expect the two temperatures to be equilibrated at the entrance of the tube, and to deviate from each other when the gas temperature is below 5000 K.

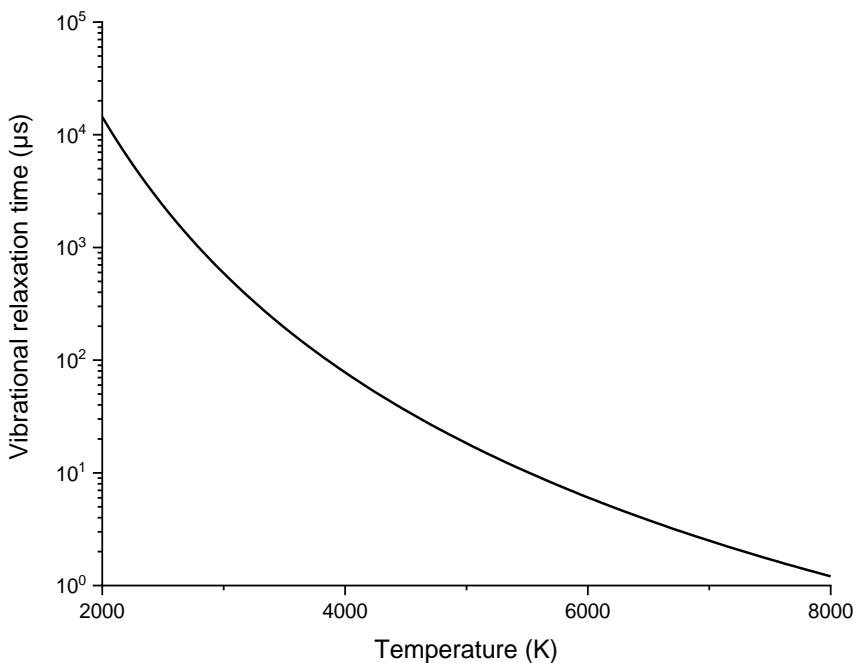


Figure 82: Vibrational relaxation time for the N₂/Ar LF case.

Let's now assume that a CFD code using a 2-temperature model can correctly predict the measured gas temperature evolution in the tube, i.e. the temperature measured using Raman spectroscopy T_{tr} . The vibrational-electronic temperature T_{ve} will relax toward T_{tr} according to the Landau-Teller equation. To calculate the evolution of T_{ve} , we perform a simple 0D computation along the centerline of the tube. Only three species are considered, argon, N and N₂, and we only look at the temperatures of nitrogen.

The velocity evolution along the axis of the tube was estimated based on the temperature profile and the mass flowrate (see Chapter 7 for more details). Because

the temperatures were only measured at three axial positions (0, 10 and 15 cm), an interpolation is necessary. This interpolation has an impact on the results. Three interpolated translational temperature profiles are considered in our calculations. Figure 83 shows the influence of this interpolation. Note that the case presented in the figure is only here to show the influence of the interpolation and does not represent a measurement. The calculated vibrational temperature profiles are also shown. Depending on the considered translational temperature profile, the vibrational temperature at the exit of the tube varies between 4800 and 5150 K while the translational temperature is 3000 K.

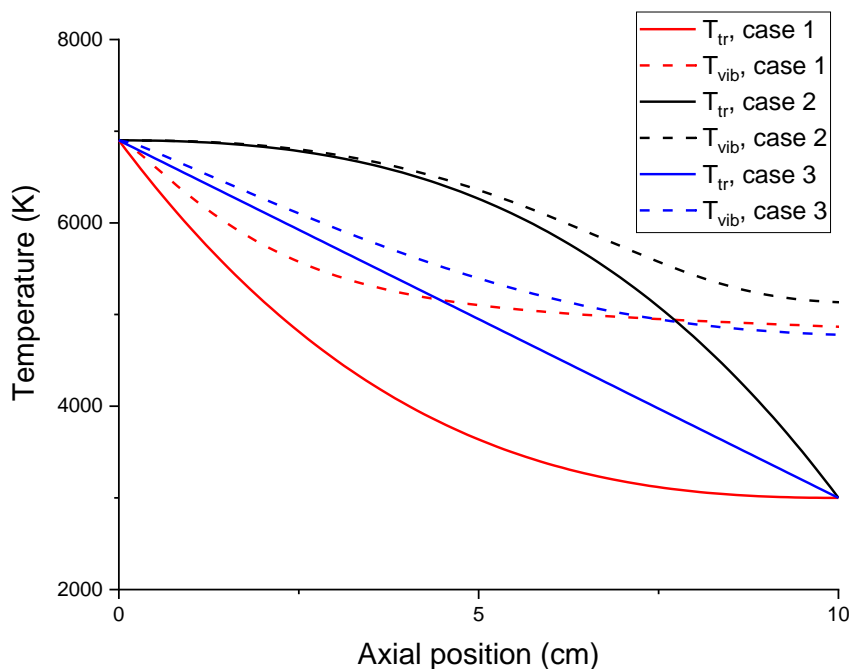


Figure 83: Vibrational temperature evolution (dashed lines) for three different interpolated gas temperature profiles (lines).

Finally, the temperature measurements also suffer from uncertainties. We took into account the uncertainties at the three axial locations measured to estimate the uncertainties of the final temperature T_{ve} . For example, we took a lower velocity bound with a nearly linear axial temperature interpolation, which results in a lower final T_{ve} (see Figure 83). This produces a lower bound for T_{ve} . The opposite assumptions were made to get the upper bound.

Calculations were performed for the N₂/Ar LF case along the tube centerline. The velocity was assumed to be 800 ± 100 m/s. Three different temperature

interpolations were taken to estimate the uncertainties. The input translational temperatures T_{tr} and the resulting vibrational temperatures T_{ve} are presented in Figure 84. Note that the temperatures at 0, 10, and 15 cm were imposed to match the measured temperatures using Raman spectroscopy at these locations. At 10 cm, $T_{ve} = 5950 \pm 200$ K is slightly higher than $T_{tr} = 5850 \pm 250$ K but the difference is higher at 15 cm with $T_{ve} = 5000 \pm 150$ K vs. $T_{tr} = 4600 \pm 200$ K.

The corresponding vibrational population distributions resulting from the 2-temperature model are presented in Figure 85 . The translational temperature is used to determine the gas number density and the vibrational-electronic temperature is used to compute the Boltzmann distribution of the vibronic levels of N₂. At 10 cm, the population computed using the 2-temperature model is lower than the measurements. At 15 cm, a better agreement is found for the first vibrational levels of N₂(B) and N₂(C). However, a large discrepancy is observed for the higher vibrational levels of N₂(B). This will be explained in Chapter 7.

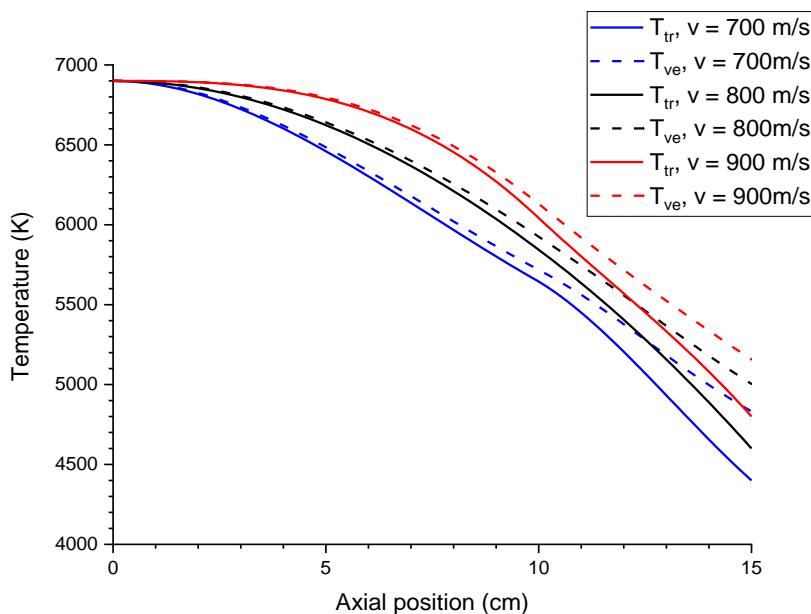


Figure 84: Translational temperature profiles (lines) used as input in the calculation and resulting vibrational temperature profiles (dashed) for the N₂/Ar LF case.

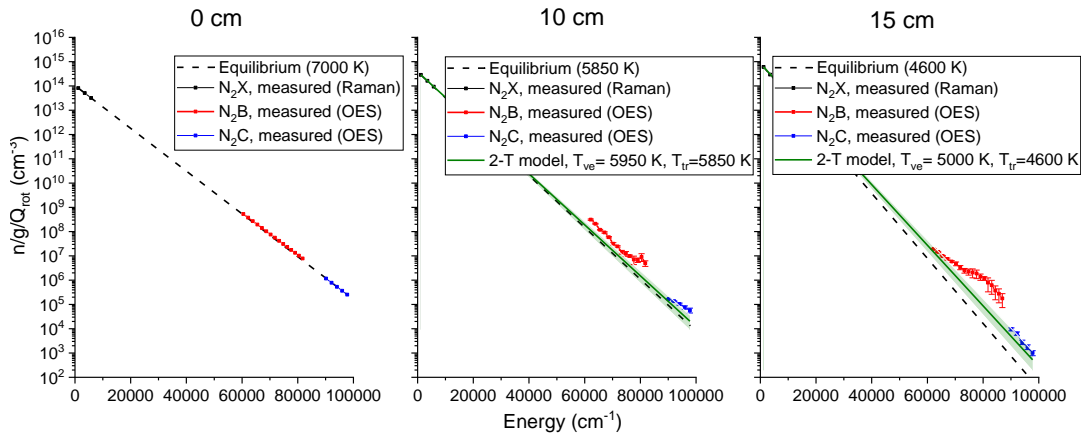


Figure 85: Comparison between the population distribution computed using a 2-temperature model (green) and the measurements for the N_2/Ar LF case. The green-shaded areas represent the uncertainty bands on the computed T_{ve} .

6.3.3 Total molecular radiation

For reentry applications, the relevant property of the plasma to predict is the radiative heat flux to the reentry capsule. In our case, radiation from 250 to 900 nm was measured. We integrate this radiation to get the total intensity of the plasma. This measured radiation is compared in Figure 86 with the radiation computed assuming equilibrium or obtained with the 2-temperature model. The plasma stays close to equilibrium at 10 cm and therefore, the total radiation is not too far from the measurements, even for the equilibrium model. However, at 15 cm, the measured radiation is about 7 times higher than equilibrium. This factor decreases to 1.5 when considering the 2-temperature model. Taking into account the uncertainties, the measured radiation actually differs from the results of the 2-temperature model by a factor from 0.75 to 3. Nevertheless, the predictions of the 2-temperature model are in better agreement with the measurements than the equilibrium model.

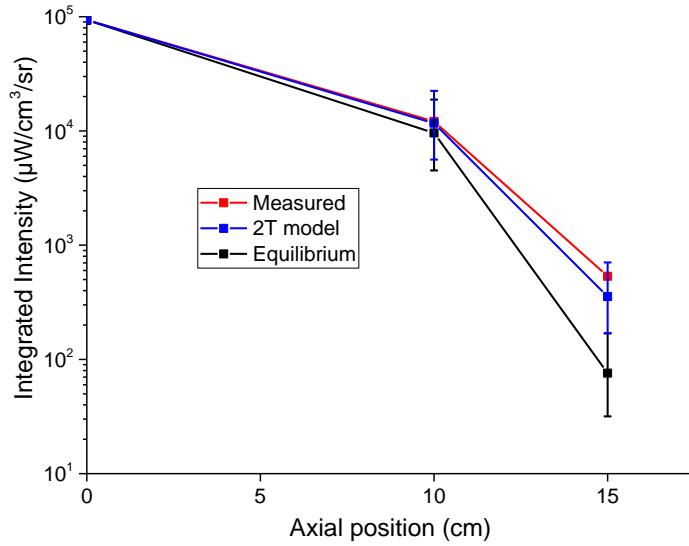


Figure 86: Integrated intensity between 250 and 900 nm. Red: measurements. Black: computed intensity assuming equilibrium at the measured gas temperature. Blue: computed intensity using the 2-temperature model.
 $\text{N}_2/\text{argon LF}$.

6.4 N_2/Ar high flowrate case

The plasma is comprised of 1.9 g/s of N_2 and 1.5 g/s of argon in this case. The plasma was found to be in equilibrium at the exit of the torch (0 cm). Spectra were measured between 250 and 900 nm, calibrated, and Abel-inverted. We present below the same analysis as the one performed for the LF case (section 6.3).

6.4.1 Emission spectra at 10 and 15 cm

The camera settings were changed to ensure a better signal-to -noise ratio and are summarized in Table 7. A 600 gr/mm grating was used with a FWHM of 0.3 nm (spectrometer slit width of 50 μm).

Table 7: Camera settings used for OES for the N_2/Ar LF case

Axial position	Below 450 nm		Above 450 nm	
	Integration time	Software accumulations	Integration time	Software accumulations

10 cm	150 ms	50	1 s	20
15 cm	500 ms	100	5 s	20

A comparison between computed spectra assuming equilibrium and nonequilibrium conditions and the measured one at 10 cm is presented in Figure 87. The measured spectra were Abel-inverted and the volumetric emission of the slab at $r = 0$ mm is plotted. The measured and equilibrium vibrational population distributions of $N_2(B)$, $N_2(C)$ and $N_2^+(B)$ used for the nonequilibrium SPECAIR calculations are also plotted. Note that 0.1% of H_2O and 0.1% of CO_2 were added in the chemical calculation but the OH, NH and CN transitions were considered as unknown in the minimization algorithm. The measured spectra are much more intense than the equilibrium spectra, indicating a large overpopulation of the excited states of nitrogen. A comparison of the computed and measured spectra at the exit of the 15-cm tube is presented in Figure 88. These spectra correspond to the volumetric emission of the center of the plasma ($r = 0$ mm). The plasma is even further away from equilibrium and the excited states of nitrogen are more overpopulated. Similar fits were made at each radial position at the exit of both the 10 and 15 cm tubes. For sake of clarity, only the case $r = 0$ mm is presented. Note also that the distribution of the vibrational levels of $N_2(B)$ is non-Boltzmann at both 10 and 15 cm. The level $v = 13$ appears to be the most overpopulated. This was already observed by Gessman (Gessman, 2000) – and will be discussed in Chapter 7.

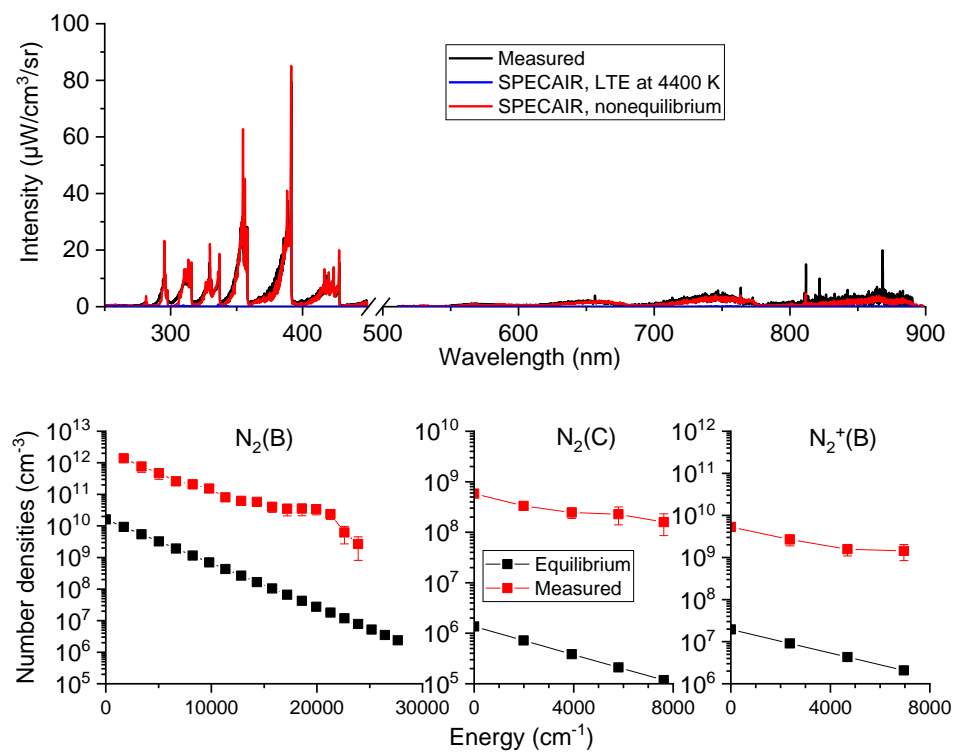


Figure 87. Top: measured and computed spectra using SPECAIR assuming equilibrium or nonequilibrium conditions at the exit of the 10-cm tube for the N_2/Ar HF case. Bottom: measured and equilibrium vibrational densities of $\text{N}_2(\text{B})$, $\text{N}_2(\text{C})$, and $\text{N}_2^+(\text{B})$ used in the SPECAIR calculations.

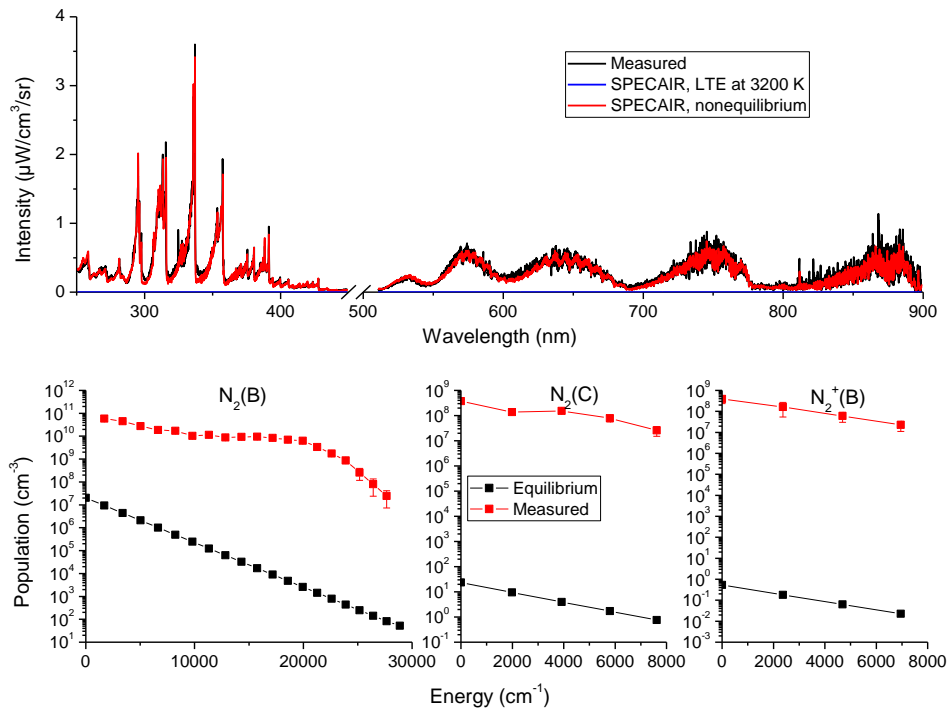


Figure 88. Top: measured and computed spectra using SPECAIR assuming equilibrium or nonequilibrium conditions at the exit of a 15-cm tube for the N_2/Ar HF case. Bottom: measured and equilibrium vibrational densities of $\text{N}_2(\text{B})$, $\text{N}_2(\text{C})$, and $\text{N}_2^+(\text{B})$ used in the SPECAIR calculations.

6.4.2 Measured densities of $\text{N}_2(\text{B})$, $\text{N}_2(\text{C})$, and $\text{N}_2^+(\text{B})$ at 10 and 15 cm.

6.4.2.1 Radial distributions

The vibrational population distributions of $\text{N}_2(\text{B})$, $\text{N}_2(\text{C})$, and $\text{N}_2^+(\text{B})$ at various radial locations are presented in Figure 89, Figure 90 and Figure 91, respectively. The densities of the vibrational levels do not change significantly with the radial position – i.e. the density profiles remain relatively flat. However, the temperature decreases rapidly with the radius. Therefore, the overpopulation of the vibrational levels increases with the radius. The plasma is then further away from equilibrium conditions close to the cold wall. Note that the equilibrium densities are only plotted out to $r = 2$ mm, which is the last location at which the Raman temperature measurements were performed.

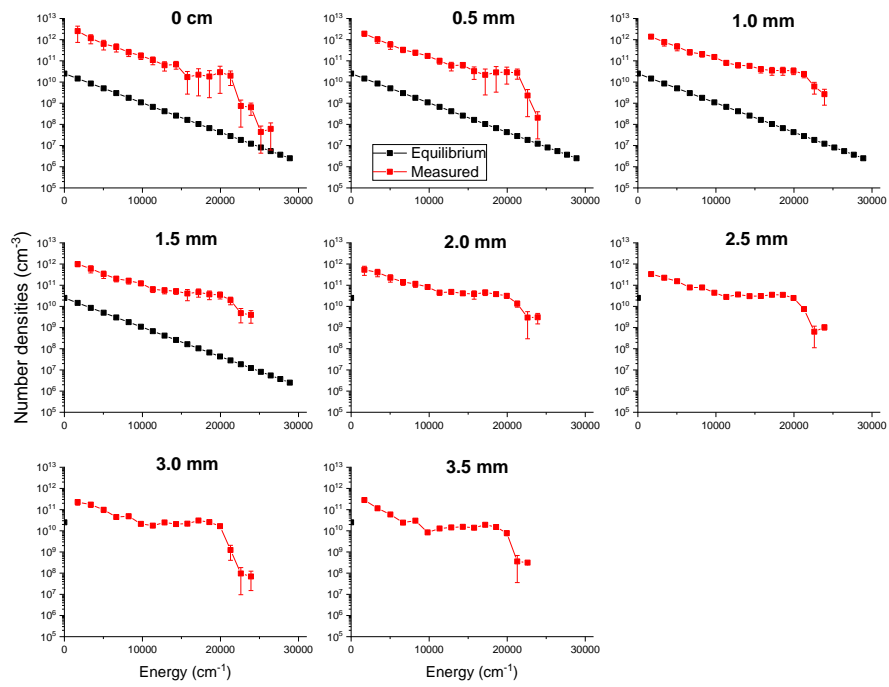


Figure 89: Radial distribution of measured and equilibrium densities of $\text{N}_2(\text{B})$ for the N_2/Ar HF case at the exit of the 10-cm tube.

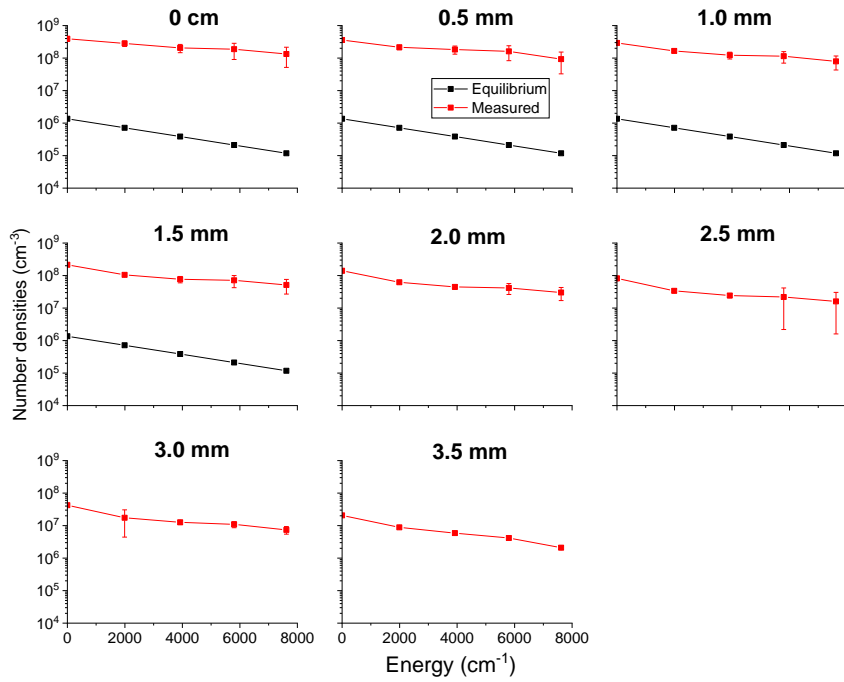


Figure 90: Radial distribution of measured and equilibrium densities of $\text{N}_2(\text{C})$ for the N_2/Ar HF case at the exit of the 10-cm tube.

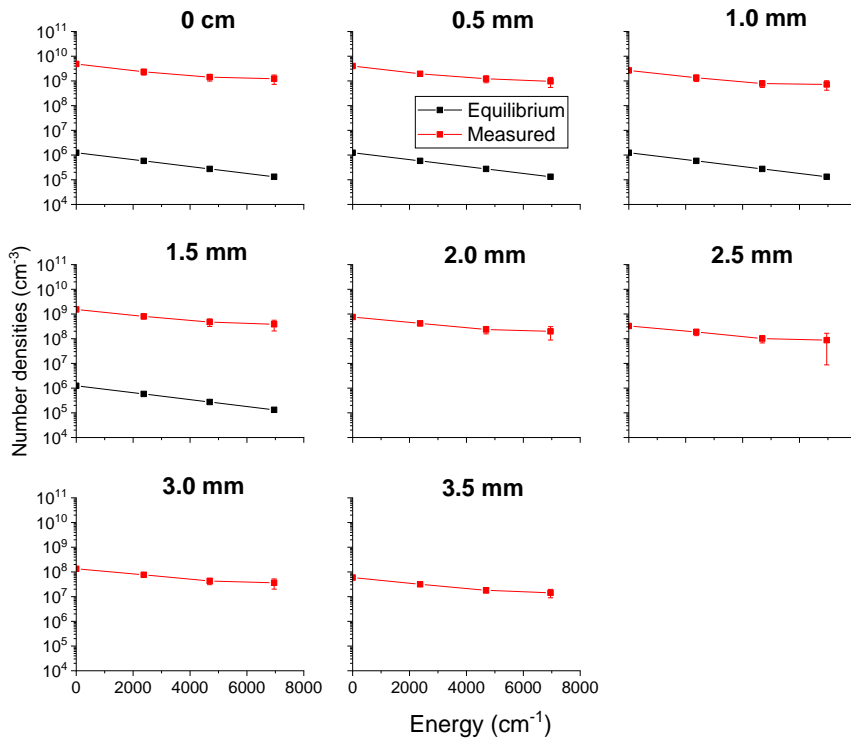


Figure 91: Radial distribution of measured and equilibrium densities of $\text{N}_2^+(\text{B})$ for the N_2/Ar HF case at the exit of the 10-cm tube.

The vibrational densities measured at 15 cm for these three states are plotted in Figure 92, Figure 93 and Figure 94. The trend observed at 10 cm is also observed here at 15 cm. The populations of these states are almost constant radially. Note that the level $v = 13$ of $\text{N}_2(\text{B})$ is always the most overpopulated level at each radial position. The vibrational population distribution of $\text{N}_2(\text{C})$ and $\text{N}_2^+(\text{B})$ is close to a Boltzmann distribution when taking into account the error bars.

These quantitative nonequilibrium density measurements of excited states of N_2 in a simple configuration represent a good database for testing the coupling between CFD and kinetic codes. Also, because the densities of the excited molecular states are nearly constant across the tube diameter, we believe that a 1D simulation may suffice for comparison with these measurements.

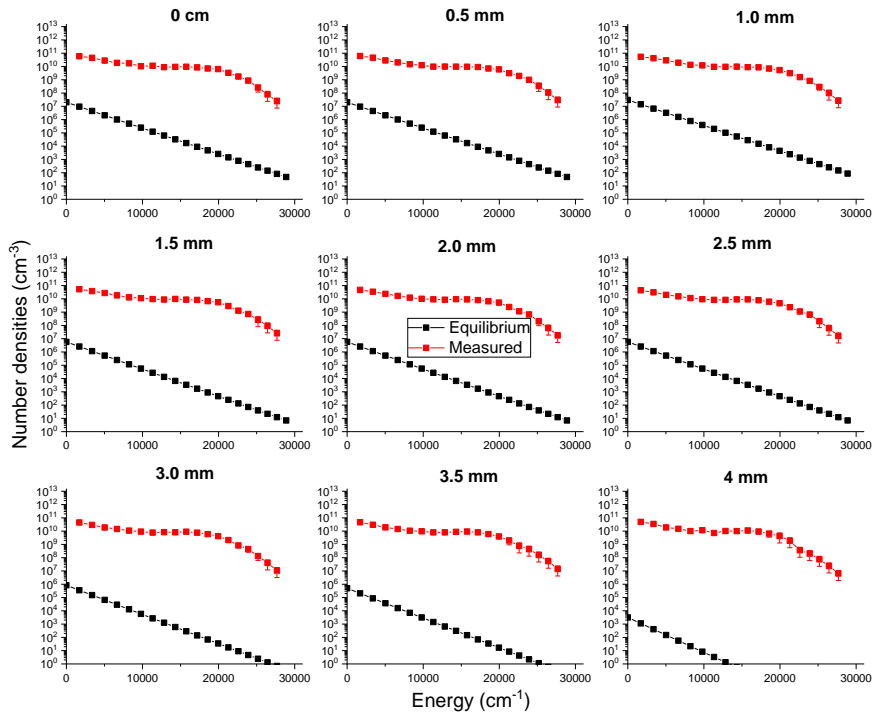


Figure 92: Radial distribution of measured and equilibrium densities of $\text{N}_2(\text{B})$ for the N_2/Ar HF case at the exit of the 15-cm tube.

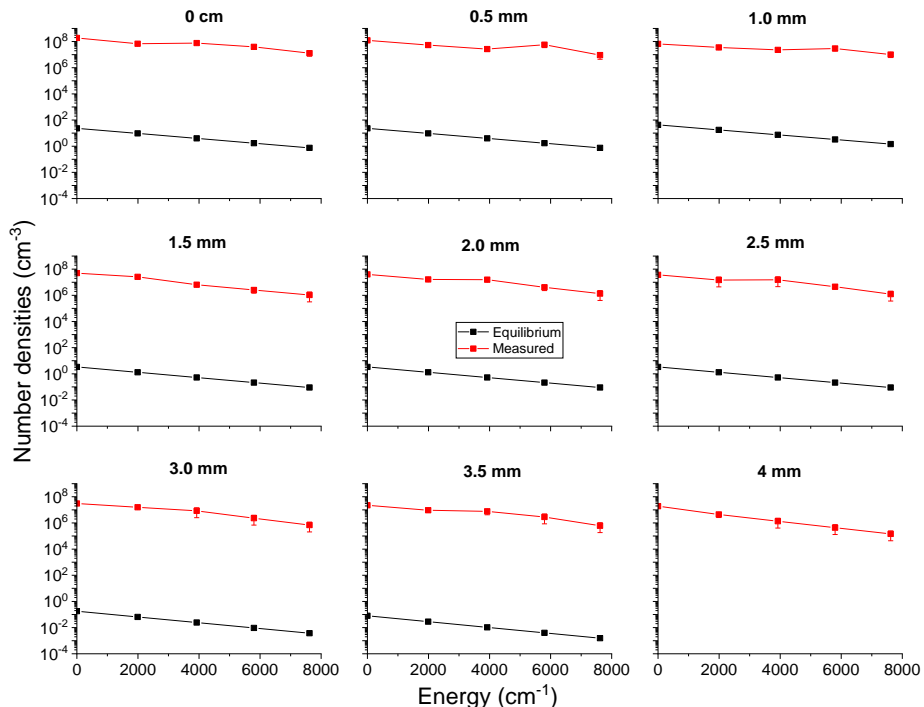


Figure 93: Radial distribution of measured and equilibrium densities of $\text{N}_2(\text{C})$ for the N_2/Ar HF case at the exit of the 15-cm tube.

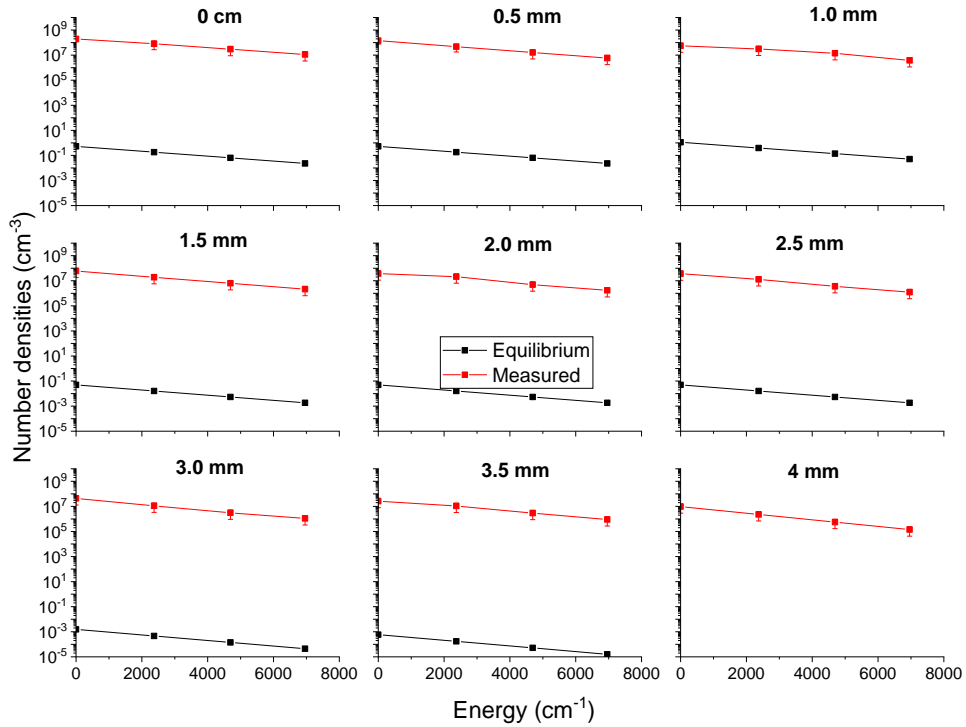


Figure 94: Radial distribution of measured and equilibrium densities of $\text{N}_2^+(\text{B})$ for the N_2/Ar HF case at the exit of the 15-cm tube.

6.4.2.2 Boltzmann diagrams

We present here the analysis of the N_2/Ar HF case using the 2-temperature modeling approach presented in section 6.3.2.2 for the N_2/Ar LF case. The different translational temperature profiles used as inputs and the resulting vibronic temperature profiles are plotted in Figure 95. Note that these profiles are similar to the one predicted by CFD simulations presented in Chapter 5. The vibrational temperature is much higher than the translational temperature at both 10 and 15 cm. At 15 cm, the predicted vibrational temperature is $T_{ve} = 4700 \pm 300$ K, which is significantly higher than $T_{tr} = 3150 \pm 150$ K.

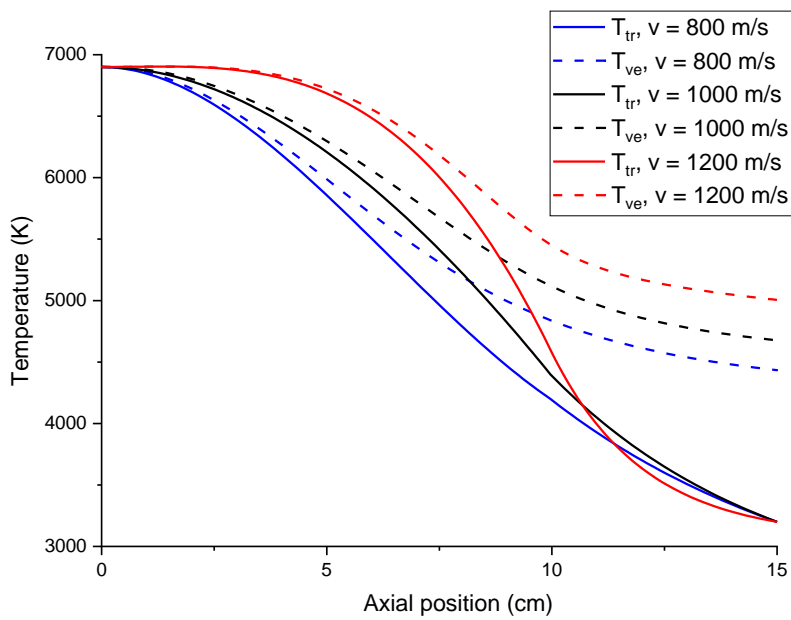


Figure 95: Translational temperature profiles (lines) used as input in the calculation and the resulting vibrational temperature (dashed) for the N₂/Ar HF case.

The measured vibrational population distributions of N₂(X), N₂(B), and N₂(C) are presented in the Boltzmann diagram shown in Figure 96. The calculated equilibrium distributions and those predicted using the 2-temperature model are also plotted. The equilibrium densities are lower than the measured densities by several orders of magnitude. Note that the vibrational temperature predicted by the 2-temperature model is higher than the maximum vibrational temperature of N₂(X) determined using Raman spectroscopy (3300 K, see Chapter 3). The 2-temperature model also underpredicts the measured densities at 10 cm, although to a smaller extent than the equilibrium model, but is in fairly good agreement for the first levels of N₂(B) at 15 cm. Overall, the 2-temperature model is much closer to the measurements than the equilibrium model, but still underpredicts the measured densities. Note that the most of the vibronic energy of the 2T model, defined in Eq (6.6), is stored into the vibration (i.e. in the E_{vib} term). This may indicate that the high-lying vibrational levels of N₂(X) are highly overpopulated which could affect the density of N₂(B) as explained by (Plain, et al., 1985). Note also that the measured distribution is non-Boltzmann. A model using a vibrational temperature assumes a Boltzmann distribution by definition and therefore cannot predict the measured distribution. Only a vibrational specific model could. Note

also the continuity between the $\text{N}_2(\text{B})$ and $\text{N}_2(\text{C})$ population distributions. This may indicate that V-V' or electronic excitation reactions between $\text{N}_2(\text{B})$ and $\text{N}_2(\text{C})$ are fast enough and the collisions at atmospheric pressure between these two species are rapid enough to equilibrate their densities. This could be explained as $\text{N}_2(\text{B})$ and $\text{N}_2(\text{C})$ have the same symmetry (II) and the same spin (1) making their V-V' reactions efficient as explained by (Herzberg, 1950).

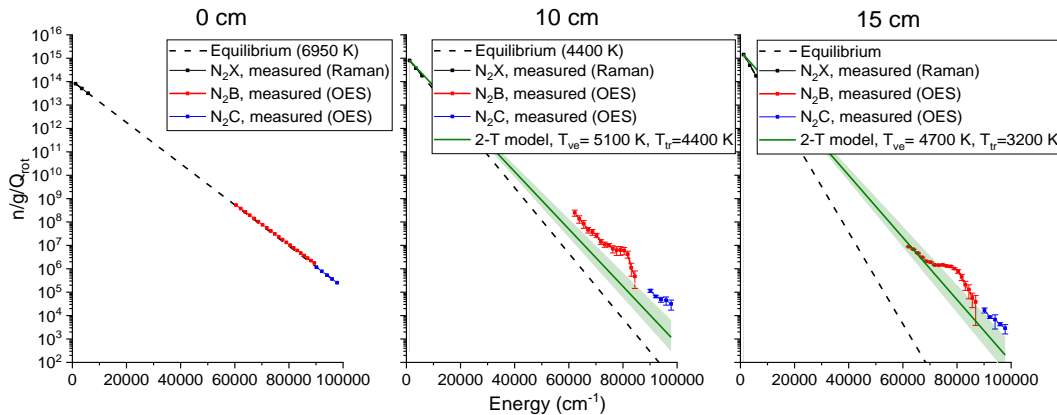


Figure 96: Comparison between the population distributions computed using the 2-Temperature model (green), the equilibrium model (dashed line) and the measurements for the N_2/Ar LF case. The green-shaded areas represent the uncertainty bands on the computed T_{ve} .

6.4.3 Total molecular radiation

The measured volumetric emission from the center of the plasma was integrated between 250 to 900 nm to compare the total radiation in the UV-visible region with the predictions of the equilibrium and 2-temperature models. The results are presented in Figure 97. As expected, the measured intensity is much higher than the equilibrium value. At 10 cm, the equilibrium radiation is 250 times smaller than the measurements, and about 100,000 times smaller than the measurements at 15 cm. The 2-temperature model improves the agreement with an underprediction by a factor of approximately 13 at 10 cm and about 6 at 15 cm. Despite the relatively large uncertainties, the 2-temperature model is clearly below the experimental values. A CFD code using only a 2-temperature model is therefore unable to correctly predict the radiation coming from such recombining plasma flows. This is an important consideration for reentry applications.

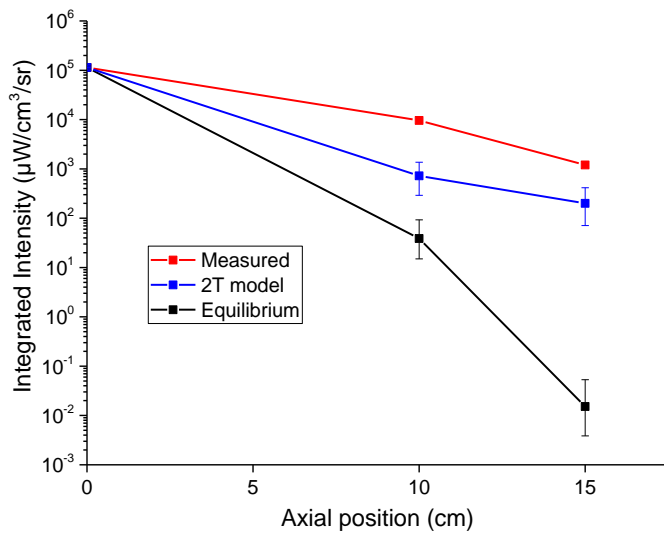


Figure 97: Integrated intensity between 250 and 900 nm. Red: measurements. Blue: computed intensity using the 2-temperature model. Black: computed intensity assuming equilibrium at the measured gas temperature. N₂/Ar HF.

6.5 Conclusions

Optical emission spectroscopy was used to measure spectra between 250 and 900 nm for the three plasma flows of interest: Air/Ar, N₂/Ar LF, and N₂/Ar HF. The Air/Ar plasma radiation was found to be in equilibrium. This confirms previous measurements of Gessman *et al* (Gessman, et al., 1997) (Gessman, 2000), who showed that the presence of oxygen ensures a fast recombination of nitrogen atoms via the reaction N + O + M → NO + M. In nitrogen or nitrogen/argon plasmas, the recombination of atomic nitrogen is slower, and as a result chemical nonequilibrium is more likely to be obtained. This was observed in both N₂/Ar recombination cases.

For these nonequilibrium cases, the measured radiation was found to be higher than its corresponding equilibrium value at the temperature measured using Raman spectroscopy. The plasma stayed relatively close to equilibrium until 10 cm for the LF case and was far from equilibrium for the high flowrate cases. The level of nonequilibrium increases with the axial position. The resulting radiation comes from an overpopulation of N₂ excited states. Three states were accurately measured in the nitrogen mixtures: N₂(B), N₂(C) and N₂⁺(B). Their vibrational level populations were measured at various axial and radial positions. These data are

useful to test CFD codes coupled with kinetic codes because the inlet conditions are well characterized (equilibrium at known temperature and pressure) and the geometry is relatively simple. Also, the densities of these excited states were found to be relatively constant with the radial position. These results could therefore be used to test quasi-steady state (QSS) codes taking as input the centerline temperature and comparing the experimental and predicted populations of excited states of nitrogen at the center of the plasma as was done by (Laux, et al., 2012). The distribution of the vibrational levels of $N_2(B)$ was also found to be non-Boltzmann. For this reason, a vibrational specific kinetic model is needed to predict the experimental results.

Finally, the measured radiation was integrated over the measured range of wavelength. This allows to get the radiative heat flux which is the important property to model for reentry applications. Hypersonic CFD codes used for reentry applications often used multiple temperature models (Candler, 1988) (Gollan, 2008) (Casseau, et al., 2016). We tried to reproduce the measured results by using a 2-temperature model taking as input the measured translational temperatures. Then, we used the Landau-Teller equation to relax the vibrational temperature to the translational one. As shown in Figure 83, the vibrational temperature stays elevated relative to the gas temperature. We compared the measured radiation with its equilibrium value and with results from the 2-temperature model. The measured radiation was found to be up to 100,000 times higher than its equilibrium values. Even the 2-temperature model underestimated the measured radiation by an order of magnitude, though the agreement was much better than the equilibrium calculation. This is an important consideration for reentry applications as the use of such model is not sufficient to correctly predict the afterbody radiation. Note also that due to the non-Boltzmann distribution of $N_2(B)$, only a vibrational specific kinetic model coupled to a CFD code will be able to correctly predict the radiation of recombining flows.

Chapter 7 Atomic Radiation

In this Chapter, we present OES measurements of the densities of several electronic states of N atoms and of the total radiation emitted by the excited states of these atoms. These densities were determined from lines in the VUV, visible, and NIR. These measurements were performed to determine the population distribution of the electronic states in a recombining plasma in order to validate CR codes for atomic nitrogen. Comparisons with the Boltzmann and Saha-Boltzmann distributions are also presented.

7.1 Introduction

Recent results showed that the atomic lines in the VUV region are the main source of radiation in the afterbody region for Earth entry at super-orbital velocities ($v > 10 \text{ km/s}$). For Stardust conditions ($v = 11.69 \text{ km/s}$) (Johnston & Brandis, 2015), it was shown that 55% of the total radiation comes from only two atomic nitrogen lines in the VUV at 149 and 174 nm (see Figure 98). The high contribution of these two lines is explained by the non-Boltzmann distribution of excited N atoms predicted by (Johnston & Brandis, 2015) and presented in Figure 98. The upper state of the transitions at 149 and 174 nm corresponds to the 5th level in the graph and is indeed overpopulated by almost five orders of magnitude relative to the Boltzmann distribution. Note that the populations of the excited states above 10 eV are close to the Saha-Boltzmann distribution, which corresponds to partial equilibrium with the free electrons at the electron temperature. The type of non-equilibrium distribution plotted in Figure 98 is typical of recombining plasmas but has never been measured in high temperature conditions.

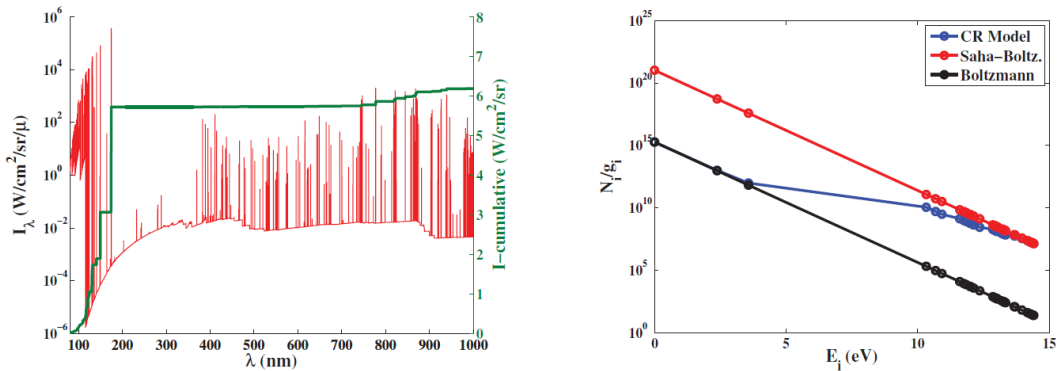


Figure 98. Left: Typical line-of-sight spectrum predicted in the afterbody region for Earth entry (Stardust conditions). Right: distribution of the electronic states of atomic nitrogen used to calculate the spectrum shown on the left. Figures taken from (Johnston & Brandis, 2015).

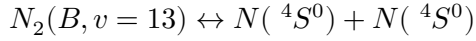
The goal of the present chapter is to provide measurements of the population distribution of excited N atoms in the nonequilibrium recombining plasma cases investigated in this thesis. These data are expected to be useful to assess and validate the kinetic codes used for atmospheric entry. First, we will present indirect measurements of the first two electronic states of atomic nitrogen. Then, we will present measurements of higher electronic states of nitrogen. The electron density, which is needed to determine the Saha-Boltzmann distribution limit presented in Figure 98, will also be measured. Finally, the entire distribution of excited N atoms will be plotted for the different recombining plasma cases. A list of the electronic states of N measured in this thesis is given in Table 8.

7.2 N(${}^4S^0$) density measurements

7.2.1 Method

To determine the population of ground state atomic nitrogen, N(${}^4S^0$), we resort to the indirect method presented by (Laux, et al., 2012). The method is indirect because it relies on the emission of nitrogen molecules in vibrational level $v=13$ of electronic state $B^3\Pi_g$, noted N₂(B, $v=13$). The vibrational level $v=13$ of N₂(B) predissociates spontaneously into N(${}^4S^0$) atoms. Conversely, two N(${}^4S^0$) atoms can recombine into N₂(B, $v=13$) via the process of inverse predissociation (Partridge, et al., 1988). Using a detailed collisional-radiative model for conditions similar to those investigated here, it was shown by (Laux, et al., 2012) that the reactions of

predisociation and inverse predisociation are the dominant production and depletion mechanisms of $N_2(B, v=13)$. As a result, a partial equilibrium exists between $N_2(B, v=13)$ and $N(^4S^0)$ atoms, i.e. :



We thus obtain the following equation:

$$k_{diss} n_{N_2(B, v=13)} \approx k_{inv-diss} n_{N(^4S)}^2 \quad (7.1)$$

where k_{diss} and $k_{inv-diss}$ are the predisociation and inverse predisociation reaction rates.

Under equilibrium conditions, the following relation always holds:

$$k_{diss} n_{N_2(B, v=13)}^* = k_{inv-diss} (n_{N(^4S)}^*)^2 \quad (7.2)$$

where the * superscript denotes equilibrium densities

Combining Eqns (7.1) and (7.2), the overpopulation of atomic nitrogen with respect to equilibrium can be expressed as a function of the overpopulation of $N_2(B, v=13)$, $\rho_{N_2, B, v=13}$, via the following equation:

$$\rho_{N(^4S^0)} = \sqrt{\rho_{N_2, B, v=13}} \quad (7.3)$$

The overpopulation of $N_2(B, v=13)$ is determined as the ratio of the density of $N_2(B, v=13)$, measured in Chapter 6, to the equilibrium density of $N_2(B, v=13)$, which can be determined with knowledge of the temperature and the pressure. This method can thus be used to determine the $N(^4S^0)$ density. This method was previously used in Refs (Gessman, 2000) (Winter, et al., 2018). We will apply it here to determine the $N(^4S^0)$ density for the two N_2/Ar cases.

7.2.2 Results

Figure 99 shows the radial profiles of atomic nitrogen density obtained with the method outlined in the previous section for the N_2/Ar LF case at 0, 10, and 15 cm. The figure also shows the calculated densities corresponding to equilibrium at the measured gas temperature. We see that the measured N densities decrease slowly with the axial distance, by a factor less than 4 from 0 to 15 cm. If the plasma were

in equilibrium, they would decrease by a factor of 40. Thus, the density of atomic nitrogen is partly frozen in the recombination tube.

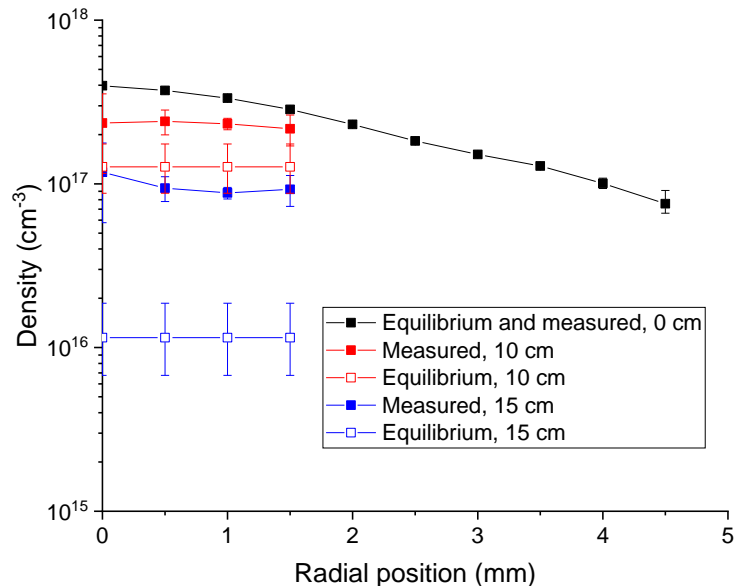


Figure 99: Measured radial profiles of nitrogen atom density at 0, 10, and 15 cm, and comparison with the equilibrium density profiles calculated at the temperature measured using Raman spectroscopy. N₂/Ar plasma at low mass flowrate.

Results for the N₂/Ar HF case are presented in Figure 100. We see that the population of N is not only constant radially as discussed before, but also decreases slowly with axial distance beyond 10 cm.

We can compare these results with those obtained by Gessman *et al.* for similar (but not identical plasma conditions) (Gessman, 2000). Gessman *et al.* measured a N density of $(1.6 \pm 0.3) \cdot 10^{17} \text{ cm}^{-3}$ at the exit of the 15 cm tube, whereas we obtain $(7.9 \pm 1.3) \cdot 10^{16} \text{ cm}^3$. The factor 2 difference is attributed to a difference in the injection mode (80% radial/20% swirl injection in our case against 60%/40% in Gessman experiments) which affects the shape of the inlet temperature profiles.

At 15 cm, the atomic nitrogen density is about three orders of magnitude larger than the equilibrium density. This means that a large portion of the plasma energy is stored into unrec combined N atoms, which could explain the low temperature measured.

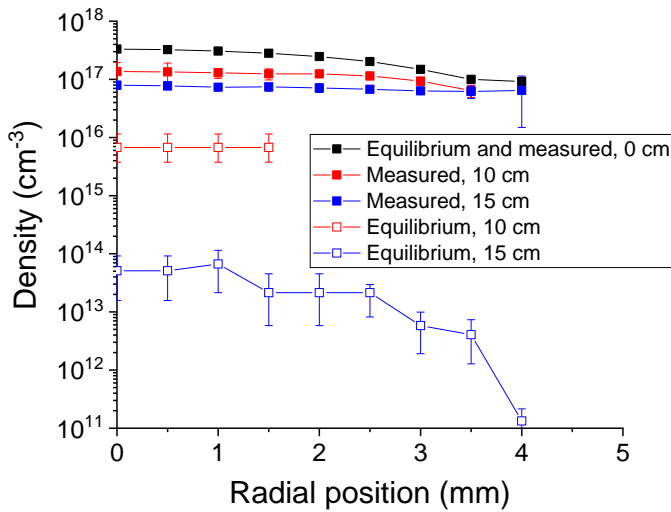
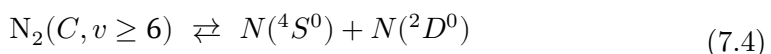


Figure 100: Measured radial profiles of nitrogen atom density at 0, 10, and 15 cm, and comparison with the equilibrium density profiles calculated at the temperature measured using Raman spectroscopy. N₂/Ar plasma case at high flow rate.

7.3 N(²D⁰) density measurements

The density of N(²D⁰) was determined using a technique similar to the one presented for N(⁴S⁰). According to Polak (Polak, et al., 1972) and Lewis (Lewis, et al., 2008), the vibrational levels $v \geq 6$ of N₂(C) predissociate into N(⁴S⁰) and N(²D⁰). Therefore, there is a partial equilibrium between the vibrational levels $v \geq 6$ and the atomic states:



(Tanaka, et al., 1959) also experimentally observed that N₂(C,v=4) can be populated via inverse predissociation. In Chapter 6, we presented measurements of the densities of levels $v \leq 4$ of N₂(C). We then obtain the following relation, in a similar way than explained in section 7.2, where ρ denotes the overpopulation of the various states:

$$\rho_{N_2(C,v=4)} = \rho_{N(^4S^0)}\rho_{N(^2D^0)} \quad (7.5)$$

The overpopulation of $N(^4S^0)$ was determined in Section 7.2 as $\rho_{N(^4S^0)} = \sqrt{\rho_{N_2(B,v=13)}}$. The overpopulation of $N_2(C,v=4)$ was measured in Chapter 6. The density of $N(^2D^0)$ can then be determined from the following relation:

$$n_{N(^2D)}^{meas} = \frac{\rho_{N_2(C,v=4)}}{\sqrt{\rho_{N_2(B,v=13)}}} n_{N(^2D)}^{eq} \quad (7.6)$$

where $n_{N(^2D)}^{eq}$ is the density of $N(^2D^0)$ in LTE at the gas temperature.

An alternative method to estimate the density of $N(^2D^0)$ is to consider that it is in partial equilibrium at the gas temperature with the ground state $N(^4S^0)$. This is generally what CR models of recombining nitrogen flows predict for the first 3 states of N, see for example Refs. (Johnston & Brandis, 2015) (Lemal, et al., 2012).

Finally, we can also calculate the $N(^2D^0)$ density by assuming LTE at the gas temperature.

Figure 101 shows a comparison of the $N(^2D^0)$ radial density profiles obtained for the N_2/Ar LF case using the three methods that were just described:

1. Radial density profile of $N(^2D^0)$ determined using Eq (7.6) – we will refer to these values as the “Equilibrated with $N_2(C)$ ” values
2. Radial density profile of $N(^2D^0)$ calculated assuming partial equilibrium with the ground state population (obtained in the previous section) – referred as “Equilibrated with $N(^4S)$ ”.
3. Radial density profile of $N(^2D^0)$ calculated by assuming LTE at the gas temperature (obtained from the Raman measurements).

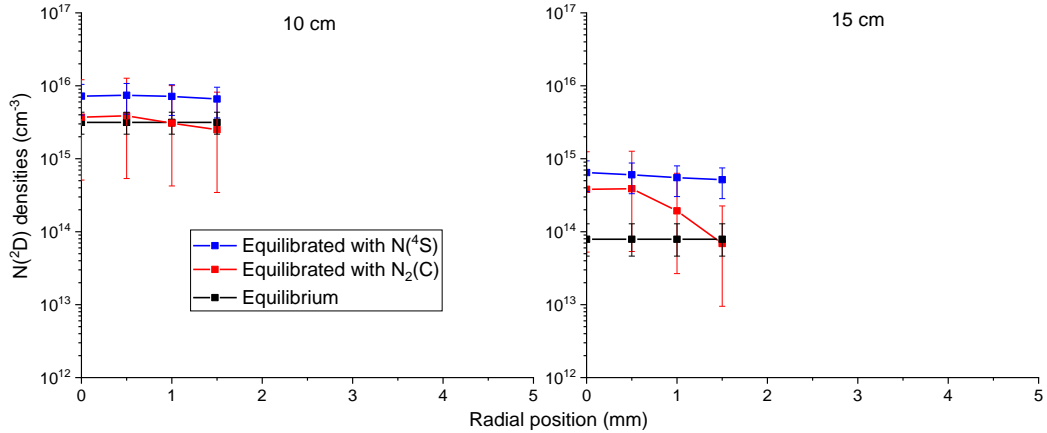


Figure 101: Radial density profiles of $N(^2D^0)$ at 10 cm (left) and 15 cm (right) for the N_2/Ar LF case. Red: measured. Blue: assuming partial equilibrium with $N(^4S^0)$ at the gas temperature. Black: assuming LTE at the gas temperature.

Figure 102 shows the same comparison for the N_2/Ar HF case. The largest uncertainties are for the measured densities determined by assuming partial equilibrium between $N_2(C,v=4)$ and the predissociated states. This is because of the relatively high uncertainties (60-70%) on the density of $N_2(C,v=4)$ combined with the ~30% uncertainties on the density of $N_2(B,v=13)$ combined with the 200% uncertainties on the equilibrium density (due to the uncertainty on the temperature).

In the following sections, we will take the $N(^2D^0)$ densities obtained by considering partial equilibrium with $N(^4S^0)$. Note that despite the large error bars, the densities of $N(^2D^0)$ determined in this section are consistent with the densities assuming partial equilibrium with $N(^4S^0)$. Finally, this assumption will be proven in section 7.6.

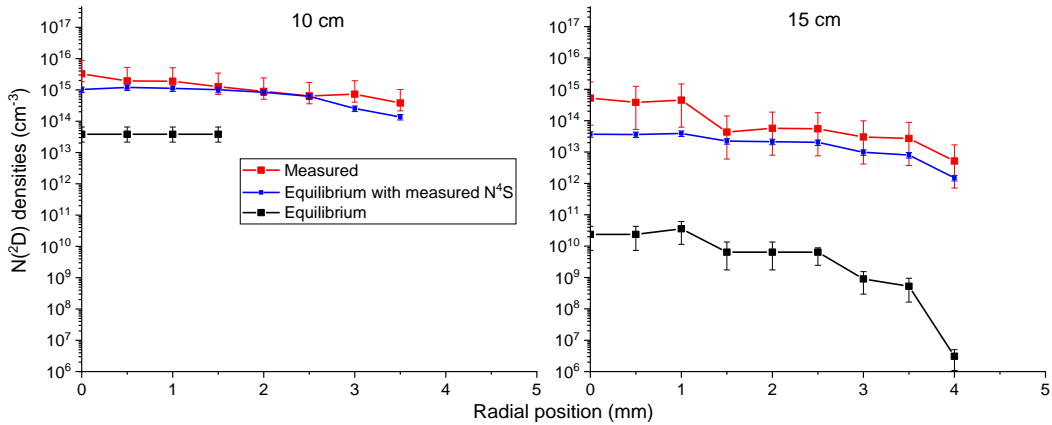


Figure 102: Radial density profiles of $N(^2D^0)$ at 10 cm (left) and 15 cm (right) for the N_2/Ar HF case. Red: measured. Blue: assuming partial equilibrium with $N(^4S^0)$ at the gas temperature. Black: assuming LTE at the gas temperature.

7.4 Excited N-atoms density measurements

7.4.1 Considered levels and measurement technique

Optical emission spectroscopy was used from the VUV to the NIR region to measure atomic lines. The results from the UV to the NIR were already presented in Chapter 6 where we focused on molecular radiation. Several atomic lines were visible in these spectra and were found to be optically thin according to the SPECAIR calculations. Therefore, the emissivity of a given atomic line is proportional of the density n_u of the upper state of the transition and can be determined using the following relation:

$$I = n_u \frac{A_{ul}}{4\pi} (\epsilon_u - \epsilon_l) \quad (7.7)$$

where A_{ul} is the Einstein coefficient, ϵ_u and ϵ_l are the energies of the upper and lower states of the considered transition, respectively. Experimentally, I corresponds to the Abel-inverted measured intensity, integrated over wavelength.

To simplify calculations, collisional-radiative codes usually group closely spaced energy states into a single level with a global degeneracy. An example of groupings for the first states of atomic nitrogen is given in Table 8.

Table 8: Grouped electronic levels of atomic N considered in collisional-radiative models with their names, energies, and degeneracies taken from (Lemal, 2013).

Label	States	Energy (cm ⁻¹)	Degeneracy
'1'	N(⁴ S ⁰)	0.0	4
'2'	N(² D ⁰)	19228.0	10
'3'	N(² P ⁰)	28840.0	6
'4'	N(⁴ P)	83337.0	12
'5'	N(² P), N(⁴ P)	87488.0	18
'6'	N(⁴ D ⁰), N(⁴ P ⁰), N(⁴ S ⁰)	95276.0	36
'7'	N(² S ⁰), N(² D ⁰), N(² P ⁰), N(² D)	96793.0	18

In this section, we also present measurements of atomic lines in the VUV. In this region, several lines are optically thick and the relation in Eq. (7.7) no longer holds. The intensity of the transition is dependent on both the lower and upper state of the transition. Another technique was therefore required to obtain measurements of the upper and lower states involved. This approach is explained in the next section. The atomic lines measured in this work are presented in Table 9 with their respective spectroscopic constants and the label of the corresponding grouped level (see Table 8).

Table 9: Spectroscopic constants for the observed atomic lines of nitrogen.
Data taken from the NIST database. The numbers in the quotation marks
correspond to the label of the grouped levels considered.

Wavelength (nm)	$\epsilon_u(cm^{-1})$	g_u	$\epsilon_l(cm^{-1})$	$A_{ul}(10^7 s^{-1})$	Grouping Labels (upper → lower)
149.26	86220.510	4	19224.46	34.3	‘5’ → ‘2’
149.47	86220.510	4	19233.18	34.6	‘5’ → ‘2’
174.27	86220.510	4	28839.306	10.5	‘5’ → ‘3’
174.525	86137.35	2	28838.92	8.35	‘5’ → ‘3’
746.83	96750.84	4	83364.62	1.96	‘7’ → ‘4’
821.07	95493.69	4	83317.83	0.523	‘6’ → ‘4’
821.63	95532.15	6	83364.62	2.26	‘6’ → ‘4’
822.31	95475.31	2	83317.83	2.62	‘6’ → ‘4’
824.24	95493.69	4	83364.62	1.31	‘6’ → ‘4’
859.4	97770.18	2	86137.35	2.09	‘7’ → ‘5’
862.92	97805.84	4	86220.51	2.67	‘7’ → ‘5’
868.03	94881.82	8	83364.62	2.53	‘6’ → ‘4’
870.33	94770.88	2	83284.07	2	‘6’ → ‘4’
871.17	94793.49	4	83317.83	2.16	‘6’ → ‘4’

In the visible/NIR region, levels ‘6’ and ‘7’ can be measured using the previously discussed approach because the transitions are optically thin. The VUV gives access to the upper level ‘5’ and to the lower levels ‘2’ and ‘3’. Level ‘1’, which is the ground state, has already been indirectly measured in section 7.2. Therefore, the densities of all levels from ‘1’ to ‘7’ can be measured, with the exception of level ‘4’. The density of level ‘2’ was also estimated in section 7.3 but it should be

experimentally confirmed. In the next section, we present the VUV optical setup developed during the thesis and the analysis performed to determine the densities of the lower and upper states of the transitions.

7.4.2 VUV optical emission spectroscopy setup

The VUV spectroscopy setup is presented in Figure 101. The VUV spectrometer is a McPherson (Model 218) spectrometer. The grating has 2400 grooves/mm and is blazed at 150 nm. The camera is a PIMAX II with a UV intensifier. An imaging box made of steel is attached to the spectrometer. Two spherical mirrors of 50 cm focal length were inserted into this box and used to image the slit onto the torch - the spectrometer slit and torch are located at the focus of each mirror and there is therefore no image magnification. These mirrors were coated with the Acton Optics #1200 coating for 120 nm. The system is placed under vacuum using a roughing pump and a turbopump (80 L/s pumping speed). The pressure is between $1 - 5 \cdot 10^{-5}$ Torr in the system for all tests. Note that the level of vacuum was found to not be the limiting parameter of the measured signal and therefore any values of pressure below 10^{-4} Torr were sufficient to prevent absorption in the optical path. The spectra are calibrated using the argon mini-arc (of radiance traceable to NIST standards (Klose, et al., 1988)) that was also used to calibrate spectra in the UV region between 200 and 400 nm. Because the plasma is not optically thin in the VUV, we did not Abel-invert the measured spectra. Instead we analyzed directly the line-of-sight spectra with the radiation code SPECAIR, as will be explained in section 7.4.3.

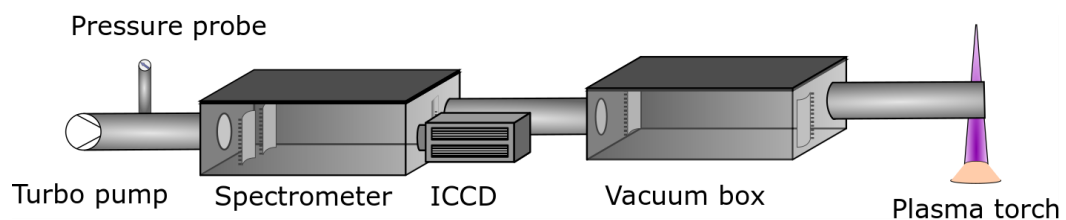


Figure 103: Experimental setup for VUV emission spectroscopy

The exit of the vacuum box is connected to a PEEK plastic arm. A first MgF₂ window separates the vacuum section from a section flushed with high purity argon (>99.99%) at atmospheric pressure. The end of the argon-flushed plastic arm is

then connected to a water-cooled copper piece placed directly in contact with the plasma at the exit of the nozzle or of the tubes. A second MgF_2 window, cooled by the copper piece, is placed just before the plasma. A schematic of the arm is shown in Figure 104. The argon flush is here to avoid any discharge in the VUV system in case the MgF_2 breaks due to thermal stress, the window being in contact with the hot plasma. If the window is broken after a given set of experiments, the results are ignored, and the measurements are redone with a new window. The focal point of the VUV system is 1.75 cm downstream of the nozzle or tube exit. This is slightly higher than the point where the temperature profiles were measured (1 cm downstream of the exit of the nozzle or of the tubes). This will be taken into account in the following sections.

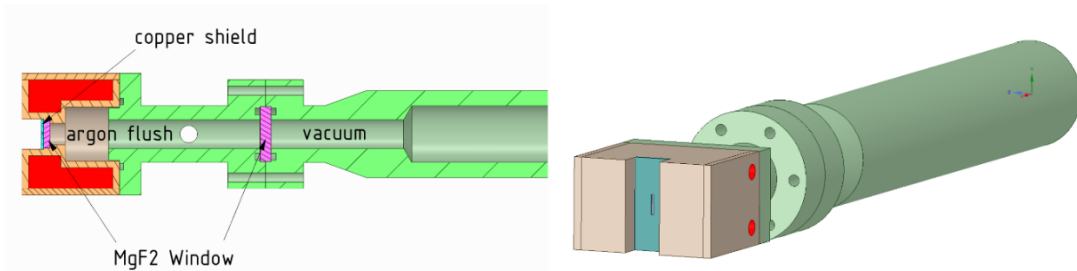


Figure 104: Head of the VUV system in contact with the plasma.

Two atomic doublets were measured in the VUV at 149 and 174 nm (see Table 9). The slit function was measured as explained in Chapter 2 and is presented in Figure 105. The FWHM was approximately 0.1 nm for all experiments. This measured slit function was used as an input for convolution with the SPECAIR calculations presented in the following sections.

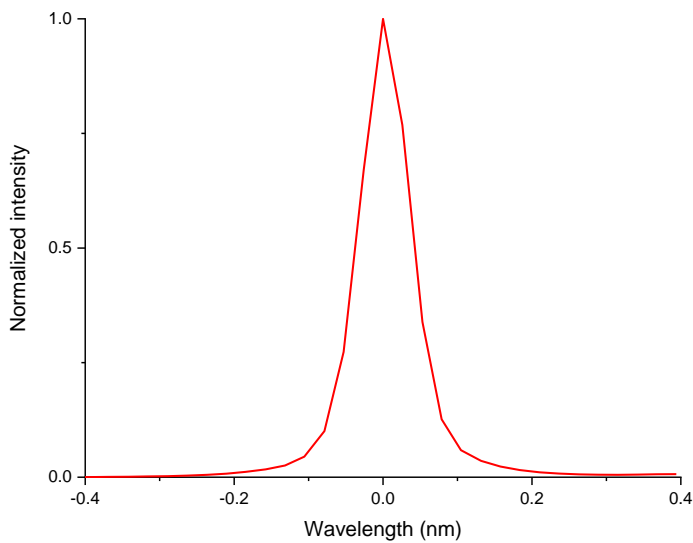


Figure 105: Measured slit function for the VUV system (FWHM = 0.1 nm)

7.4.3 Analysis of the nitrogen lines at 149 and 174 nm

Measurements of the 149 and 174 nm transitions were performed at three radial positions (0, 1, and 2 mm) and three axial positions (0, 10, and 15 cm) for the two N₂/Ar cases. Both transitions have the same upper N(²P) state, belonging to group ‘5’ in Table 8, and two different lower states, N(²D⁰) (‘2’) and N(²P⁰) (‘3’) for the 149 and 174-nm transitions, respectively. The plasma is expected to be out of equilibrium at the exit of the water-cooled tubes for these N₂/Ar mixtures. The states of the transition are therefore not expected to follow a Boltzmann distribution at the measured temperature. For a given mixture, axial and radial position, we have two measurements (the two measured transitions) and three unknowns (the common upper state and the two lower states). Without assumptions or extra measurements, we cannot derive the densities of these three states. As a first step, we consider that N(²D⁰) is in equilibrium at the gas temperature with the measured ground state N(⁴S⁰). This was discussed in section 7.3 and justified by numerical predictions of recombining flows, for example see (Johnston & Brandis, 2015). Then we use the measured 149-nm line to determine the density of N(²P) using SPECAIR. Because the line is optically thick, the measured line-of-sight intensity depends on the radial density profile of the upper and lower states. The lower state density profile was taken to be in equilibrium

with the ground state (see section 7.3) and used as an input to SPECAIR. This temperature profile was measured only out to a radial position of 2 to 4 mm depending on the case. The profile was subsequently extrapolated out to 5 mm (radius of the plasma) with a cubic spline extrapolation. We will present more details on this for each of the cases. Finally, the radial density profile of the upper state is assumed to be self-similar to that of the lower state of the transition. This assumption is partly justified because the measured upper state radial density profiles in the visible/NIR have approximately the same shape as the $N(^2D^0)$ state. An example is shown in Figure 106 at the exit of the 15-cm tube for the N_2/Ar HF case. Note that the uncertainties are not shown for all densities but are about 35% for this condition.

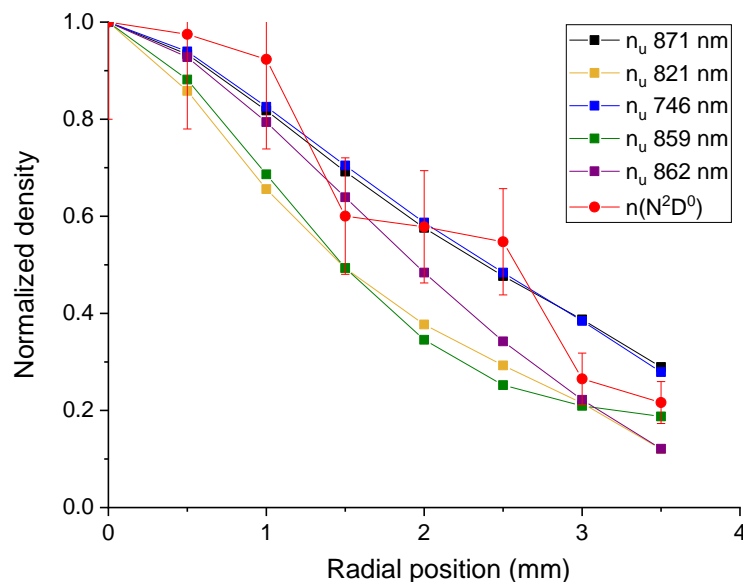


Figure 106: Normalized density profiles for the upper states of transitions in the visible/NIR region compared with the density profile of $N(^2D^0)$ (in equilibrium with N ground state) for the N_2/Ar HF mixture. These profiles are measured at the exit of the 15-cm tube. The uncertainties are about 35%.

In practice, we use the following procedure:

The radial density profile of $N(^2D^0)$ is expressed as:

$$n_{N^2D^0}(r) = A \cdot f(r) \quad (7.8)$$

where $f(r)$ is a normalized function (shown for one condition in Figure 106) and A is the maximum radial density of $N(^2D^0)$ obtained in section 7.3. Then we consider various homothetic radial density profiles of the upper state of the 149-nm (N^2P) transition. A given density profile i is expressed as:

$$n_{N^2P}^i(r) = B_i \cdot f(r) \quad (7.9)$$

where B_i is an arbitrary parameter ($B_i = 10^i \text{ cm}^{-3}, i = 1, 2, \dots N$, for example). Then every pair of profiles ($n_{N^2D^0}$, $n_{N^2P}^i(r)$) is used as input for SPECAIR. Three spectra are computed corresponding to the line-of-sight spectra at lateral positions 0, 1, and 2 mm. The error between the measured and computed spectra at the three considered lateral locations is calculated using a L_2 norm. These three errors are summed and the value of B_i minimizing the error is considered to be the best estimate. This gives us a measurement of the density profile of $N(^2P)$. The uncertainties on this measurement are found by varying the lower state density within the range of its error bars.

Now we can return to the measured transition at 174 nm. This transition has the same upper state, $N(^2P)$, as the 149-nm transition but a different lower state, $N(^2P^0)$. We use the same procedure as before except that we now fix the upper level to the previously determined density profile to get a measurement of the lower state radial density profile $n_{N^2P^0}^i$ written as:

$$n_{N^2P^0}^i(r) = C_i f(r) \quad (7.10)$$

The $n_{N(^2P^0)}^i$ that minimizes the error between the computed and experimental spectra gives the best estimate of $n_{N(^2P^0)}$.

A summary of all measurements and calculations made for the various excited states of atomic nitrogen is presented in Figure 107. The optically thin transitions are in the visible-Near-Infrared region, as presented in Table 9. Note that the 174-nm line was also found to be optically thin under some conditions as will be presented in section 7.6.

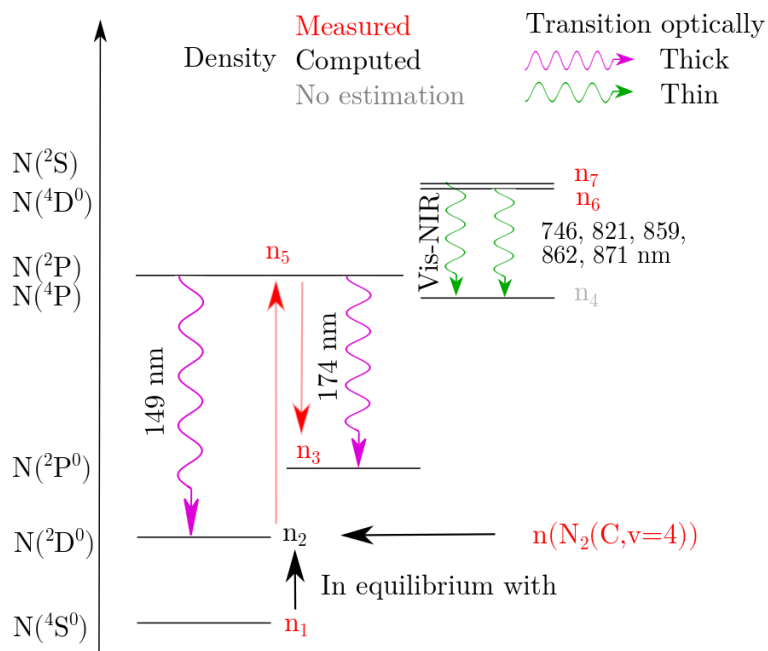


Figure 107: Summary scheme of all measurements of excited electronic states of N

7.5 Electron number density measurements

In nonequilibrium flows, the high energy states of atoms are usually in equilibrium with electrons (Johnston & Brandis, 2015). To check this assumption, it is important to measure the electron density in our case.

7.5.1 Method

Electron number densities were determined experimentally from the Stark broadening of the Balmer H_β line. Details of the procedure can be found by (Laux, et al., 2003) and will be summarized here. A small amount of hydrogen (0.5%) was added to the Air/Ar and N_2 /Ar mixtures. Stark broadening is produced by interactions with charged particles and results in a slight change of the species electronic energy. When the species is a radiator, the emission lineshape is broadened and can be approximated by a Lorentzian curve. Ions and electrons are both responsible for Stark broadening, but electrons are responsible for the dominant part of the broadening because of their higher velocity. The Half Width at Half Maximum (HWHM) of the Lorentzian lineshape is related to the electron number density. Measurements of an atomic line can then be used to infer the

electron density. However, in order to yield good results, Stark broadening should be the predominant broadening mechanism. The other broadening mechanisms are well known (Laux, et al., 2003). Resonance and Van der Waals broadening are caused, respectively, by collisions with similar particles and by neutral particles. Doppler broadening is due to the relative speed between an observer and the particle, shifting the observed photon frequency as a consequence of the Doppler effect. Finally, natural broadening is a consequence of the Heisenberg uncertainty principle, and is usually very small. The lineshapes induced by these various broadening mechanisms are lorentzian, with the exception of Doppler broadening which gives a gaussian lineshape. Expressions of the broadening HWHMs for the H_{β} transition are given in Table 10. They are taken from (Laux, et al., 2003). Values for an atmospheric pressure Air/Ar plasma in equilibrium at 7000 and 4000 K are given to illustrate the relative importance of each broadening mechanism. At 7000 K, Stark broadening is dominant. The lineshape of the transition can therefore be used to measure the electron density. At 4000 K, on the other hand, the Stark broadening width is much smaller than the Doppler and Van der Waals widths, and it is not possible to determine the electron density by measuring the broadening. However, the electron number density could still be measured, even at 4000 K, if there were a large overpopulation of electrons (nonequilibrium plasma). The electron density may only be measured as long as Stark broadening is the dominant mechanism. There is therefore a lower limit of electron density that can be measured using this technique.

Table 10: Analytical expressions of the various broadening widths (HWHM in nm) (taken from (Laux, et al., 2003)) and their corresponding numerical values at $P = 1$ atm and $T = 7000$ and 4000 K for the Air/Ar plasma case. n_e is the electron density and X_H the mole fraction of hydrogen, both computed using the CEA code.

	$\Delta \lambda_{Stark}$	$\Delta \lambda_{Resonance}$	$\Delta \lambda_{Van\ der\ Waals}$	$\Delta \lambda_{Doppler}$	$\Delta \lambda_{Natural}$
HWHM (nm)	$1.0 \cdot 10^{-11} n_e^{0.668}$	$30.2 X_H \left(\frac{P}{T} \right)$	$1.8 \frac{P}{T^{0.7}}$	$1.74 \cdot 10^{-4} T^{0.5}$	$3.1 \cdot 10^{-5}$
Air/Ar, 7000 K,	$7.11 \cdot 10^{-2}$	$4.55 \cdot 10^{-4}$	$3.71 \cdot 10^{-3}$	$1.46 \cdot 10^{-2}$	$3.1 \cdot 10^{-5}$

1 atm, $x_H = 0.01$					
Air/Ar, 4000 K, 1 atm, $x_H = 0.01$	$2.67 \cdot 10^{-3}$	$8.23 \cdot 10^{-4}$	$5.49 \cdot 10^{-3}$	$1.10 \cdot 10^{-2}$	$3.1 \cdot 10^{-5}$

The slit function also plays a role in the final broadening of the H_β line. A He-Ne laser was used to measure it in our experiments. A grating with 2400 grooves per millimeter was used and the spectrometer entrance slit width was set to 50 μm . The measured slit function is presented in Figure 108, along with a gaussian fit. The curve labeled “Gaussian discretization” represents a discrete decomposition of the gaussian curve at the wavelengths corresponding to the pixels of the CCD. Note that the measured slit function is well fitted by the discretized gaussian with a relative error (using an L_2 norm) of about 15%. The HWHM is about 1.5×10^{-2} nm, which is approximately equal to the Doppler broadening width (see Table 10).

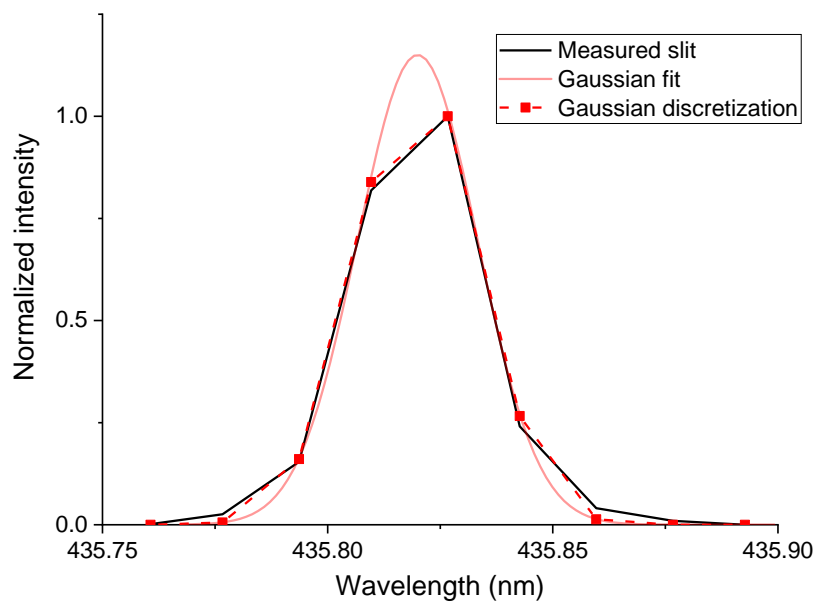


Figure 108: Measured slit function and the corresponding gaussian fit. The HWHM is 0.015 nm.

The total Lorentzian HWHM is the sum of the individual HWHMs, and the total gaussian HWHM is the quadratic mean of the various gaussian components. The overall lineshape is the convolution between the gaussian and the Lorentzian components, known as the Voigt profile.

$$\text{Voigt}(l, g) = \text{Lorentz}(l) * \text{Gaussian}(g) \quad (7.11)$$

where l and g are the HWHMs of the lorentzian and the gaussian lineshapes, respectively. These can be decomposed as:

$$\begin{aligned} g &= \sqrt{g_{\text{slit}}^2 + g_{\text{Doppler}}^2} \\ l &= l_{\text{Stark}} + l_{\text{res}} + l_{\text{vdw}} + l_{\text{nat}} \end{aligned} \quad (7.12)$$

When calculating the HWHM line broadening for comparison against measurements, the only adjustable parameter is the electron density for the Stark broadening. The measurement of the H_β line is therefore used to get the HWHM of the Stark broadening and therefore the electron density. If $L_{H_{\text{beta}}}^{\text{meas}}(\lambda)$ is the measured lineshape of H_β , the error between the measured and computed lineshapes is:

$$E(x) = \frac{\sqrt{\sum_{\lambda} \left(L_{H_{\text{beta}}}^{\text{meas}}(\lambda) - \text{Voigt}(l^* + x, g, \lambda) \right)^2}}{\sqrt{\sum_{\lambda} \left(L_{H_{\text{beta}}}^{\text{meas}}(\lambda) \right)^2}} \quad (7.13)$$

where $l^* = l_{\text{res}} + l_{\text{vdw}} + l_{\text{nat}}$. The value of x that minimizes the error gives the best estimate of the Stark broadening HWHM.

7.5.2 Results

The Air/Ar plasma case was first investigated. For this case, the plasma was found to remain in equilibrium, and therefore the electron density measurements can be compared with the equilibrium values computed with the CEA code. A comparison of the measured and fitted H_β lineshapes at 0, 10, and 15 cm is presented in Figure 109. The Voigt profile excluding Stark broadening is also plotted to show the relative importance of Stark broadening.

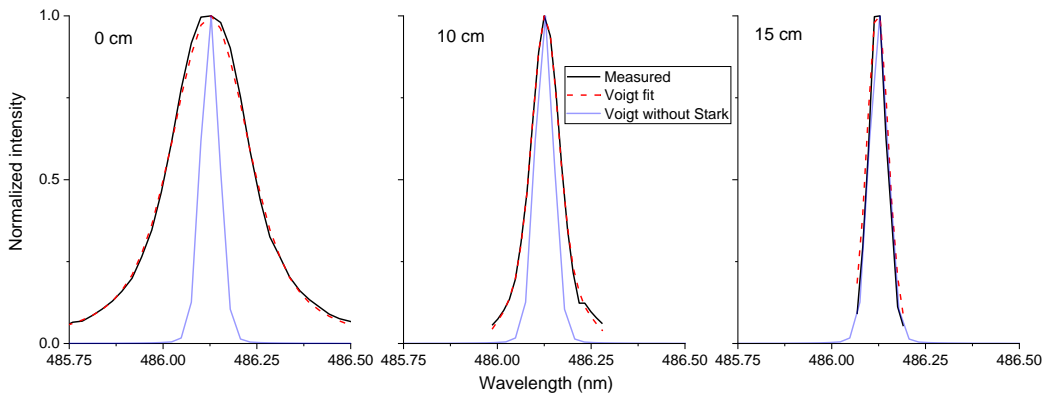


Figure 109: Comparison between the measured H β lineshape (black) and the fitted Voigt profiles (red dash) at 0 cm (left), 10 cm (middle) and 15 cm (right). The Voigt profiles excluding Stark broadening are plotted in blue.

Air/Ar case.

At 0 and 10 cm, Stark broadening is dominant and can be extracted from the measured lineshape. At 15 cm however, Stark broadening is small in comparison with the measured lineshape, and therefore we can only estimate an upper bound of its value, hence of the electron number density. To estimate this bound, we proceeded as follows. We computed the relative error using an L₂ norm between two theoretical lineshapes: the first one was calculated using all broadening mechanisms and the second one excluding Stark broadening. This error measures the relative importance of the Stark effect on the global broadening and is plotted in Figure 110. To determine the limit of this technique, we find the minimal HWHM of the Stark broadening width that can be measured with our setup. First, this technique suffers from a systematic error of about 15%, as presented in Figure 108, because of the discrete decomposition of the fitted slit function. We added to this error the residual of the best fit presented in Figure 109, which was 3% at an axial position of 0 cm. The error tolerance for acceptable values is then 18%. Below this level, Stark broadening cannot be estimated. According to Figure 110, this corresponds to electron densities below $n_e = 2.5 \cdot 10^{13} \text{ cm}^{-3}$. This value corresponds to the lower value of electron densities that can be measured with our setup.

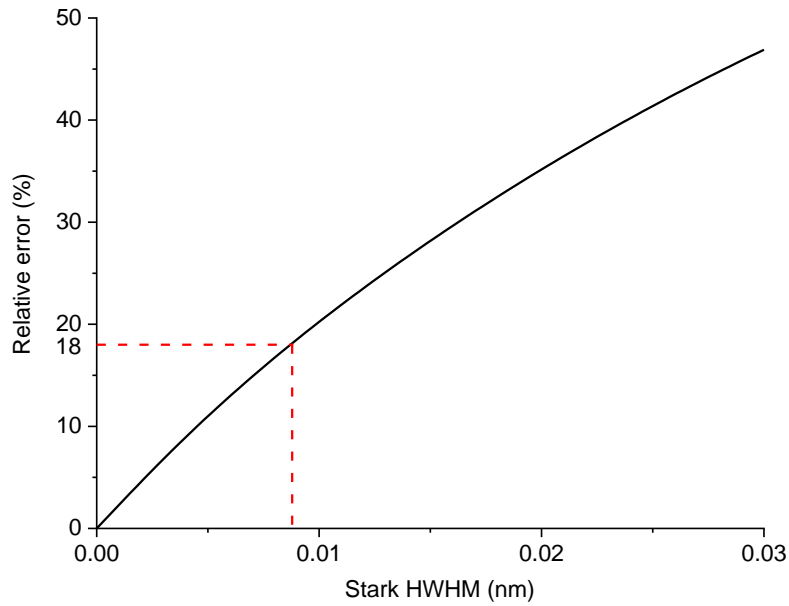


Figure 110: Relative error between a Voigt profile ignoring or not Stark broadening as a function of the HWHM Stark broadening. The limit of acceptable errors is 18%, corresponding to HWHM=0.009 nm.

Measurements were made for the three cases (Air/Ar, N₂/Ar LF and HF) at 0, 10, and 15 cm. The results are presented in Figure 111. The lower bound of the electron densities that can be measured with this technique is also plotted. For the Air/Ar case, there is good agreement between the measurements and equilibrium densities. This supports once more that this plasma remains in LTE. For the N₂/Ar mixtures, the measured electron number densities are close to the equilibrium values at 0 cm, as expected. At 10 cm, a slight overpopulation of electrons appears for the LF case and a large one for the HF case. At 15 cm, in all three cases the measured values correspond to an upper bound of the actual electron number densities.

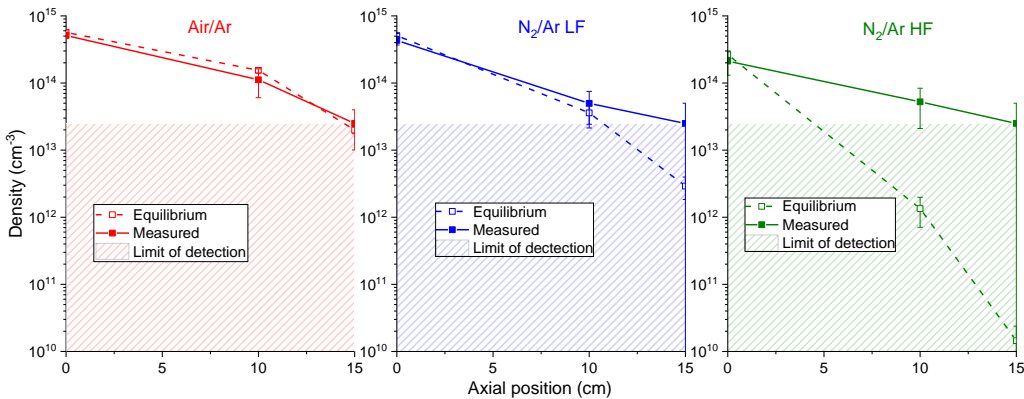


Figure 111: Electron density measurements using Stark broadening of the H_β line for the Air/Ar (left), N_2/Ar LF (middle) and N_2/Ar HF (right) cases at 0, 10 and 15 cm. The lower limit of detection is $2.5 \times 10^{13} \text{ cm}^{-3}$.

7.5.3 Conclusion

Electron density measurements, using Stark broadening of the H_β line, were performed for the three different cases studied. This relatively simple technique is very useful to get accurate density measurements but suffers from one limitation: Stark broadening must be the predominant broadening effect in the experimental conditions. For our cases, values below $n_e = 2.5 \cdot 10^{13} \text{ cm}^{-3}$ could not be measured. For this reason, only an upper bound was found for certain measurement points – notably at the axial position of 15 cm. Values for axial positions of 10 cm can still be used. Note that reducing the FWHM of the slit function will not lower this lower threshold as Doppler broadening is of the same order as the slit function width.

7.6 Results on atomic line measurements

7.6.1 N_2/Ar LF case

7.6.1.1 At the exit of the torch (0 cm)

At 0 cm, the plasma is in LTE and the measured atomic lines should be in good agreement with the SPECAIR spectra computed at LTE with the temperature profile measured in Chapter 3 (called T_{measured}) for the three spectra measured

radially at 0, 1, and 2 mm. As shown in Figure 112, the agreement is not perfect. This is because the measurement is performed 1.75 cm downstream of the nozzle exit compared to 0.5 cm in Chapter 6, leading to a small decrease of the plasma temperature. The temperature was measured 1.75 cm downstream to be consistent. Temperature profiles at 0.5 cm and 1.75 cm are presented in Figure 113. The resulting spectra is shown in Figure 112 and the discrepancy due to the temperature difference is seen to be noticeable but still relatively small. At 10 and 15 cm, this influence is also believed to be relatively small, and therefore it is assumed that the presence of the water-cooled copper piece (see Figure 104) has a negligible effect on the measured densities of excited N atoms.

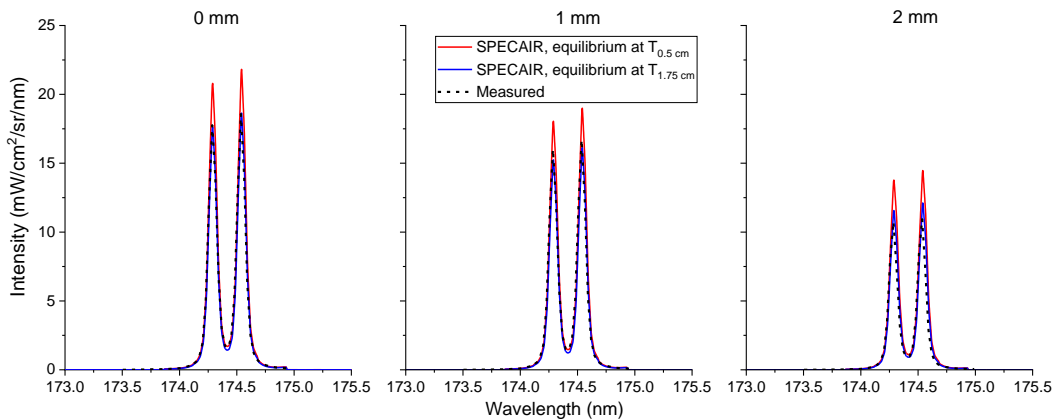


Figure 112: Comparison between measured spectrum (black dash) and SPECAIR calculation assuming the measured temperature profile 0.5 cm downstream (red) or 1.75 cm downstream (blue) at the exit of the torch (0 cm) for the N₂/Ar LF case. Three line-of-sight spectra were taken at different lateral positions (0, 1, and 2 mm).

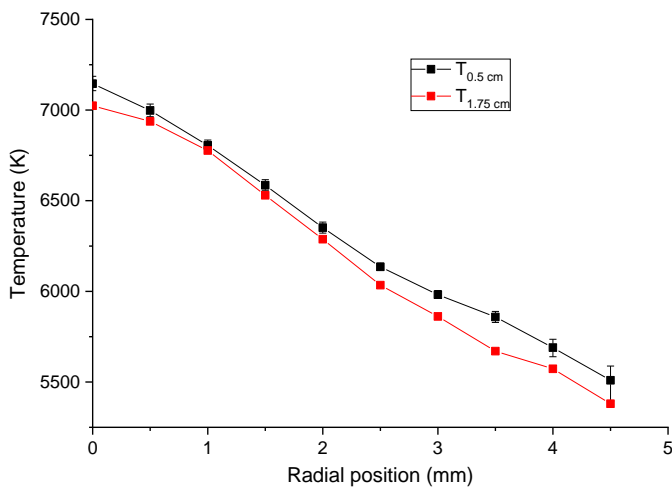


Figure 113: Temperature profiles at the exit of the torch (0 cm) for the N₂/Ar LF case measured 0.5 cm (black) and 1.75 cm (red) downstream

The above analysis focused on the nitrogen doublet at 174 nm. We were also able to observe the 149-nm nitrogen line. The temperature profile measured 1.75 cm downstream of the torch exit is now used to calculate a theoretical spectrum for the 149-nm line. Figure 114 shows the comparison with the experiment. The agreement is not good, likely because of the reduced transmissivity of the window in contact with the plasma. After an experiment, this window is coated with a dark film which may degrade the transmissivity at 149 nm. We measure the transmittivity of this window using the argon mini arc. Results are presented in Figure 115 and are compared with the transmittivity of a virgin window. Note that this window is not present with the mini arc and therefore should be taken into account in the calibration process. The measured transmittivity at 149 nm is around 30%. The resulting spectra when adding this transmissivity in the calibration are also shown in Figure 114. Note that several measurements were made and yields similar results at different times and with different windows. Therefore, this dark film is assumed to reach steady state quickly during the experiment. Note that an uncertainty of 10% was taken on this transmittivity, corresponding to the maximum variations around 149 nm observed in Figure 115. In the following experiments at 10 and 15 cm, we will apply the same transmittivity correction to the SPECAIR calculations when comparing with experiments.

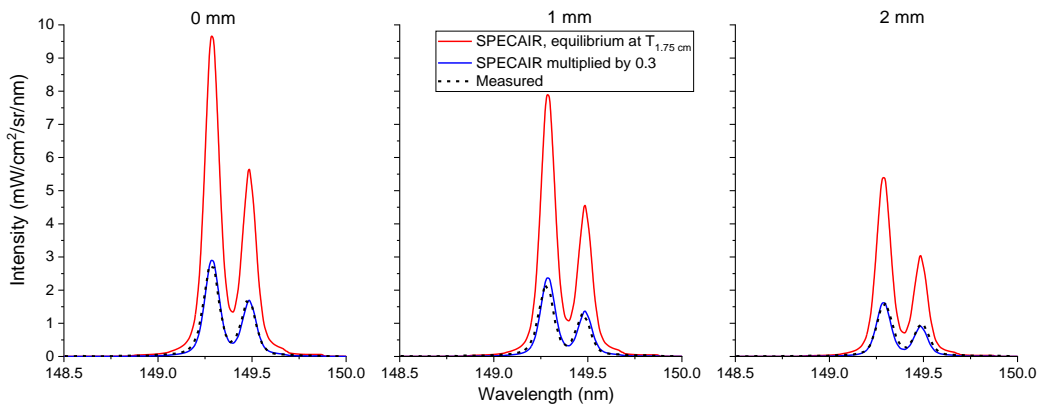


Figure 114: Comparison between measured spectra (black dash) and SPECAIR calculations assuming the measured temperature profile 1.75 cm downstream of the torch exit (0 cm) for the N₂/Ar LF case. The blue line corresponds to SPECAIR spectra multiplied by a transmissivity of 0.3. These three line-of-sight spectra were taken at different lateral positions (0, 1, and 2 mm).

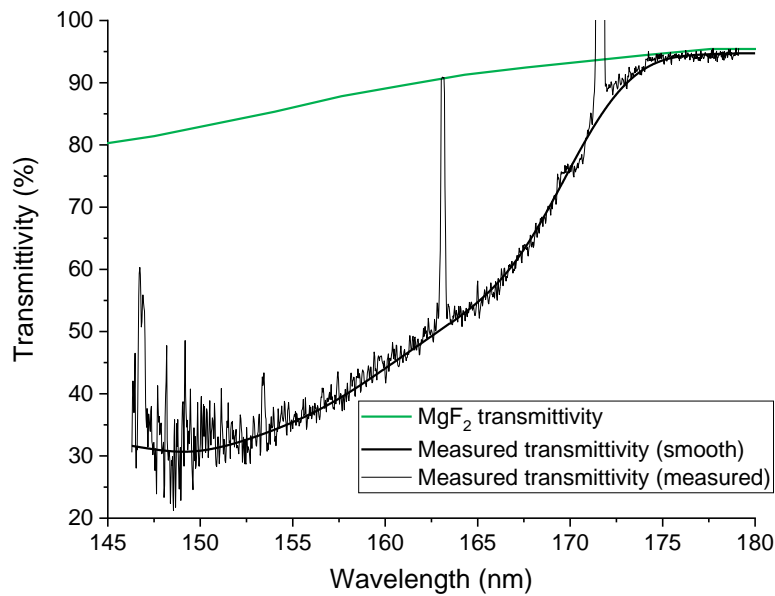


Figure 115: Transmittivity of a virgin MgF₂ window (green) and a window coated with a dark film after an experiment (black). The atomic features observed come from impurities in the argon mini arc.

7.6.1.2 At the exit of the 10-cm tube

Measurements of the 149 and 174-nm lines were performed at the exit of the 10-cm tube for the N₂/Ar case. Three line-of-sight spectra were measured at 0, 1, and

2 mm laterally. The spectra computed using SPECAIR were multiplied by a transmittivity of 0.3 as explained in section 7.6.1.1. The procedure detailed in section 7.4.3 was used to determine from this measurement the density of the upper state of the transition, namely $N(^2P^0)$. The sum of the error between the measured and computed spectra at the different lateral positions as a function of the upper state density profile is shown in Figure 116. Comparisons between the best fits and the measurements at the three lateral positions are shown in Figure 117.

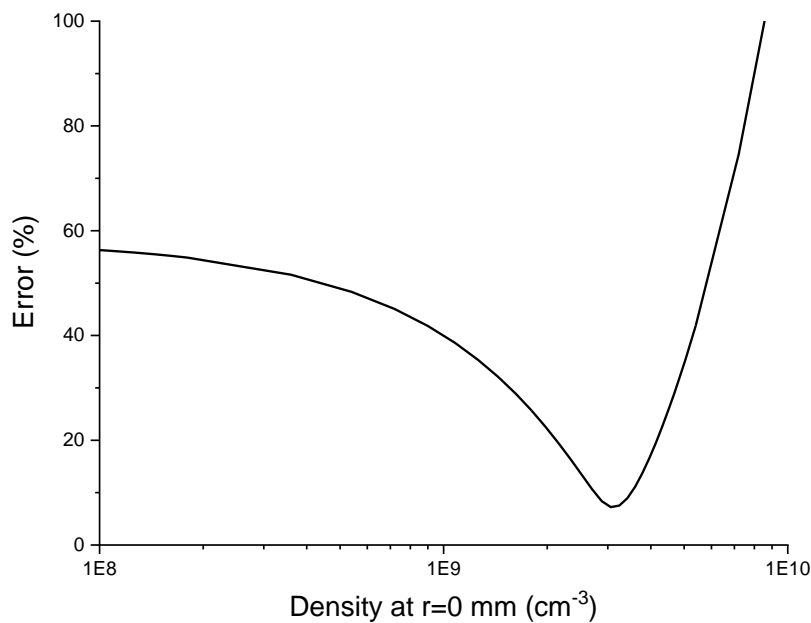


Figure 116: Relative error between measured and computed spectra of the 149-nm line at the exit of the 10-cm tube for the N₂/Ar LF case as a function of the amplitude of the density of the upper state taken in SPECAIR calculations.

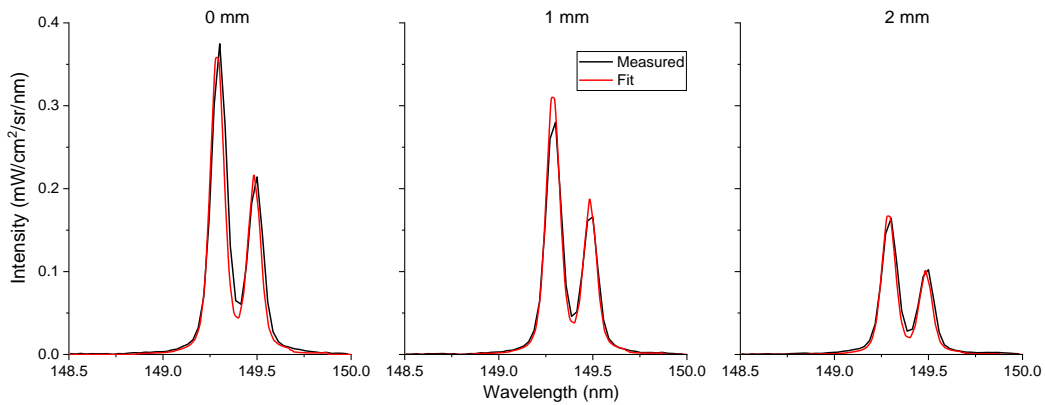


Figure 117: 149-nm line: comparison between the measured spectra and the computed SPECAIR spectra resulting from the best fit at the exit of the 10-cm tube for the N₂/Ar LF case. These three line-of-sight spectra were taken at different lateral positions (0, 1, and 2 mm).

The density of the lower state was imposed to be in equilibrium with N(⁴S⁰) but only radial measurements out to 2 mm were performed before as explained in section 7.4.2. The radial density profile was extrapolated using a cubic spline with an imposed equilibrium density at 300 K at 5 mm. Then, the density profile of the upper state was assumed to be self-similar to the lower state. The radial density profile of the lower state resulting from the extrapolation and the radial density profile of the upper state resulting from the error minimization are presented in Figure 118. Note that the uncertainties on the upper state were found after the same error minimization by imposing the lower and upper bounds of the lower state density.

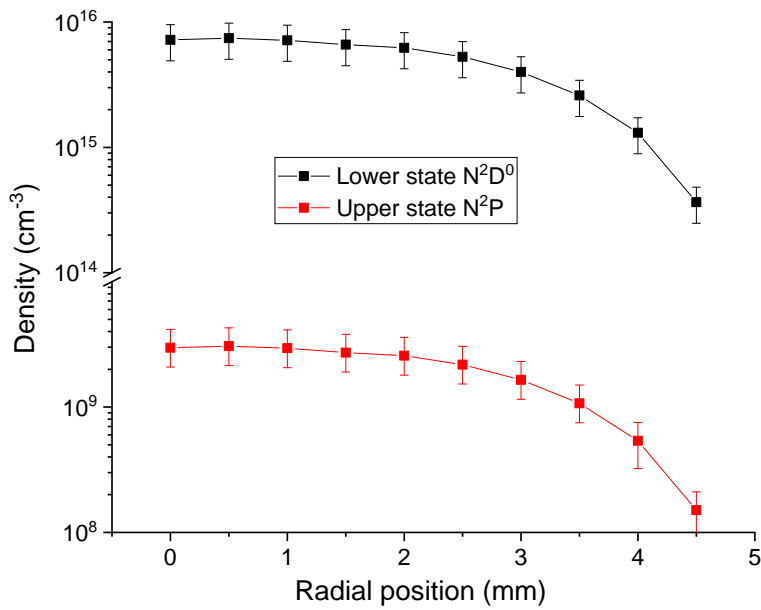


Figure 118: Lower and upper state densities of the 149-nm transition at the exit of the 10-cm tube for the N₂/Ar LF case. Only the points out to 2 mm were measured for N(²D⁰) and the others result from the extrapolation procedure.

The same procedure was applied for the 174-nm line, this time imposing the density of the upper state, in order to determine the lower state density. The error as a function of the amplitude of the density of the lower state N(²P⁰) is presented in Figure 119. The error is higher than before, which explains the higher uncertainties. Comparisons between the best fits and the measured spectra are presented in Figure 120.

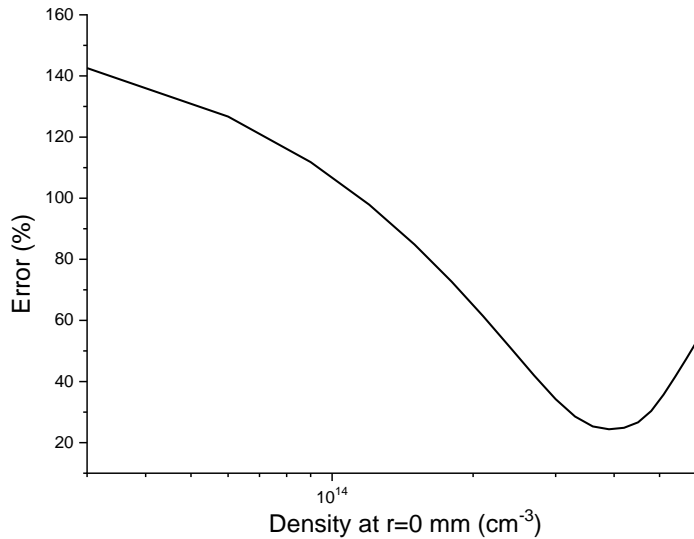


Figure 119: Relative error between measured and computed spectra of the 174-nm line at the exit of the 10-cm tube for the N₂/Ar LF case as a function of the density of the lower state taken in SPECAIR calculations.

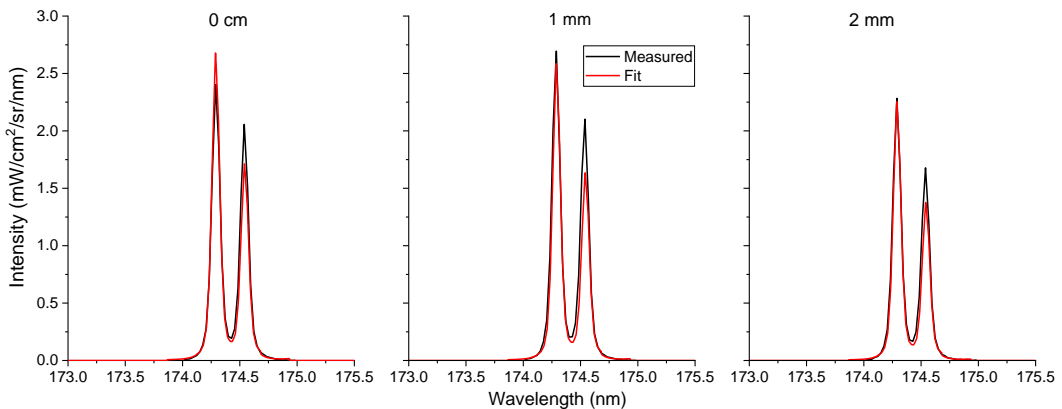


Figure 120: 174-nm line: comparison between the measured spectra and the computed SPECAIR spectra resulting from the best fit at the exit of the 10-cm tube for the N₂/Ar LF case. These three line-of-sight spectra were taken at different lateral positions (0, 1, and 2 mm).

All radial density profiles measured using the VUV lines are summarized in Figure 121. The assumptions made for these measurements were the following:

- N(²D⁰) was assumed to be in equilibrium with the measured ground state
- The density profiles of the upper and lower states of the 174-nm and 149-nm transitions were assumed similar to the measured ground state

- The SPECAIR calculations were multiplied by a transmittivity of 0.3. An uncertainty of 40% was taken in the uncertainty analysis, corresponding to the maximum differences observed from experiment to experiment at 0 cm.

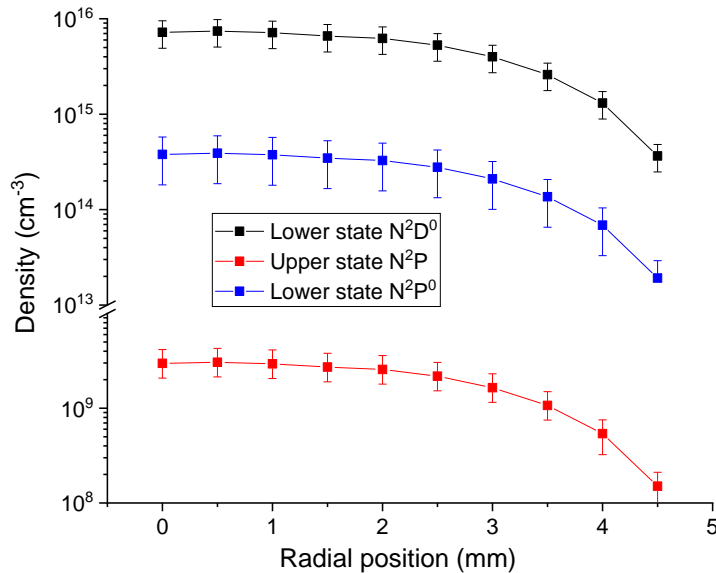


Figure 121: Lower and upper states densities of the 149-nm and 174-nm transitions at the exit of the 10-cm tube for the N_2/Ar LF case.

7.6.1.3 At the exit of the 15-cm tube

The exact same procedure was used at the exit of the 15-cm tube. The errors between the computed and measured spectra are presented in Figure 122. The minimum is found at $7.8 \cdot 10^7 \text{ cm}^{-3}$. The corresponding computed spectra are shown in Figure 123 and compared with the measurements. Finally, the radial density profiles are plotted in Figure 124. Once again, radial measurements of $N(^2D^0)$ were only performed out to 2 mm and extrapolated using a cubic spline to 5 mm.

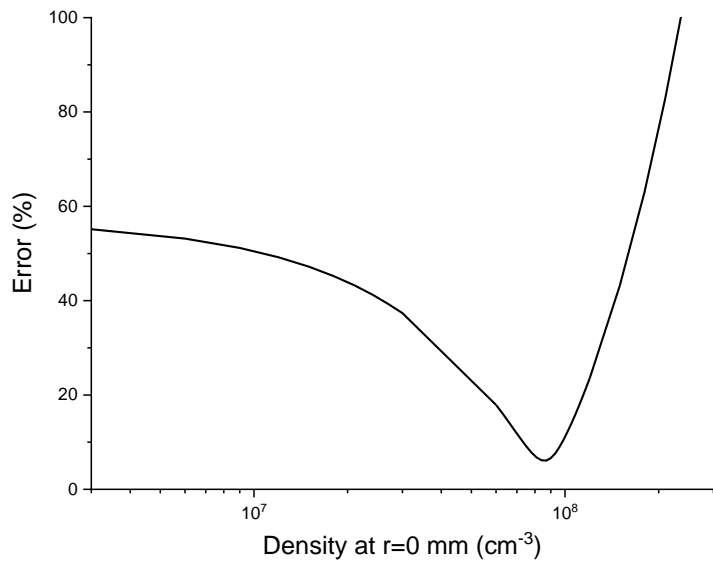


Figure 122. Relative error between measured and computed spectra of the 149-nm line at the exit of the 15-cm tube for the N₂/Ar LF case as a function of the amplitude of the density of the upper state taken in SPECAIR calculations.

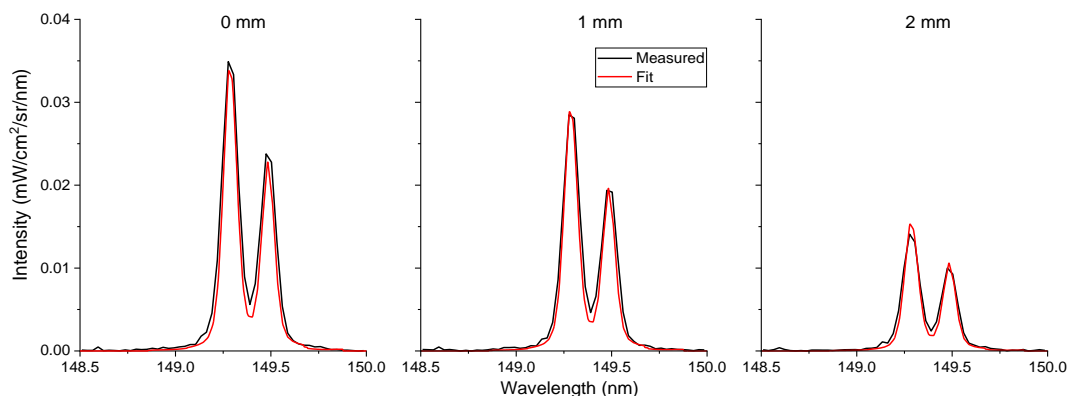


Figure 123. 149-nm line: Comparison of the measured spectra and the computed SPECAIR spectra resulting from the best fit at the exit of the 15-cm tube for the N₂/Ar LF case. These three line-of-sight spectra were taken at different lateral positions (0, 1, and 2 mm).

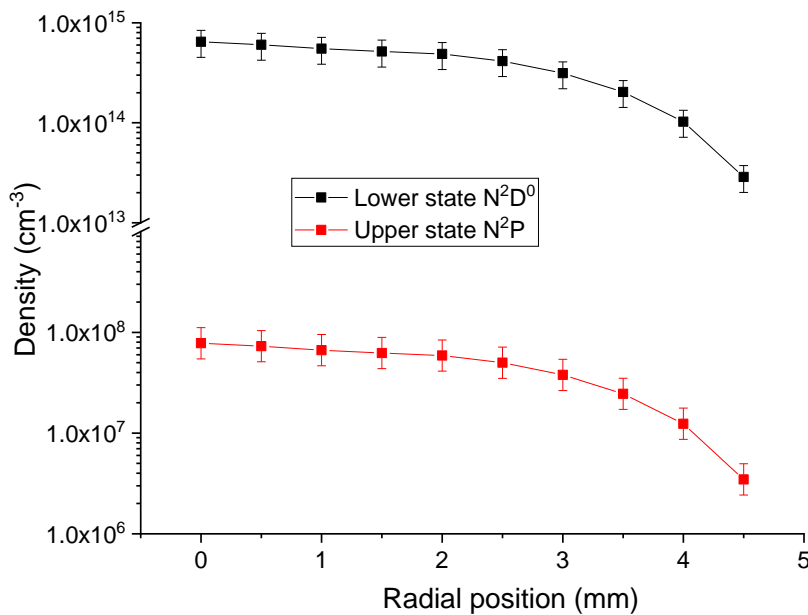


Figure 124 Lower and upper state densities of the 149-nm transition at the exit of the 15-cm tube for the N_2/Ar LF case. Only the points out to 2 mm were measured for $N_2^{(2D^0)}$ and the others result from the extrapolation procedure.

For the 174-nm line, the plasma was found to be optically thin. Indeed, we plotted in Figure 125 a comparison between measured and computed spectra using SPECAIR assuming optically thin conditions using the previous measurement of the upper state (taken from Figure 124), and we found good agreement. Unfortunately, this means that this transition cannot be used to measure the density of the lower state. However, we can give an upper bound of this density – namely, it cannot be above the value that causes the spectrum to become optically thick. Assuming the 174-nm line optically thin, a second analysis can be performed: we start with this line to get a measurement of the density of the upper state ($N_2^{(2P)}$, n_5 in Figure 107). The 149-nm line is then used to get the density of its lower state $N_2^{(2D^0)}$. This analysis was performed and yields the same results, as was obtained with the 149-nm line. This second analysis allow to measure the density of $N_2^{(2D^0)}$ and result in the same densities assumed in the first analysis. Therefore, $N_2^{(2D^0)}$ is in equilibrium with the measured ground state. This serves as a validation of the assumption made in section 7.3.

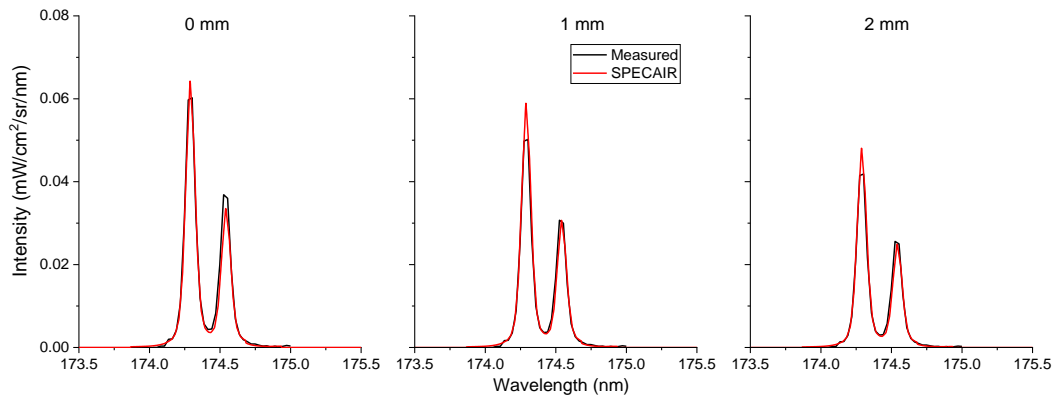


Figure 125. 174-nm line: comparison between the measured spectra and the optically thin computed SPECAIR spectra using the measured density profile of the upper state at the exit of the 15-cm tube for the N₂/Ar LF case. These three line-of-sight spectra were taken at different lateral positions (0, 1, and 2 mm).

7.6.1.4 Distribution of excited N atoms

Atomic lines were measured from the VUV to the NIR region to get the densities of excited N atoms. Details about these transitions can be found in Table 9. We will now present the various measured N excited state densities in a Boltzmann diagram.

In nonequilibrium plasmas, the density of the excited states n_i close to the ground state are expected to follow a Boltzmann distribution at the gas temperature, as given by:

$$\frac{n_i}{g_i} = \frac{n_0}{g_0} \exp\left(-\frac{\epsilon_i}{k_B T}\right) \quad (7.14)$$

where n_0 is the density of the ground state of atomic nitrogen and where g_i and g_0 represent the degeneracies, ϵ_i the energy of the considered level, k_B the Boltzmann constant, and T the gas temperature. The ground state density n_0 was measured in section 7.2.

The densities of the excited states close to the ionization limit often are in Saha-Boltzmann equilibrium with the electron/ion densities, and are given by:

$$\frac{n_i}{g_i} = \frac{n_+ n_e}{2Q_+} \left(\frac{h^2}{2\pi k_B T}\right)^{\frac{3}{2}} \exp\left(\frac{\epsilon_{ion} - \epsilon_i}{k_B T}\right) \quad (7.15)$$

where n_+ is the density of atomic ions, n_e the density of electrons, Q_+ the partition function of the atomic ion (approximately equal to 8 for N^+ (Drellishak, et al., 1965)), h the Planck constant, and ϵ_{ion} the ionization energy. Because the electrons/ions recombine slowly, the overpopulation of these species results in an overpopulation of the excited state densities with respect to the Boltzmann distribution. The electron density measurements were presented in section 7.5.2. The density of N^+ was not measured but was estimated assuming that the overpopulation of N^+ was equal to the overpopulation of the electrons.

In Figure 126, we plot the Boltzmann and Saha-Boltzmann distributions and the excited N-atom densities measured previously at the exit of the 10-cm tube. Although we only plot the results at the centerline of the tube, similar behavior is observed radially across the tube. While the low energy states of atomic nitrogen remain close to the Boltzmann distribution, the higher energy states are highly overpopulated relative to their equilibrium values and tend to be above the Boltzmann distribution and close to the Saha-Boltzmann distribution. This suggests that the high energy states of nitrogen tend to be in equilibrium with the free electrons. Note that the uncertainties for the high energy states are also plotted but are too small to be seen. An additional Boltzmann distribution assuming $T_{el} = 6250$ K is also plotted in the figure and agree relatively well with the measured distribution. This could indicate that the distribution remains Boltzmann in this case but at a different temperature than the gas

Results at the exit of the 15-cm tube are presented in Figure 127. In this case, the density of $\text{N}(^2\text{P}^0)$ could not be measured but instead an upper bound was found. A similar trend as at 10 cm is observed; the measured low energy state $\text{N}(^2\text{D}^0)$ remains in equilibrium with the ground state while the high energy states are highly overpopulated and closer to the Saha-Boltzmann distribution. As previously observed for the molecules, the degree of nonequilibrium increases at 15 cm compared to 10 cm as the overpopulation of the high energy states increases.

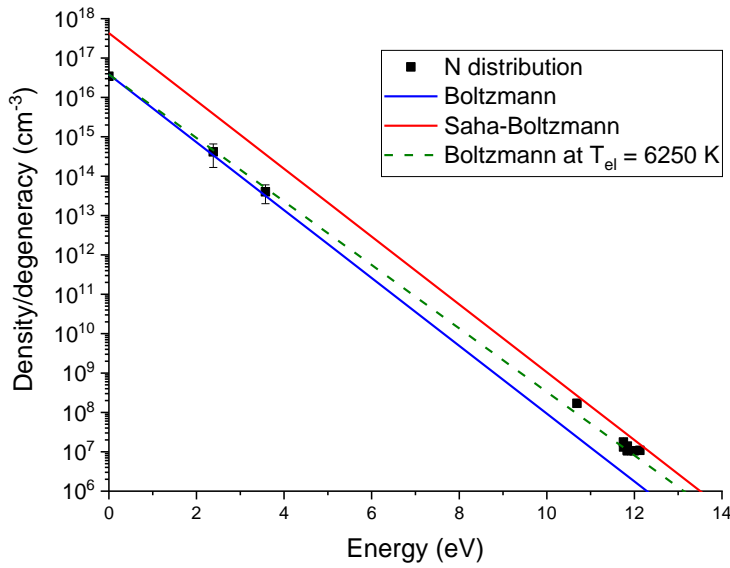


Figure 126: Measured population distribution of ground and excited states of atomic nitrogen (black) at the exit of the 10-cm tube for the N_2/Ar LF case at $r = 0$ mm. The Boltzmann (blue) and Saha Boltzmann (red) distributions are also plotted. A Boltzmann distribution at $T_{\text{el}} = 6250$ K is also plotted in green.

The populations of the high-lying states fall a factor of 20 below the Saha-Boltzmann distribution. There are two possible explanations for this difference: either the measured levels are not high enough to be in Saha-Boltzmann equilibrium with the free electrons, or the free electron density was overestimated, which is likely to be the case based on the discussion of Section 7.5. If we assume that the density of the highest measured electronic state should fall on the Saha-Boltzmann curve, this would mean that the electron number density at the exit of the 15-cm tube is equal to $5.6 \cdot 10^{12}$ i.e. a factor of $\sqrt{20}$ lower than the measured density of $2.5 \cdot 10^{13}$. The latter explanation is plausible, given that our measured electron number density was an upper bound of the real electron number density.

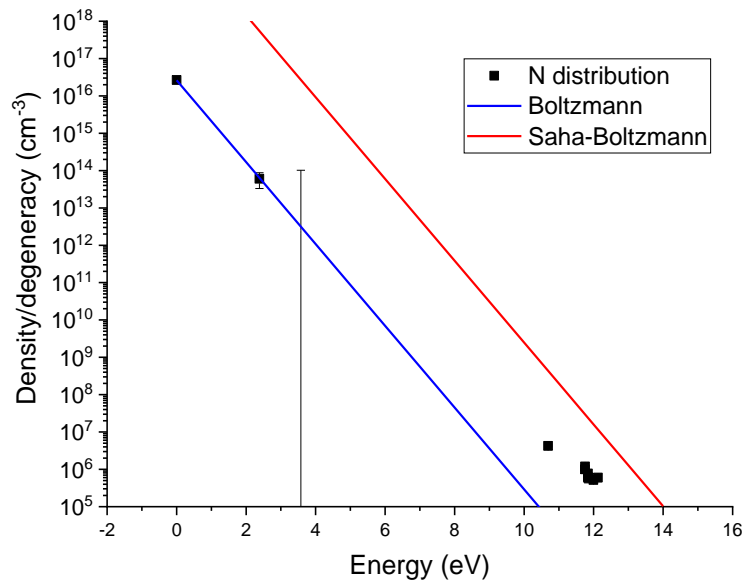


Figure 127: Measured population distribution of ground and excited states of atomic nitrogen (black) at the exit of the 15-cm tube for the N₂/Ar LF case at r = 0 mm. The Boltzmann (blue) and Saha Boltzmann (red) distributions are also plotted.

7.6.2 N₂/Ar high flowrate case

7.6.2.1 At the exit of the torch (0 cm)

The atomic lines at 149 and 174 nm were measured, and the same analysis was performed as for the previous test-case. A comparison between the temperature profiles measured 1.75 cm and 0.5 cm downstream of the torch exit is presented in Figure 129. The spectra computed using SPECAIR assuming these temperature profiles are compared with the measurements in Figure 128. Once again, the measured spectrum and the spectrum computed with the temperature profile measured 1.75 cm downstream of the torch exit are in good agreement.

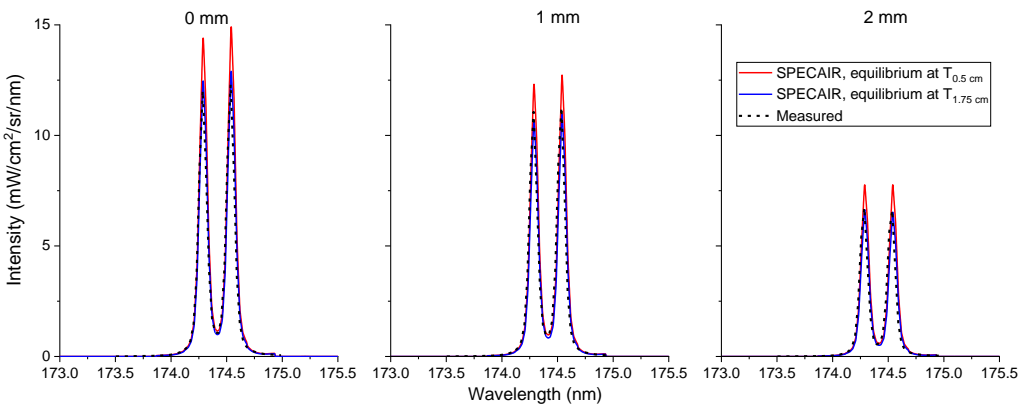


Figure 128: Comparison between measured spectrum (black dash) and SPECAIR calculation assuming the measured temperature profile 0.5 cm (red) or 1.75 cm downstream (blue) of the torch exit (0 cm) for the N₂/Ar HF case. Three line-of-sight spectra were taken at different lateral positions (0, 1, and 2 mm).

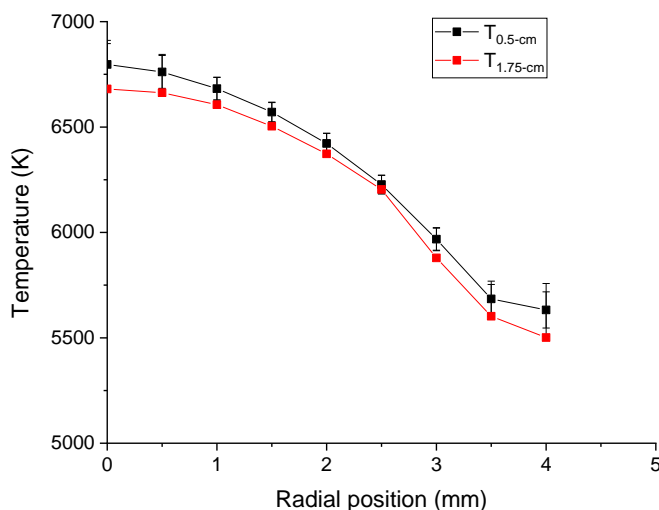


Figure 129: Temperature profiles at the exit of the torch (0 cm) for the N₂/Ar HF case measured 0.5 cm (black) and 1.75 cm (red) downstream of the torch exit.

The comparison between the measured 149-nm line and the SPECAIR spectrum computed with the temperature measured 1.75 cm downstream of the torch exit is presented in Figure 130. The agreement is very poor once again. We used this measurement to determine the equivalent transmittivity of the window. The best agreement was found by taking a transmittivity of 0.33. The spectra multiplied by

this transmittivity at 10 and 15 cm are also plotted in Figure 130. Once again, an uncertainty of 40% was taken on this transmittivity.

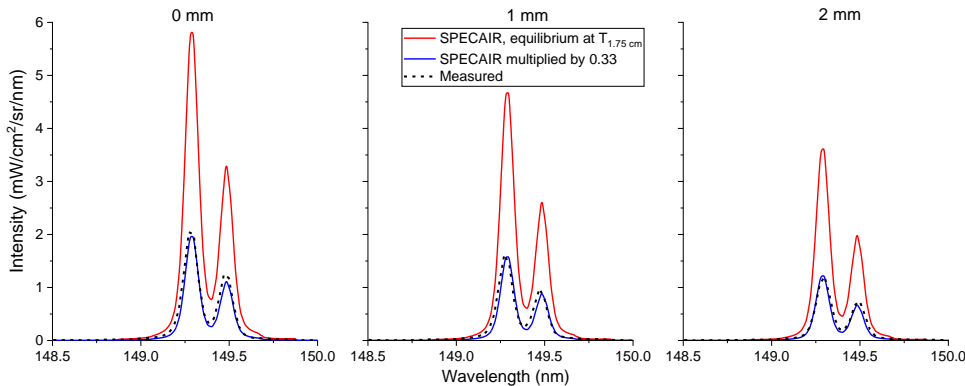


Figure 130: Comparison between measured spectrum (black dash) and SPECAIR calculation assuming the measured temperature profile 1.75 cm downstream of the torch exit (0 cm) for the N₂/Ar HF case. The blue line corresponds to the same calculation multiplied by a transmissivity of 0.33. Three line-of-sight spectra were taken at different lateral positions (0, 1, and 2 mm).

7.6.2.2 At the exit of the 10-cm tube

The 149-nm line was measured at the exit of the 10-cm tube at three different lateral positions, namely 0, 1, and 2 mm. The density of the lower level N(²D⁰) presented in section 7.3 was used as input for the SPECAIR calculations. The computed spectra were multiplied by a transmissivity of 0.33 as explained in 7.6.2.1. The density profile of the upper state was assumed to be self-similar to N(²D⁰) and the amplitude was changed to compute the relative error between calculations and measurements at the three lateral positions. The sum of the error between the measurements and the computed spectra as a function of the input amplitude of the upper state density is shown in Figure 131. The minimum of the error represents the best fit which is $2.3 \cdot 10^8 \text{ cm}^{-3}$ in this case. The comparison between the best fit spectra computed using SPECAIR and the measurements is presented in Figure 132. The good agreement at the three different lateral positions gives confidence in the self-similar density assumption for the upper state. The radial density profiles of the upper and lower states of the 149-nm transition are given in Figure 133.

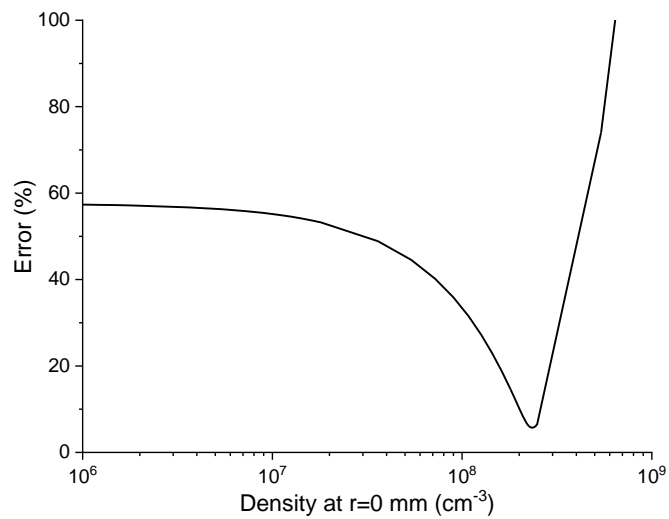


Figure 131: Relative error between measured and computed spectra of the 149-nm line at the exit of the 10-cm tube for the N_2/Ar HF case as a function of the amplitude of the density of the upper state taken in the SPECAIR calculations.

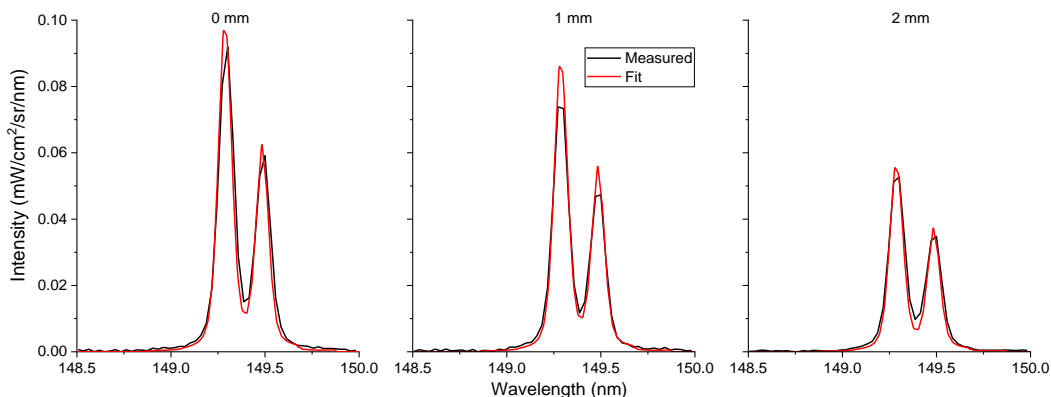


Figure 132: Comparison of the 149-nm line between the measured spectra and the computed spectra using SPECAIR resulting from the best fit at the exit of the 10-cm tube for the N_2/Ar HF case.

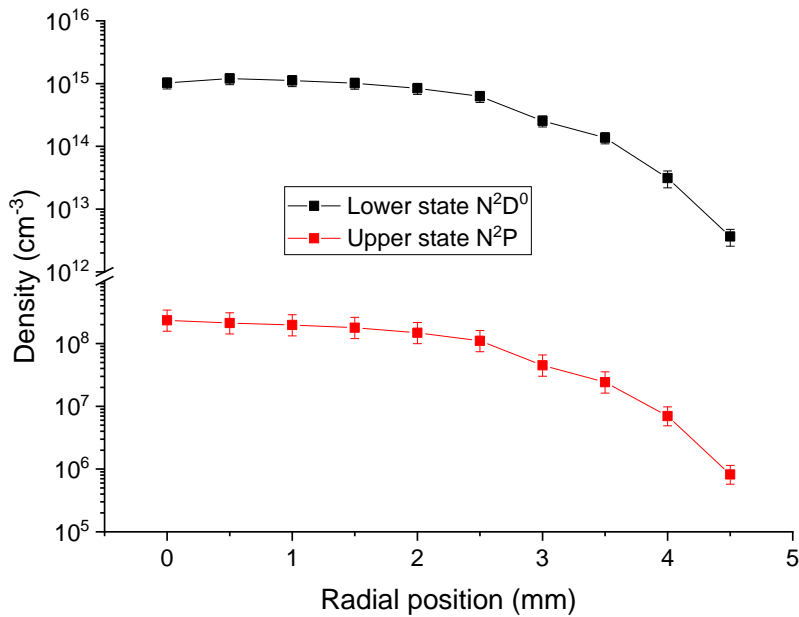


Figure 133: densities of the lower and upper states of the 149-nm transition at the exit of the 10-cm tube for the N_2/Ar HF case. Only the points out to 2 mm were measured for $N(^2D^0)$ and the others were extrapolated.

A comparison between the measured 174-nm doublet and the spectra computed with SPECAIR assuming an optically thin transition and the measured radial density profile of the upper state presented in Figure 133, is shown in Figure 134. The good agreement supports the fact that the transition is optically thin in our conditions. Therefore, the density of the lower state could not be measured. We performed a sensitivity analysis to check the value of the lower state above which the transition is not optically thin anymore and found a value of $1 \cdot 10^{14} \text{ cm}^{-3}$. This represents an upper bound for the density of $N(^2P^0)$ in this condition.

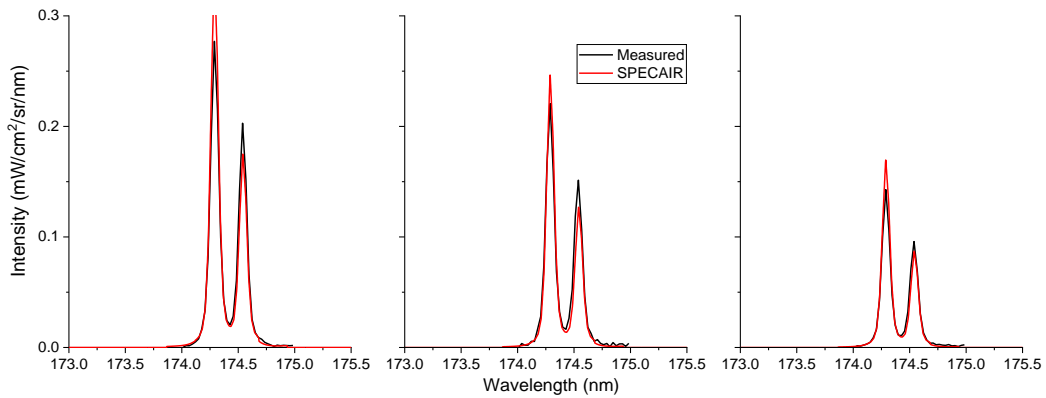


Figure 134. 174-nm line: comparison between the measured spectra and the optically thin computed SPECAIR spectra using the measured density profile of the upper state at the exit of the 10-cm tube for the N₂/Ar HF case. These three line-of-sight spectra were taken at different lateral positions (0, 1, and 2 mm).

7.6.2.3 At the exit of the 15-cm tube

The same analysis was performed at the exit of the 15-cm tube. The error calculated between the experimental and computed spectra is presented in Figure 135 as a function of the N(²D⁰) density amplitude. The best fit corresponds to a value of $2.7 \cdot 10^7 \text{ cm}^{-3}$ and is compared to the measured spectra in Figure 136. Once again, good agreement for each lateral position is observed, supporting the self-similar assumption made for the upper state radial density profile. Both the upper and lower state radial density profiles are presented in Figure 137.

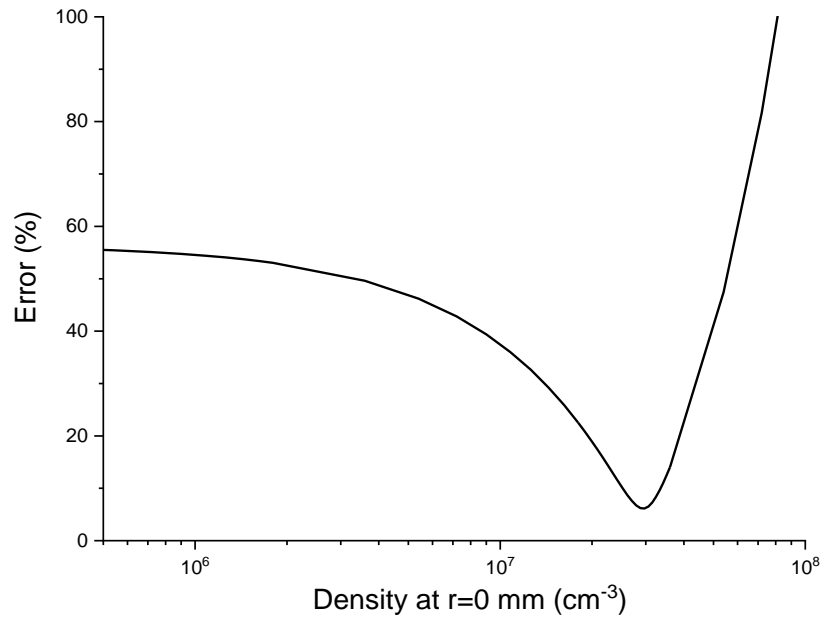


Figure 135: Relative error between measured and computed spectra of the 149-nm line at the exit of the 15-cm tube for the N_2/Ar HF case as a function of the amplitude of the density of the upper state taken in the SPECAIR calculations.

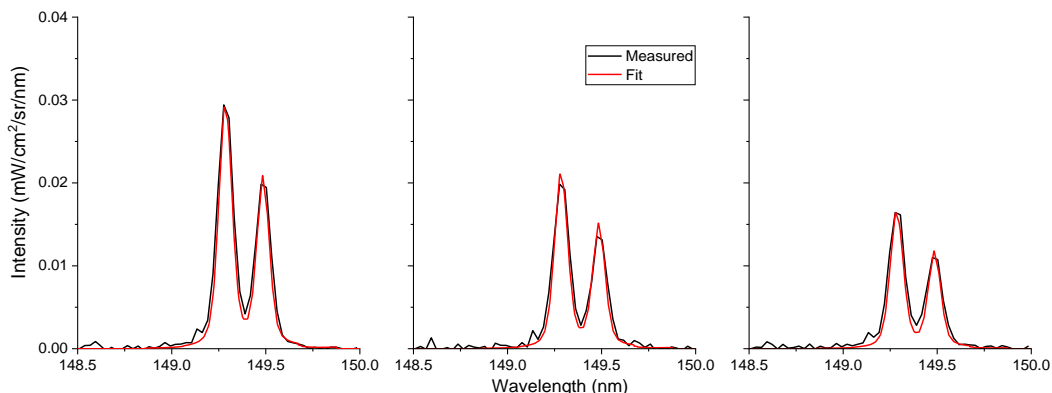


Figure 136. 149-nm line: comparison between the measured spectra and the computed SPECAIR spectra resulting from the best fit at the exit of the 15-cm tube for the N_2/Ar HF case.

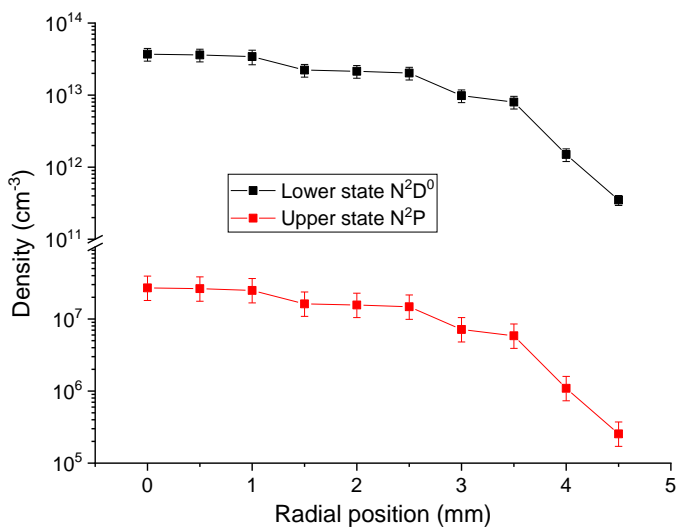


Figure 137: Lower and upper state densities of the 149-nm transition at the exit of the 15-cm tube for the N₂/Ar HF case. Only the points out to 2 mm were measured for N(²D⁰) and the others result from the extrapolation procedure.

The 174-nm transition was found to be optically thin also in this case with the same upper bound of $1 \cdot 10^{14}$ cm⁻³. The comparison between measured and computed spectra at the three lateral positions is given in Figure 138. The good agreement between the spectra at 149 and 174 nm assuming the same density profile for the upper state supports the correction by a transmittivity of 0.33.

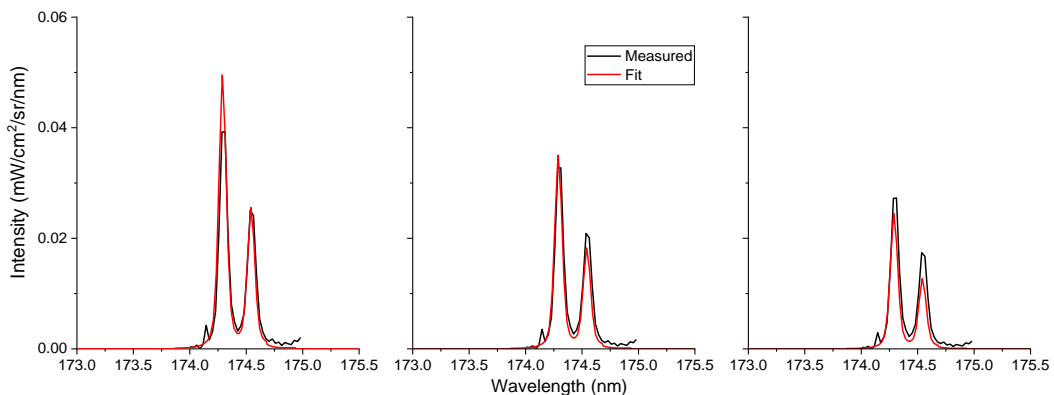


Figure 138. 174-nm line: comparison between the measured spectra and the optically thin computed SPECAIR spectra using the measured density profile of the upper state at the exit of the 15-cm tube for the N₂/Ar HF case. These three line-of-sight spectra were taken at different lateral positions (0, 1, and 2 mm).

7.6.2.4 Distribution of excited N atoms

In Figure 139, we plot the Boltzmann and Saha-Boltzmann distributions along with the densities of excited states of nitrogen measured in the VUV, visible, and NIR at the exit of the 10-cm tube for the N_2/Ar HF case. The electron densities used to determine the Saha-Boltzmann distribution were previously measured in section 7.5. The density of atomic ions was estimated assuming that the overpopulation of N^+ was equal to the overpopulation of the electrons. The higher energy states of atomic nitrogen are highly overpopulated with respect to their equilibrium values. They are well above the Boltzmann distribution and close to the Saha-Boltzmann distribution. If the highest electronic state is in Saha-Boltzmann with the free electrons, then the actual electron number density should be around $1.75 \cdot 10^{13} \text{ cm}^{-3}$, which is close to the estimated lower bound on the measured electron number density (see Figure 111).

This suggests that the high energy states of nitrogen tend to be in equilibrium with the electrons.

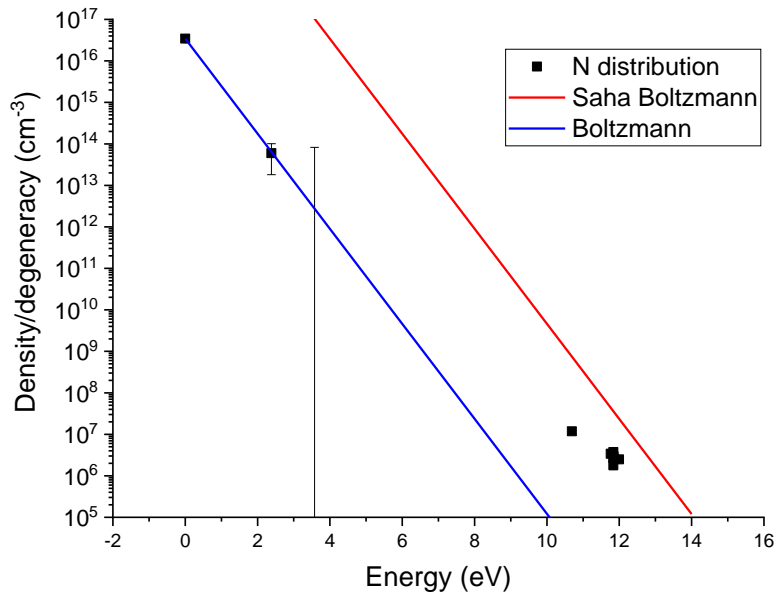


Figure 139: Measured population distribution of ground and excited states of atomic nitrogen (black) at the exit of the 10-cm tube for the N_2/Ar HF case at $r = 0 \text{ mm}$. The Boltzmann (blue) and Saha-Boltzmann (red) distributions are also plotted.

The results at 15 cm are presented in Figure 140. We observe the same trend as at 10 cm. The higher energy levels of atomic nitrogen are highly overpopulated relative to the Boltzmann distribution at the measured temperature and tend to be closer to the Saha-Boltzmann distribution.

If the highest electronic state is in Saha-Boltzmann with the free electrons, then the actual electron number density should be around $4.5 \cdot 10^{12} \text{ cm}^{-3}$.

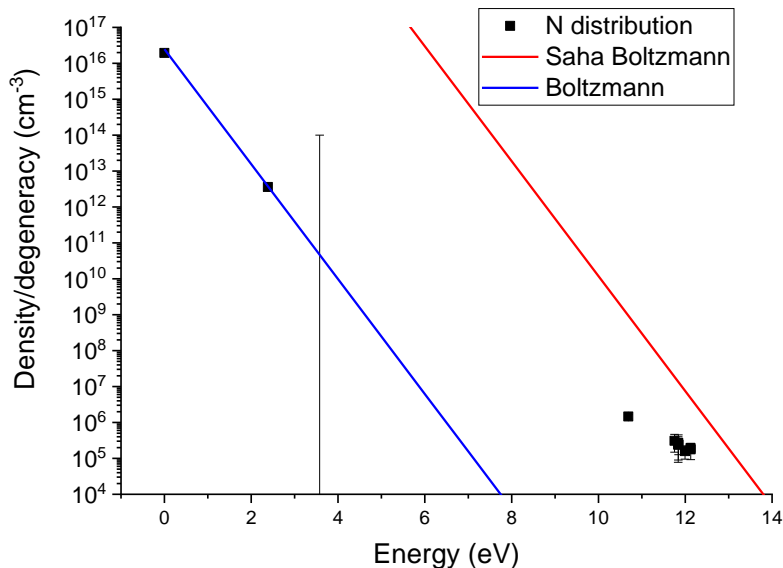


Figure 140: Measured population distribution of ground and excited states of atomic nitrogen (black) at the exit of the 15-cm tube for the N₂/Ar HF case at r = 0 mm. The Boltzmann (blue) and Saha-Boltzmann (red) distributions are also plotted.

7.7 Conclusions

Optical emission spectroscopy from VUV to NIR was performed in a recombining nitrogen flow to measure the population distribution of the electronic states of atomic nitrogen.

At 0 cm (torch exit), the plasma is initially in LTE and the electronic states follow a Boltzmann distribution at the measured temperature.

At both 10 and 15 cm, we observe a departure from the Boltzmann distribution for the densities of the high energy states of atomic nitrogen. These states are close

to the Saha-Boltzmann distribution, which indicates that they are close to a partial equilibrium with the free electrons. This was previously experimentally observed and predicted in previous works.

For example, this was observed in compression flows such as in the Fire II flight experiment (Cauchon, 1967). Panesi *et al* (Panesi, et al., 2009) and Johnston (Johnston, 2006) predicted high excited states of atomic nitrogen underpopulated with respect to the Boltzmann distribution. In their conditions, as is usually the case in such hypersonic compression flows, the chemistry is partly frozen, and the Saha-Boltzmann distribution curve is lower than the Boltzmann one due to an underpopulation of electrons compared to equilibrium conditions. The density of excited atomic nitrogen approaches the Saha-Boltzmann distribution for high energy levels.

In expanding flows such as in the afterbody region of a reentry capsule, Johnston and Brandis (Johnston & Brandis, 2015) predicted a similar trend. In this case, the Saha-Boltzmann distribution yields higher densities than the Boltzmann distribution as the chemistry is partly frozen. The excited states of atomic nitrogen are overpopulated compared to the Boltzmann distribution and their densities tend to follow the Saha-Boltzmann one for high energy levels. This model was compared to Fire II (Cauchon, 1967) and Stardust Echelle experiments (Jenniskens, 2010) and was able to improve the radiation prediction.

The CR models are also used to predict the radiation in shock tubes such as the EAST facility. Previous work (Lemal, et al., 2012) showed the importance of correctly predicting the density of atomic nitrogen to avoid uncertainties on the resulting radiation.

The present data are the first measurements of such distributions in high temperature nitrogen plasmas. Our experiments provide a set of data that can be used to validate CR models for atomic nitrogen. Also, the simple configuration of our experiment may be useful to validate the kinetics of nitrogen by coupling CR and CFD models.

Chapter 8 Power Balance

In this Chapter, a power balance is performed to compare the power removed by the water-cooling system of the tubes and the change in power of the plasma flow. This power balance verification is intended to validate the measurements of temperatures and chemical composition in the three cases considered, Air/Ar, N₂/Ar LF, and N₂/Ar HF.

8.1 Power balance assuming equilibrium

8.1.1 Model

In Chapter 3, the temperature of the gas was measured. Large drops in temperature were observed for the different cases. The main source of gas cooling is by heat transfer to the tube wall, which is maintained at a temperature of 300 K by water-cooling. The water temperature and mass flowrate were measured at the inlet and outlet of the tube using thermocouples and flowmeters. These data can be used to perform a power balance on the water-cooling system. The power lost by the plasma while flowing through the tube must be equal to the power evacuated via water cooling. A schematic of the system is presented in Figure 141.

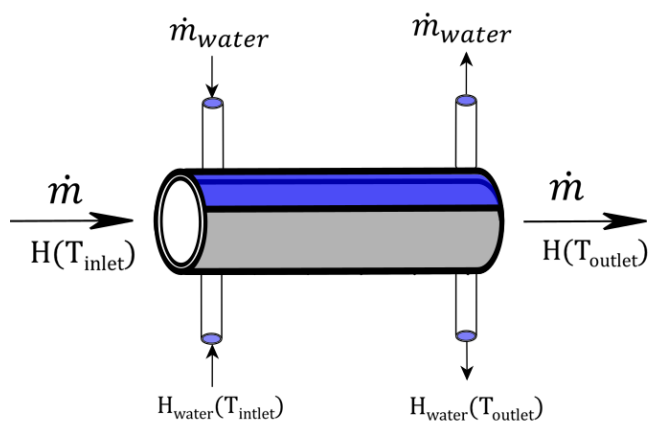


Figure 141: System considered for the power balance. The energy lost by the gas is gained by the water.

The gas enthalpy was estimated from the measured temperature profiles at both the inlet and outlet of the tube. The power balance, assuming equilibrium conditions, is then:

$$\begin{aligned} \Delta P_{gas \text{ (equilibrium)}} &= \left[\int_{r=0 \text{ mm}}^{r=5 \text{ mm}} \rho_{gas} V_{gas} h_{gas}^{eq} 2\pi r dr \right]_{outlet} \\ &\quad - \left[\int_{r=0 \text{ mm}}^{r=5 \text{ mm}} \rho_{gas} V_{gas} h_{gas}^{eq} 2\pi r dr \right]_{inlet} \end{aligned} \quad (8.1)$$

where V_{gas} represents the gas velocity, ρ_{gas} the mass density, and h_{gas}^{eq} the specific enthalpy at equilibrium. The thermodynamic properties of the plasma were calculated using the CEA code (McBride & Gordon, June 1996) at the measured temperatures. Note that the velocity is estimated by matching the mass flow rate. Two cases were considered in order to estimate the uncertainties on the velocity. First, a radial velocity profile self-similar to the measured temperature profile was taken. This is justified by the fact that the Prandtl number is close to unity. The amplitude of the velocity was then adjusted by matching the measured mass flow rate. Second, we considered a constant velocity profile ($V_{gas} = \text{constant}$) and adjusted it to match the mass flow rate. An example of the velocity profiles used for the N₂/Ar HF case is presented in Figure 142.

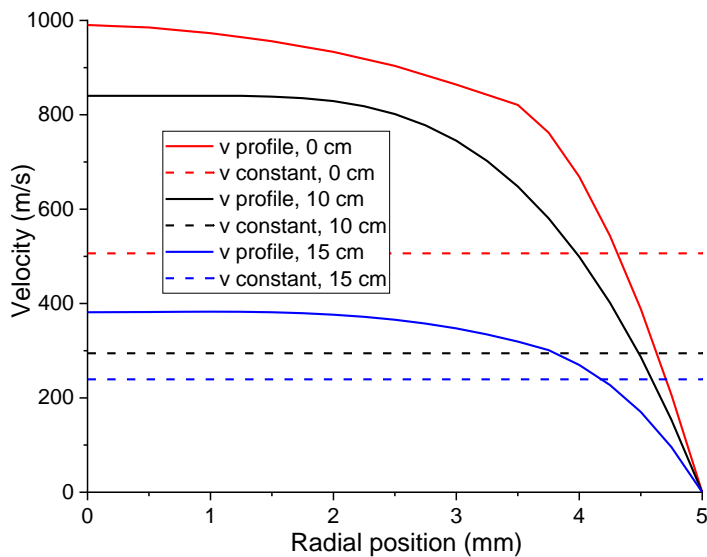


Figure 142: Velocity profiles considered in the power balance for the N₂/Ar HF case at the three axial positions.

The calorimetric power balance on the water that traverses the water-cooled tube gives the power removed and is equal to:

$$\Delta P_{water} = \dot{m}_{water} c_{p_{water}} (T_{wo} - T_{wi}) \quad (8.2)$$

where \dot{m}_{water} is the measured water mass flow rate, and T_{wi} and T_{wo} are the temperatures of the water at the inlet and the outlet of the cooling tube, respectively. The mass flowrate of water was measured using calibrated rotameters. The specific heat capacity of water was taken equal to 4185 J/K/kg (Taine, et al., 2008).

Other energy loss terms were also considered that could potentially alter the power balance. First, radiative losses through the top orifice of the tube were estimated using SPECAIR. The total volumetric intensity radiated by the Air/Ar plasma at 7000 K is about 0.2 W/cm³/sr. We consider the plasma to be at a uniform temperature throughout a 15-cm tube. This represents an upper bound as the temperature over a large portion of the tube is significantly less than 7000 K. In this case, the power loss due to radiation escape at the top of the tube is about 25 W. This is found to be negligible compared to other contributions.

The water temperature was measured 0.5 m upstream of the tube water inlet and 0.5 m downstream of the tube water outlet. Convective losses to the walls of the tubing were estimated. The inlet temperature was measured to be at room temperature and therefore negligible heat exchange is expected before entering the tube. At the tube outlet, the maximum measured temperature was 10 K above its entry value. The heat transfer coefficient between the wall and the water was estimated using standard correlations from (Taine, et al., 2008) and presented in Chapter 5. The power loss is then calculated using:

$$P_{loss} = h_{water \rightarrow wall} S_{tube} (T_{water} - T_{wall}) \quad (8.3)$$

where S_{tube} is the surface area of the 0.5 m long portion of tubing. As an upper bound, T_{wall} was taken to be equal to the room temperature. This results in $P_{loss} \cong 20 W$, which is also negligible compared to other contributions. Thus, the primary loss responsible for changing the plasma power is the heat transfer at the wall.

The kinetic energy loss along the 15-cm tube was also estimated and found to be below 100 W for the N₂/Ar HF case, which is negligible compared to other contributions.

Assuming equilibrium conditions for the plasma, the power balance then reads:

$$\dot{m}_{water} c_{p_{water}} (T_{wo} - T_{wi}) = h_{water \rightarrow wall} S_{tube} (T_{water} - T_{wall}) \quad (8.4)$$

8.1.2 Results

The results for ΔP_{water} and $\Delta P_{gas \text{ (equilibrium)}}$ for the Air/Ar case are presented in Figure 143.

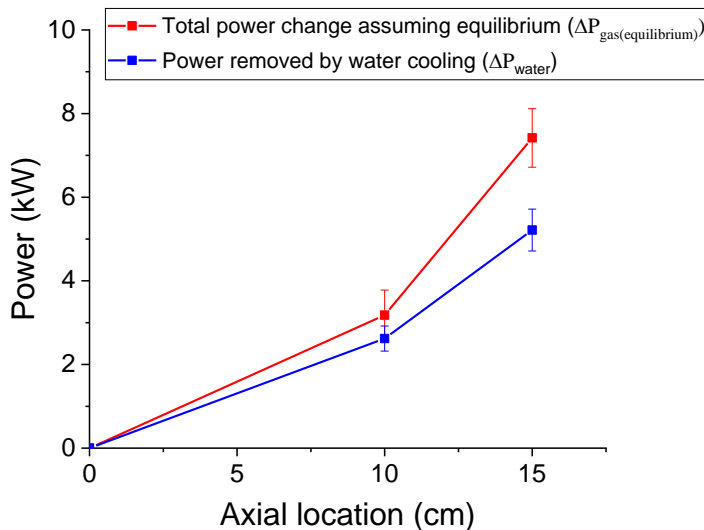


Figure 143: Power measurements for the Air/Ar case. Blue: measured power removed by water cooling. Red: Power lost between the inlet and the exit of the tube assuming equilibrium throughout the tube.

At 10 cm, both approaches give the same results to within their respective uncertainty. This provides additional evidence for the equilibrium assumption. At 15 cm, we see a difference between the two lines. This may indicate that some power is stored as chemical energy (likely into unrec combined N atoms or rovibronic states), the power loss assuming equilibrium being higher than the power removed by water cooling. Note that the measured spectra were measured from 0 to 4 mm radially and were found to agree with computed spectra assuming equilibrium.

However, no measurements were performed near the wall, because the signal was too low, where the gas could be out of equilibrium, explaining the difference in the power balance.

Results for the N₂/Ar LF case are presented in Figure 144. In this case, ΔP_{water} largely differs from $\Delta P_{gas (equilibrium)}$. The plasma for this case was found to be in nonequilibrium and therefore energy can be stored into unrec combined excited states or nitrogen atoms. Similar conclusions can be drawn for the N₂/Ar HF case presented in Figure 145, with a measured difference between the two curves of about 7 kW at 15 cm. These two cases show that a large amount of power is stored into chemistry as the plasmas are not in equilibrium. A main source of power storage could come from the unrec combined nitrogen atoms, previously measured using emission spectroscopy. In the next section, we will estimate the amount of power related to these unrec combined species.

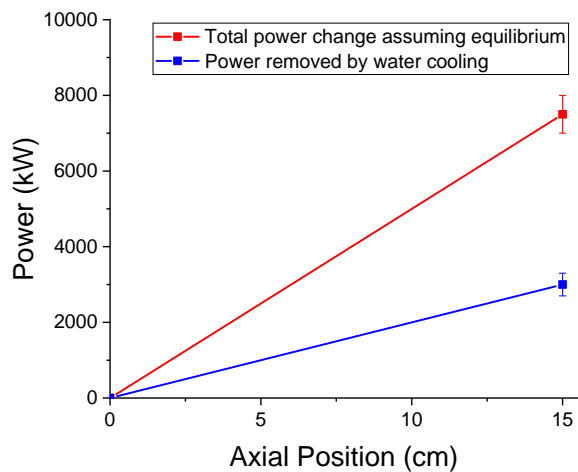


Figure 144: Power measurements for the N₂/Ar LF case. Blue: measured power removed by water cooling. Red: Power change between the exit and the inlet of the tube assuming equilibrium throughout the tube.

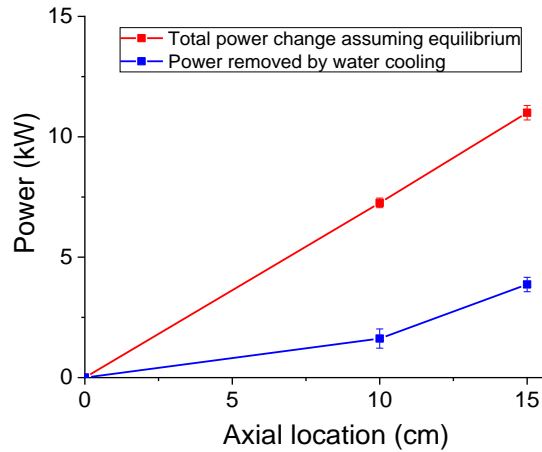


Figure 145: Power measurements for the N₂/Ar HF case. Blue: measured power removed by water cooling. Red: Power change between the exit and the inlet of the tube assuming equilibrium throughout the tube.

8.2 Power balance including chemical nonequilibrium

8.2.1 Chemical energy storage

As presented in Chapter 7, the nitrogen atoms are highly overpopulated for the two N₂/Ar nonequilibrium cases. This is an important consideration for the power balance. Considering the density of nitrogen atoms measured in Chapter 7, the volumetric enthalpy stored in unrec combined ground state nitrogen atoms is given by the following relation, taking into account the corresponding underpopulation of N₂:

$$\Delta h_{N-N} = (n_N - n_N^*)(E_{diss_{N_2}}/2 - E_{N_2}) \quad (8.5)$$

where n_N is the measured number density of N, n_N^* is the equilibrium density of N, E_{N_2} is the energy stored into rovibrational levels of N₂ and $E_{diss_{N_2}} = 9.8$ eV the energy of dissociation of N₂. The excess power stored in dissociated nitrogen, relative to equilibrium, at axial location x is then:

$$\Delta P_{N-N} = \int_{r=0}^{r=R} \Delta h_{N-N} V_{gas}(x, r) 2\pi r dr \quad (8.6)$$

where $V_{gas}(x, r)$ is the velocity of the gas at the axial position x and radius r. Note that the velocity was not measured and is therefore estimated. An example of the different velocity profiles considered can be found in Figure 142.

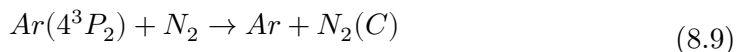
The chemical energy stored in the overpopulated electronic states of N and the vibrational levels of $N_2(B)$, $N_2^+(B)$ and $N_2(C)$, measured using emission spectroscopy, was also considered. The energy per unit volume stored into $N_2(B)$ vibrational levels, for example, is:

$$\Delta h_{N_2B} = \sum_{v=0}^{v_{max}} (n_{N_2B}^{meas}(v) - n_{N_2B}^*(v)) E_{N_2B}(v) \quad (8.7)$$

where $n_{N_2B}^{meas}(v)$ is the measured density of the vibrational level v of $N_2(B)$ and $E_{N_2B}(v)$ its energy. Finally, the total power stored in the plasma chemistry is:

$$\Delta P_{chemistry} = \Delta P_{N-N} + \sum_{A^*} \Delta P_{A^*} \quad (8.8)$$

where ΔP_{A^*} is the energy stored into the overpopulated excited state of species A. In our case, we measured it for $N_2(B)$, $N_2(C)$ and $N_2^+(B)$. The power stored into the excited molecular levels was found to be negligible when compared to the power stored into unrecombined N atoms. For example, the power stored into the $N_2(B)$ vibrational levels at the exit of the 15-cm tube in the N_2/Ar HF case is only about 1 mW. Note that A could also be an ion. Using the measured electron number density and assuming that N_2^+ is the only ion present in the plasma, the energy stored into ions is around 1 W, which is negligible compared to other contributions. Based on these measurements, we assumed $\sum_{A^*} \Delta P_{A^*}$ to be negligible compared to ΔP_{N-N} . Note that the energy stored into argon excited states was not measured. Reactions between argon metastable and $N_2(C)$ and $N_2(B)$ could occur in N_2/Ar plasmas, as explained by (Shneider, et al., 2011) (Zhang, et al., 2018), such as:



The overpopulation of $Ar(4^3P_2)$ was not measured, but using Eq.(8.9) we can assume that its overpopulation will be close to the overpopulation of $N_2(C)$. Their energies are also very close leading to an energy stored into argon close to the one

stored into $N_2(C)$ or $N_2(B)$ which was found to be negligible. Therefore, we assumed that the energy stored into excited states of argon was also negligible compared to other contributions.

The power balance presented in section 8.1 now becomes:

$$\Delta P_{water} = \Delta P_{gas \text{ (equilibrium)}} - \Delta P_{chemistry} \quad (8.10)$$

8.2.2 Results

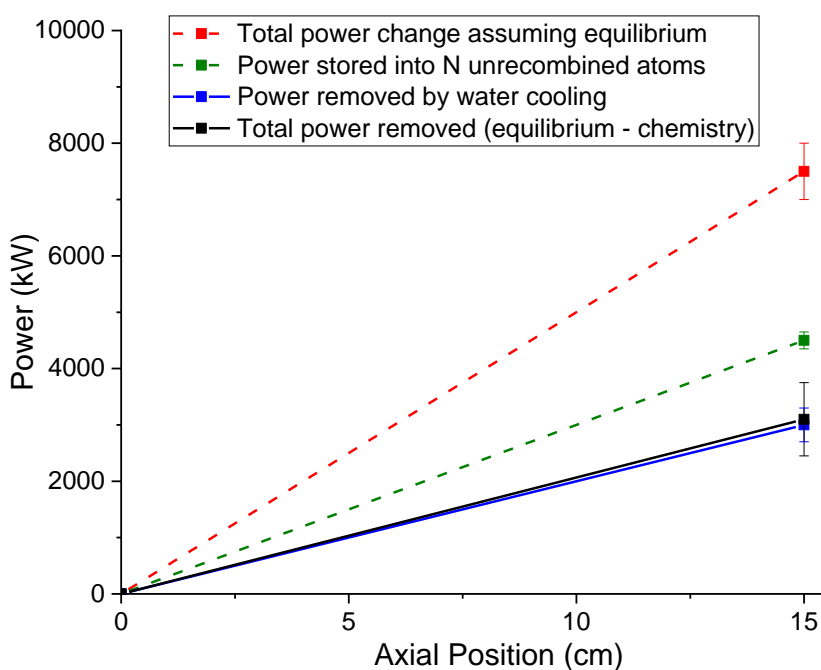


Figure 146: Power balance measurements for the N_2/Ar plasma (low mass flowrate), using two different approaches. Blue: measured power removed by water cooling. Red: Power change between the outlet and the inlet of the tube assuming equilibrium throughout the tube. Green: power stored into unrec combined N atoms using the measured overpopulation factors. Black (red minus green curve): total power removed from the gas.

Figure 146 shows the results obtained for the power measurements in the N_2/Ar LF case. Note that at 15 cm, the temperature was measured using Raman spectroscopy only out to $r = 2$ mm and was then extrapolated to $r = 5$ mm, leading to higher uncertainties for the power measurement depending on this temperature profile chosen. The good agreement between the black and the blue curves suggests

that the unrec combined N atoms account for the missing power. Figure 146 shows the importance of accounting for chemical nonequilibrium in the power balance.

The results for the N_2/Ar HF case are presented in Figure 19. The good agreement between the black and the blue curves suggests again that the unrec combined N atoms account for the missing power. Note that all the calculations were done using the temperature measured via Raman spectroscopy.

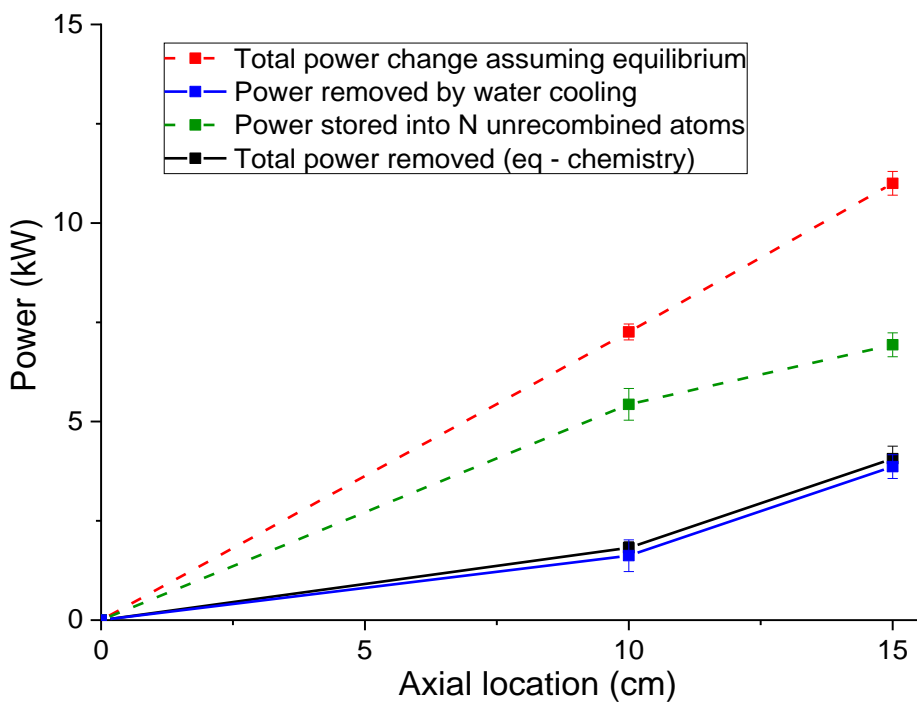


Figure 147: Power balance measurements for the N_2/Ar plasma (high mass flowrate), using two different approaches. Blue: measured power removed by water cooling. Red: Power change between the outlet and the inlet of the tube assuming equilibrium throughout the tube. Green: power stored into unrec combined N atoms using the measured overpopulation factors. Black (red minus green curve): total power removed from the gas.

This power balance gives us confidence in the emission spectroscopy and Raman measurements as, together, they form a consistent set of data.

Although our measurements are self-consistent, they cannot allow us to conclude on which mechanism causes the rapid drop in temperature observed for all test cases: nitrogen/argon, air/argon and pure air plasmas. We examined this question with CFD models in Chapter 5 and were unable to reproduce the measured drop

in temperature. Evidently, this chemical effect is as important as the heat transfer to the water-cooled tube walls. An accurate kinetic model is therefore required to correctly predict the drop in temperature using a CFD code.

8.3 Conclusion

A power balance analysis was performed for the three different cases. For the Air/Ar case, it yields relatively good agreement if the plasma is assumed to stay in LTE throughout the tube, in agreement with the spectroscopic measurements presented in the previous chapters. A slight discrepancy was observed in Figure 143 at 15 cm. This was attributed to a slight non-measured overpopulation of atomic nitrogen near the wall. This plays an important role in the N₂/Ar cases but could not be measured near the wall in the Air/Ar case due to the low emission near the wall. Moreover, the cooling is expected to be faster near the wall, which could induce in this case a small nonequilibrium.

For the two N₂/Ar cases, the power removed by water cooling and the power loss calculated by assuming the gas to be in equilibrium largely differed. For these cases, the plasma is not in equilibrium and therefore energy is stored in the unrec combined N atoms. The density of $N(^4S)$ was measured for 10 and 15 cm tube lengths as presented in Chapter 7 and was found to be highly overpopulated. We found that the unrec combined N atoms accounted for the missing power. This is an interesting observation as it links multiple measurements performed using different diagnostics. Together with the emission and Raman spectroscopy measurements, we now have a consistent data set.

This power balance also shows the importance of the kinetic modeling used in CFD codes because the power stored in the chemistry can exceed the thermal power and can only be predicted using a detailed kinetic code.

Chapter 9 Conclusions

9.1 Contributions of this thesis

Experiments were conducted in a 50-kw inductively coupled plasma torch facility. The plasma torch provides a plasma in LTE. A water-cooled tube is mounted on top of the torch to force rapid plasma recombination. This experimental setup aims to reproduce conditions relevant to the study of radiation phenomena in the afterbody region of a capsule during Earth reentry, the sharp expansion encountered during a real reentry being approximated by a rapid temperature decrease enforced by the water-cooled tube. It represents a seemingly simple test case for numerical codes used for reentry. However, the discrepancy between CFD predictions and our measurements indicates that there remains a large discrepancy in understanding. Three different mixtures were studied: two nitrogen/argon mixtures and one air/argon mixture. Optical diagnostics were performed at the exit of the plasma torch facility and at the exit of 10-cm and 15-cm water-cooled tubes. Previous experiments using this configuration were performed at Stanford university. These previous results had shown that the air plasmas tend to stay under LTE at the exit of the water-cooled tubes while a departure from chemical equilibrium was observed for the nitrogen/argon plasmas. Moreover, the measured temperature drop was found to be much larger than the predicted one using CFD codes for all three mixtures. Our results confirm this but add several new levels of detail.

The temperature of the plasma was measured using Raman spectroscopy to get the vibrational and rotational temperatures of $N_2(X)$. The rotational temperature of the ground state of N_2 is viewed as representative of the bulk gas temperature. Emission spectroscopy was used to get the rotational temperature of the excited $N_2(B)$, $N_2(C)$ and $N_2^+(B)$ states. All measured temperatures showed good agreement at the exit of the plasma torch, as expected for an LTE plasma. At the exit of the 10 and 15-cm tubes for the nitrogen test cases, good agreement was observed between the Raman and OES temperature measurements, except for the rotational temperature of $N_2^+(B)$ which yields a larger value. The rotational temperature of $N_2^+(B)$ was found to differ from the gas temperature as the rotational-translational relaxation time of this excited state is smaller than its

production time. Temperature estimates using emission spectroscopy need to be critically viewed before being assumed to be representative of the gas temperature. Our work indicates that, for recombining plasmas, $N_2^+(B)$ is not a suitable candidate, whereas $N_2(B)$ and $N_2(C)$ appear much better. The gas temperature measured with Raman spectroscopy was found to be lower than the temperature measured at Stanford using emission spectroscopy, further increasing the disagreement between experiments and simulations. CFD simulations using the Eilmer3 code were performed. The poor agreement shows the continued inability of the CFD codes to correctly predict the measured temperature drop even in an equilibrium, laminar, air plasma case. This remains an open question.

Optical emission spectroscopy was also used to measure the radiation emitted by the plasmas. The plasmas were found to be in nonequilibrium at the exit of the water-cooled tubes for the nitrogen/argon test cases. The molecular radiation, measured from the UV to NIR region, was much larger than the corresponding equilibrium value - up to 10,000 times stronger. This factor decreases to 10 if a two-temperature (2T) model is used. The radiation measurements were used to determine the vibrational population distribution of the emitting molecular electronic states, namely $N_2(B)$, $N_2(C)$, and $N_2^+(B)$. These were found highly overpopulated relative to their equilibrium values, explaining the difference in the observed radiation. The distribution of the $N_2(B)$ vibrational levels did not follow a Boltzmann distribution. The disagreement between the computed radiation using the 2T model and the measurement was attributed to the inability of the 2T model to predict the measured distribution of these levels and especially the non-Boltzmann distributions. Measurements of atomic lines were also performed, from the VUV to NIR, to get the distribution of electronic levels of atomic nitrogen. Atomic nitrogen is of particular interest as it is the main source of radiation in the afterbody region during reentry. The lower electronic states were in equilibrium with the ground state following a Boltzmann distribution, but the higher levels were found to be closer to the Saha-Boltzmann distribution. Such a distribution is typical for nonequilibrium recombining flows and was experimentally shown in this work.

To conclude, we measured the radiation of nonequilibrium recombining nitrogen plasma flows and measured populations of excited molecular and atomic nitrogen to provide test-cases for the kinetic and CFD codes used to model Earth reentry

conditions. The measured atomic nitrogen distribution represents the first measurement of such a distribution for nonequilibrium recombining flows. We hope that this experimental data can be used to validate the codes used for reentry to improve the prediction of the radiative heat fluxes on the afterbody during Earth entry.

9.2 Recommendations for future work

The inability of the CFD codes to predict the temperature drop measured across the recombining tube raises many questions. Results were presented for the simplest case we could implement – simple geometry (a tube), laminar (no turbulence model needed), equilibrium (no kinetic model needed) and air (well-known gas), and yet a large disagreement with experimental measurements was found. The discrepancy seems to come from an insufficient radial heat transfer in the gas. This case should be the first step to solve this CFD problem. To achieve the first step, a physical reason needs to be found to increase the radial transport. We believe it could come from different effects: either a hydrodynamic effect (3D vortex, swirl, turbulence...) or a radiative effect (radiative conductivity). Attempts to solve this problem on our part have failed. Once good agreement is achieved for this first test case, the air/argon mixture case is viewed as a logical next step, as it adds only turbulence. Finally, the last step is viewed as the modeling of the nitrogen/argon test cases. These add nonequilibrium dynamics, beginning with a relatively low level of nonequilibrium for the low flowrate test-case and proceeding to a higher level with the high flow rate test cases.

From a kinetic point of view, the data presented in this work can be very valuable to validate the codes used to simulate recombining flows, for which fewer data exist than for compression flows. Collisional-Radiative models can be used to simulate the presented cases, independently of the CFD problem, considering the measured temperature profile along the axis of the tube as input. This is of particular interest for CR codes modeling the atomic nitrogen distribution as it represents the main source of radiation in a real reentry scenario and is therefore the most important species to correctly predict. Note that measurements below 149 nm could also be considered in the future to extract the density of additional excited atomic nitrogen cases.

From an experimental point of view, we presented mainly data for nitrogen kinetics. It would be interesting to perform similar studies with nonequilibrium air cases, so as to provide data to test kinetic models with oxygen species and their interactions with the nitrogen species. Also, the study of the influence of ablative products, in particular carbon-containing molecules such as CN and CO, would be an interesting next step for this study. Finally, for Mars entry experiments CO plasmas could also be studied to provide validation data. A new Ph.D. thesis is currently underway at CentraleSupélec to explore nonequilibrium recombination mechanisms in CO₂ plasmas.

A) Appendix: Reaction rates constants and gas composition

In this appendix, we summarize the reaction rates constant used in the thesis and the gas composition of the different gas mixture presented.

A.1) Reaction rates constants

Name	Reaction	Rate constant	Ref.
R1	$N_2^+(B) + N_2 \rightarrow N_2^+(X) + N_2$	$6.8 \cdot 10^{-10}$	(Valk, et al., 2010)
R2	$N + N \rightarrow N_2^+(X) + e^-$	$2.32 \cdot 10^{-11} \exp\left(-\frac{67800}{T}\right)$	(Park, 1993) (Gupta, et al., 1990)
R3	$N^+ + N_2 \rightarrow N_2^+(X) + N$	$3.35 \cdot 10^{-13} T^{0.8} \exp\left(-\frac{13000}{T}\right)$	(Park, 1993) (Gupta, et al., 1990)
R4	$Ar^+ + N_2 \rightarrow N_2^+(X) + Ar$	$4.5 \cdot 10^{-10}$	(Shneider, et al., 2011)
R5	$N_2(Y) + N_2(a') \rightarrow N_2(X) + N_2^+(X). \quad Y = A, a'$	$2.2 \cdot 10^{-10}$	(Linss, et al., 2004) (Brunet, et al., 1983)
R6	$N_2^+(X) + e^- \rightarrow N_2^+(B) + e^-$	$1 \cdot 10^{-11}$	(Crandall, et al., 1974)
R7	$N_2^+(X) + Ar^* \rightarrow N_2^+(B) + Ar$	$9.8 \cdot 10^{-12}$	(Shneider, et al., 2011)
R8	$N_2^+(X) + N_2(X, v \geq 12) \rightarrow N_2^+(B) + N_2(X, v - 12)$	$(1\sim5) \cdot 10^{-8}$	(Massabieu, et al., 1983)

R9	$N_2(X) + e^- \rightarrow N_2^+(B) + 2e^-$	$1 \cdot 10^{-12}$	(Massabieux, et al., 1983)
----	--	--------------------	-------------------------------

A.2) Gas composition

N_2/Ar high flow rate mole fraction:

T	e^-	N_2^+	N^+	N	Ar	N_2	Ar^+
2000	0	0	0	0	3.55E-01	6.45E-01	0
2250	0	0	0	0	3.55E-01	6.45E-01	0
2500	0	0	0	0	3.55E-01	6.45E-01	0
2750	0	0	0	0	3.55E-01	6.45E-01	0
3000	0	0	0	1.11E-05	3.55E-01	6.45E-01	0
3250	0	0	0	4.92E-05	3.55E-01	6.45E-01	0
3500	0	0	0	1.77E-04	3.55E-01	6.45E-01	0
3750	0	0	0	5.35E-04	3.55E-01	6.45E-01	0
4000	0	0	0	1.41E-03	3.54E-01	6.44E-01	0
4250	0	0	0	3.33E-03	3.54E-01	6.43E-01	0
4500	0	0	0	7.15E-03	3.53E-01	6.39E-01	0
4750	0	0	0	1.41E-02	3.52E-01	6.34E-01	0
5000	0	0	0	2.60E-02	3.50E-01	6.24E-01	0
5250	0	0	0	4.50E-02	3.47E-01	6.08E-01	0
5500	0	0	0	7.35E-02	3.42E-01	5.85E-01	0
5750	1.33E-05	0	0	1.14E-01	3.34E-01	5.52E-01	0
6000	2.87E-05	0	1.45E-05	1.68E-01	3.25E-01	5.07E-01	0
6250	5.83E-05	1.27E-05	3.40E-05	2.36E-01	3.13E-01	4.51E-01	1.16E-05
6500	1.12E-04	1.94E-05	7.33E-05	3.15E-01	2.99E-01	3.86E-01	1.96E-05
6750	2.05E-04	2.75E-05	1.46E-04	4.01E-01	2.84E-01	3.15E-01	3.19E-05
7000	3.57E-04	3.60E-05	2.71E-04	4.86E-01	2.68E-01	2.45E-01	5.01E-05
7250	5.93E-04	4.39E-05	4.72E-04	5.63E-01	2.55E-01	1.82E-01	7.72E-05
7500	9.44E-04	5.02E-05	7.77E-04	6.26E-01	2.43E-01	1.29E-01	1.17E-04
7750	1.45E-03	5.47E-05	1.22E-03	6.75E-01	2.34E-01	8.84E-02	1.76E-04
8000	2.15E-03	5.73E-05	1.83E-03	7.08E-01	2.28E-01	5.95E-02	2.61E-04

N_2/Ar low flow rate mole fraction:

T	e^-	N_2^+	N^+	N	Ar	N_2	Ar^+
2000	0	0	0	0	4,55E-01	5,45E-01	0
2250	0	0	0	0	4,55E-01	5,45E-01	0
2500	0	0	0	0	4,55E-01	5,45E-01	0
2750	0	0	0	0	4,55E-01	5,45E-01	0
3000	0	0	0	1,02E-05	4,55E-01	5,45E-01	0

3250	0	0	0	4,52E-05	4,55E-01	5,45E-01	0
3500	0	0	0	1,62E-04	4,55E-01	5,45E-01	0
3750	0	0	0	4,92E-04	4,55E-01	5,45E-01	0
4000	0	0	0	1,30E-03	4,54E-01	5,44E-01	0
4250	0	0	0	3,06E-03	4,54E-01	5,43E-01	0
4500	0	0	0	6,57E-03	4,53E-01	5,40E-01	0
4750	0	0	0	1,30E-02	4,52E-01	5,35E-01	0
5000	0	0	0	2,39E-02	4,49E-01	5,27E-01	0
5250	0	0	0	4,13E-02	4,45E-01	5,13E-01	0
5500	0	0	0	6,75E-02	4,39E-01	4,93E-01	0
5750	1,32E-05	0	0	1,05E-01	4,31E-01	4,65E-01	0
6000	2,84E-05	0	1,34E-05	1,54E-01	4,20E-01	4,26E-01	0
6250	5,76E-05	1,08E-05	3,16E-05	2,16E-01	4,06E-01	3,78E-01	1,53E-05
6500	1,11E-04	1,65E-05	6,81E-05	2,88E-01	3,89E-01	3,23E-01	2,60E-05
6750	2,02E-04	2,33E-05	1,36E-04	3,66E-01	3,71E-01	2,63E-01	4,25E-05
7000	3,50E-04	3,04E-05	2,52E-04	4,42E-01	3,54E-01	2,03E-01	6,75E-05
7250	5,80E-04	3,70E-05	4,38E-04	5,11E-01	3,38E-01	1,50E-01	1,05E-04
7500	9,23E-04	4,22E-05	7,20E-04	5,68E-01	3,25E-01	1,06E-01	1,60E-04
7750	1,41E-03	4,58E-05	1,13E-03	6,10E-01	3,15E-01	7,23E-02	2,42E-04
8000	2,10E-03	4,78E-05	1,69E-03	6,40E-01	3,08E-01	4,86E-02	3,61E-04

References

- Agrawal, P., Ellerby, D., Switzer, M. & Squire, T., 2010. Multidimensional Testing of Thermal Protection Materials in the Arcjet Test Facility. *American Institute of Aeronautics and Astronautics*, Issue AIAA 2010-4664.
- Amme, R. C. & Hayden, H. C., 1965. IonBeam Excitation Effects on the Single Charge Transfer between Argon and Nitrogen. *The Journal of Chemical Physics*, Volume 42, pp. 2011-2015.
- Anderson Jr, J. D., 2006. *Hypersonic and High-Temperature Gas Dynamics*. s.l.:AIAA Education Series.
- Anderson, J. D. J., 1969. An engineering survey of radiating shock layers. *AIAA Journal*, 7(9), pp. 1665-1675.
- Anon., 2006. *Hypersonic and High-Temperature Gas Dynamics, Second Edition*. s.l.:AIAA Education Series.
- Aristotle, n.d.. *Politics, Book V*. s.l.:s.n.
- Bihari, B. et al., 2011. Orion Capsule Handling Qualities for Atmospheric Entry. *American Institute of Aeronautics and Astronautics*, Issue AIAA 2011-6264.
- Bogdanoff, D. W., 2009. Shock Tube Experiments for Earth and Mars Entry Conditions. *Technical report*.
- Brandis, A. M. & Cruden, B. A., 2017. Benchmark Shock Tube Experiments of Radiative Heating Relevant to Earth Re-entry. *American Institute of Aeronautics and Astronautics*, Issue AIAA 2017-1145.
- Brandis, A. M. & Cruden, B. A., 2018. Shock Tube Radiation Measurements in Nitrogen. *American Institute of Aeronautics and Astronautics*, Issue AIAA 2018-3437.
- Bruggeman, P. J., Sadeghi, N., Schram, D. C. & Linss, V., 2014. Gas temperature determination from rotational lines in nonequilibrium plasmas: a review. *Plasma Sources Science and Technology*, 23(2), p. 023001.
- Brunet, H., Vincent, P. & Rocca Serra, J., 1983. Ionization mechanism in a nitrogen glow discharge. *Journal of Applied Physics*, 54(9), pp. 4951-4957.
- Brussaard, G. et al., 1998. Evidence for charge exchange between N^+ and $N_2(A^3\Sigma_u^+)$ in a low-temperature nitrogen plasma. *Chemical Physics Letters*, 290(4), pp. 379 - 384.
- Buldakov, M. A., Cherepanov, V. N., Korolev, B. V. & Mastrosov, I. I., 2002. Role of intramolecular interactions in Raman spectra of N₂ and O₂ molecules. *Journal of Molecular Spectroscopy* , 217(1), pp. 1-8.

Candler, G., 1988. The computation of weakly ionized hypersonic flows in thermo-chemical nonequilibrium. *PhD Thesis, Stanford University*.

Candler, G. V., Laux, C. O., Gessman, R. J. & Kruger, C. H., 1998. Numerical Simulation of a Nonequilibrium Nitrogen Plasma Experiment. *28th Plasmadynamics and Lasers Conference, Fluid Dynamics and Co-located Conferences*, Issue AIAA 1997-2365.

Casseau, V., Palharini, R. C., Scanlon, T. J. & Brown, R. E., 2016. A Two-Temperature Open-Source CFD Model for Hypersonic Reacting Flows, Part One: Zero-Dimensional Analysis. *Aerospace*, 4(34).

Cauchon, D. L., 1967. Radiative Heating Results from the Fire II Flight Experiment at a Reentry velocity of 11.4 km/s. *NASA TM-X-1402*.

Chan, G. C.-Y. et al., 2011. Elucidation of Reaction Mechanisms Responsible for Afterglow and Reagent-Ion Formation in the Low-Temperature Plasma Probe Ambient Ionization Source. *Analytical Chemistry*, 83(10), pp. 3675-3686.

Cipullo, A., Savino, L., Marenna, E. & De Filippis, F., 2012. Thermodynamic state investigation of the hypersonic air plasma flow produced by the arc-jet facility SCIROCCO". *Aerospace Science and Technology*, 23(1), pp. 358-362.

Committee on Human Spaceflight, U. N. R. C., 2014. *PATHWAYS TO EXPLORATION RATIONALES AND APPROACHES FOR A U.S. PROGRAM OF HUMAN SPACE EXPLORATION*. Washington D.C.: The National Academies Press.

Crandall, D. H. et al., 1974. Absolute cross sections for electron-impact excitation of N_2^+ . *Physical Review A*, Volume 9, pp. 2545-2551.

Cruden, B. A. & Brandis, A. M., 2017. Measurement and Prediction of Radiative Non-equilibrium for Air Shocks Between 7-9 km/s. *American Institute of Aeronautics and Astronautics*, Issue AIAA 2017-4535.

Da Silba, M. & Carvalho, B., 2016. High-Pressure $\text{H}_2/\text{He}/\text{O}_2$ Combustion Experiments for the Design of the ESTHER Shock-Tube Driver. *American Institute of Aeronautics and Astronautics*, Issue AIAA 2016-4156.

De Condorcet, N., 1795. *Outlines of an historical view of the Progress of the human mind*. s.l.:s.n.

Dec, J., Laub, B. & Braun, R., 2011. Two-Dimensional Finite Element Ablative Thermal Response Analysis of Arcjet Stagnation Tests. *American Institute of Aeronautics and Astronautics*, Issue AIAA 2011-3617.

Descartes, 1637. *Discours de la méthode*.

Devoto, R. S., Bauder, U. H., Cailleteau, J. & Shires, E., 1978. Air transport coefficients from electric arc measurements. *The Physics of Fluids*, Volume 21:4, pp. 552-558.

Dotchin, L. W., Chupp, E. L. & Pegg, D. J., 1973. Radiative lifetimes and pressure dependence of the relaxation rates of some vibronic levels in N₂⁺, N₂, CO⁺, and CO. *The Journal of Chemical Physics*, 59(8), pp. 3960-3967.

Drellishak, K. S., Aeschliman, D. P. & Cambel, A. B., 1965. Partition Functions and Thermodynamic Properties of Nitrogen and Oxygen Plasma. *The Physics of Fluids*, 8(9), pp. 1590-1600.

Eckbreth, A. C., 1996. *Laser Diagnostics for Combustion Temperature and Species*. s.l.:Taylor & Francis.

Edquist, K., Dyakonov, A., Wright, M. & Tang, C., 2009. Aerothermodynamic Design of the Mars Science Laboratory Backshell and Parachute Cone. *American Institute of Aeronautics and Astronautics*, Issue AIAA 2009-4078.

Fujita, K., Sato, S. & Abe, T., 2002. Experimental Investigation of Air Radiation from Behind a Strong Shock Wave. *Journal of Thermophysics and Heat Transfer*, 16(1), pp. 77-82.

Fujita, K., Sato, S., Abe, T. & Ebinuma, Y., 2002. Experimental Investigation of Air Radiation from Behind a Strong Shock Wave. *Journal of Thermophysics and Heat Transfer*, Volume 16, pp. 77-82.

Gessman, R. J., 2000. *An experimental investigation of the effects of chemical ionizational nonequilibrium in recombining atmospheric pressure air plasmas*, Stanford University: PhD Thesis.

Gessman, R. J., Laux, C. O. & Kruger, C. H., 1997. Experimental study of kinetic mechanisms of recombining atmospheric pressure air plasmas. *28th AIAA Plasmadynamics and Lasers Conference*, Issue AIAA 97-2364.

Gildfind, D. E., 2012. *Development of High Total Pressure Scramjet Flow Conditions using the X2 Expansion Tube*, Brisbane, Australia, University of Queensland: PhD Thesis.

Gildfind, D. E., Morgan, R. G. & Jacobs, P. A., 2016. Expansion Tubes in Australia. In: *Experimental Methods of Shock Wave Research*. s.l.:Springer International Publishing.

Gnoffo, P. A., 1999. Planetary-Entry Gas Dynamics. *Annual Review of Fluid Mechanics*, Issue 31.1, pp. 459-494.

Gollan, R. J., 2008. The computational modelling of high-temperatures gas effects with application to hypersonic flows. *PhD Thesis, University of Queensland*.

Gollan, R. J. & Jacobs, P. A., 2013. About the formulation, verification and validation of the hypersonic flow solver Eilmer. *International Journal for Numerical Methods in Fluids*, Volume 73.1, pp. 19-57.

Griem, H. R., 2005. *Principles of Plasma Spectroscopy*. s.l.:Cambridge University Press.

Grinstead, J. et al., 2011. Airborne Observation of the Hayabusa Sample Return Capsule Re-entry. *American Institute of Aeronautics and Astronautics*, Issue AIAA 2011-3329.

Gupta, R. N., Yos, J. M., Thompson, R. A. & Lee, K.-P., 1990. A Review of Reaction Rates and Thermodynamic and Transport Properties for an 11-Species Air Model for Chemical and Thermal Nonequilibrium Calculations to 30 000 K. *NASA technical report, NASA-RP-1232*.

Heppenheimer, T. A., 2007. Facing the Heat Barrier: A History of Hypersonics. *National Aeronautics & Space Administration*.

Hermann, T. et al., 2017. Influence of Ablation on Vacuum-Ultraviolet Radiation in a Plasma Wind Tunnel Flow. *Journal of Thermophysics and Heat Transfer*, 31(3), pp. 575-585.

Hermann, T. et al., 2019. Characterization of a Reentry Plasma Wind-Tunnel Flow with Vacuum-Ultraviolet to Near-Infrared Spectroscopy. *Journal of Thermophysics and Heat Transfer*, 30(3), pp. 673-688.

Herman, R. & Wallis, R. F., 1955. Influence of Vibration-Rotation Interaction on Line Intensities in Vibration-Rotation Bands of Diatomic Molecules. *The Journal of Chemical Physics*, 23(4), pp. 637-646.

Herzberg, G., 1950. *Molecular Spectra and Molecular Structure I: Spectra of Diatomic Molecules*. D. Van Nostrand.

Huber, K. P. & Herzberg, G., 1939. *Molecular Spectra And Molecular Structure, IV. Constants Of Diatomic Molecules*. Springer.

Igra, O. & Houas, L., 2016. Shock Tubes. In: *Experimental Methods of Shock Wave Research*. Springer International Publishing,, pp. 13-53.

Igra, O. & Seiler, F., 2016. *Experimental Methods of Shock Wave Research*. Springer International Publishing.

Jenniskens, P., 2010. Observations of the Stardust Sample Return Capsule Entry with a Slitless Echelle Spectrograph. *Journal of Spacecraft and Rockets*, 47(5), pp. 718-735.

Jenniskens, P., 2010. Observations of the Stardust Sample Return Capsule Entry with a Slitless Echelle Spectrograph. *Journal of Spacecraft and Rockets*, 47(5), pp. 718-735.

Johnson, S. M., 2013. *Thermal Protection Materials and Systems: Past, Present, and Future*. Daytona Beach, s.n.

Johnston, C. O., 2006. *Nonequilibrium Shock-Layer Radiative Heating for Earth and Titan Entry*, Virginia: Polytechnic Institute and State University.

Johnston, C. O. & Brandis, A. M., 2015. Features of Afterbody Radiative Heating for Earth Entry. *Journal of Spacecraft and Rockets*, Vol. 52, Volume 52, pp. 105-119.

Johnston, C. O., Brandis, A. M. & Panesi, M., 2016. Refinements to Afterbody Radiative Heating Simulations for Earth Entry. *American Institute of Aeronautics and Astronautics*, Issue AIAA 2016-3693.

Johnston, C. O., Gnoffo, P. A. & Mazaheri, A., 2013. Influence of Coupled Radiation and Ablation on the Aerothermodynamic Environment of Planetary Entry Vehicles. *Radiation and Gas-Surface Interaction Phenomena in High Speed Re-Entry; 6-8- May 2013.*

Johnston, C. O. & Kleb, B., 2012. Uncertainty Analysis of Air Radiation for Lunar-Return Shock Layers. *Journal of Spacecraft and Rockets*, 49(3), pp. 425-434.

Johnston, C. et al., 2013. Investigation of Nonequilibrium Radiation for Mars Entry. *American Institute of Aeronautics and Astronautics*, Issue AIAA 2013-1055.

Kistemaker, P. G. & De Vries, A. E., 1975. Rotational relaxation times in nitrogen-noble-gas mixtures. *Chemical Physics*, 7(3), pp. 371-382.

Klose, J. Z., Mervin Bridges, J. & Ott, W. R., 1988. Radiometric calibrations of portable sources in the vacuum ultraviolet. *Journal of Research of the National Bureau of Standards*, 93(1), pp. 21-39.

Krueger, A. J. & Minzner, R. I., 1976. A mid-latitude ozone model for the 1976 U.S. Standard Atmosphere. *Journal of Geophysical Research*, 81(24), pp. 4477-4481.

Larrabee, R. D., 1957. The Spectral Emissivity and Optical Properties of Tungsten. *Technical report (Massachusetts Institute of Technology. Research Laboratory of Electronics)* ; 328..

Laub, B., 2006. Use of Arc-Jet Facilities in the Design and Development of Thermal Protection Systems. *American Institute of Aeronautics and Astronautics*, Issue AIAA 2006-3292.

Laub, B. & Venkatapathy, E., 2003. Thermal protection system technology and facility needs for demanding future planetary missions. *Proceedings of the International Workshop Planetary Probe Atmospheric Entry and Descent Trajectory Analysis and Science*, pp. 239-247.

Laux, C., Gessman, R., Hilbert, B. & Kruger, C., 1995. Experimental study and modeling of infrared air plasma radiation. *American Institute of Aeronautics and Astronautics*, Issue AIAA 1995-2124.

Laux, C. O., 1993. Optical diagnostics and radiative emission of air plasmas. *PhD Thesis, Stanford University.*

Laux, C. O., Gessman, R. J., Kruger, C. H. & Davis, S. P., 2001. Rotational temperature measurements in air and nitrogen plasmas using the first negative system of N_2^+ . *Journal of Quantitative Spectroscopy and Radiative Transfer* 68, Volume 68, pp. 473-482.

Laux, C. O., Pierrot, L. & Gessman, R. J., 2012. State-to-state modeling of a recombining nitrogen plasma experiment. *Chemical Physics*, Volume 398, pp. 46-55.

Laux, C. O., Spence, T. G., Kruger, C. H. & Zare, R. N., 2003. Optical diagnostics of atmospheric pressure air plasmas. *Plasma Sources Science and Technology*, 12(2), pp. 125-138.

Laux, C. O. et al., 2009. Influence of Ablation Products on the Radiation at the Surface of a Blunt Hypersonic Vehicle at 10 km/s. *American Institute of Aeronautics and Astronautics*, Issue AIAA 2009-3925.

Lemal, A., Jacobs, C. M., Perrin, M.-Y. & Laux, C. O., 2012. Simulation of shock tube radiation measurements with a Collisional-Radiative model. *43rd AIAA Thermophysics Conference*, Issue AIAA 2013-1059.

Lempert, W. R. & Adamovich, I. V., 2014. Coherent anti-Stokes Raman scattering and spontaneous Raman scattering diagnostics of nonequilibrium plasmas and flows. *Journal of Physics D: Applied Physics*, 47(43).

Lewis, B. R. et al., 2008. A coupled-channel model of the Π_{3u} states of N₂: Structure and interactions of the $3s\sigma_g F_3^3\Pi_u$ and $3p\pi_u G_3^3\Pi_u$ Rydberg states. *The Journal of Chemical Physics*, 129(16), p. 164306.

Linss, V., Kupfer, H., Peter, S. & Richter, F., 2004. Two N₂⁺(B² Σ_u^+) populations with different Boltzmann distribution of the rotational levels found in different types of N₂/Ar discharges—improved estimation of the neutral gas temperature. *Journal of Physics D: Applied Physics*, 37(14), pp. 1935-1944.

Lo, A., Cléon, G., Vervisch, P. & Cessou, A., 2012. Spontaneous Raman scattering: a useful tool for investigating the afterglow of nanosecond scale discharges in air. *Applied Physics B*, 107(1), pp. 229-242.

Lofthus, A. & Krupenie, P. H., 1977. The spectrum of molecular nitrogen. *Journal of Physical and Chemical Reference Data*, 6(1), pp. 113-307.

Löhle, S., Hermann, T. & Zander, F., 2018. Experimental assessment of the performance of ablative heat shield materials from plasma wind tunnel testing. *CEAS Space Journal*, 10(2), pp. 203-211.

Long, D. A., 2002. *The Raman Effect: A Unified Treatment of the Theory of Raman Scattering by Molecules*. Wiley.

MacDonald, M. E. et al., 2015. Measurements of air plasma/ablator interactions in an inductively coupled plasma torch. *J. Thermophys. Heat Transfer*, Volume 29, pp. 12-23.

Massabieux, B. et al., 1983. Excitation of vibrational and electronic states in a glow discharge column in flowing N₂. *Journal of Physics B: Atomic and Molecular Physics*, 16(10), pp. 1863-1874.

McBride, B. J. & Gordon, S., June 1996. Computer Program for Calculation of Complex Chemical Equilibrium Compositions and Applications II. User's Manual and Program Description. *NASA RP-1311-P2*.

McGilvray, M., Doherty, L. J., Morgan, R. G. & Gildfind, D. E., 2015. T6: The Oxford University Stalker Tunnel. *American Institute of Aeronautics and Astronautics*, Issue AIAA 2015-3545.

McGuire, S. D., Tibère-Inglesse, A. C. & Laux, C. O., 2016. Infrared spectroscopic measurements of carbon monoxide within a high temperature ablative boundary layer. *Journal of Physics D: Applied Physics*, p. 49.

McGuire, S. D., Tibère-Inglesse, A. C. & Laux, C. O., 2017. Ultraviolet Raman spectroscopy of N₂ in a recombining atmospheric pressure plasma. *Plasma Sources Science and Technology*, 26(11), p. 115005.

Millikan, R. C. & White, D. R., 1963. Vibrational Energy Exchange between N₂ and CO. The Vibrational Relaxation of. *The Journal of Chemical Physics*, 39(1), pp. 98-101.

Millikan, R. C. & White, D. R., 1964. Vibrational relaxation in air. *American Institute of Aeronautics and Astronautics Journal*, 2(10), pp. 1844-1846.

Nagulapally, M. et al., 1998. Numerical Simulation of Nonequilibrium Nitrogen and Air Plasma Experiments. *29th AIAA, Plasmadynamics and Lasers Conference, Fluid Dynamics and Co-located Conferences*, Issue AIAA 1998-2665 .

Orwell, O., 1949. *1984*.

Owano, T. G., Kruger, C. H. & Beddini, R. A., 1993. Electron-ion three-body recombination coefficient of argon. *AIAA Journal*, 31(1), pp. 75-82.

Panesi, M., Jaffe, R. L., Schwenke, D. W. & Magin, T. E., 2013. Rovibrational internal energy transfer and dissociation of N₂(¹S_g⁺)—N(⁴S_u) system in hypersonic flows. *The Journal of Chemical Physics*, 138(4), p. 044312.

Panesi, M. et al., 2009. Fire II Flight Experiment Analysis by Means of a Collisional-Radiative Model. *Journal of Thermophysics and Heat Transfer*, 23(2), pp. 236-248.

Park, C., 1993. Review of chemical-kinetic problems of future NASA missions. I - Earth entries. *Journal of Thermophysics and Heat Transfer*, Volume 7:3, pp. 385-398 .

Park, C., 2004. Rotational Relaxation of N₂ Behind a Strong Shock Wave. *Journal of Thermophysics and Heat Transfer*, 18(4), pp. 527-533.

Parker, J. G., 1959. Rotational and Vibrational Relaxation in Diatomic Gases. *The Physics of Fluids*, Volume 2:4, pp. 449-462.

Partridge, H., Langhoff, S. R., Bauschlicher, C. W. & Schwenke, D. W., 1988. Theoretical study of the A'⁵S_g⁺ and C'⁵P_u states of N₂: Implications for the N₂ afterglow. *The Journal of Chemical Physics*, 88(5), pp. 3174-3186.

Plato, n.d.. *Laws*.

Polak, L. S., Slovetskii, D. I. & Sokolov, A. S., 1972. Dissociation of Nitrogen Molecules from Excited Electronic States. *High Energy Chemistry*, 6(340).

- Potter, D., 2011. *Modelling of radiating shock layers for atmospheric entry at Earth and Mars*, Brisbane, Australia: PdH Thesis, University of Queensland.
- Programme, U. N. D., 2000. *Human development report*.
- Rusterholtz, D., 2012. Nanosecond Repetitively Pulsed Discharges in Atmospheric Pressure Air. *PhD Thesis, Ecole Centrale Paris*, p. 113.
- Saint Augustine, n.d.. *The City of God against the Pagans*.
- Sharma, P. M. et al., 2018. One-dimensional modeling methodology for shock tubes: Application to the EAST facility. *American Institute of Aeronautics and Astronautics*, Issue AIAA 2018-4181.
- Sharma, S. P., 1992. Vibrational and rotational temperature measurements in a shock tube. *Proceedings of the Eighteenth International Symposium on Shock Waves*, Volume 1, pp. 683-690.
- Sharma, S. P. & Gillespie, W., 1991. Nonequilibrium and equilibrium shock front radiation measurements. *Journal of Thermophysics and Heat Transfer*, 5(3), pp. 257-265.
- Shneider, M. N., Baltuška, A. & Zheltikov, A. M., 2011. Population inversion of molecular nitrogen in an Ar: N₂ mixture by selective resonance-enhanced multiphoton ionization. *Journal of Applied Physics*, 110(8), p. 083112.
- Smith, R., Wagner, R. & Cunningham, J., 1998. A survey of current and future plasma arc-heated test facilities for aerospace and commercial applications. *American Institute of Aeronautics and Astronautics*, Issue AIAA 1998-146.
- Sonnenfroh, D. M. & Leone, S. R., 1989. A laser-induced fluorescence study of product rotational state distributions in the charge transfer reaction: Ar⁺(²P_{3/2})+N₂→Ar+N₂⁺(X) at 0.28 and 0.40 eV. *The Journal of Chemical Physics*, 90(3), pp. 1677-1685.
- Spencer, H., 1864. *Principles of Biology*.
- Stalker, R. J., 1967. Isentropic compression of shock tube driver gas. *Aerospace Research Laboratories*, Volume 30.
- Studer, D. & Vervisch, P., 2007. Raman scattering measurements within a flat plate boundary layer in an inductively coupled plasma wind tunnel. *Journal of Applied Physics*, 102(3), p. 033303.
- Sutton, G. W., 1982. The Initial Development of Ablation Heat Protection, An Historical Perspective. *Journal of Spacecraft and Rockets*, 19(1), pp. 3-11.
- Taine, J., Iacona, E. & Petit, J.-P., 2008. *Transferts thermiques: Introduction aux transferts thermiques*. s.l.:Dunod.
- Tauber, M. E. & Sutton, K., 1991. Stagnation-point radiative heating relations for earth and Mars entries. *Journal of Spacecraft and Rockets*, 28(1), pp. 40-42.

Taylor, M. J. & Jenniskens, P., 2010. Near-Infrared Spectroscopy of Stardust Sample Return Capsule Entry: Detection of Carbon. *Journal of Spacecraft and Rockets*, 47(6), pp. 878-883.

Touzeau, M. & Pagnon, D., 1978. Vibrational excitation of N₂(C) and N₂(B) by metastable argon atoms and the determination of the branching ratio. *Chemical Physics Letters*, Volume 15, pp. 355-360.

Turgot, 1750. *A Philosophical Review of the Successive Advances of the Human Mind..*

Valk, F. et al., 2010. Measurement of collisional quenching rate of nitrogen states N₂(C³Π_u, v = 0) and N₂⁺ (B²Σ_g⁺, v=0). *Journal of Physics D: Applied Physics*.

Venable, W., 1969. Observations of departures from equilibrium in a nitrogen arc. *Journal of Quantitative Spectroscopy and Radiative Transfer*, Volume 9, pp. 1215-1226.

Viggiano, A. A., Van Doren, J. M., Morris, R. A. & Paulson, J. F., 1990. Evidence for an influence of rotational energy on the rate constants for the reaction of Ar⁺(²P_{3/2}) with N₂. *The Journal of Chemical Physics*, 93(7), pp. 4761-4765.

Wada, Y. & Liou, M.-S., 1994. A flux splitting scheme with high-resolution and robustness for discontinuities. *American Institute of Aeronautics and Astronautics*, Issue AIAA 1994-0083.

Wei, H., 2017. *Air Radiation In Superorbital Expanding Flow*, Brisbane, Australia, University of Queensland: PhD Thesis.

Wei, H. et al., 2017. Experimental and Numerical Investigation of Air Radiation in Superorbital Expanding Flow. *American Institute of Aeronautics and Astronautics*, Issue AIAA 2017-4531.

Werner, H. & Reinsch, E., 1984. Accurate ab initio calculations of radiative transition probabilities between the A³Σ_u⁺, B³Π_g, W³Δ_u, B'³Σ_u⁻, and C³Π_u states of N₂. *The Journal of Chemical Physics*, 81(5), pp. 2420-2431.

Winter, M. W. et al., 2019. Radiation Modeling for Reentry of Hayabusa Sample Return Capsule. *Journal of Spacecraft and Rockets*, pp. 1-13.

Winter, M. W., Srinivasan, C., Charnigo, R. & Prabhu, D. K., 2018. Spectroscopic Analysis of Nonequilibrium Excited State Chemistry in a NASA Arc Jet. *Journal of Thermophysics and Heat Transfer*, 32(4), pp. 1088-1098 .

Wright, M. et al., 2011. Defining Ablative Thermal Protection System Margins for Planetary Entry Vehicles. *American Institute of Aeronautics and Astronautics*, Issue AIAA 2011-3757.

Wright, M., Loomis, M. & Papadopoulos, P., 2003. Aerothermal Analysis of the Project Fire II Afterbody Flow. *Journal of Thermophysics and Heat Transfer*, 17(2), pp. 240-249.

Yamada, G., Takayanagi, H., Fujita, K. & Suzuki, T., 2008. Measurements of Rovibrational Temperatures Derived from N₂(1+) and N₂(2+) behind Shock Waves. *40th Thermophysics Conference, Fluid Dynamics and Co-located Conference*.

Titre : Rayonnement de plasmas hors-équilibre en recombinaison

Mots clés : Entrée atmosphérique, plasmas d'air et d'azote, plasmas de recombinaison, spectroscopie d'émission, spectroscopie Raman spontanée, cinétique des plasmas

L'un des plus grands défis des missions prévues sur Mars est la phase d'entrée atmosphérique, lorsque le vaisseau spatial entre dans l'atmosphère de Mars à l'aller, ou de la Terre au retour. Les capsules spatiales entrent dans l'atmosphère à des vitesses hypersoniques ce qui comprime le gaz à l'avant de l'appareil et résulte en une augmentation de température jusqu'à la dissociation et l'ionisation du gaz. Ces phénomènes engendrent un rayonnement intense du gaz. Le flux radiatif arrivant sur la capsule est la principale source de chauffage de l'appareil mais de grandes incertitudes demeurent dans sa prédiction. En conséquence, le bouclier thermique est surdimensionné, augmentant la masse totale de l'appareil et diminuant sa charge utile. Ces

incertitudes sont maximales sur l'arrière-corps de l'appareil où le plasma l'entourant est forcé de se recombiner hors équilibre. Cette thèse présente une caractérisation expérimentale de plasma hors équilibre d'air et d'azote en recombinaison, typique des plasmas d'arrière-corps. Les distributions de la population de l'azote atomique et moléculaire sont mesurées, ainsi que le rayonnement hors équilibre de ces espèces. Des comparaisons avec les prédictions de codes numériques sont données, et de larges différences sont observées, soulignant les limites des modèles de mécanique des fluides numériques. Ces données expérimentales ont pour but d'être utilisées dans la validation des modèles présents dans les codes d'entrée atmosphérique.

Title : Radiation of nonequilibrium recombining plasma flows

Keywords : Atmospheric entry, air and nitrogen plasmas, recombining plasmas, Optical Emission Spectroscopy, Spontaneous Raman Spectroscopy, plasma kinetics

One of the main challenges for the upcoming Mars missions is the atmospheric entry phase when the spacecraft enters the Martian atmosphere or the Earth's atmosphere upon return. The hypersonic velocity of the capsule entering the atmosphere leads to extreme gas heating and results in intense gas radiation. The radiative flux emitted by the plasma in front and around the capsule is the main source of heating, but its prediction suffers from large uncertainties, leading engineers to apply safety margin on the heat shield, thereby decreasing the useful payload of the capsule. These uncertainties are maximal in the afterbody region where the plasma is forced to recombine

and can depart from equilibrium. This thesis presents an experimental characterization of recombining non-equilibrium air and nitrogen plasma flows to mimic the chemical kinetic dynamics encountered in the afterbody region. The population distributions of radiating atomic and molecular species of nitrogen are measured, along with the nonequilibrium radiation emitted by these species. Comparisons with predictions from numerical codes are made and large differences are observed even in simple test cases, thus highlighting the limits of current computational fluid dynamics models. These data are intended to serve as a basis to validate the models used in reentry codes

